TU Delft

Delft University of Technology

Document Version
Final published version

Citation (APA)
Li, M. (2026). *Catalyst Engineering and Mechanistic Insights into Electrochemical NOx Conversion in PEM Electrolyzer*. [Dissertation (TU Delft), Delft University of Technology]. https://doi.org/10.4233/uuid:9a710eb7-4fe1-4bc3-a159-181b788ae9d5

Important note
To cite this publication, please use the final published version (if applicable).
Please check the document version above.

Copyright
In case the licence states “Dutch Copyright Act (Article 25fa)”, this publication was made available Green Open Access via the TU Delft Institutional Repository pursuant to Dutch Copyright Act (Article 25fa, the Taverne amendment). This provision does not affect copyright ownership.
Unless copyright is transferred by contract or statute, it remains with the copyright holder.

Sharing and reuse
Other than for strictly personal use, it is not permitted to download, forward or distribute the text or part of it, without the consent of the author(s) and/or copyright holder(s), unless the work is under an open content license such as Creative Commons.

Takedown policy
Please contact us and provide details if you believe this document breaches copyrights.
We will remove access to the work immediately and investigate your claim.

This work is downloaded from Delft University of Technology.

Catalyst Engineering and Mechanistic Insights into Electrochemical NOx Conversion in PEM Electrolyzer

李 敏
Min Li

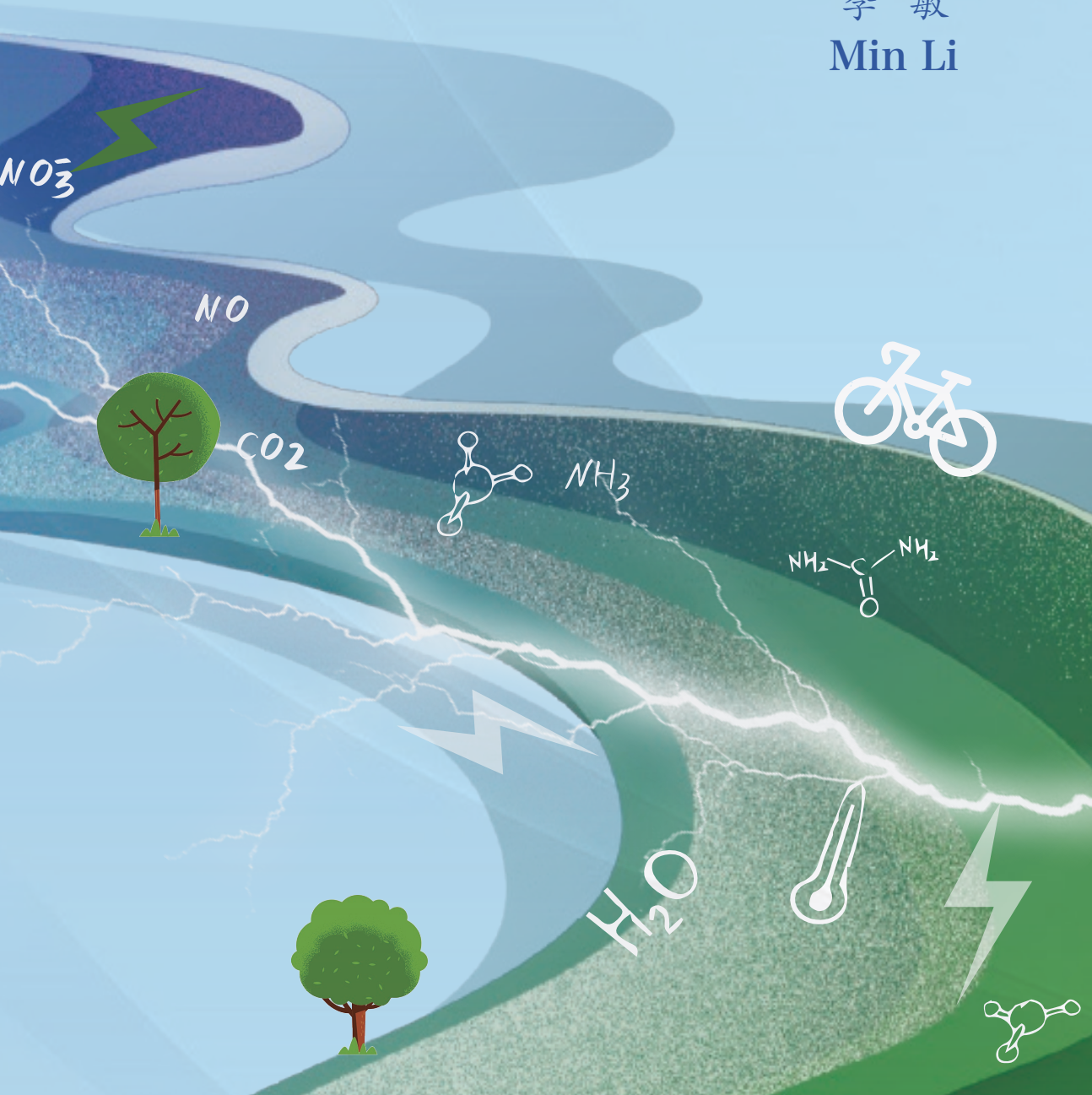

Catalyst Engineering and Mechanistic Insights into Electrochemical NO_x Conversion in PEM Electrolyzer

Catalyst Engineering and Mechanistic Insights into Electrochemical NO_x Conversion in PEM Electrolyzer

Dissertation

for the purpose of obtaining the degree of doctor

at Delft University of Technology

by the authority of the Rector Magnificus Prof.dr.ir. H. Bijl;

Chair of the Board for Doctorates

to be defended publicly on

Tuesday 31, March 2026 at 15:00

by

Min LI

This dissertation has been approved by the promotors.

Promotor: Prof. dr. ir. A. Urakawa
Promotor: Dr. R. Kortlever

Composition of the doctoral committee:

Rector Magnificus,	chairperson
Prof. dr. ir. A. Urakawa	Delft University of Technology (NL, promotor)
Dr. R. Kortlever	Delft University of Technology (NL, promotor)
Independent members:	
Prof. dr. F.M. Mulder	Delft University of Technology (NL)
Prof. dr. M.T.M. Koper	Leiden University (NL)
Prof. dr. F. Jiao	Washington University in St. Louis (USA)
Dr. D.M. Morales Hernández	University of Groningen (NL)
Dr. T.E. Burdyny	Delft University of Technology (NL)
Reserve member:	
Prof. dr. ir. J.R. Van Ommen	Delft University of Technology (NL)

The work in this dissertation has been carried out in the Catalysis Engineering (CE) section of the Department of Chemical Engineering, at the Faculty of Applied Sciences of the Delft University of Technology in the Netherlands. This work was funded by the China Scholarship Council.



Printed by: Proefschriftmaken | proefschriftmaken.nl

Front & Back: M. Li

Copyright © 2026 by M. Li
ISBN 978-94-6534-310-5

An electronic version of this dissertation is available at
http://repository.tudelft.nl/.

CONTENTS

Summary **vii**

Samenvatting **ix**

1 Introduction **1**
- 1.1 Background and context . . . 2
  - 1.1.1 The role of ammonia in our economy . . . 2
  - 1.1.2 Haber-Bosch process . . . 3
- 1.2 Electrochemical green ammonia production . . . 3
  - 1.2.1 Closing the nitrogen-cycle . . . 4
  - 1.2.2 Basic understanding of electrocatalytic NO_3^- and NO reduction . . . 5
  - 1.2.3 Electrochemical NO_3^- reduction coupling with bicarbonate for urea production . . . 9
- 1.3 Challenges towards carbon-neutral fertilizers . . . 10
- 1.4 Outline of this dissertation . . . 10

2 Electrochemical Nitrate Reduction with Polymer Modified Ru Nanoparticles **21**
- 2.1 Introduction . . . 22
- 2.2 Experimental method . . . 23
- 2.3 Results and discussion . . . 28
- 2.4 Conclusion . . . 39

Appendices **47**

3 Tuning Product Selectivity in Electroreduction of NO by MoS_2 Nanosheets **65**
- 3.1 Introduction . . . 66
- 3.2 Experimental method . . . 68
- 3.3 Results and Discussion . . . 70
- 3.4 Conclusion . . . 79

Appendices **87**

4 Selective-poisoning of HER by CO in NO Electroreduction **99**
- 4.1 Introduction . . . 100
- 4.2 Experimental method . . . 101
- 4.3 Results and Discussion . . . 102
- 4.4 Conclusion . . . 107

Appendices **113**

5 Bicarbonate and Nitrate co-electroreduction to Urea **123**
- 5.1 Introduction . . . 124
- 5.2 Experimental method . . . 125

5.3 Results and discussion . . . 129
5.3.1 Urea detection methods and challenges . . . 129
5.3.2 Bicarbonate reduction . . . 133
5.3.3 Electrochemical nitrate reduction . . . 139
5.3.4 Electrochemical urea synthesis . . . 140
5.4 Conclusion . . . 141

Appendices **149**

6 Probing Mechanistic Insights via ***operando*** ATR-IR Spectroscopy-Cell Design **155**
6.1 Introduction . . . 156
6.2 Design of a *operando* electrochemical ATR-IR cell . . . 158

7 Conclusion and Outlook **163**
7.1 Conclusion . . . 163
7.2 Outlook . . . 164

Acknowledgements **167**

Curriculum Vitæ **173**

List of Publications **175**

Summary

The rapid transition to zero-carbon fertilizers presents substantial challenges for conventional ammonia production via the Haber–Bosch process. Electrochemical ammonia synthesis offers a direct, sustainable route that relies only on water, electricity, and nitrogen recovered from waste streams-such as nitrate and gaseous nitrogen oxides (NO_x). To achieve high reaction rates under industrially relevant conditions, this dissertation employs a polymer electrolyte membrane (PEM) electrolyzer to conduct the experiments. Due to the high operating costs, we target the principal cost drivers through coordinated advances in catalyst design, interfacial mechanistic analysis, and cell-level engineering. In particular, mechanistic insight into the reaction pathway guides rational catalyst development.

In chapter 2, the size and surface properties of Ru/C catalyst for electrochemical nitrate reduction were re-engineered using polyvinylpyrrolidone (PVP). The Ru loading decreased from 40 to 10 wt.% while achieving the highest NH_3 faradaic efficiency. Meanwhile, the addition of PVP enhanced the electrochemically active surface area, hydrogen binding energy (HBE) and electrode wettability, which gives an insight into the catalyst design and tuning the selectivity.

In chapter 3, we explore non-critical, earth-abundant transition metal dichalcogenides (MoS_2) for the application of direct NO electroreduction. Our investigation shows that phase engineering regulates the electrocatalytic selectivity by steering sequential proton-electron-transfer pathways, thereby tuning product distributions in this complex multi-electron reduction.

In chapter 4, we report a CO-mediated selective poisoning strategy to suppress the hydrogen evolution reaction (HER) during electrochemical NO reduction, thereby enhancing NH_3 selectivity. By comparing catalysts with different CO*, NO*, and H* binding affinities, the study clarifies how competitive adsorption can be leveraged to the product distributions and provides valuable information to further C-N coupling reaction.

In chapter 5, we show a proof of concept of C-N coupling for urea synthesis from bicarbonate (HCO_3^-, sourced from direct air capture) and nitrate (NO_3^-, from wastewater). A robust, low-handling urea quantification protocol was established. First bicarbonate re-

duction was systematically optimized using gas-diffusion electrodes in PEM electrolyzer. After which, urea synthesis was performed, showing promising urea production, meanwhile further opening a door for more systematic investigation.

In the final chapter, we propose a new *operando* ATR-IR cell design which integrates a membrane and flow of reactant (both suitable for liquid phase nitrate and gaseous NO), to probe the reaction mechanism under operating conditions. The new design aims to bridge the current mechanistic gap between conventional batch-cell and membrane electrode assembly operation.

SAMENVATTING

De snelle overgang naar koolstofvrije meststoffen vormt een grote uitdaging voor de conventionele ammoniakproductie via het Haber-Bosch-proces. Elektrochemische ammoniaksynthese biedt een directe, duurzame route die alleen gebruikmaakt van water, elektriciteit en stikstof die wordt teruggewonnen uit afvalstromen, zoals nitraat en gasvormige stikstofoxiden (NO_x). Om hoge reactiesnelheden te bereiken onder industrieel relevante condities, maakt dit proefschrift gebruik van een elektrolyse-apparaat Met een polymeerelektrolytmembraan (PEM) om de experimenten uit te voeren. Vanwege de hoge exploitatiekosten richten we ons op de belangrijkste kostenfactoren door middel van gecoördineerde verbeteringen in het ontwerp van katalysatoren, mechanistische analyse van grensvlakken en technische ontwikkeling op celniveau. Met name mechanistisch inzicht in het reactiepad leidt tot rationele ontwikkeling van katalysatoren.

In hoofdstuk 2 zijn de grootte en oppervlakte-eigenschappen van de Ru/C-katalysator voor elektrochemische nitraatreductie opnieuw ontworpen met behulp van polyvinylpyrrolidon (PVP). De Ru-belading daalde van 40 naar 10 wt.%, terwijl de hoogste NH_3 faradaïsche efficiëntie werd bereikt. Tegelijkertijd verbeterde de toevoeging van PVP het elektrochemisch actieve oppervlak, de waterstofbindingsenergie (HBE) en de bevochtigbaarheid van de elektrode, wat inzicht geeft in het katalysatorontwerp en het afstemmen van de selectiviteit.

In hoofdstuk 3 hebben we niet-kritieke, in de aardbodem overvloedig aanwezige overgangsmetaaldichalcogeniden MoS_2 onderzocht voor de toepassing van directe NO elektroreductie. Ons onderzoek toonde aan dat fase-engineering de elektrokatalytische selectiviteit reguleert door sequentiële proton-elektron-overdrachtsroutes te sturen, waardoor de productverdelingen in deze complexe multi-elektronreductie worden afgestemd.

In hoofdstuk 4 rapporteerden we een CO-gemedieerde selectieve vergiftigingsstrategie om de waterstofevolutiereactie (HER) tijdens elektrochemische NO-reductie te onderdrukken, waardoor de NH_3 selectiviteit wordt verbeterd. Door katalysatoren met verschillende CO*, NO* en H* bindingsaffiniteiten te vergelijken, verduidelijkt de studie hoe competitieve adsorptie kan worden benut voor de productverdelingen en biedt het waardevolle informatie voor verdere C-N-koppelingsreacties.

In hoofdstuk 5 hebben we een haalbaarheidsonderzoek getoond van C-N-koppeling voor ureumsynthese uit bicarbonaat (HCO_3^-, afkomstig van directe luchtopvang) en nitraat (NO_3^-, uit afvalwater). Er werd een robuust protocol voor ureumkwantificering met weinig handelingen opgesteld. Eerst werd de bicarbonaatreductie systematisch geoptimaliseerd met behulp van gasdiffusie-elektroden in een PEM-elektrolyse-installatie. Daarna werd ureumsynthese uitgevoerd, wat veelbelovende ureumproductie opleverde en tegelijkertijd de deur opende voor verder systematisch onderzoek.

In het laatste hoofdstuk hebben we een nieuw *operando* ATR-IR celontwerp voorgesteld dat een membraan en een reactantstroom (beide geschikt voor nitraat in vloeibare fase en gasvormig NO) integreert om het reactiemechanisme onder bedrijfsomstandigheden te onderzoeken. Het nieuwe ontwerp heeft tot doel de huidige mechanistische kloof tussen conventionele batchcellen en membraanelektrode-assemblages te overbruggen.

1

Introduction

1

1.1 Background and context

Nitrogen, the fifth most abundant element on the earth, plays an essential role as a macronutrient for all living organisms. It is a fundamental constituent of numerous nitrogen-containing compounds, including proteins and hormones [1, 2]. Since the origin of life, a natural nitrogen cycle has regulated the flow of nitrogen among marine, terrestrial, and atmospheric ecosystems [3]. However, from the 20th century, human activities with massive fossil fuel combustion and extensive utilization of artificial nitrogen fertilizers in agriculture have significantly disrupted this cycle [4]. With the increasing demand of the growing global population, nitrogen fertilizers have been widely applied as a primary approach of nitrogen fixation to enhance agricultural productivity [5].

1.1.1 The role of ammonia in our economy

Currently, ammonia (NH_3) is a crucial nitrogen-containing compound widely used in agriculture and industries. The annual global ammonia demand reached 184 million metric tons in 2021 and is expected to grow at around 232 million metric tons in 2050 [6]. Beyond its traditional role in agriculture, NH_3 holds significant potential in facilitating the transition to a zero-carbon economy [7] (Figure 1.1):

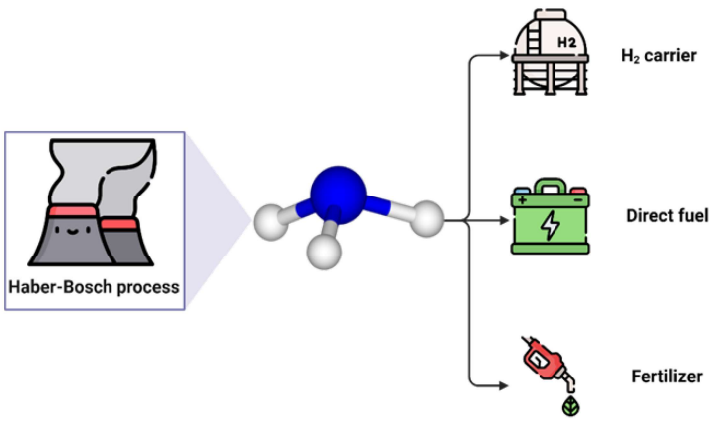

Figure 1.1: The role of ammonia in our society.

- **Medium for energy storage and transportation:** NH_3 can be easily liquefied by compression to around 10 bars at room temperature or by reducing the temperature to -33 °C at atmospheric pressure [8]. Its relatively low vapor pressure and high boiling point further simplify safe storage and transportation. Owing to its substantial hydrogen content (17.65%), high volumetric energy density (12.9 – 14.4 $MJ \cdot L^{-1}$) [9, 10], and well-developed infrastructure, NH_3 is considered an attractive

and sustainable hydrogen and energy carrier for future stationary and mobile uses [11].

- **Direct fuel:** In the context of direct ammonia fuel cells, NH_3 can be utilized directly as a fuel, producing nitrogen (N_2) and water (H_2O) as end products, thereby eliminating the emission of carbon monoxide (CO) and carbon dioxide (CO_2) [11, 12]. Notably, liquid NH_3 holds a high volumetric energy density, which significantly exceeds that of compressed hydrogen at 700 bars (approximately 8.5 $MJ \cdot L^{-1}$). This superior volumetric energy density renders NH_3 an attractive candidate for sustainable energy applications [13, 14].

- **Fertilizer:** Nitrogen is a critical nutrient required by plants and is frequently the primary factor limiting plant growth and agricultural productivity [15]. Synthetic fertilizers provide N primarily in the form of NH_3, which plants can readily absorb and utilize [16]. The application of NH_3-based fertilizers improves N availability, thereby promoting plant growth, enhancing photosynthesis, and ultimately resulting in higher crop yields [14, 17].

1.1.2 Haber-Bosch process

The Haber-Bosch process currently accounts for approximately 96% of global NH_3 production [6]. The process involves the reaction of nitrogen (N_2) and hydrogen (H_2) at high temperatures (500 °C) and pressures (>100 bar) [18]. H_2 feedstock is primarily produced via steam reforming of hydrocarbons such as natural gas, heavy oil, and coal, while emitting significant amounts of CO_2 [19] (Figure 1.2). Consequently, the Haber-Bosch process consumes around 2% of global annual energy and contributes over 300 million metric tons of greenhouse gas emissions each year [20]. To enhance single-pass conversion efficiency, the process incorporates chemical looping and demands continuous operation with sophisticated control and optimization [21]. This leads to high capital investments and substantial operating costs, thereby requiring the establishment of centralized NH_3 plants near abundant sources of H_2 feedstock. Such centralization limits the integration of intermittent renewable energy and restricts NH_3 availability in remote regions.

1.2 Electrochemical green ammonia production

Therefore, there is an urgent need to develop decarbonization strategies for NH_3 production, particularly to align with the net-zero carbon emission target [22, 23].

1

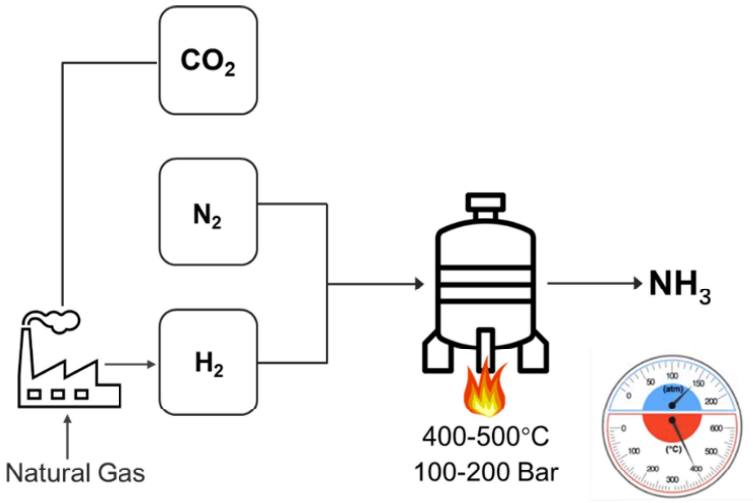

Figure 1.2: Simplified schematic of the conventional Haber-Bosch process.

1.2.1 Closing the nitrogen-cycle

In the nitrogen cycle, a diverse array of nitrogen-containing inorganic compounds is generated, including NH_3, hydrazine (N_2H_4), hydroxylamine (NH_2OH), nitrite (NO_2^-), nitrate (NO_3^-), nitrogen dioxide (NO_2) nitric oxide (NO), and nitrous oxide (N_2O), with many of which are recognized as environmental pollutants [4]. Extensive agricultural fertilization has led to significant NO_3^- and NO_2^- contamination in groundwater, posing serious risks to human health [24, 25]. NO_3^- removal remains challenging because of its intrinsic stability and high solubility. Current remediation strategies, such as anaerobic bacteria method or physicochemical process (e.g., electrodialysis, reverse osmosis, ion exchange resins, and hydrogen catalytic reduction) can achieve NO_3^- conversion [26]. However, the high installation expenses or substantial ongoing operational and maintenance costs limit their applicability [27]. In addition, the combustion of fossil fuels in power plants, automotive engines, and industrial facilities releases large quantities of gaseous nitrogen oxides (NO_x), which contribute substantially to atmospheric pollution [28]. Therefore, the removal of NO_x from flue gas represents a major focus in current catalytic chemistry. At present, the predominant method for NO_x mitigation is selective catalytic reduction (SCR), typically employing NH_3 [29, 30] or H_2 [31] as a reductant within a temperature range of 200-400 °C. However, the high energy demand and requirement of reducing agent of SCR processes presents a key limitation to sustainability and economic feasibility [32].

Therefore, electrocatalytic reduction offers a more energy-efficient way to close the artificial nitrogen cycle. This dissertation focuses mainly on electrochemical NO_3^- reduction

(NO_3RR) and NO reduction (NORR), as shown in Figure 1.3. Nonetheless, compared to electrochemical N_2 reduction (NRR), which suffers from the high dissociation energy of the N≡N (941 kJ·mol^{-1}) and the competition of the hydrogen evolution reaction (HER), electrochemical NO_3^-/NO reduction has low bonding energies (204 kJ·mol^{-1} for the N=O and 176 kJ·mol ^{1} for the N-O bond) [33, 34]. Thus, the process presents thermodynamic advantages: the standard reduction potential of NO_3^- and NO to NH_3 (0.88 V and 0.71 V vs. RHE, respectively) is significantly more positive than that of the nitrogen reduction reaction (0.093 V vs. RHE) [35]. Moreover, low concentration gaseous NO_x can be generated through the plasma N_2 oxidation process, which can be further combined with the NORR for NH_3 production [36, 37].

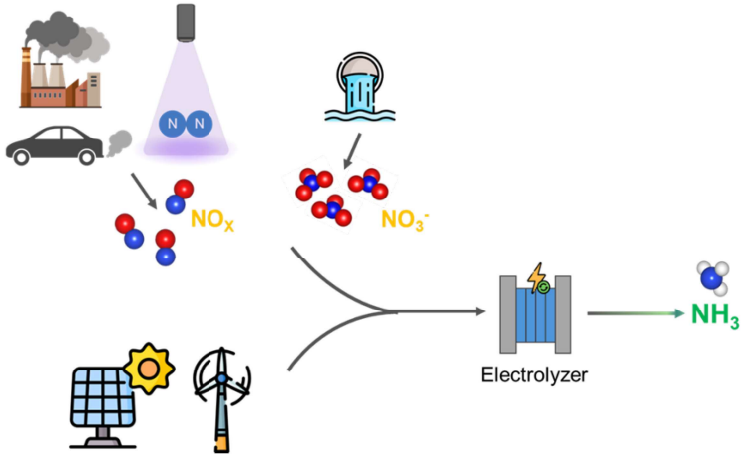

Figure 1.3: Schematic of NO_3RR and NORR for NH_3 production.

1.2.2 Basic understanding of electrocatalytic NO_3^- and NO reduction

Electrolyzers

The application of renewable electricity in electrolyzers enables the electrochemical reduction of NO_3^- or NO into NH_3, effectively facilitating chemical storage of renewable energy. This approach, operating under ambient conditions, is driven by electricity in the form of electrochemical potential. Consequently, it avoids harsh operational conditions and substantial capital investments of traditional Haber-Bosch process, thereby enhancing the operational flexibility.

Historically, electrochemical H-cells dominated the landscape of cell technology. In this configuration, illustrated schematically in Figure 1.4(a), a cathode-typically a metallic electrode-facilitates the reduction reactions within an electrolyte solution. Meanwhile,

1

a reference electrode is commonly used to maintain potential control, and an anode is used as the counter electrode for concurrent oxidation reactions. Despite its widespread early application, the H-cell configuration exhibits significant limitations when applied to NO_3RR or NORR. Primarily, the pronounced ohmic losses lead to substantial overpotentials, undermining industrial applicability. Moreover, severe mass-transport constraints emerge at gaseous NO reduction, due to the low solubility of NO in aqueous media (1.92 $mmol \cdot L^{-1} \cdot atm^{-1}$ at 25 °C) [38] and NO_3^- reduction at high current densities [39].

Therefore, utilizing membrane electrode assembly (MEA) configurations can overcome the above issues. Our focus is more specifically on a polymer electrolyte membrane (PEM) electrolyzer, which is widely used in the field of water electrolysis and fuel cells (Figure 1.4 (b). In this configuration, a polymeric ion exchange membrane is employed to replace the liquid catholyte layer, which reduces the ionic pathway of species involved in the reaction and enables the cell to operate at a lower total voltage due to reduced ohmic resistance [40]. Beyond the traditional H-cell configuration, a PEM electrolyzer facilitates more controlled reagent flow and reaction kinetics, making it attractive for future NO_3RR and NORR technologies [41].

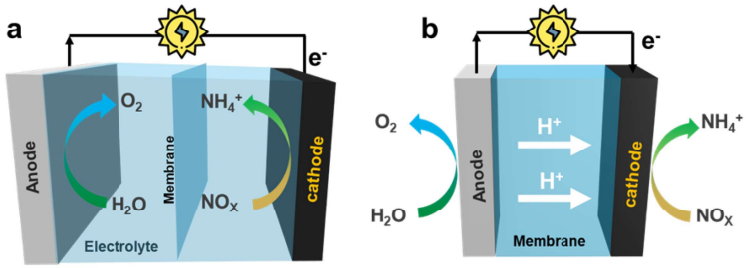

Figure 1.4: (a) H-cell and (b) PEM cell for NO_3RR and NORR (Here, NO_3^- and NO are simplified to NO_x).

Catalysts

Product selectivity among the numerous possible reaction pathways is predominantly determined by the selected catalyst. Typically, a metallic catalytic layer at the cathode-electrolyte interface facilitates the process by absorbing reactants (e.g.NO_3^- or NO), transferring electrons to the catalytic active sites, and subsequently releasing the reduced products. Recent advances in NO_3RR and NORR have primarily emphasized the development and evaluation of metal-based catalyst, both precious [40, 42, 43] and non-precious [40, 44–46], as illustrated in Figure 1.5.

The NO_3RR and NORR to NH_3 is a complex multi-electron and proton transfer pro-

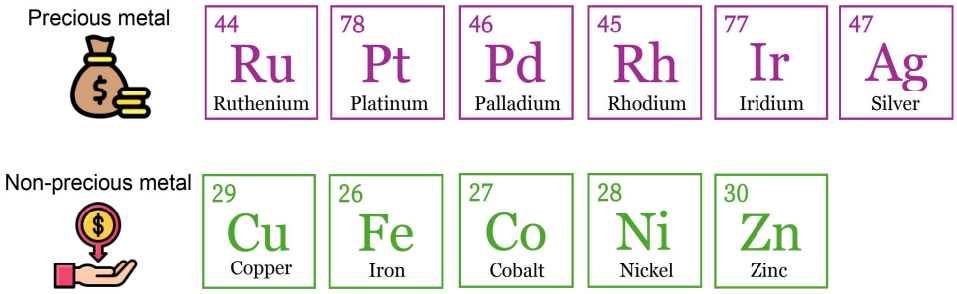

Figure 1.5: Most studied catalysts for NO_3RR and NORR for NH_3 production.

cess, which involves both the adsorbed active atomic hydrogen-mediated pathway and the electron transfer and proton reduction pathway [34]. The mechanism significantly varies depending on the catalysts. The adsorbed active atomic hydrogen-mediated pathway involves adsorbed atomic hydrogen (H*), which is produced through the Volmer process, while the other pathway proceeds directly through sequential electron and proton transfer [47]. For catalysts with strong adsorption affinity toward atomic hydrogen (e.g., Pt, Pd, Rh) [48], the reduction predominantly follows the atomic hydrogen-mediated mechanism (as shown in Figure 1.6(a)-blue path). For NO_3^-, atomic hydrogen reduced NO_3^-* to form adsorbed nitrogen N* intermediates. These nitrogen intermediates are subsequently hydrogenated to NH_3. The N-H bond mediated by H* is easier to obtain than the N-N bond formation, which results in the high selectivity of NH_3 production [49]. In addition, this atomic hydrogen-mediated reduction path generally occurs under relatively low overpotential conditions, thus HER will be more competitive [50].

The electron transfer and proton reduction pathway is typically predominant on the catalysts with lower binding affinity for H but a strong affinity towards NO_3^- [51], as shown in Figure 1.6(a)-red path. In this pathway, firstly, the NO_3^-* reduced to NO_2^-* via an electrochemical-chemical-electrochemical (ECE) process, which is considered the rate-determining step [52], because electron injection into the lowest unoccupied molecular orbital (LUMO *) of NO_3^- is energetically challenging [53]. Using catalysts (Cu, Ag, Pt, etc.) with d-orbital energy levels closely aligned with the LUMO * of NO_3^-, can facilitate more efficient electron transfer for the reduction of NO_3^- [54, 55]. Then, NO_2^-* is reduced to NO* by electron transfer and hydrolysis reactions, which is a crucial intermediate for further reactions [50, 56].

For electrochemical NO reduction, NO* is the reactant and key intermediate, which is aligned with the nitrate reduction mechanism (Figure 1.6(b)). Therefore, for the further

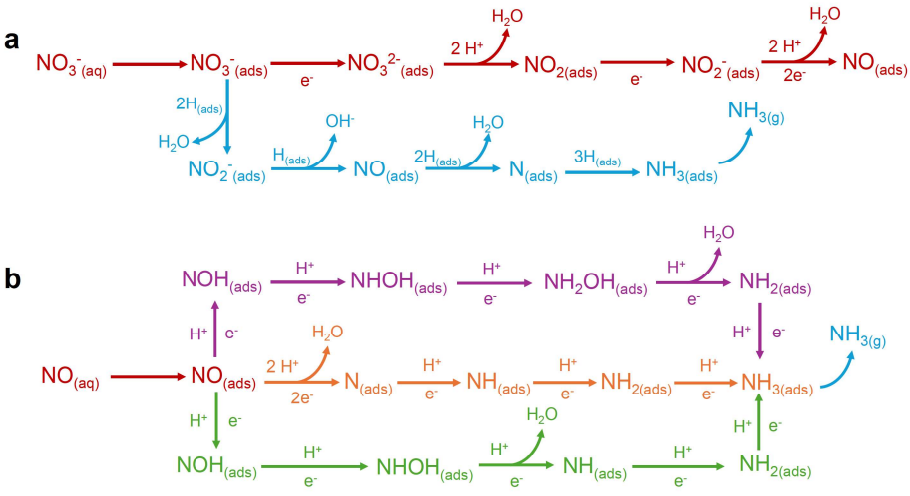

Figure 1.6: Overview of reaction mechanisms in NO_3RR and NORR [54].

reduction of NO*, similar reaction mechanisms are expected with similar catalysts for both reactions. For the direct electrochemical NO reduction, the reaction could also be conducted through atomic hydrogen-mediated mechanism, as described before [57, 58].

Continuing with the electron transfer and proton reduction pathway, the NO* could get an electron to produce HNO* and subsequently go through the reaction path of HNOH*→NH_2OH*→NH_2*→NH_3 [59] or HNOH*→NH*→NH_2*→NH_3 [60]. Notably, the NH_2OH* intermediates are easily desorbed from the catalyst surface to produce byproduct NH_2OH [61]. In contrast, the formation of N_2O formation could proceed via a Langmuir–Hinshelwood mechanism, involving dimeric intermediates such as ON-NO, NOH-NO, and HON-NOH, or through an Eley–Rideal pathway facilitated by solvated NO molecules [62, 63].

For an electrocatalyst to be ideal for NO_3^-/NO reduction, it should have high faradaic efficiency at low overpotentials. This requirement is challenging because the hydrogen evolution reaction (HER) competes in a similar potential region [64]. For instance, Cu demonstrates higher selectivity toward NH_3 than Pt [51, 60], primarily because Pt-based catalysts, known for their exceptional HER activity, compete for active sites for NO* and H* [58]. Moreover, sluggish HER kinetics can limit proton availability, hindering subsequent hydrogenation steps. As a result, optimal catalysts should operate at potentials slightly above the HER onset to maximize NH_3 faradaic efficiency.

1.2.3 Electrochemical NO_3^- reduction coupling with bicarbonate for urea production

In recent years, significant progress has been made to enhance the electrocatalytic conversion of NO_3^- to NH_3. Beyond that, an emerging and relatively unexplored direction is the direct synthesis of urea from NO_3^- and bicarbonate (HCO_3^-). Electrochemical bicarbonate reduction (HCO_3RR) can be conducted in a PEM electrolyzer which has a local acidic environment at the cathode. Protons (H^+) from water splitting and transported through membrane react with HCO_3^- and form CO_2 for subsequent reduction. The in-situ generation of CO_2 increases its local concentration near the electrode surface, facilitating efficient conversion. Thus, combing HCO_3^- and NO_3^- reduction offers a promising alternative pathway for direct nitrogen-based fertilizer-urea production [65].

One of the earliest known studies on electrochemical urea synthesis from CO_2 and NO_3^- was conducted by Shibata et al. in 1998 [66], where various metal catalysts were evaluated using a flow cell system. Among the tested catalysts, zinc exhibited the highest FE for urea production (40%), followed by copper (25% FE). However, due to the lack of control experiments and comprehensive characterization, this study shows low credibility but inspires the researchers to study this field. At present, research in electrochemical urea synthesis remains at an early stage, with a primary focus on developing advanced catalysts and materials [67]. In the one-step synthesis approach, the design of catalysts offers both high efficiency and selectivity, meanwhile suppressing side reactions is crucial.

In urea synthesis, achieving effective C-N coupling significantly depends on the spatial proximity of reaction intermediates [68]. Recent investigations have highlighted the importance of surface-bound species such as NO* and CO* as pivotal intermediates during this process [69]. A DFT study performed by Qiu et al. [70] suggested a stepwise reaction pathway where two adsorbed NO* species initially couple with CO*, forming the ONCONO* intermediate, which subsequently undergoes protonation steps towards urea production. Similarly, Luo et al. [71] proposed a mechanism involving alternating coupling and protonation steps but extended this concept by incorporating higher oxidation-state intermediates, such as NO_2* and CO_2*. These mechanistic insights emphasize that the efficiency of urea formation via C-N coupling is influenced by the interplay between coupling and protonation steps [22, 72–74]. Thus, further investigation into balancing these competing reactions present promising directions for enhancing electrochemical urea synthesis performance.

1

1.3 Challenges towards carbon-neutral fertilizers

Based on the advancements discussed earlier in this chapter, several critical knowledge gaps remain in the field of electrochemical synthesis of nitrogen-based fertilizers. Although the field has experienced rapid progress and continues to expand, there are inherent limitations that must be addressed to enable practical scale-up of these technologies.

A primary challenge is the limited understanding of reaction mechanisms under realistic operating conditions. Most mechanistic studies are conducted in batch or H-cell configurations, which differ substantially from MEA electrolyzers, where local reactant concentration, pH, current densities and overpotential strongly influence activity and selectivity. Consequently, mechanisms derived from simplified systems may not accurately describe actual operating conditions. This limitation is further complicated by the increasing focus on complex electrocatalyst designs. Without a detailed, *operando*-level understanding of reaction pathways, efforts to design the next generation of electrocatalysts optimized for MEA systems will be greatly hampered.

Secondly, extended from the original applications such as fuel cells and water electrolysis [75], PEM electrolyzers have great potential for liquid phase HCO_3^-/NO_3^- electrolysis or gaseous NO or CO_2 electrolysis, but they face inherent technical challenges that remain difficult to overcome. The acidic cathode-membrane interface promotes the HER, especially at high current densities. Excess hydrogen generation not only reduces selectivity but also introduces safety concerns during prolonged operation. Additionally, the hydrophobicity of gas diffusion layers (GDLs) is critical for stable gas-phase electroreduction. In gas-fed NO/CO_2 systems, flooding of carbon-based GDLs can lead to the formation of a water layer over the cathode, impairing catalytic performance. While industrial vapor-fed hydrogen systems partially mitigate this problem, they do not eliminate it entirely. Conversely, liquid-phase NO_3^-/HCO_3^- reduction processes benefit from more hydrophilic carbon-based GDLs. Overall, optimizing cell architecture and operating parameters is essential to achieve stable and efficient performance across different electrochemical systems.

1.4 Outline of this dissertation

This dissertation aims to increase the insight into electrocatalytic synthesis of nitrogen-based fertilizer. More specifically, it focuses on electrocatalytic NO_x (both gas and liquid phase) conversion to NH_3 using PEM electrolyzer and provides novel insights into reaction mechanisms at the cathode interface. Furthermore, utilizing waste materials (such as HCO_3^- from capturing CO_2 in the air, and NO_3^- from wastewater) as reactants in elec-

trochemical processes can create new remediation directions towards C-N coupling urea synthesis.

Chapter 2 aims to lower the metal loading of as-studied Ru based electrocatalyst and increase the performance for electrochemical nitrate reduction. By using PVP (polyvinylpyrrolidone) as the capping agent to control the Ru particle size and improve the metal utilization efficiency, we successfully reduced the metal loading from 40 to 10 wt.% with achieving the highest NH_3 faradic efficiency and study the effect of PVP on the electrochemically active surface area (ECSA), hydrogen binding energy (HBE) and electrode wettability over the cathode catalyst. This chapter has been submitted for publication.

Chapter 3 attempts to utilize non-critical materials-based catalysts for the direct nitric oxide electroreduction reaction, mainly focusing on low-cost transition metal dichalcogenides (TMDs) of MoS_2. These materials have been widely studied in electrochemical hydrogen evolution reaction for green hydrogen production with a comparable performance to Pt-based electrocatalysts. In this light, we synthesized these materials to study their performance towards electrochemical ammonia synthesis. A publication based on this chapter is ready to be submitted.

Chapter 4 reports a CO-mediated selective poisoning strategy with the aim of enhancing the faradaic efficiency towards ammonia by suppressing the hydrogen evolution reaction in direct electroreduction of nitric oxide. To gain a deeper understanding, catalysts with different binding affinities towards CO*, NO* and H* were investigated, which provides insightful basis and understanding for the extended application of coupling of C-N products reaction. This chapter has been published in ChemSusChem.

Chapter 5 provides a preliminary investigation of direct synthesis of C-N coupling products of urea from bicarbonate and nitrate. In this chapter, we detail a suitable, reliable and robust method for urea detection with less sample handling and pre-treatment compared to other reported methods. This chapter also includes a systematic investigation of the different carbon-based gas diffusion layers (GDL), Nafion loading based on Cu catalyst to optimize the cell configuration for electrochemical bicarbonate reduction separately. After conducting both bicarbonate and nitrate electroreduction successfully, we proceed to combine both for C-N coupling reaction. This work shows potential for direct electrocatalytic C-N synthesis in PEM electrolyzer. Systematic cell operation parameters investigation and catalysts design are necessary to achieve the activity towards urea synthesis.

Chapter 6 introduces an innovative *operando* ATR-IR cell design that advances beyond conventional batch-cell configurations, establishing a direct bridge to membrane elec-

trode assembly (MEA) systems. This design enables mechanistic studies under practical operating conditions by incorporating both membrane and dynamic reactant flow.

This dissertation is concluded by a summary and outlook of all the chapters mentioned above.

References

1. Canfield, D. E., Glazer, A. N. & Falkowski, P. G. The evolution and future of earth's nitrogen cycle. *Science* **330,** 192–196 (2010).
2. Lehnert, N., Dong, H. T., Harland, J. B., Hunt, A. P. & White, C. J. Reversing nitrogen fixation. *Nature Reviews Chemistry* **2,** 278–289 (2018).
3. Falkowski, P. G. Evolution of the nitrogen cycle and its influence on the biological sequestration of CO_2 in the ocean. *Nature* **387,** 272–275 (1997).
4. Galloway, J. N., Townsend, A. R., Erisman, J. W., Bekunda, M., Cai, Z., Freney, J. R., Martinelli, L. A., Seitzinger, S. P. & Sutton, M. A. Transformation of the nitrogen cycle: recent trends, questions, and potential solutions. *Science* **320,** 889–892 (2008).
5. Mingolla, S. & Rosa, L. Low-carbon ammonia production is essential for resilient and sustainable agriculture. *Nature Food* (2025).
6. Smith, C., Hill, A. K. & Torrente-Murciano, L. Current and future role of Haber–Bosch ammonia in a carbon-free energy landscape. *Energy & Environmental Science* **13,** 331–344 (2020).
7. Chatterjee, S., Parsapur, R. K. & Huang, K.-W. Limitations of ammonia as a hydrogen energy carrier for the transportation sector. *ACS Energy Letters* **6,** 4390–4394 (2021).
8. Giddey, S., Badwal, S. P. S., Munnings, C. & Dolan, M. Ammonia as a renewable energy transportation media. *ACS Sustainable Chemistry & Engineering* **5,** 10231–10239 (2017).
9. Lan, R., Irvine, J. T. S. & Tao, S. Ammonia and related chemicals as potential indirect hydrogen storage materials. *International Journal of Hydrogen Energy* **37,** 1482–1494 (2012).
10. Andersson, J. & Grönkvist, S. Large-scale storage of hydrogen. *International Journal of IIydrogen Energy* **44,** 11901–11919 (2019).
11. Wan, Z., Tao, Y., Shao, J., Zhang, Y. & You, H. Ammonia as an effective hydrogen carrier and a clean fuel for solid oxide fuel cells. *Energy Conversion and Management* **228,** 113729 (2021).
12. Valera-Medina, A., Xiao, H., Owen-Jones, M., David, W. I. F. & Bowen, P. J. Ammonia for power. *Progress in Energy and Combustion Science* **69,** 63–102 (2018).

13. Lan, R. & Tao, S. Ammonia as a suitable fuel for fuel cells. *Frontiers in Energy Research* **Volume 2 - 2014** (2014).
14. Zhao, Y., Setzler, B. P., Wang, J., Nash, J., Wang, T., Xu, B. & Yan, Y. An efficient direct ammonia fuel cell for affordable carbon-neutral transportation. *Joule* **3,** 2472–2484 (2019).
15. Zarebska, A., Romero Nieto, D., Christensen, K. V., Fjerbæk Søtoft, L. & Norddahl, B. Ammonium fertilizers production from manure: A critical review. *Critical Reviews in Environmental Science and Technology* **45,** 1469–1521 (2015).
16. Philibert, C. Producing ammonia and fertilizers: new opportunities from renewables. *IEA Rep,* 1–6 (2017).
17. Society, R. *Ammonia: Zero-carbon fertiliser, fuel and energy store: policy briefing* (Royal Society, 2020).
18. Appl, M. in *Ullmann's Encyclopedia of Industrial Chemistry* (2000).
19. Rafiqul, I., Weber, C., Lehmann, B. & Voss, A. Energy efficiency improvements in ammonia production—perspectives and uncertainties. *Energy* **30,** 2487–2504 (2005).
20. Chen, J. G., Crooks, R. M., Seefeldt, L. C., Bren, K. L., Bullock, R. M., Darensbourg, M. Y., Holland, P. L., Hoffman, B., Janik, M. J., Jones, A. K., *et al.* Beyond fossil fuel–driven nitrogen transformations. *Science* **360,** eaar6611 (2018).
21. Fernandez, C. A. & Hatzell, M. C. Economic considerations for low-temperature electrochemical ammonia production: achieving Haber-Bosch parity. *Journal of The Electrochemical Society* **167,** 143504 (2020).
22. Cheng, M., Wang, S., Dai, Z., Xia, J., Zhang, B., Feng, P., Zhu, Y., Zhang, Y. & Zhang, G. Rectifying heterointerface facilitated C-N coupling dynamics enables efficient urea electrosynthesis under ultralow potentials. *Angewandte Chemie International Edition* **64,** e202413534 (2025).
23. Soloveichik, G. Electrochemical synthesis of ammonia as a potential alternative to the Haber–Bosch process. *Nature Catalysis* **2,** 377–380 (2019).
24. Manassaram Deana, M., Backer Lorraine, C. & Moll Deborah, M. A review of nitrates in drinking water: maternal exposure and adverse reproductive and developmental outcomes. *Environmental Health Perspectives* **114,** 320–327 (2006).
25. Brender, J. D. in *Just Enough Nitrogen: Perspectives on how to get there for regions with too much and too little nitrogen* (eds Sutton, M. A., Mason, K. E., Bleeker, A., Hicks, W. K., Masso, C., Raghuram, N., Reis, S. & Bekunda, M.) 283–294 (Springer International Publishing, Cham, 2020).
26. Rezvani, F., Sarrafzadeh, M.-H., Ebrahimi, S. & Oh, H.-M. Nitrate removal from drinking water with a focus on biological methods: a review. *Environmental Science and Pollution Research* **26,** 1124–1141 (2019).

27. Niu, S., Yang, J., Qian, L., Zhou, D., Du, P., Si, N., Gu, X., Jiang, D. & Feng, Y. Electrochemical nitrate reduction to ammonia – recent progress. *ChemElectroChem* **10,** e202300419 (2023).
28. Armor, J. N. Environmental catalysis. *Applied Catalysis B: Environmental* **1,** 221–256 (1992).
29. Mathieu, O. & Petersen, E. L. Experimental and modeling study on the high-tempera ture oxidation of ammonia and related NO_x chemistry. *Combustion and Flame* **162,** 554–570 (2015).
30. Shrestha, K. P., Seidel, L., Zeuch, T. & Mauss, F. Detailed kinetic mechanism for the oxidation of ammonia including the formation and reduction of nitrogen oxides. *Energy & Fuels* **32,** 10202–10217 (2018).
31. Muhammad Farhan, S., Pan, W., Zhijian, C. & JianJun, Y. Innovative catalysts for the selective catalytic reduction of NO_x with H_2: A systematic review. *Fuel* **355,** 129364 (2024).
32. Zhao, S., Peng, J., Ge, R., Wu, S., Zeng, K., Huang, H., Yang, K. & Sun, Z. Research progress on selective catalytic reduction (SCR) catalysts for NO_x removal from coal-fired flue gas. *Fuel Processing Technology* **236,** 107432 (2022).
33. Van Langevelde, P. H., Katsounaros, I. & Koper, M. T. M. Electrocatalytic nitrate reduction for sustainable ammonia production. *Joule* **5,** 290–294 (2021).
34. Lu, X., Song, H., Cai, J. & Lu, S. Recent development of electrochemical nitrate reduction to ammonia: A mini review. *Electrochemistry Communications* **129,** 107094 (2021).
35. Wan, H., Bagger, A. & Rossmeisl, J. Electrochemical nitric oxide reduction on metal surfaces. *Angewandte Chemie International Edition* **60,** 21966–21972 (2021).
36. Wang, W., Patil, B., Heijkers, S., Hessel, V. & Bogaerts, A. Nitrogen fixation by gliding arc plasma: Better insight by chemical kinetics modelling. *ChemSusChem* **10,** 2145–2157 (2017).
37. Wu, A., Yang, J., Xu, B., Wu, X.-Y., Wang, Y., Lv, X., Ma, Y., Xu, A., Zheng, J., Tan, Q., *et al.* Direct ammonia synthesis from the air via gliding arc plasma integrated with single atom electrocatalysis. *Applied Catalysis B: Environmental* **299,** 120667 (2021).
38. Sander, R. Compilation of Henry's law constants (version 5.0.0) for water as solvent. *Atmos. Chem. Phys.* **23,** 10901–12440 (2023).
39. Yuan, T., Li, M., Subramanian, S., Kok, J., Li, M., Urakawa, A., Voznyy, O. & Burdyny, T. Sequential electrocatalytic reactions along a membrane electrode assembly drive efficient nitrate-to-ammonia conversion. *Cell Reports Physical Science* **5** (2024).

40. Bunea, S., Clemens, K. & Urakawa, A. Electrified conversion of contaminated water to value: selective conversion of aqueous nitrate to ammonia in a polymer electrolyte membrane cell. *ChemSusChem* **15,** e202102180 (2022).
41. Bunea, S., Coppens, M. & Urakawa, A. Electrochemical conversion of NO to NH_3 in a PEM cell. *ACS Catalysis* **13,** 11345–11351 (2023).
42. Zhu, J.-Y., Xue, Q., Xue, Y.-Y., Ding, Y., Li, F.-M., Jin, P., Chen, P. & Chen, Y. Iridium nanotubes as bifunctional electrocatalysts for oxygen evolution and nitrate reduction reactions. *ACS applied materials & interfaces* **12,** 14064–14070 (2020).
43. Wang, Z., Young, S. D., Goldsmith, B. R. & Singh, N. Increasing electrocatalytic nitrate reduction activity by controlling adsorption through PtRu alloying. *Journal of Catalysis* **395,** 143–154 (2021).
44. Fan, X., Xie, L., Liang, J., Ren, Y., Zhang, L., Yue, L., Li, T., Luo, Y., Li, N. & Tang, B. In situ grown Fe_3O_4 particle on stainless steel: A highly efficient electrocatalyst for nitrate reduction to ammonia. *Nano Research* **15,** 3050–3055 (2022).
45. Wang, D., Chen, Z.-W., Gu, K., Chen, C., Liu, Y., Wei, X., Singh, C. V. & Wang, S. Hexagonal cobalt nanosheets for high-performance electrocatalytic NO reduction to NH_3. *Journal of the American Chemical Society* **145,** 6899–6904 (2023).
46. Wang, Y., Xu, A., Wang, Z., Huang, L., Li, J., Li, F., Wicks, J., Luo, M., Nam, D.-H., Tan, C.-S., *et al.* Enhanced nitrate-to-ammonia activity on copper–nickel alloys via tuning of intermediate adsorption. *Journal of the American Chemical Society* **142,** 5702–5708 (2020).
47. Gao, J., Jiang, B., Ni, C., Qi, Y. & Bi, X. Enhanced reduction of nitrate by noble metal-free electrocatalysis on P doped three-dimensional Co_3O_4 cathode: Mechanism exploration from both experimental and DFT studies. *Chemical Engineering Journal* **382,** 123034 (2020).
48. Yang, J., Sebastian, P., Duca, M., Hoogenboom, T. & Koper, M. T. M. pH dependence of the electroreduction of nitrate on Rh and Pt polycrystalline electrodes. *Chemical Communications* **50,** 2148–2151 (2014).
49. Liang, X., Zhu, H., Yang, X., Xue, S., Liang, Z., Ren, X., Liu, A. & Wu, G. Recent advances in designing efficient electrocatalysts for electrochemical nitrate reduction to ammonia. *Small Structures* **4,** 2200202 (2023).
50. Zeng, Y., Priest, C., Wang, G. & Wu, G. Restoring the nitrogen cycle by electrochemical reduction of nitrate: progress and prospects. *Small Methods* **4,** 2000672 (2020).
51. Long, J., Chen, S., Zhang, Y., Guo, C., Fu, X., Deng, D. & Xiao, J. Direct electrochemical ammonia synthesis from nitric oxide. *Angewandte Chemie International Edition* **59,** 9711–9718 (2020).

52. Garcia-Segura, S., Lanzarini-Lopes, M., Hristovski, K. & Westerhoff, P. Electrocatalytic reduction of nitrate: Fundamentals to full-scale water treatment applications. *Applied Catalysis B: Environmental* **236,** 546–568 (2018).
53. Da Cunha, M., Weber, M. & Nart, F. C. On the adsorption and reduction of NO_3 ions at Au and Pt electrodes studied by in situ FTIR spectroscopy. *Journal of Electroanalytical Chemistry* **414,** 163–170 (1996).
54. Ren, T., Sheng, Y., Wang, M., Ren, K., Wang, L. & Xu, Y. Recent advances of Cu-based materials for electrochemical nitrate reduction to ammonia. *Chinese Journal of Structural Chemistry* **41,** 2212089–2212106 (2022).
55. Khomutov, N. & Stamkulov, U. Nitrate reduction at various metal electrodes. *Sov. Electrochem* **7,** 312–316 (1971).
56. Wang, Y., Wang, C., Li, M., Yu, Y. & Zhang, B. Nitrate electroreduction: mechanism insight, in situ characterization, performance evaluation, and challenges. *Chemical Society Reviews* **50,** 6720–6733 (2021).
57. Theerthagiri, J., Karuppasamy, K., Mahadi, A. H., Moon, C. J., Rahamathulla, N., Kheawhom, S., Alameri, S., Alfantazi, A., Murthy, A. P. & Choi, M. Y. Electrochemical reduction of gaseous nitric oxide into ammonia: a review. *Environmental Chemistry Letters* **22,** 189–208 (2024).
58. Carro, P., Choi, J., MacFarlane, D. R., Simonov, A. N., Doña-Rodríguez, J. M. & Azofra, L. M. Competition between metal-catalysed electroreduction of dinitrogen, protons, and nitrogen oxides: a DFT perspective. *Catalysis Science & Technology* **12,** 2856–2864 (2022).
59. Li, P., Jin, Z., Fang, Z. & Yu, G. A single-site iron catalyst with preoccupied active centers that achieves selective ammonia electrosynthesis from nitrate. *Energy & Environmental Science* **14,** 3522–3531 (2021).
60. Hu, T., Wang, C., Wang, M., Li, C. M. & Guo, C. Theoretical insights into superior nitrate reduction to ammonia performance of copper catalysts. *ACS Catalysis* **11,** 14417–14427 (2021).
61. Pérez-Gallent, E., Figueiredo, M. C., Katsounaros, I. & Koper, M. T. Electrocatalytic reduction of Nitrate on Copper single crystals in acidic and alkaline solutions. *Electrochimica Acta* **227,** 77–84 (2017).
62. Rosca, V., Duca, M., de Groot, M. T. & Koper, M. T. M. Nitrogen cycle electrocatalysis. *Chemical Reviews* **109,** 2209–2244 (2009).
63. Clayborne, A., Chun, H.-J., Rankin, R. B. & Greeley, J. Elucidation of pathways for NO electroreduction on Pt(111) from first principles. *Angewandte Chemie International Edition* **54,** 8255–8258 (2015).

64. Crawford, J., Yin, H., Du, A. & O'Mullane, A. P. Nitrate-to-ammonia conversion at an insn-enriched liquid-metal electrode. *Angewandte Chemie International Edition* **61,** e202201604 (2022).

65. Wang, X., Zhao, L.-K., Li, S., Wei, R., Gao, X.-W., Liu, Z. & Luo, W.-B. Co-reduction coupling of bicarbonate and nitrate toward efficient urea synthesis. *Nanoscale* **17,** 9086–9093 (2025).

66. Shibata, M., Yoshida, K. & Furuya, N. Electrochemical synthesis of urea at gas-diffusion electrodes: IV. simultaneous reduction of carbon dioxide and nitrate ions with various metal catalysts. *Journal of The Electrochemical Society* **145,** 2348 (1998).

67. Kohlhaas, Y., Tschauder, Y. S., Plischka, W., Simon, U., Eichel, R. A., Wessling, M. & Keller, R. Electrochemical urea synthesis. *Joule* **8,** 1579–1600 (2024).

68. Liu, X., Jiao, Y., Zheng, Y., Jaroniec, M. & Qiao, S.-Z. Mechanism of C-N bonds formation in electrocatalytic urea production revealed by ab initio molecular dynamics simulation. *Nature Communications* **13,** 5471 (2022).

69. Jouny, M., Lv, J.-J., Cheng, T., Ko, B. H., Zhu, J.-J., Goddard, W. A. & Jiao, F. Formation of carbon–nitrogen bonds in carbon monoxide electrolysis. *Nature Chemistry* **11,** 846–851 (2019).

70. Qiu, M., Zhu, X., Bo, S., Cheng, K., He, N., Gu, K., Song, D., Chen, C., Wei, X., Wang, D., *et al.* Boosting electrocatalytic urea production via promoting asymmetric C–N coupling. *CCS Chemistry* **5,** 2617–2627 (2023).

71. Luo, Y., Xie, K., Ou, P., Lavallais, C., Peng, T., Chen, Z., Zhang, Z., Wang, N., Li, X.-Y., Grigioni, I., *et al.* Selective electrochemical synthesis of urea from nitrate and CO_2 via relay catalysis on hybrid catalysts. *Nature Catalysis* **6,** 939–948 (2023).

72. Muhyuddin, M., Zuccante, G., Mustarelli, P., Filippi, J., Lavacchi, A., Elbaz, L., Chen, Y.-H., Atanassov, P. & Santoro, C. Electrochemical urea production using carbon dioxide and nitrate: state of the art and perspectives. *Energy & Environmental Science* **17,** 3739–3752 (2024).

73. Feng, Z., Zhang, L.-H., Guo, Y., Guo, J., Li, F. & Yu, F. Charge polarization boosting electrochemical urea synthesis by co-reduction of CO_2 and nitrite in dilute concentrations with a unity carbon selectivity. *Angewandte Chemie International Edition* **64,** e202500262 (2025).

74. Singh, R. & Dey, R. S. Recent innovations in urea synthesis via electrochemical C-N coupling reaction: insights and perspectives. *Proceedings of the Indian National Science Academy* (2025).

75. Aricò, A., Siracusano, S., Briguglio, N., Baglio, V., Di Blasi, A. & Antonucci, V. Polymer electrolyte membrane water electrolysis: status of technologies and potential ap-

plications in combination with renewable power sources. *Journal of Applied Electrochemistry* **43,** 107–118 (2013).

2

Electrochemical Nitrate Reduction with Polymer Modified Ru Nanoparticles

Ammonia (NH_3) is vital for synthesizing fertilizers and has gained great attention as a carbon-free hydrogen carrier and a hydrogen-rich fuel. Electrochemical ammonia synthesis from nitrate in a water-fed PEM electrolyzer is an innovative approach to wastewater treatment. However, the major hurdles to practical implementation are the competing hydrogen evolution reaction (HER) and constrained catalytic efficiency. Herein, we demonstrate the use of polyvinylpyrrolidone (PVP) modified ruthenium (Ru) nanoparticles as a strategy to drive the desired reaction of nitrate to ammonia. The particle size of Ru was controlled by PVP, enhancing the metal utilization and electrochemical active surface area. The PVP modification was found to alter the electron density on Ru, suppressing HER by increasing the energy barrier of hydrogen coupling to form H_2, while promoting absorbed hydrogen (H*) formation , facilitating the hydrogenation of intermediates to ammonia. Benefiting from the combined effects, PVP-10 wt.% Ru/C achieved an ammonia production rate of 3800 $\mu g \cdot mgRu^{-1} \cdot h^{-1}$, compared to 590 $\mu g \cdot mgRu^{-1} \cdot h^{-1}$ for 40 wt.% Ru/C.

This chapter has been published in ACS Catalysis.

2.1 Introduction

Nitrogen is the fifth most abundant element on earth and is a crucial nutrient element for all living organisms [1].The increased use of fertilizers has resulted in global environmental pollution and an energy crisis. Particularly, plants absorb only about 40% of applied fertilizer, with the rest remaining in the soil [2]. This leftover ammonium (NH_4^+) is converted into nitrate (NO_3^-) by soil bacteria [3, 4]. The soluble NO_3^- can leach into aquatic systems, causing eutrophication, acidification, and ecosystem disturbances [5, 6]. Numerous technologies have been developed for the removal of nitrate from groundwater, including chemical and biological denitrification, reverse osmosis, ion exchange processes, and electrocatalytic denitrification [7]. Among these, electrochemical nitrate reduction reaction (NO_3RR) has emerged as a promising approach for both wastewater treatment and ammonia synthesis [8–10]. This process shows a promising alternative to the conventional energy-intensive Haber-Bosch process [11, 12] which owes to high energy consumption (1-2% of globally available energy annually [13]) and large amounts of CO_2 emission (1-1.5% of global emissions) [14].

However, a principal challenge in this eight-electron transfer process is achieving high selectivity towards ammonia against the competing hydrogen evolution reaction (HER) [15, 16]. This competition arises mechanistically from the involvement of the surface absorbed active hydrogen (*H), which is generated on the catalyst via the initial Volmer step ($H_2O + * + e^- \rightarrow *H + OH^-$) [17]. This *H species is fundamentally important, as it serves as the hydrogenating agent for the sequential reduction of nitrate to ammonia. However, the accumulation of *H also promotes HER through two competing pathways: the Tafel step ($*H + *H \rightarrow H_2 + 2*$), [18] involving the recombination of two adsorbed *H intermediates, or the Heyrovsky step ($*H + H^+ + e^- \rightarrow H_2 + *$), where an *H intermediate reacts with a proton-electron pair [19]. Consequently, the catalytic surface kinetics dictate a delicate balance: insufficient *H coverage limits the NO_3RR rate, whereas excessive coverage kinetically favors H_2 evolution, thereby diminishing the faradaic efficiency towards ammonia synthesis.

Therefore, great efforts have been devoted to catalyst development for this process aiming to suppress HER while facilitating efficient NO_3RR. One effective approach is to modulate the electronic structure of the catalyst to weaken hydrogen (*H) binding, which could selectively promote the nitrate hydrogenation while suppressing the competing HER [20–26]. Another promising approach is to use bifunctional catalysts that have separate active sites - one designed for adsorbing and activating nitrate and another for hydrogenation. [27, 28] Thus, a deeper knowledge of the competitive interplay between NO_3RR and HER intermediates, along with the specific behavior of *H, remains essen-

tial for future catalyst design breakthroughs. To achieve high performance in NO_3RR, it is crucial not only to focus on the suppression of HER but also to increase the number of active sites for the reaction, especially when using costly noble metals like ruthenium. [29, 30] One effective strategy to solve this problem is to decrease the metal loading while downsizing the particle to increase the active surface area, which is a straightforward way to improve the catalytic activity with economic advantages. [31–34]

Meanwhile, currently most studies aiming at developing efficient electrocatalysts are conducted in H-cells or batch cells that cannot be operated continuously and hinder the commercialization and large-scale operation. [35] Thus, performing NO_3RR in a continuous manner using a membrane electrode assembly (MEA) electrolyzer is a promising approach which can significantly reduce the internal ohmic resistances and improve energy efficiency [36, 37]. Recently, the electrochemical nitrate reduction to ammonia in an alkaline flow cell has been reported, but the electrolytes used are typically concentrated KOH solutions, which can cause serious corrosion problems and difficulties in device management [38, 39]. Therefore, conducting electrochemical nitrate reduction in a polymer electrolyte membrane (PEM) flow cell with NO_3^--pure water co-electrolysis towards ammonia synthesis is a more practical approach for large-scale application.

In this study, we report an unforeseen but profound HER suppression effect from the capping ligand polyvinylpyrrolidone (PVP, structure shown in 2.A.1 [40]) modified Ru nanoparticles (NPs). Specifically, we discovered that residual PVP, which is difficult to remove completely after synthesis, rather than inhibiting the reaction, critically enhances ammonia selectivity by suppressing the competing HER. Through detailed physical and electrochemical characterization, it can be concluded that the PVP controls the particle size of Ru on carbon support, which greatly enhances the metal utilization efficiency and electrochemical active surface area (ECSA). Remarkably, PVP-modified 10 wt.% Ru/C catalyst achieved an ECSA 4 times higher than a conventional 40 wt.% Ru/C catalyst, despite the lower metal content. Additionally, the PVP modulates the electron density on the Ru surface. This change increases the energy barrier for the coupling of adsorbed hydrogen (*H) to form H_2, thereby suppressing HER, while simultaneously promoting the formation of the *H for the hydrogenation of reaction intermediates into ammonia. These insights discover a simple and effective strategy for designing highly active and selective electrocatalysts for electrochemical nitrate reduction to ammonia.

2.2 Experimental method

Synthesis of different Ru loadings on carbon support Ru NPs with different loadings (5, 10, 20 and 40 wt.%) on a Vulcan XC72 carbon black support, named 5Ru/C, 10Ru/C,

20Ru/C and 40Ru/C were prepared by an impregnation reduction method and reduced by $NaBH_4$ [41], as shown in Figure 2.A.2. In a typical process, with 40 wt.% Ru/C as an example, 164.18 mg $RuCl_3 \cdot xH_2O$ (99.9%, Sigma Aldrich) was dissolved in 50 mL water in a round-bottom flask under stirring (1000 rpm). After 15 minutes, 120 mg Vulcan XC 72 carbon black (Cabot Corporation) was added and stirred for 15 minutes at room temperature and then sonicated for another 30 minutes in an ultrasonic bath (the bath temperature was kept below 20 °C). Subsequently, a freshly made $NaBH_4$ (Sigma Aldrich) solution (179.67 mg, $NaBH_4$: Ru = 6:1, in mole, sixfold excess with respect to the stoichiometric amount of Ru precursors) slowly added dropwise into the suspended solution, followed by stirring for 1 hour (1000 rpm) at room temperature. The catalyst was then collected and washed several times by centrifugation (6000 rpm and 15 minutes each cycle) with Milli-Q water to remove Na^+ and Cl^- ions. Finally, the catalyst was collected and dried in an oven at 80 °C overnight. 10 wt.% and 20 wt.% Ru/C catalysts were synthesized using the same method with different amounts of metal precursors.

Synthesis of different Ru loadings on carbon support with PVP PVP modified Ru NPs with different loadings (10 wt.%, 20 wt.%, and 40 wt.%) supported on Vulcan XC 72 carbon black catalysts, named PVP-10Ru/C, PVP-20Ru/C and PVP-40Ru/C were prepared by the same impregnation reduction method as described before. As shown in Figure 2.A.3, polyvinylpyrrolidone (PVP, MW = 40000, Sigma Aldrich) aqueous solution (PVP/Ru=1.2/1, in w/w) [42] was added after the dissolution of $RuCl_3 \cdot xH_2O$, the remaining steps were kept the same as the previous Ru/C synthesis.

PVP removal experiment in PVP-10Ru/C To exclude the possible effect of PVP itself on the electrocatalytic activity for the Ru/C catalyst, PVP removal was conducted for PVP-10Ru/C by heat treatment [43, 44], named PVP-10Ru/C-removed. Thermogravimetric analysis (TGA) of PVP (K30, MW = 40000) was carried out in a Mettler Toledo SF/1100 thermogravimetric analyzer in N_2 (100 mL $\cdot$ min^{-1}) inert atmosphere with 2 °C $\cdot$ min^{-1} heating rate to 800 °C. As shown in Figure 2.A.4, the results revealed that the decomposition starts at around 300 °C and finishes at around 660 °C. It is well known that the nanoparticles will coalesce when the stabilizing agent starts decomposing and will eventually form large agglomerations [45, 46]. Thus, in order to remove PVP completely and avoid radical change to the morphology of the prepared PVP-10Ru/C, the catalyst was heat-treated at 300 °C with 2 °C $\cdot$ min^{-1} heating rate in N_2 (100 mL $\cdot$ min^{-1}) and kept for 8 hours.

Materials characterization Powder X-ray diffraction (XRD) was performed with a Bruker D8 Advance X-ray diffractometer using a Cu K-α radiation source in a range of 5° to 90° with a step of 0.05°. Transmission electron microscopy (TEM) images were taken

with JEOL JEM-1400 plus system to measure the surface morphology and particle size distributions. To study the surface chemical compositions and chemical states, X-ray photoelectron spectroscopy (XPS) was performed on a Thermo Scientific ESCLAB 250. The source used Al K-α radiation, and the mean X-ray photon energy is 1486.69 eV.

Membrane electrode assembly preparation The Nafion™ 115 membrane (Ion power) was pre-treated according to the activation procedure, by soaking for 1 hour in 3 wt.% hydrogen peroxide (H_2O_2, Sigma Aldrich) solution at 80 °C, 1 hour in 1 M H_2SO_4 (Sigma Aldrich) solution at 80 °C and 1 hour in boiling MilliQ water. After the activation step, the membranes were stored in MilliQ water to prevent membrane swelling. 10 mg of the prepared cathode catalyst and 30 wt.% Nafion ionomers (Nafion™ perfluorinated resin solution, Sigma Aldrich) were ultrasonically dispersed in 2 mL of isopropanol for 30 minutes to generate a homogenous ink. Then, the catalyst ink was spray-coated (Figure 2.A.5) onto a Nafion membrane with an active area of $2 \times 2 cm^2$ at 60 °C to obtain 2.5 $mg \cdot cm^{-2}$ catalyst loading. The anode ink was prepared by the same method consisting of 1.2 mg commercial IrO_2 (0.3 $mg \cdot cm^{-2}$ catalyst loading), 20 wt.% Nafion ionomer and 2 mL isopropanol. After spray coating, the catalyst-coated membranes (CCMs) were hot-pressed at 120 °C and 1 MPa for 3 minutes using an automatic press (Speca Press). The MEA was prepared by pressing two porous sintered titanium gas diffusion layers ($2 \times 2 cm^2$) (GDL, Bekaert) on both sides of the membrane. The PEM cell was assembled by sandwiching the MEA, two titanium bipolar plates with flow channels, and two aluminum cartridge-heated end plates with 5 $N \cdot m$ screw torque (Figure 2.A.6).

Electrochemical nitrate reduction experiments The electrochemical nitrate reduction experiments were conducted in the PEM electrolyzer (Figure 2.A.7) using an AUTOLAB PGSTAT302N potentiostat. The electrocatalytic performance of different loading Ru/C catalysts for NO_3RR to ammonia was compared under ambient pressure at 80 °C where the electrolyzer was heated by heating cartridges. At the anode chamber, MilliQ water was supplied and at the cathode chamber, a 1000 ppm KNO_3 aqueous solution was supplied. For both chambers, the flowrate was set at 0.5 $mL \cdot min^{-1}$ by peristaltic pump (Ismatec). Chronoamperometry (CA) at different cell voltages from 1.7 V to 2.1 V was performed until a stable current was reached. Each potential measurement was recorded for 30 minutes. Electrochemical impedance spectroscopy (EIS) was measured under the catalytically relevant potential (1.7 V) in the frequency range from 100 kHz to 0.1 Hz, with 10 points per frequency decade and perturbation wave of 10 mV.

Product analysis and data processing Ion chromatography (Metrohm 883 Basic) was used to analyze the concentration of the product in electrolyte composition. A Metrosep C6 column was used for the quantification of NH_4^+ and a Metrosep Supp 5 column was

used for the quantification of NO_2^- and NO_3^-. The NH_3 and NO_2^- faradaic efficiencies (FE's) of NO_3RR were calculated according to Equation (2.1) and (2.2):

$$FE_{NH_3} = \frac{nzF}{Q} = \frac{8 \times C_{NH_3} \times V \times F}{Q} \tag{2.1}$$

$$FE_{NO_2} = \frac{nzF}{Q} = \frac{2 \times C_{NO_2} \times V \times F}{Q} \tag{2.2}$$

Here, z = 2 and 8, representing the number of electron transfers required to form NO_2 and NH_3, n is the molar concentration of NO_2 and NH_3 in the catholyte stream, V is the volume of the catholyte stream, F is the faraday constant 96485 $C \cdot mol^{-1}$, Q is the charge passing through the cell.

The single pass conversion rate of NO_3^- was calculated based on equation (2.3):

$$X_{NO_3^-} = \frac{C_{NO_3^-}^{(t=0)} - C_{NO_3^-}^{(t=30)}}{C_{NO_3^-}^{(t=0)}} \times 100 \tag{2.3}$$

where $C_{NO_3^-}^{(t=0)}$ represents the initial nitrate concentration and $C_{NO_3^-}^{(t=30)}$ represents the nitrate concentration after 30 minutes reaction.

Electrochemically active surface area (ECSA) experiment

Copper underpotential deposition (Cu_{upd}) is used to characterize the electrochemically active surface area (ECSA) of Ru/C and PVP modified Ru/C catalysts [47, 48]. Integration of the peak area corresponding to UPD stripping allows the surface area to be calculated with the assumption of an adsorption ratio of a single Cu atom to each surface Ru metal atom and an electro sorption valency of +2 (2.4) [49].

$$Cu_{upd} \rightarrow Cu^{2+} + 2e^- \tag{2.4}$$

All the measurements were performed in a typical three-electrode cell. A graphite rod was used as the counter electrode, and a reversible hydrogen electrode was used as the reference electrode, and a 5 mm glassy carbon electrode with the drop-cast cathode catalyst was used as the working electrode. The catalyst ink was prepared in the same way as described previously, then 10 μL ink was dropped cast on the glassy carbon electrode and the electrode was dried. The obtained catalyst loading was 0.25 $mg \cdot cm^{-2}$. All the experiments were performed in 0.1 M H_2SO_4 and 2 mM Cu_2SO_4. Before all measurements, the electrolyte was purged with helium gas (He) for 20-30 minutes to remove the dissolved oxygen . First, cyclic voltammetry was performed 20 cycles from 0.03 V to 0.7 V

at a scan rate of 10 $mV \cdot s^{-1}$ in 0.1 M H_2SO_4 to obtain the background. Then, the electrode was polarized at 0.29 V for 100s in He-purged 2 mM $Cu_2SO_4$and 0.1 M H_2SO_4 solution. After Cu deposition, a linear voltametric scan from 0.29 V to 0.7 V at a scan rate of 10 $mV \cdot s^{-1}$ oxide all the UPD copper (2.5).

$$ECSA = \frac{Q_{Cu_{upd}}}{420\mu C \cdot cm^{-2} \times L_{Ru}} \tag{2.5}$$

where Q_{Cu} is the Cu_{upd} striping charge in $\mu C \cdot cm^{-2}$, L_{Ru} is the Ru loading in the catalyst in $g \cdot m^{-2}$.

Hydrogen binding energy (HBE) Ru has a strong interaction with hydrogen that leads to hydrogen underpotential deposition (H_{upd}) which means hydrogen adsorbs at positive potentials vs. reversible hydrogen electrode (RHE) [50, 51]. The hydrogen binding energy (HBE) is the descriptor of hydrogen evolution reaction (HER). Hydrogen binding energy (ΔG^0_H) is defined by (2.6):

$$\frac{1}{2}H_2 + {}^* \rightarrow H_{\text{ad}} \tag{2.6}$$

Hydrogen adsorption/desorption is (2.7):

$$H^+ + e^- + {}^* \rightarrow H_{\text{ad}} \tag{2.7}$$

Overall reaction (2.8):

$$H^+ + e^- \rightarrow \frac{1}{2}H_2 \tag{2.8}$$

The overall reaction could go through a Tafel-Volmer pathway, which is described as (2.9), (2.10):

$$\frac{1}{2}H_2 + M \rightleftharpoons M\text{-}H_{ad} \tag{2.9}$$

$$M\text{-}H_{ad} \rightleftharpoons H^+ + e^- + M \tag{2.10}$$

For the second reaction, the H_{upd} adsorption and desorption can be defined by CVs, ΔG^0_H can be derived to be related to the H_{upd} desorption peak (E_{peak}) in CVs, assuming a Langmuir adsorption isotherm, according to the following equation (2.11):

$$H^+ + e^- \rightarrow \frac{1}{2}H_2 \tag{2.11}$$

where F is the faraday constant (96485 $C \cdot mol^{-1}$) [52, 53].

Water contact angle measurements Contact angle measurements were performed via

the sessile drop method using an OCA 25 goniometer (Dataphysics instruments Gmbh, Filderstadt, Germany), and 2 μL of droplets were dispensed onto substrates using an automatic pipetting unit. Measurements were taken in ambient air with a temperature in the range of 20-24 °C, (Figure 2.A.8).

2.3 Results and discussion

Promotional effects of PVP on the ammonia production on Ru/C catalysts

We first synthesized Ru/C catalysts with different loadings (10 wt.%, 20 wt.% and 40 wt.%). The NO_3RR often has various byproducts. As per our observations, the nitrogen balance during the NO_3RR with the catalysts after varying potentials was well closed (<5% loss, Figure 2.A.9) revealing It is well-known and also confirmed in this study that the hydrogen evolution reaction (HER) is the main competitive reaction [17, 23]. Hydrogen and ammonia were the only two detectable products from NO_3RR using the Ru/C electrocatalysts.

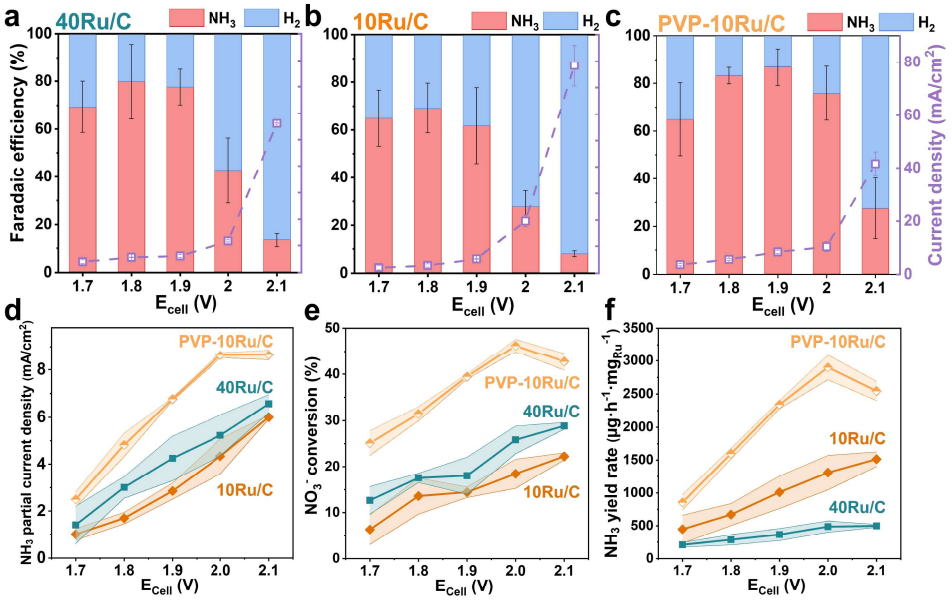

Figure 2.1: Electrocatalytic NO_3RR performance. Faradaic efficiency (Left) and total current densities (Right) for electrochemical nitrate reduction on (a) 40Ru/C; (b) 10Ru/C and (c) PVP-10Ru/C; (d) NH_3 partial current density; (e) NO_3^- single pass conversion and (f) NH_3 yield rate regarding to Ru metal loading.

Figures 2.1 (a) and (b) compare the electrocatalytic performance of 40Ru/C and 10Ru/C in the PEM electrolyzer, and the performance of 20Ru/C is shown in Figure 2.A.10 (a). A clear decrease in catalytic activity in terms of nitrate conversion to ammonia is observed

upon reducing the Ru loading from 40 to 10 wt.% on the carbon black support. The FE towards NH_3 first increased and then decreased within the tested cell voltage range, while HER became dominant at higher voltages. The highest FEs towards NH_3 are 80% for 40Ru/C, 76% for 20Ru/C and 69% for 10Ru/C at 1.9 V, respectively. Among all the catalysts, 40Ru/C shows the highest FE towards NH_3. However, it should be noted that the total cell current densities were similar, implying that a lower Ru loading appears to reduce ammonia synthesis efficiency, with a greater proportion of electrons being consumed by the competing HER, yielding H_2. As shown in Figure 2.1 (d) and Figure 2.A.10 (b), the NH_3 partial current density is higher with 40Ru/C than 10Ru/C and 20Ru/C, indicating the lower ammonia production with decreasing Ru metal loading. A similar trend can also be found in NO_3^- single pass conversion, where higher conversions are observed together with higher Ru metal loading (Figure 2.1 (e)).

Polyvinylpyrrolidone (PVP) was introduced as a capping agent to engineer and control the size of Ru NPs and aim at achieving higher activity and selectivity to NH_3 with lower Ru loading on carbon black supports. To investigate the PVP effects systematically, the same loading of PVP modified Ru/C catalysts were synthesized and tested under the same condition as Ru/C catalysts for nitrate reduction to ammonia. The Ru loading of all the samples is measured by TGA (Table 2.A.1). Blank samples of PVP modified carbon black (PVP-C) were also prepared using the same method. From the previous research in our group, we know that bare carbon black shows nearly no activities towards nitrate reduction to ammonia [32]. The control experiments with PVP-C (Figure 2.A.11 (a-b)) also show only a very small amount of ammonia formed with almost 100% nitrogen balances, indicating that PVP has no catalytic effect on the carbon support.

For the PVP-modified Ru/C catalysts, nitrogen balances were also calculated to verify the FE results (Figure 2.A.12) and nearly 100% of total nitrogen species were detected. Strikingly, PVP-10Ru/C shows the highest FE (86%) and reached 45% NO_3^- single pass conversion which is the highest among all the catalysts (Figure 2.1). The electrocatalytic NO_3RR performance for PVP-20Ru/C and PVP-40Ru/C is depicted in Figure 2.A.14. The FE towards NH_3 decreased with the increasing loading, showing the lowest NO_3^- conversion and NH_3 partial current density in PVP-40Ru/C, which indicates the limitation of the PVP medication method at high Ru loading. For better understanding of the production rate regarding metal utilization, Figure 2.1 (f) and Figure 2.A.13 show the ammonia production rate as a function of cell voltages. We observed that with PVP-modification, the Ru utilization is higher, leading to higher NH_3 production rates per mg Ru. Among all catalysts, PVP-10Ru/C remarkably shows the highest NH_3 yield of 3800 $\mu g \cdot mg_{Ru}^{-1} \cdot h^{-1}$ at 2 V, compared to 590 $\mu g \cdot mg_{Ru}^{-1} \cdot h^{-1}$ for 40Ru/C and 1636 $\mu g \cdot mg_{Ru}^{-1} \cdot h^{-1}$ for 10Ru/C.

Exploring structural and electron density effects of PVP for Ru nanoparticles

With PVP as a stabilizing agent, PVP-10Ru/C shows the highest performance for ammonia production on Ru-based carbon-supported catalyst. As shown in Figure 2.2 (a-c), the transmission electron microscopy (TEM) images of as prepared PVP-10Ru/C, 10Ru/C and 40Ru/C clearly indicate the decrease in the size of Ru NPs. Size distributions are studied by analyzing 150 Ru NPs, resulting in average particle sizes of 3.2 nm, 2.3 nm, and 1.1 nm, for 40Ru/C, 10Ru/C and PVP-10Ru/C, respectively. For 40Ru/C, the Ru NPs particle size ranges from 1 to 12 nm, with evident aggregations. As the Ru loading decreased to 20 wt.%, the NPs particle size range narrowed to 0.5 to 8 nm, while some aggregations were still observed (Figure 2.A.15). Further reduction of the Ru loading to 10 wt.% resulted in a particle size distribution of 0.5 to 8 nm with an approximate average size of 2.5 nm, with fewer aggregations. This shows that decreasing the Ru loading led to a reduction in aggregation formation. In contrast, compared to bare Ru/C catalysts, the Ru NPs size clearly decreased for the PVP-modified Ru/C catalysts (Figure 2.2 (a) and Figure 2.A.16 (a)). For PVP-20Ru/C and PVP-10Ru/C, the Ru NPs particle size distributions are in the range of 0 to 4 nm and 0 to 3 nm, respectively, without obvious large aggregations and the mean particle size distribution for PVP-10Ru/C is 1.1 nm. However, when the Ru loading is as high as 40 wt.%, the presence of PVP cannot effectively prevent agglomeration (Figure 2.A.16 (b)).

The X-ray diffraction (XRD) patterns (Figure 2.2 (d) and Figure 2.A.17) also suggest that the particle size of the PVP-modified Ru is smaller compared to the unmodified one. The broad diffraction peak around $2\theta = 25°$ is amorphous Vulcan XC-72 carbon black support [54]. All Ru catalysts exhibited broad diffraction peaks around $2\theta = 44°$ which is attributed to metallic Ru (PDF 06-0663 and PDF 88-2333) and indicates a less-crystalline Ru structure rather than a well-faceted crystalline Ru [55]. Notably, the PVP-modified Ru/C catalysts display a distinct border peak in contrast to the Ru/C catalysts, indicating smaller particle size of Ru NPs, which is in agreement with the TEM results.

The electronic structure and components of the as-prepared Ru-based catalysts were investigated by X-ray photoelectron spectroscopy . The XPS spectra of different loading 40Ru/C, 10Ru/C and PVP-10Ru/C are presented in Figures 2.2 (e) and 2.2 (f), and those for the rest of the studied catalysts are shown in Figure 2.A.18. The most intense C 1s peak was set at 284.6 eV as the reference for calibration [56]. The PVP-modified Ru/C catalysts show N 1s signals around 399-400 eV, which were attributed to the presence of N in PVP [57]. Conversely, no distinct N 1s were observed in as-prepared Ru/C catalysts, which confirms the incorporation of PVP in Ru/C electrocatalysts.

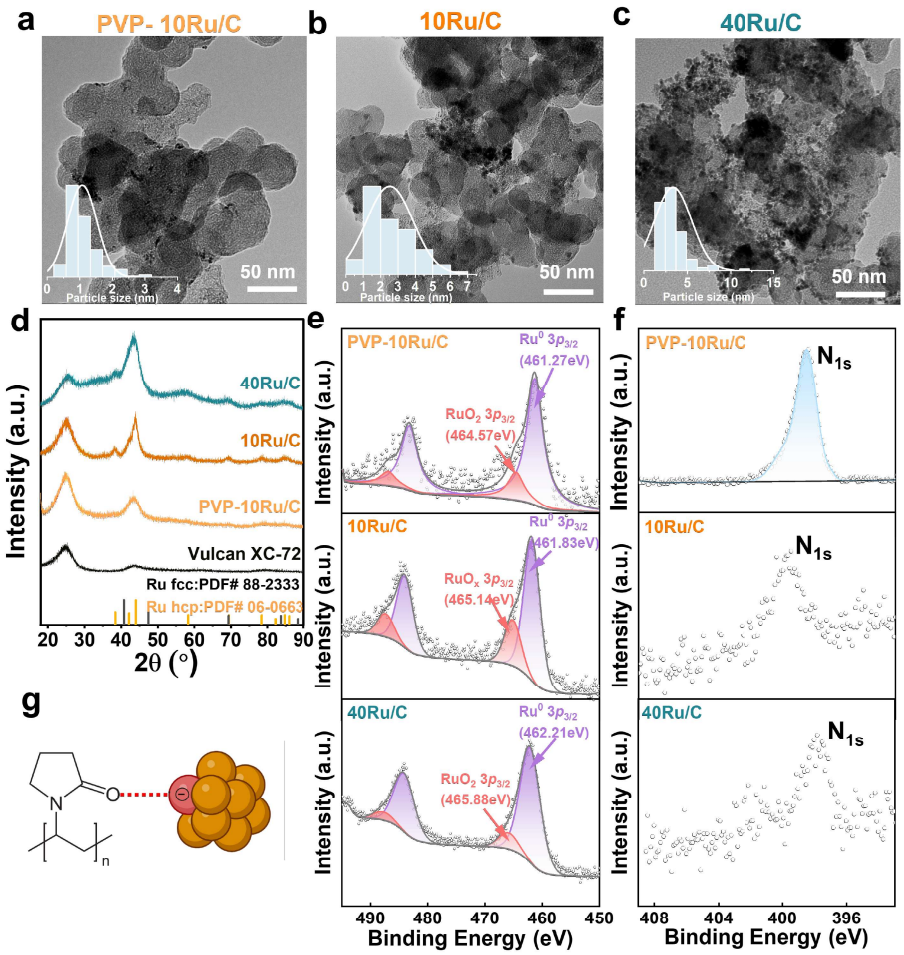

Figure 2.2: TEM images for (a) PVP-10Ru/C; (b) 10Ru/C; (c) 40Ru/C; (d) XRD patterns; (e) and (f) XPS data; (g) scheme of interaction between Ru and PVP.

The electronic structure of Ru was investigated based on the binding energy (BE) of Ru 3p, due to a significant overlap between the Ru 3d and C 1s regions. XPS spectra of Ru 3p showed a doublet at the binding energy of 461 eV and 484 eV, corresponding to Ru $3p_{3/2}$ and Ru $3p_{1/2}$ respectively. For Ru $3p_{3/2}$, the peaks at the binding energy of 462.21 eV and 465.88 eV represent valence state of metallic Ru^0 and oxidized RuO_x, respectively. The presence of RuO_x suggests the formation of an oxide layer on the Ru surface when the catalyst is exposed to air. Table 2.A.2 shows the Ru $3p_{3/2}$ peak value of Ru/C and PVP-modified Ru/C. Negative shifts in binding energy were observed which suggest interaction between the Ru NPs and PVP, where PVP serves as the electron donor and Ru is

the electron acceptor (Figure 2.2 (g)) [58]. Interaction of PVP and Ru NPs lead to charge transfer from PVP to Ru surface, resulting in a negative charge on Ru surface, lowering the binding energy of Ru 3p orbitals. Similar observations of PVP decreasing metal binding energy were reported on Pt [59] and Au [60]. Additionally, the PVP-modified Ru catalysts exhibited higher electron density compared to unmodified Ru/C catalysts with smaller particle sizes. Overall, PVP-10Ru/C showed the lowest binding energy, indicating the highest electron density (Figure 2.A.19).

Electrochemical characterizations for electrochemical active surface area (ECSA) and hydrogen binding energy (HBE)

The electrochemical active surface area (ECSA) is a possible key descriptor in NO_3RR. The copper underpotential deposition (Cu_{upd}) stripping voltammetry method was used to investigate the ECSA of Ru catalysts with different particle sizes. Underpotential deposition (UPD) entails the adsorption of metal atoms onto an electrode surface, forming a monolayer or sub-monolayer at electrode potentials more positive than the potentials necessary for bulk deposition of the respective metal. Cu_{upd} is an ideal method for measuring the ECSA for Ru due to the similarity of atomic radii for both metals, 0.128 nm and 0.134 nm for Cu and Ru, respectively [47, 60, 61]. As shown in Figure 2.A.20, the blank measurement represents the voltammogram obtained in 0.1 M H_2SO_4 solution. To form the Cu UPD layers, the electrode was initially polarized at potentials of 0.29, 0.285, 0.28, 0.275, and 0.27 V vs. RHE for 100 seconds. Subsequently, the deposited Cu was oxidized between the deposition potential and 0.7 V vs. RHE, using a sweep rate of 10 $mV \cdot s^{-1}$. Under polarization potentials of 0.29 V vs. RHE, only one oxidation peak was observed around 0.4 V vs. RHE indicating the presence of Cu monolayer. Another oxidation peak emerged while decreasing the polarization voltage which is attributed to the oxidation of bulk copper. Therefore, the polarization voltage of 0.29 V vs. RHE was employed in this study.

Figure 2.3 (a-d) and Figure 2.A.21 present that the PVP-modified and lower Ru loading electrocatalysts exhibited higher ECSA values compared to unmodified and higher loading Ru/C catalysts. This suggests that the utilization efficiency of Ru metals was improved by downsizing the Ru NPs (Table 2.A.3). As expected, PVP-10Ru/C shows the largest ECSA value of 98 $m^2 \cdot g^{-1}$ among all the synthesized catalysts. Compared with 40Ru/C and 10Ru/C catalysts which show 25 $m^2 \cdot g^{-1}$ and 61 $m^2 \cdot g^{-1}$ ECSA values, PVP-10Ru/C exhibits a much higher value; almost 4 times higher than that of 40Ru/C.

To further elucidate the impact of PVP on Ru/C catalysts, the double-layer capacitance (C_{dl}) values were evaluated by cyclic voltammetry (CV) over a non-faradic range as de-

picted in Figure 2.A.22. The C_{dl} is the indicator of the accessibility of electrolyte ions to the electrode surface. Notably, the C_{dl} values for the PVP-modified Ru/C catalysts exceed those of the unmodified Ru/C catalysts. For instance, the Cdl value for PVP-10Ru/C is 30 $mF \cdot cm^{-2}$, compared to 23 $mF \cdot cm^{-2}$ for unmodified 10Ru/C. This trend is consistent over all the Ru/C catalysts with 20 wt.% and 40 wt.% loadings, further proving that the enhancement in the exposure of Ru active sites and the improved interaction between the electrolyte and the electrode with PVP modification.

Intriguingly, the electrochemical NO_3RR performance of the Ru/C catalysts (with or without PVP modification) was not consistent with the ECSA values. Among the Ru/C catalysts without PVP modification, 10Ru/C has a higher ECSA value and higher current density, but it shows lower FE towards NH_3 and lower NO_3^- conversion compared to 40Ru/C, which is unexpected. However, as expected, PVP-10Ru/C exhibits the largest ECSA values together with the highest FE towards NH_3 and the highest NO_3^- conversion among all the prepared Ru-based catalysts. Besides, the current density of PVP-10Ru/C was lower than Ru/C catalysts with same loading, which indicates the suppression of HER in the reaction.

To further prove the above findings, it is of great importance to clarify the relations among electrocatalytic NO_3RR performance, ECSA and HER reaction. Thus, HBE was investigated as descriptor for HER activity of the studied catalysts [51, 62]. To this end, the HBE values were measured experimentally via CVs in blank solution (He-saturated 0.1 M H_2SO_4) from 0.03 V to 0.7 V vs. RHE at 10 $mV \cdot s^{-1}$ (Figure 2.A.23 (a-c)). HBE was obtained from H_{upd} peak position (E_{peak}), which has a direct relationship with H_{upd} by the equation: $\Delta G_H^0 = -FE_{peak}$. According to the equation, the HBE values of the catalysts were calculated and summarized in Figures 2.3 (e), 2.A.23 (d) and Table 2.A.3. It is widely accepted that the HER activity in the acid electrolyte is only determined by the HBE of the electrocatalyst surface [63]. Therefore, the higher HBE can be attributed to the decrease in HER activity for the Ru/C catalysts. For the Ru/C catalysts, the HBE decreases with the decreasing Ru loading, indicating superior HER activity on 10Ru/C than 40Ru/C. This is consistent with the electrocatalytic performance of NO_3RR that 10Ru/C shows higher current density with lower FE towards NH_3, and more electrons were utilized to HER reaction. As for the PVP-modified Ru/C catalysts, the HBE shows a higher value which demonstrates inferior HER activity compared to Ru/C catalysts. PVP-10RuC with the highest HBE values displays the most suppression of HER in comparison to all the other catalysts. XPS spectra also shows that the electronic structure of the Ru modified by PVP shifts to a higher electron density. Previous research indicates that higher electron density can suppress the HER reaction which benefits the nitrate reduction to

ammonia formation [64]. Overall, the ECSA and HBE results confirm the importance of PVP for enhancing the active surface area and suppressing hydrogen production.

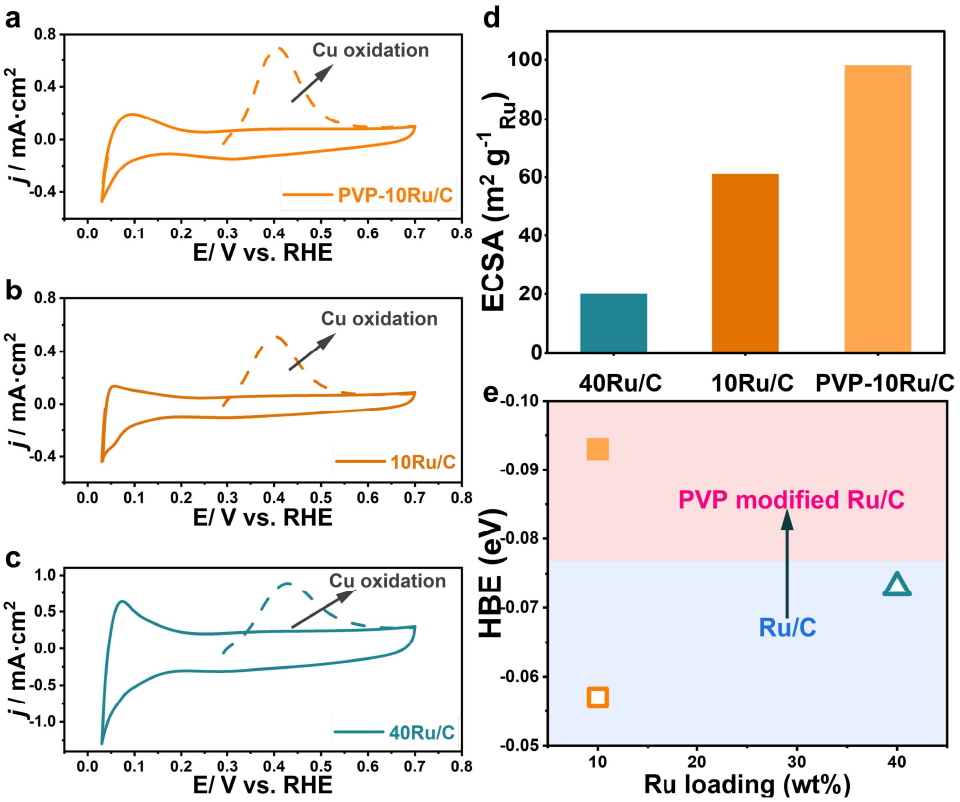

Figure 2.3: Cu UPD voltammogram for (a) PVP-10Ru/C; (b) 10Ru/C; (c) 40Ru/C; (d) ESCA and (e) HBE for PVP-10Ru/C, 10Ru/C and 40Ru/C.

Kinetic investigations via Electrochemical Impedance Spectroscopy (EIS) Further, we investigated the effects of PVP on interfacial charge transfer kinetics. Electrochemical impedance spectroscopy (EIS) was conducted under the electrocatalytically relevant conditions at 1.7 V and used to study the charge transport and transfer phenomena on the electrode surface. The Randles equivalent circuit module (ECM) (Figure 2.4 (a)) was constructed consisting of omit resistance (R_s), polarization charge transfer resistance (R_{ct}) in NO_3RR, constant phase elements (CPE) which replaces the electric double layer capacitor to simulate the distribution of double-layer charging along the length of pores and the inhomogeneities on porous electrode and a Warburg coefficient (W) considering the loss related with the diffusion process [63, 65]. Among all the elements in the ECM, Rct represents the resistance encountered by ions crossing the electrode/electrolyte interface and inserting into the electrodes, which occurs at the solid–liquid contact area

under low frequency region [66, 67]. NO_3RR takes place at the interface between the solid cathode electrode and the liquid electrolyte, hence, we focus on analyzing the Rct to reveal the relation between charge transfer kinetics at the electrode/electrolyte interface. The fitting results from EIS (Figure 2.4 (b-d) and Figure 2.A.24 (a-c)) show that the ohmic resistances for different electrodes are at similar values. With regard to Rct obtained from the ECM fitting (Figure 2.4 (e)), as shown in Figure 2.4 (f), PVP-10Ru/C showed significantly smaller values of 14 $m\Omega \cdot cm^{-2}$, compared to those of 10Ru/C catalyst (26.5 $m\Omega \cdot cm^{-2}$) and 40Ru/C catalyst (38.3 $m\Omega \cdot cm^{-2}$). For NO_3RR, smaller R_{ct} is more favorable for better charge transfer kinetics. The EIS results show that the charge transfer kinetics decrease substantially with decreasing the Ru metal loading with or without PVP modifications (Figure 2.A.24 (d) and Table 2.A.4) which is in a good agreement with the electronic structure modulation of Ru induced by the smaller particle size (Figure 2.A.19).

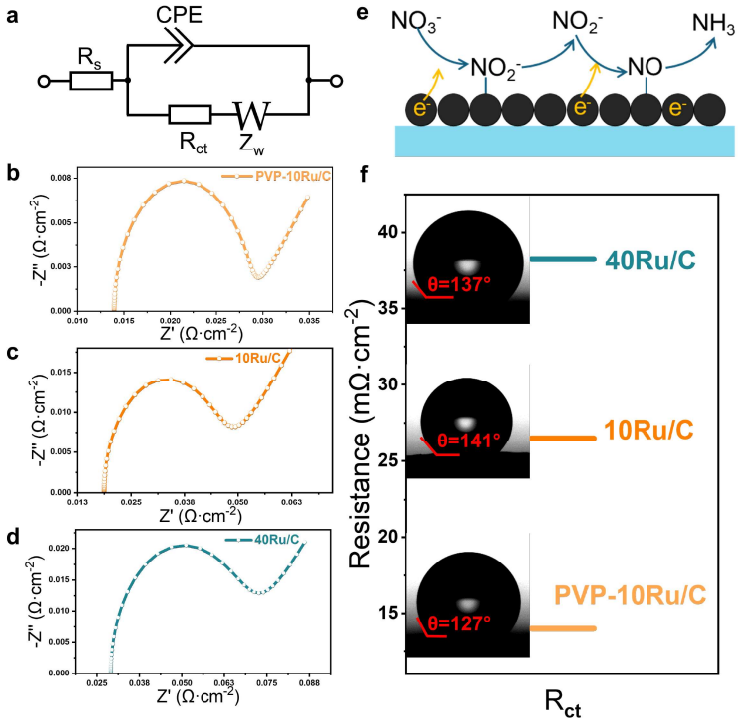

Figure 2.4: Electrochemical Impedance Spectroscopy (EIS). (a) The equivalent circuit used for EIS fitting; (b-d) fitted Nyquist plots of the EIS data of PVP-10Ru/C, 10Ru/C and 40Ru/C; (e) illustration of charge transfer through the electrode surface and (f) water contact angle and charge transfer resistance.

Moreover, PVP is a highly hydrophilic polymer [68] which may improve the electrode wettability. The water contact angle results show that the PVP-modified catalysts have

smaller contact angles (Figure 2.4 (f) and Figure 2.A.25), resulting in better wettability which likely improves the ability of liquid electrolytes to spread out on the electrode surface and facilitates the NO_3^- ions transportation through the interface. In summary, the EIS measurements further confirm the importance of PVP modification for enhanced charge transfer kinetics and effective wetting area and ion transport.

Investigating the PVP coverage effects on electrocatalytic performance

To investigate whether PVP hinders the electrocatalytic performance, a PVP removal experiment was conducted with the best performing PVP-10Ru/C catalyst. To remove PVP efficiently, while keeping the same Ru particle size at the samples was heated to 300 °C in a N_2 atmosphere for 8 hours. To further validate this, XRD, XPS and TEM are used to characterize the PVP-10Ru/C-removed sample. As shown in Figure 2.A.26 (a), the PVP-10Ru/C-removed catalyst showed a significant decreased N 1s peak intensity which confirmed the effective removal of PVP but indicated that it cannot be removed completely. The XRD results (Figure 2.A.26 (b)) show still a broad peak indicating that the Ru NPs are still in a small size. Moreover, TEM images show that the particle size distribution is similar to that of PVP-10Ru/C (Figure 2.A.26 (c)). After removal of PVP in PVP-10Ru/C catalyst, the binding energy of Ru 3p showed a similar level of 10 Ru/C which also indicated the successful removal of PVP without changing the Ru structure (Figure 2.A.26 (a)).

The electrochemical NO_3RR experiments were performed under the same conditions as other catalysts, where we observe that the FE towards NH_3 (Figure 2.5 (a)) and NO_3^- (Figure 2.5 (b)) conversion is lower than PVP-10Ru/C. This indicates that more electrons are used to produce H_2. However, all these values are slightly higher than 10Ru/C, showing that remaining PVP likely plays a positive role in the electrocatalytic performance. Furthermore, the ECSA, HBE and Rct of PVP-10Ru/C-removed catalyst is 74 $m^2 \cdot g^{-1}$, -0.079 eV and 16 $m\Omega \cdot cm^{-2}$. (Table 2.A.5) Overall, the PVP removal experiments further confirm the significance of PVP for suppressing HER and enhancing ammonia synthesis.

To decouple the particle size effect from the contribution of the capping agent and get a better understanding of PVP effects, 5 wt.% Ru/C (named 5Ru/C) without PVP was synthesised as a control catalyst. By decreasing the metal loading, a similar mean particle size distribution (about 1.2 nm) was successfully achieved for 5Ru/C as compared to the optimized PVP-10Ru/C (1.2 nm), which is confirmed by the particle size distribution from TEM measurement (Figure 2.A.27 (a)). Figure 2.A.27 (b) shows the electrochemical NO3RR performance of 5Ru/C in PEM electrolyzer while Figure 2.A.27 (c) confirms that the N balances are well closed, similar to the other catalysts. The highest FE towards NH_3

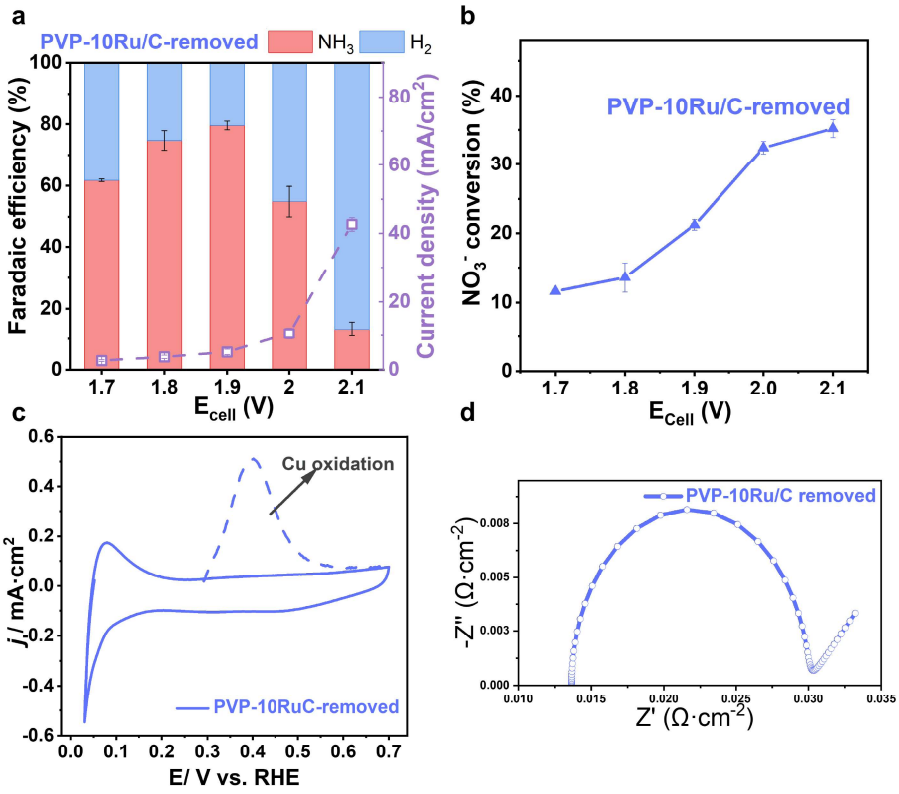

Figure 2.5: PVP-10Ru/C-removed catalyst. (a) faradaic efficiency (Left) and total current densities (Right) for electrochemical nitrate reduction; (b) NO_3^- conversion; (c) Cu UPD voltammogram and (d) fitted Nyquist plots of the EIS data.

is 55% at 1.8 V and decreased slightly to 51% at 1.9 V, which is inferior to the Ru loading catalysts (10 wt.%, 20 wt.%, 40 wt.%) without PVP. Despite lower selectivity, the total cell current densities of 5Ru/C were comparable to, or slightly higher than, the other catalysts without PVP. This suggests that smaller Ru NPs result in larger ECSA, which drives the high total current densities. However, a significant portion of this current contributes to form H_2 instead of NH_3. This observation aligns with our main conclusion that decreasing the size of Ru NPs lowers the HBE, thereby promoting HER and decreases the FE towards NH_3.

When normalizing the NH_3 yield rate by Ru metal loading (Figure 2.A.27 (d)), PVP-10Ru/C shows the highest NH_3 production rate (3800 $\mu g \cdot mgRu^{-1} \cdot h^{-1}$ at 2 V) significantly outperforming 5Ru/C (2700 $\mu g \cdot mgRu^{-1} \cdot h^{-1}$). For the nitrate conversion rate (Figure 2.A.27 (e)), PVP-10Ru/C shows the highest, while 5Ru/C shows similar conversion as 10Ru/C, further confirming that the excess current in 5Ru/C is consumed by HER. Overall, the

PVP removal experiments and the control experiments of NPs size-matched 5Ru/C further confirm the significance of PVP for suppressing HER and enhancing ammonia synthesis.

2

Tackling the stability for PVP-modified Ru/C catalysts

PVP was introduced as a capping agent that can prevent Ru NPs aggregation on carbon support besides altering the electronic structure and wettability as described above. TEM images after NO_3RR for all the catalysts were taken to study the stability of Ru NPs on carbon support. Results were summarized in Figure 2.6 (a-c) and 2.A.28, exhibiting the particle size distribution of various Ru/C and the PVP-modified Ru/C electrocatalysts before and after NO_3RR.

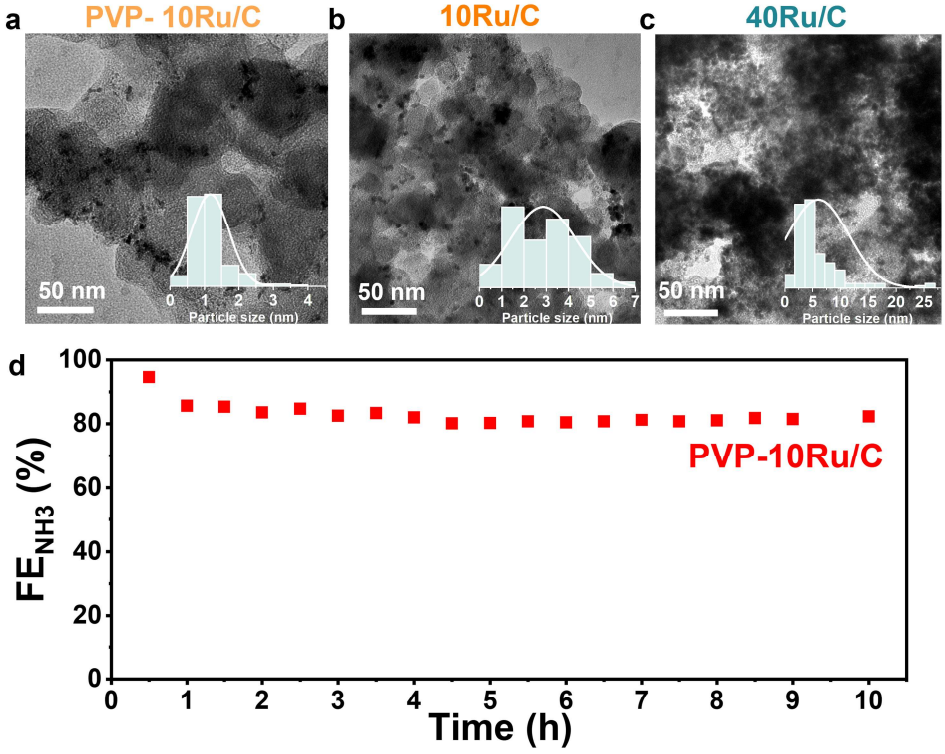

Figure 2.6: TEM images after reaction (a) PVP-10Ru/C; (b) 10Ru/C; (c) 40Ru/C and (d) FE towards NH_3 for PVP-10Ru/C as a function of time for 10 hours.

Comparing the particle size distributions between Ru/C and the PVP-modified Ru/C catalysts, the results showed a significant particle growth over Ru/C catalysts than PVP modified catalysts. In the case of 40Ru/C, the particle size increased from 3.2 nm to 6.0 nm after the reaction, however, with PVP modification, the particle size only increased

0.9 nm. For 10Ru/C, it can be observed that the Ru NPs agglomerated more prominently after the reaction compared PVP modified one. The same observation is also held for 20Ru/C. All the results indicated that the PVP helps stabilize the particle during the electroreduction and prevent the agglomeration of Ru NPs, which results in better particle stability (Table 2.A.6).

For the practical application of an effective NO_3RR electrocatalyst, long-term durability is essential. We performed the stability test of PVP-10Ru/C at a constant voltage of 1.9 V for 10 hours (Figure 2.6). The FE towards NH_3 stabilized at around 82%, suggesting that PVP-10Ru/C has excellent stability for NO_3RR to NH_3. Besides, the synthesis procedure is straightforward, containing only two steps: impregnation and followed by sodium boron hydrate reduction which offers significant potential for large-scale applications.

2.4 Conclusion

In conclusion, we have uncovered the promotion effect of PVP modified Ru nanoparticles supported on carbon black for NO_3RR to ammonia production and elucidated a twofold origin of this promotion effect. Electronically, PVP increases the electron density on the Ru surface, which suppresses the competing HER by increasing the hydrogen bonding energy, thus further inhibiting the H-H formation. Physically, the PVP modification controls Ru nanoparticle size, which in turn amplifies the metal utilization efficiency, increases the electrochemical active surface area, and improves charge transfer and hydrophilicity. As a result, the PVP-10 Ru/C exhibited outstanding performance, achieving a maximum NH_3 faradic efficiency of 86% and a single pass NO_3^- conversion of 46% at 1.9 V. Notably, its NH_3 production rate is 3800 $\mu g \cdot mgRu^{-1} \cdot h^{-1}$ at 2 V, which is 5.8 times higher than that of the conventional 40 wt.% Ru/C. Overall, the excellent electrocatalytic performance and simple strategy of PVP modification can be a versatile method for developing superior electrocatalysts for demanding electrochemical reactions.

References

1. Lehnert, N., Dong, H. T., Harland, J. B., Hunt, A. P. & White, C. J. Reversing nitrogen fixation. *Nature Reviews Chemistry* **2,** 278–289 (Oct. 2018).
2. Mahvi, A. H., Nouri, J., Babaei, A. A. & Nabizadeh, R. Agricultural activities impact on groundwater nitrate pollution. *International Journal of Environmental Science & Technology* **2,** 41–47 (Mar. 2005).
3. Canfield, D. E., Glazer, A. N. & Falkowski, P. G. The evolution and future of earth's nitrogen Cycle. *Science* **330,** 192–196 (2010).
4. Galloway, J. N., Townsend, A. R., Erisman, J. W., Bekunda, M., Cai, Z., Freney, J. R., Martinelli, L. A., Seitzinger, S. P. & Sutton, M. A. Transformation of the nitrogen cycle: recent trends, questions, and potential solutions. *Science* **320,** 889–892 (2008).
5. Wang, Z., Richards, D. & Singh, N. Recent discoveries in the reaction mechanism of heterogeneous electrocatalytic nitrate reduction. *Catalysis Science & Technology* **11,** 705–725 (2021).
6. Bijay, S. & Craswell, E. Fertilizers and nitrate pollution of surface and ground water: an increasingly pervasive global problem. *SN Applied Sciences* **3,** 518 (2021).
7. Archna, Sharma, S. K. & Sobti, R. C. Nitrate removal from ground water: a review. *Journal of Chemistry* **9,** 154616 (2012).
8. Xu, D., Li, Y., Yin, L., Ji, Y., Niu, J. & Yu, Y. Electrochemical removal of nitrate in industrial wastewater. *Frontiers of Environmental Science & Engineering* **12,** 9 (2018).
9. Van Langevelde, P. H., Katsounaros, I. & Koper, M. T. M. Electrocatalytic nitrate reduction for sustainable ammonia production. *Joule* **5,** 290–294 (2021).
10. Wang, Y., Xu, A., Wang, Z., Huang, L., Li, J., Li, F., Wicks, J., Luo, M., Nam, D.-H., Tan, C.-S., *et al.* Enhanced nitrate-to-ammonia activity on copper–nickel alloys via tuning of intermediate adsorption. *Journal of the American Chemical Society* **142,** 5702–5708 (2020).
11. Pattabathula, V. & Richardson, J. Introduction to ammonia production. *Chemical Engineering Progress* **112,** 69–75 (Sept. 2016).
12. Capdevila-Cortada, M. Electrifying the Haber–Bosch. *Nature Catalysis* **2,** 1055–1055 (2019).
13. Service, R. F. New recipe produces ammonia from air, water, and sunlight. *Science* **345,** 610–610 (2014).

14. Nørskov, J., Chen, J., Miranda, R., Fitzsimmons, T. & Stack, R. *Sustainable ammonia synthesis – exploring the scientific challenges associated with discovering alternative, sustainable processes for ammonia production* Report (US DOE Office of Science, 2016-02-18 2016).
15. Wu, Z.-Y., Karamad, M., Yong, X., Huang, Q., Cullen, D. A., Zhu, P., Xia, C., Xiao, Q., Shakouri, M., Chen, F.-Y., *et al.* Electrochemical ammonia synthesis via nitrate reduction on Fe single atom catalyst. *Nature Communications* **12,** 2870 (2021).
16. Chen, G.-F., Yuan, Y., Jiang, H., Ren, S.-Y., Ding, L.-X., Ma, L., Wu, T., Lu, J. & Wang, H. Electrochemical reduction of nitrate to ammonia via direct eight-electron transfer using a copper–molecular solid catalyst. *Nature Energy* **5,** 605–613 (2020).
17. Fu, L., Li, Y., Yao, N., Yang, F., Cheng, G. & Luo, W. IrMo Nanocatalysts for Efficient Alkaline Hydrogen Electrocatalysis. *ACS Catalysis* **10,** 7322–7327 (2020).
18. Wang, X., Yao, H., Zhang, C., Li, C., Tong, K., Gu, M., Cao, Z., Huang, M. & Jiang, H. Double-Tuned RuCo Dual Metal Single Atoms and Nanoalloy with Synchronously Expedited Volmer/Tafel Kinetics for Effective and Ultrastable Ampere-Level Current Density Hydrogen Production. *Advanced Functional Materials* **33,** 2301804 (2023).
19. Wang, J., Zang, W., Liu, X., Sun, J., Xi, S., Liu, W., Kou, Z., Shen, L. & Wang, J. Switch Volmer-Heyrovsky to Volmer-Tafel Pathway for Efficient Acidic Electrocatalytic Hydrogen Evolution by Correlating Pt Single Atoms with Clusters. *Small* **20,** 2309427 (2024).
20. Chen, F.-Y., Wu, Z.-Y., Gupta, S., Rivera, D. J., Lambeets, S. V., Pecaut, S., Kim, J. Y. T., Zhu, P., Finfrock, Y. Z., Meira, D. M., *et al.* Efficient conversion of low-concentration nitrate sources into ammonia on a Ru-dispersed Cu nanowire electrocatalyst. *Nature Nanotechnology* **17,** 759–767 (2022).
21. Wang, Y., Li, H., Zhou, W., Zhang, X., Zhang, B. & Yu, Y. Structurally disordered RuO_2 nanosheets with rich oxygen vacancies for enhanced nitrate electroreduction to ammonia. *Angewandte Chemie International Edition* **61,** e202202604 (2022).
22. Yang, R., Li, H., Long, J., Jing, H., Fu, X. & Xiao, J. Potential dependence of ammonia selectivity of electrochemical nitrate reduction on copper oxide. *ACS Sustainable Chemistry & Engineering* **10,** 14343–14350 (2022).
23. Cerrón-Calle, G. A., Wines, A. & Garcia-Segura, S. Atomic hydrogen provision by cobalt sites in a bimetallic $Ni/Co(OH)_X$ and trimetallic $Ni/Cu_2O/Co(OH)_X$ configurations for superior ammonia production. *Applied Catalysis B: Environmental* **328,** 122540 (2023).
24. He, W., Zhang, J., Dieckhöfer, S., Varhade, S., Brix, A. C., Lielpetere, A., Seisel, S., Junqueira, J. R. C. & Schuhmann, W. Splicing the active phases of copper/cobalt-

based catalysts achieves high-rate tandem electroreduction of nitrate to ammonia. *Nature Communications* **13,** 1129 (2022).

25. Jeon, T. H., Wu, Z.-Y., Chen, F.-Y., Choi, W., Alvarez, P. J. J. & Wang, H. Cobalt–copper nanoparticles on three-dimensional substrate for efficient ammonia synthesis via electrocatalytic nitrate reduction. *The Journal of Physical Chemistry C* **126,** 6982–6989 (2022).
26. Li, J., Zhan, G., Yang, J., Quan, F., Mao, C., Liu, Y., Wang, B., Lei, F., Li, L., Chan, A. W. M., *et al.* Efficient ammonia electrosynthesis from nitrate on strained ruthenium nanoclusters. *Journal of the American Chemical Society* **142,** 7036–7046 (2020).
27. Tan, H., Tian, Y., Peng, W., Liu, X., Wang, L., Peng, Y., Wang, C., Liang, J. & Yan, X. Advances in Electrocatalytic Nitrate Reduction: Insights into Mechanisms and Reaction Optimization. *Advanced Sustainable Systems* **n/a,** 2400934 (2025).
28. Chen, W., Wang, L., Wang, Y., Sun, Z., Liu, M., Shang, H., Wang, R., Yang, C., Wang, D., Chen, W., *et al.* Atomic-Level Modulation of N-Bridge-Induced Built-In Electric Fields for Enhanced Hydrogen Spillover in Ammonia Electrosynthesis. *ACS Catalysis* **15.** doi: 10.1021/acscatal.5c05138, 16493–16505 (2025).
29. Ye, D. & Tsang, S. C. E. Prospects and challenges of green ammonia synthesis. *Nature Synthesis* **2,** 612–623 (2023).
30. John, J., MacFarlane, D. R. & Simonov, A. N. The why and how of NO_x electroreduction to ammonia. *Nature Catalysis* **6,** 1125–1130 (2023).
31. Wu, T., Han, M.-Y. & Xu, Z. J. Size effects of electrocatalysts: more than a variation of surface area. *ACS Nano* **16,** 8531–8539 (2022).
32. Speck, F. D., Paul, M. T. Y., Ruiz-Zepeda, F., Gatalo, M., Kim, H., Kwon, H. C., Mayrhofer, K. J. J., Choi, M., Choi, C. H., Hodnik, N., *et al.* Atomistic insights into the stability of Pt single-atom electrocatalysts. *Journal of the American Chemical Society* **142,** 15496–15504 (2020).
33. Roy, C., Sebok, B., Scott, S. B., Fiordaliso, E. M., Sørensen, J. E., Bodin, A., Trimarco, D. B., Damsgaard, C. D., Vesborg, P. C. K., Hansen, O., *et al.* Impact of nanoparticle size and lattice oxygen on water oxidation on $NiFeO_xH_y$. *Nature Catalysis* **1,** 820–829 (2018).
34. Holby, E. F., Sheng, W., Shao-Horn, Y. & Morgan, D. Pt nanoparticle stability in PEM fuel cells: influence of particle size distribution and crossover hydrogen. *Energy & Environmental Science* **2,** 865–871 (2009).
35. Li, S., Han, D., Jiang, G., Han, Z., Lu, H., Gao, J., Wang, X., Wang, Y., Geng, C., Weng, Z., *et al.* Proton exchange membrane electrode assembly for ammonia electrosynthesis from nitrate. *ACS Applied Energy Materials* **6,** 5067–5073 (2023).

36. Bunea, S., Clemens, K. & Urakawa, A. Electrified conversion of contaminated water to value: selective conversion of aqueous nitrate to ammonia in a polymer electrolyte membrane cell. *ChemSusChem* **15,** e202102180 (2022).
37. Ampurdanés, J., Bunea, S. & Urakawa, A. PEM electrolysis-assisted catalysis combined with photocatalytic oxidation towards cmplete abatement of nitrogen-containing contaminants in water. *ChemSusChem* **14,** 1534–1544 (2021).
38. Yuan, T., Li, M., Subramanian, S., Kok, J., Li, M., Urakawa, A., Voznyy, O. & Burdyny, T. Sequential electrocatalytic reactions along a membrane electrode assembly drive efficient nitrate-to-ammonia conversion. *Cell Reports Physical Science* **5,** 101977 (2024).
39. Huang, P.-W., Song, H., Yoo, J., Chipoco Haro, D. A., Lee, H. M., Medford, A. J. & Hatzell, M. C. Impact of local microenvironments on the selectivity of electrocatalytic nitrate reduction in a BPM-MEA system. *Advanced Energy Materials* **14,** 2304202 (2024).
40. Kyrychenko, A., Korsun, O. M., Gubin, I. I., Kovalenko, S. M. & Kalugin, O. N. Atomistic simulations of coating of silver nanoparticles with Poly (vinylpyrrolidone) oligomers: effect of oligomer chain length. *The Journal of Physical Chemistry C* **119,** 7888–7899 (2015).
41. Ilinitch, O. M., Cuperus, F. P., Nosova, L. V. & Gribov, E. N. Catalytic membrane in reduction of aqueous nitrates: operational principles and catalytic performance. *Catalysis Today* **56,** 137–145 (2000).
42. Wu, S., Sun, W., Chen, J., Zhao, J., Cao, Q., Fang, W. & Zhao, Q. Efficient imine synthesis from oxidative coupling of alcohols and amines under air atmosphere catalysed by Zn-doped Al_2O_3 supported Au nanoparticles. *Journal of Catalysis* **377,** 110–121 (2019).
43. Lopez-Sanchez, J. A., Dimitratos, N., Hammond, C., Brett, G. L., Kesavan, L., White, S., Miedziak, P., Tiruvalam, R., Jenkins, R. L., Carley, A. F., *et al.* Facile removal of stabilizer-ligands from supported gold nanoparticles. *Nature Chemistry* **3,** 551–556 (2011).
44. Rioux, R. M., Song, H., Grass, M., Habas, S., Niesz, K., Hoefelmeyer, J. D., Yang, P. & Somorjai, G. A. Monodisperse platinum nanoparticles of well-defined shape: synthesis, characterization, catalytic properties and future prospects. *Topics in Catalysis* **39,** 167–174 (2006).
45. Armenise, S., Cazaña, F., Monzón, A. & García-Bordejé, E. In situ generation of CO_x -free H_2 by catalytic ammonia decomposition over Ru-Al-monoliths. *Fuel* **233,** 851–859 (2018).

46. Kim, T. W., Oh, J. & Suh, Y.-W. Hydrogenation of 2-benzylpyridine over alumina-supported Ru catalysts: Use of $Ru_3(CO)_{12}$ as a Ru precursor. *Applied Catalysis A: General* **547,** 183–190 (2017).
47. Green, C. L. & Kucernak, A. Determination of the platinum and ruthenium surface areas in platinumruthenium electrocatalysts by underpotential deposition of copper. 2. effect of surface composition on activity. *The Journal of Physical Chemistry B* **106,** 11446–11456 (2002).
48. Green, C. L. & Kucernak, A. Determination of the platinum and ruthenium surface areas in platinumruthenium alloy electrocatalysts by underpotential deposition of copper. I. unsupported catalysts. *The Journal of Physical Chemistry B* **106,** 1036–1047 (2002).
49. Machado, S. A. S., Tanaka, A. A. & Gonzalez, E. R. Underpotential deposition of copper and its influence in the oxygen reduction on platinum. *Electrochimica Acta* **36,** 1325–1331 (1991).
50. Karlberg, G. S., Jaramillo, T. F., Skúlason, E., Rossmeisl, J., Bligaard, T. & Nørskov, J. K. Cyclic Voltammograms for H on Pt(111) and Pt(100) from First Principles. *Physical Review Letters* **99,** 126101 (2007).
51. Hu, Q., Gao, K., Wang, X., Zheng, H., Cao, J., Mi, L., Huo, Q., Yang, H., Liu, J. & He, C. Subnanometric Ru clusters with upshifted D band center improve performance for alkaline hydrogen evolution reaction. *Nature Communications* **13,** 3958 (2022).
52. Wang, Q., Xu, C.-Q., Liu, W., Hung, S.-F., Bin Yang, H., Gao, J., Cai, W., Chen, H. M., Li, J. & Liu, B. Coordination engineering of iridium nanocluster bifunctional electrocatalyst for highly efficient and pH-universal overall water splitting. *Nature Communications* **11,** 4246 (2020).
53. Zheng, J., Nash, J., Xu, B. & Yan, Y. Perspective—towards establishing apparent hydrogen binding energy as the descriptor for hydrogen oxidation/evolution reactions. *Journal of The Electrochemical Society* **165,** H27 (2018).
54. Ungár, T., Gubicza, J., Ribárik, G., Pantea, C. & Zerda, T. W. Microstructure of carbon blacks determined by X-ray diffraction profile analysis. *Carbon* **40,** 929–937 (2002).
55. Lee, W.-J., Bera, S., Woo, H.-J., An, J.-W., Bae, J.-S., Oh, I.-K. & Kwon, S.-H. Controllable size and crystallinity of Ru nanoparticles on a carbon support synthesized by fluidized bed reactor-atomic layer deposition for enhanced hydrogen oxidation activity. *Journal of Materials Chemistry A* **9,** 17223–17230 (2021).
56. Awasthi, M. K., Rai, R. K., Behrens, S. & Singh, S. K. Low-temperature hydrogen production from methanol over a ruthenium catalyst in water. *Catalysis Science Technology* **11,** 136–142 (2021).

57. Hantsche, H. High resolution XPS of organic polymers, the scienta ESCA300 database. By G. Beamson and D. Briggs, Wiley, Chichester 1992, 295 pp., hardcover, £ 65.00, ISBN 0-471-93592-1. *Advanced Materials* **5,** 778–778 (1993).
58. Ye, J.-Y., Attard, G. A., Brew, A., Zhou, Z.-Y., Sun, S.-G., Morgan, D. J. & Willock, D. J. Explicit detection of the mechanism of platinum nanoparticle shape control by polyvinylpyrrolidone. *The Journal of Physical Chemistry C* **120,** 7532–7542 (2016).
59. Haesuwannakij, S., Kimura, T., Furutani, Y., Okumura, K., Kokubo, K., Sakata, T., Yasuda, H., Yakiyama, Y. & Sakurai, H. The impact of the polymer chain length on the catalytic activity of poly(N-vinyl-2-pyrrolidone)-supported gold nanoclusters. *Scientific Reports* **7,** 9579 (2017).
60. Moffat, T. P., Walker, M., Chen, P. J., Bonevich, J. E., Egelhoff, W. F., Richter, L., Witt, C., Aaltonen, T., Ritala, M., Leskelä, M., *et al.* Electrodeposition of Cu on Ru barrier layers for damascene processing. *Journal of The Electrochemical Society* **153,** C37 (2006).
61. Bogolowski, N., Huxter, S., Abd-El-Latif, A.-E.-A. A., Attard, G. A. & Baltruschat, H. Copper underpotential deposition on Ru quasi-single-crystal films. *Journal of Electroanalytical Chemistry* **646,** 68–74 (2010).
62. Shi, Y., Ma, Z.-R., Xiao, Y.-Y., Yin, Y.-C., Huang, W.-M., Huang, Z.-C., Zheng, Y.-Z., Mu, F.-Y., Huang, R., Shi, G.-Y., *et al.* Electronic metal–support interaction modulates single-atom platinum catalysis for hydrogen evolution reaction. *Nature Communications* **12,** 3021 (2021).
63. Yuan, X.-Z., Song, C., wang, H. & Zhang, J. *Electrochemical Impedance Spectroscopy in PEM Fuel Cells* (Springer Verlag London Limited, 2010).
64. Wang, Y., Zhou, W., Jia, R., Yu, Y. & Zhang, B. Unveiling the activity origin of a copper-based electrocatalyst for selective nitrate reduction to ammonia. *Angewandte Chemie International Edition* **59,** 5350–5354 (2020).
65. Zhao, X., Zhou, Y., Wang, L., Pan, B., Wang, R. & Wang, L. Classification, summarization and perspective on modeling techniques for polymer electrolyte membrane fuel cell. *International Journal of Hydrogen Energy* **48,** 21864–21885 (2023).
66. Lou, F. & Chen, D. Aligned carbon nanostructures based 3D electrodes for energy storage. *Journal of Energy Chemistry* **24,** 559–586 (2015).
67. Zhang, D. & Nagayama, G. Effective wetting area based on electrochemical impedance analysis: hydrophilic structured surface. *Langmuir* **35,** 16508–16513 (2019).
68. Tiron, L. G., Vlad, M. & Baltă, Ş. Research on hydrophilic nature of polyvinylpyrrolidone on polysulfone membrane F. *IOP Conference Series: Materials Science and Engineering* **374,** 012059 (2018).

APPENDIX

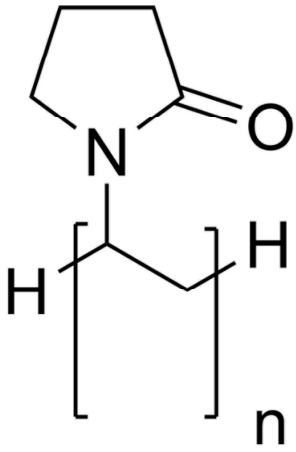

Figure 2.A.1: Chemical structure of polyvinylpyrrolidone (PVP).

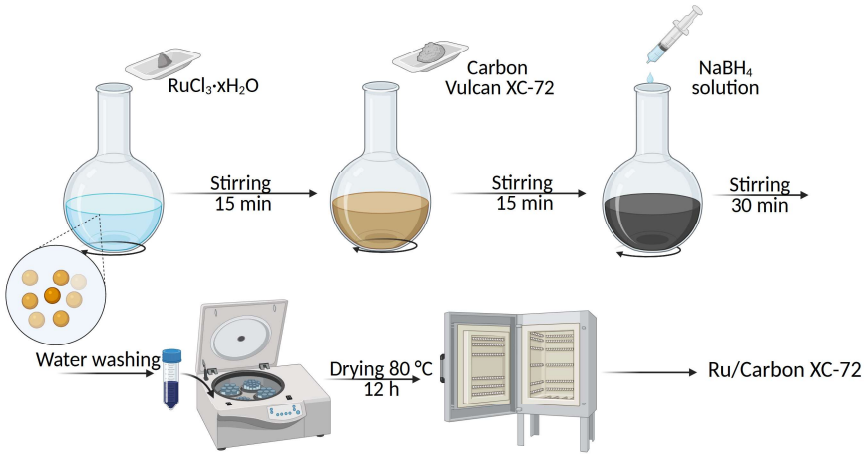

Figure 2.A.2: Catalyst synthesis: impregnation-reduction method x wt.% Ru/C (x= 10, 20 and 40).

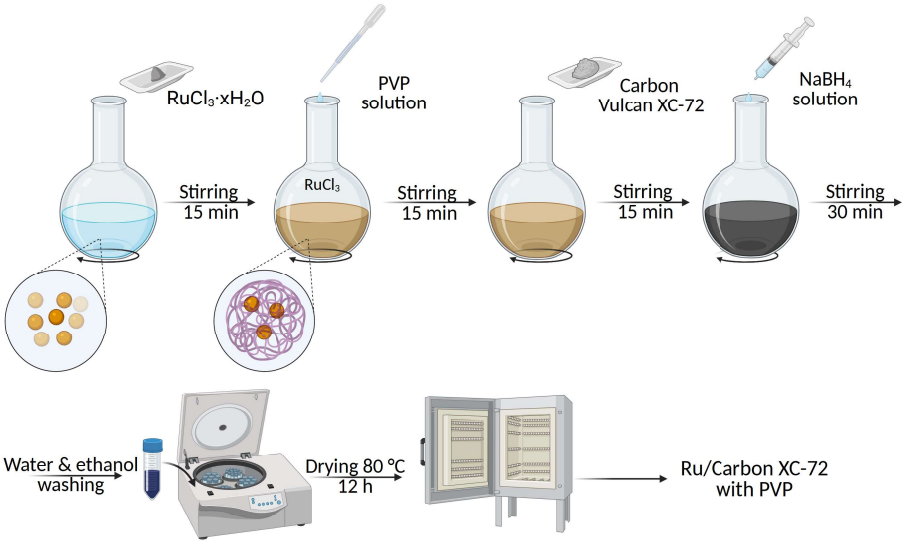

Figure 2.A.3: PVP modified catalysts synthesis: impregnation-reduction method x wt.% Ru/C (x= 10, 20 and 40).

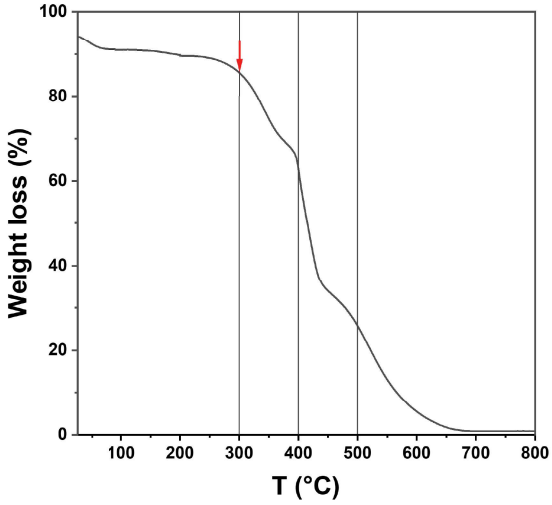

Figure 2.A.4: TGA for pure PVP (K30, MW = 40000) in N_2.

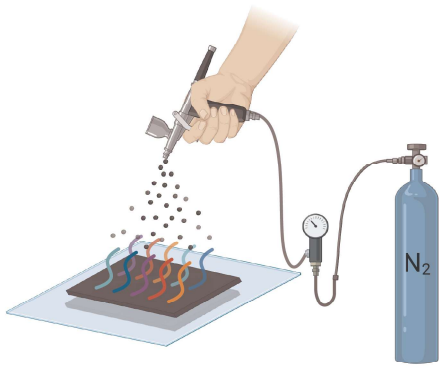

Figure 2.A.5: Scheme of spray coating catalysts on membrane.

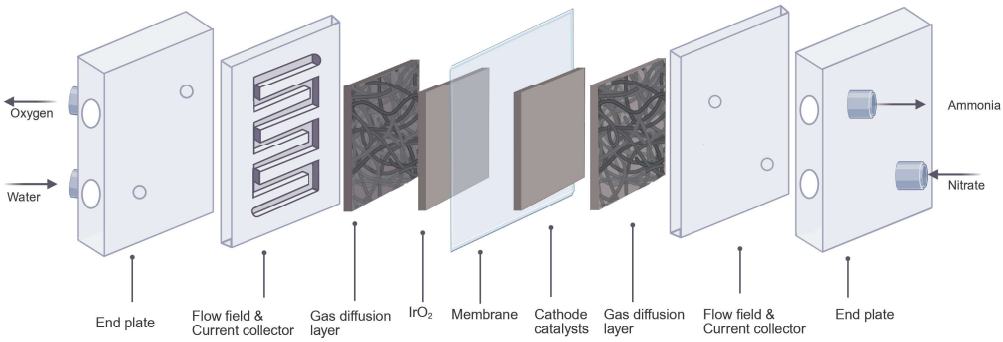

Figure 2.A.6: Exploded view of the flow cell illustrating key components. From left to right: aluminum block, bipolar plate (BP) with gold coating flow channel, titanium gas diffusion layer (GDL), anode catalyst layer, Nafion 115 membrane, cathode catalyst layer, titanium gas diffusion layer (GDL), bipolar plate (BP) with gold coating flow channel and aluminum block.

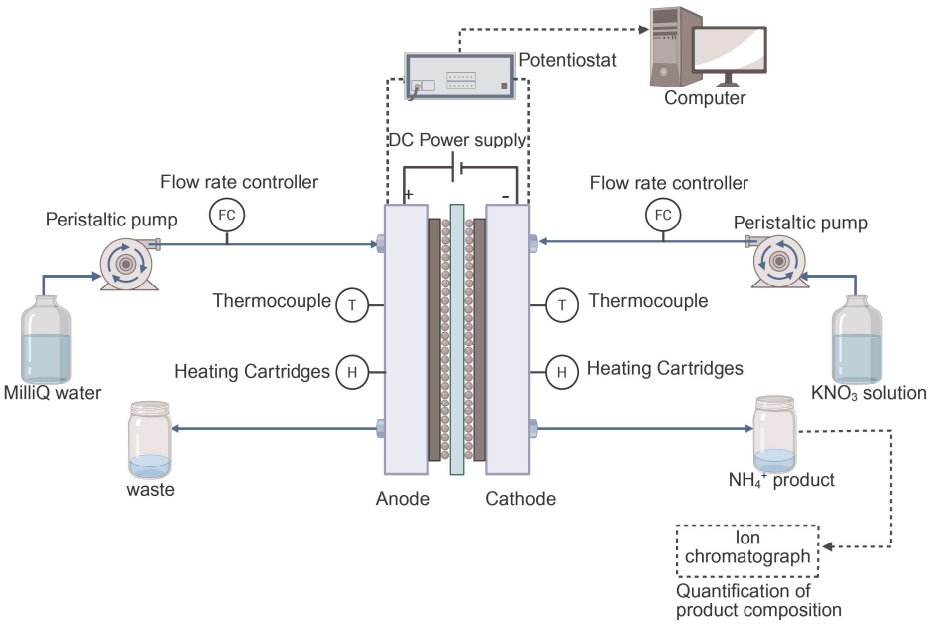

Figure 2.A.7: Flow diagram of electrochemical nitrate reduction to ammonia experimental setup.

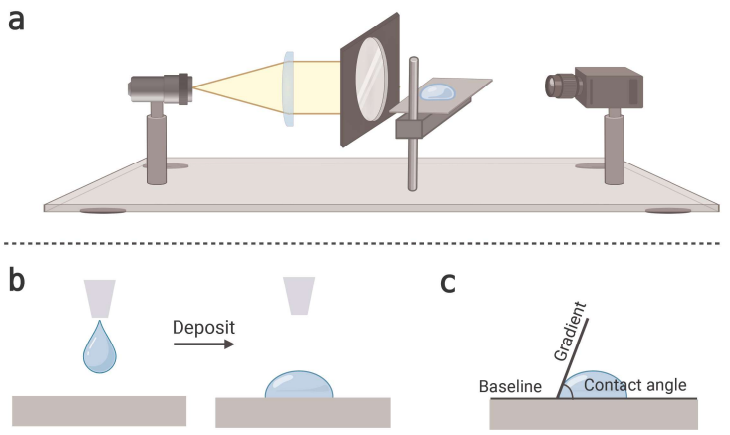

Figure 2.A.8: (a) Contact angle measurement setup, which includes a light source, lens, sample holder, and camera; (b) schematic illustration of a droplet of water deposited onto the catalyst layer; (c) measurement of the contact angle.

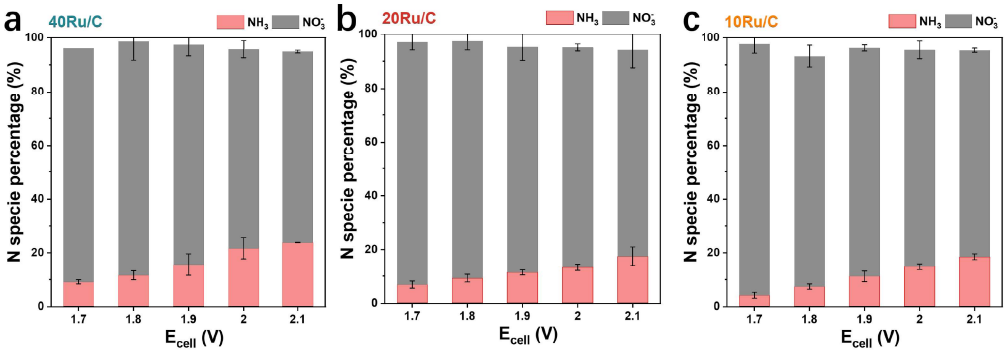

Figure 2.A.9: Nitrogen balances of Ru/C after NO3RR (a) 40Ru/C; (b) 20Ru/C; (c) 10Ru/C.

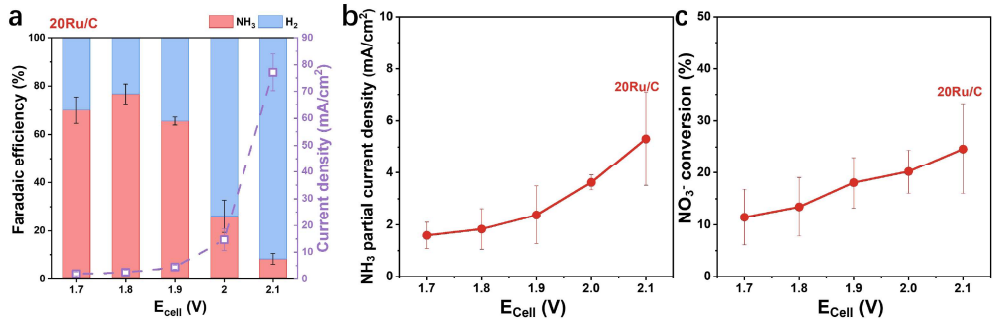

Figure 2.A.10: Electrocatalytic NO_3RR performance for 20Ru/C. (a) Faradaic efficiency (Left) and total current densities (Right); (b) NH_3 partial current density; (c) NO_3^- single pass conversion.

Table 2.A.1: As-prepared catalysts Ru loading determination by TGA

As-prepared catalysts	Ru loading (wt.%)
40% Ru/C	32.6%
40% Ru/C+PVP	28.0%
20% Ru/C	17.6%
20% Ru/C+PVP	15.2%
10% Ru/C	8.0%
10% Ru/C+PVP	7.3%

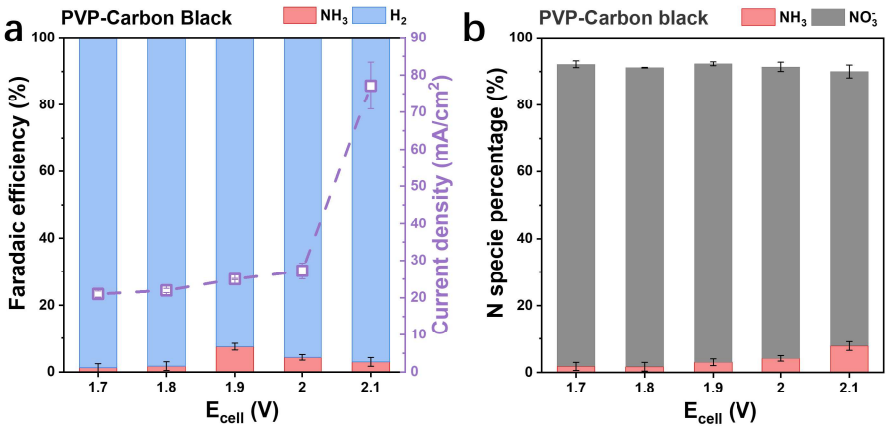

Figure 2.A.11: Electrocatalytic NO_3RR performance for PVP-Carbon black. (a) Faradaic efficiency (Left) and total current densities (Right); (b) Nitrogen balances.

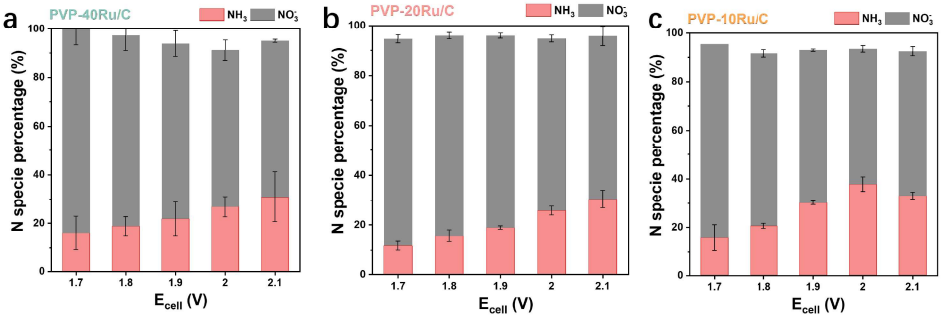

Figure 2.A.12: Nitrogen balances of PVP modified Ru/C after NO3RR (a) PVP-40Ru/C; (b) PVP-20Ru/C; (c) PVP-10Ru/C.

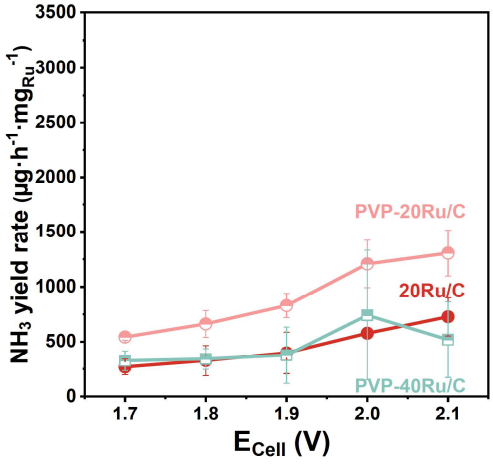

Figure 2.A.13: NH_3 yield rate regarding Ru metal loading..

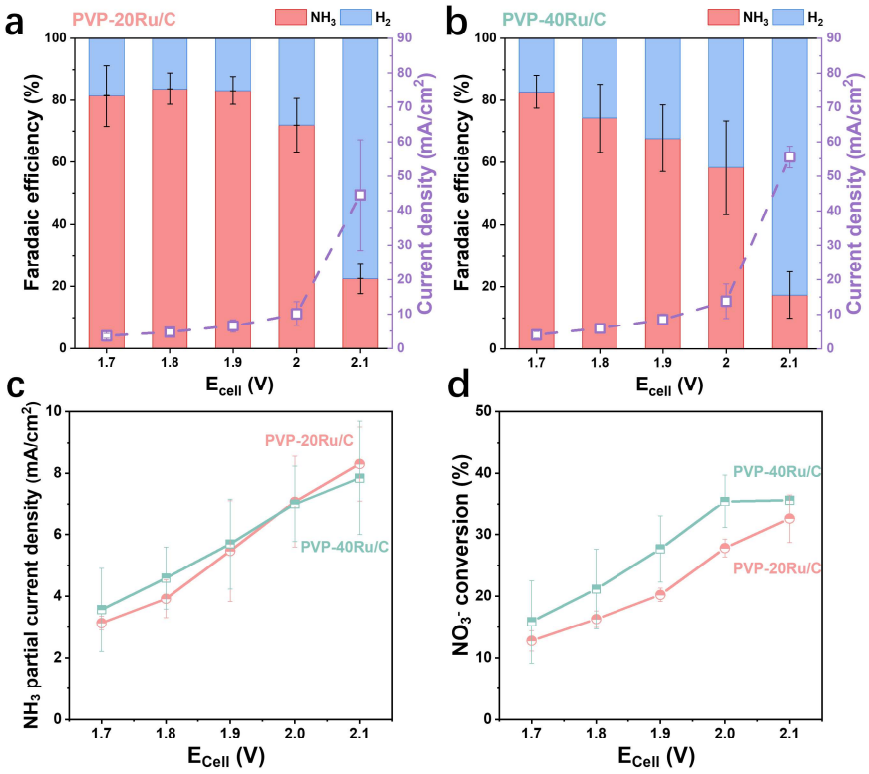

Figure 2.A.14: Electrocatalytic NO_3RR performance. Faradaic efficiency (Left) and total current densities (Right) for electrochemical nitrate reduction on (a) PVP-40Ru/C; (b) PVP-20Ru/C; (c) NH_3 partial current density and (d) NO_3^- single pass conversion.

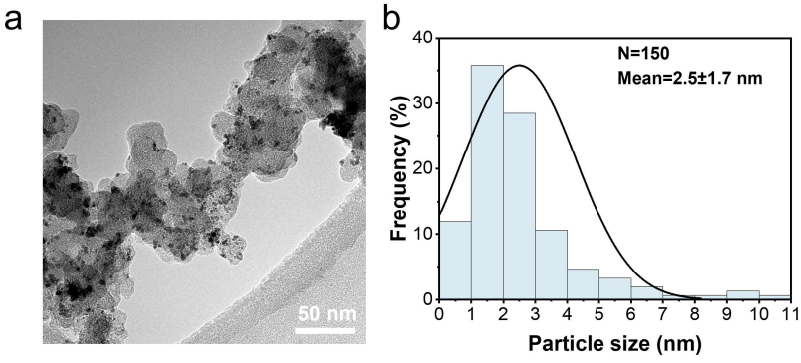

Figure 2.A.15: (a) TEM images for 20Ru/C; (b) particle size distribution for 20Ru/C.

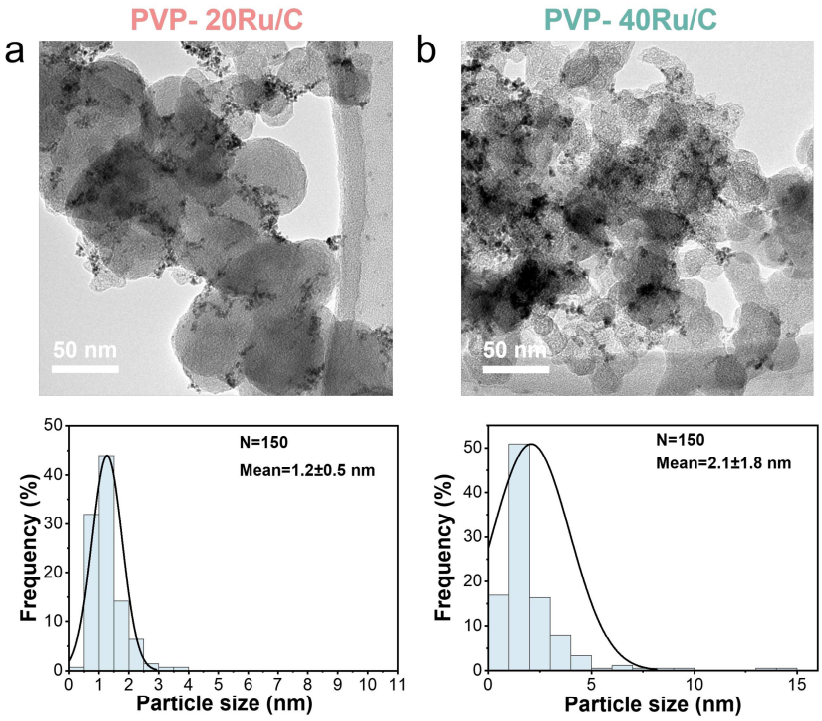

Figure 2.A.16: TEM images and particle size distribution for (a) PVP-20Ru/C and (b) PVP-40Ru/C.

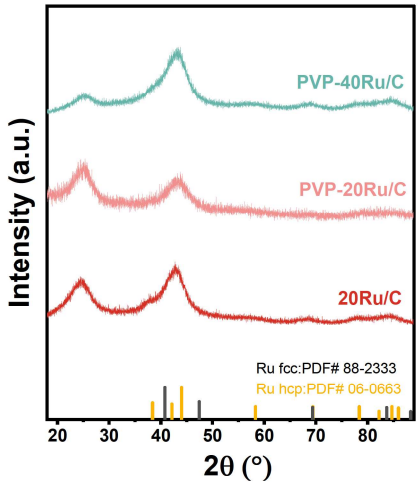

Figure 2.A.17: XRD for 20Ru/C, PVP-20Ru/C and PVP-40Ru/C.

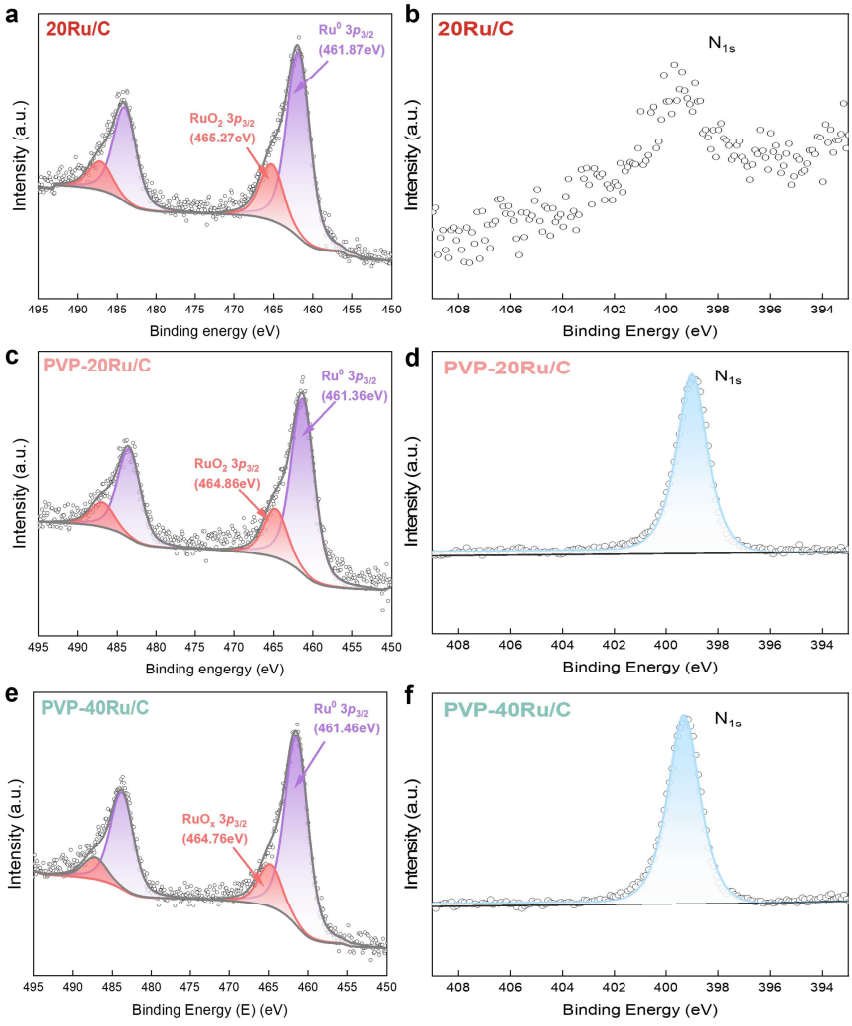

Figure 2.A.18: Ru 3p and N 1s spectra. (a, b) 20Ru/C; (c, d) PVP-20Ru/C and (e, f) PVP-40Ru/C.

Table 2.A.2: As-prepared catalysts Ru loading

As-prepared catalysts	Average particle size (nm)	RuOx 3p3/2 BE (eV)	Ru(0) 3p3/2 BE (eV)
10Ru/C	2.3± 1.3	465.14	461.83
20Ru/C	2.5 ± 1.7	465.27	461.87
40Ru/C	3.2 ± 1.5	465.88	462.21
PVP-10Ru/C	1.1 ± 0.4	464.57	461.27
PVP-20Ru/C	1.2 ± 0.5	464.86	461.36
PVP-40Ru/C	2.1 ± 1.8	464.76	461.46

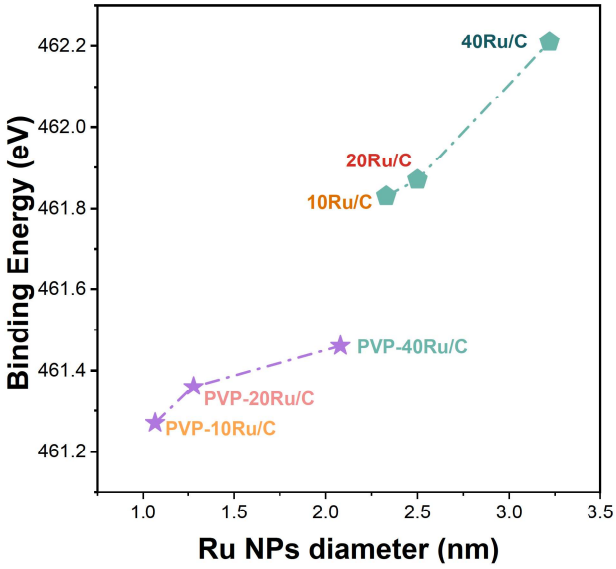

Figure 2.A.19: Relationship between binding energy and particle size.

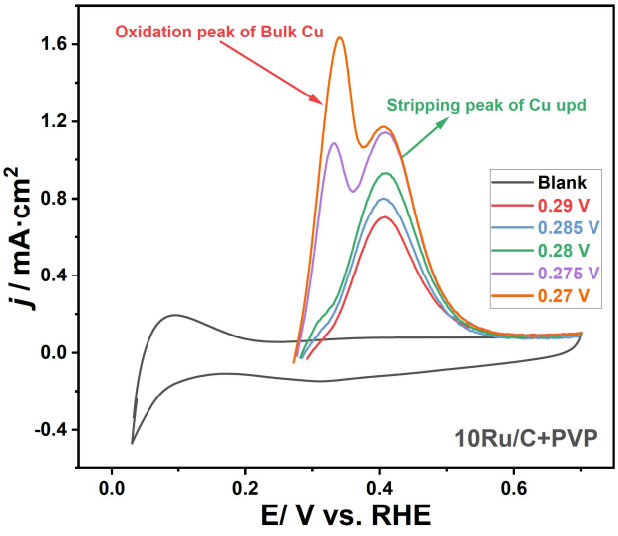

Figure 2.A.20: Determination of the potential for Cu UPD striping voltammogram.

Table 2.A.3: ECSA and HBE for as-prepared catalysts

As-prepared catalysts	ECSA (m2/g)	HBE (eV)
10Ru/C	61	-0.057
20Ru/C	60	-0.074
40Ru/C	25	-0.073
PVP-10Ru/C	98	-0.093
PVP-20Ru/C	81	-0.083
PVP-40Ru/C	43	-0.09

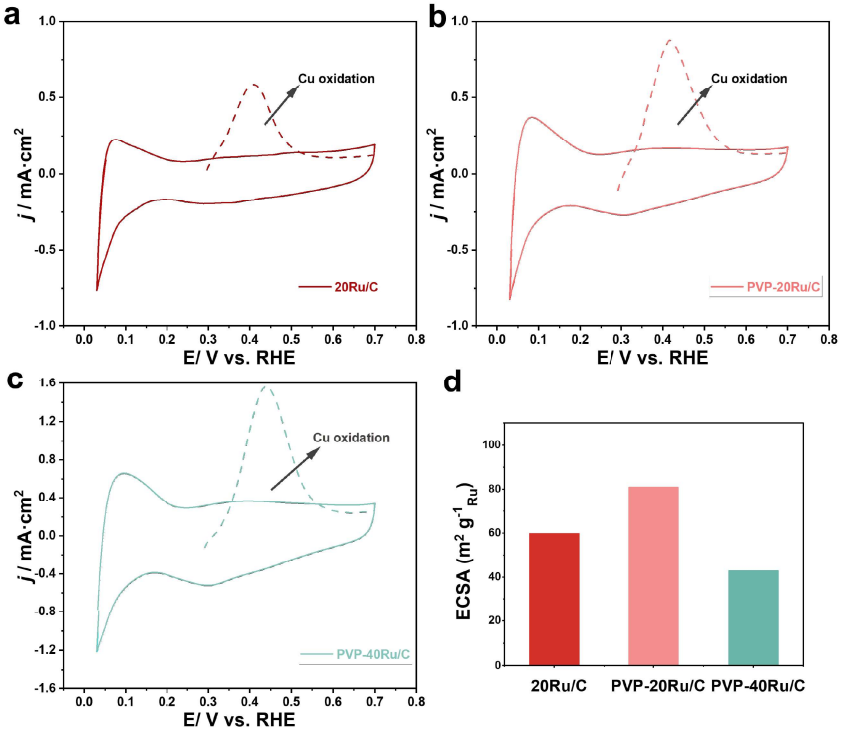

Figure 2.A.21: Cu UPD voltammogram for (a) 20Ru/C; (b) PVP-10Ru/C; (c) 40Ru/C; (d) ESCA.

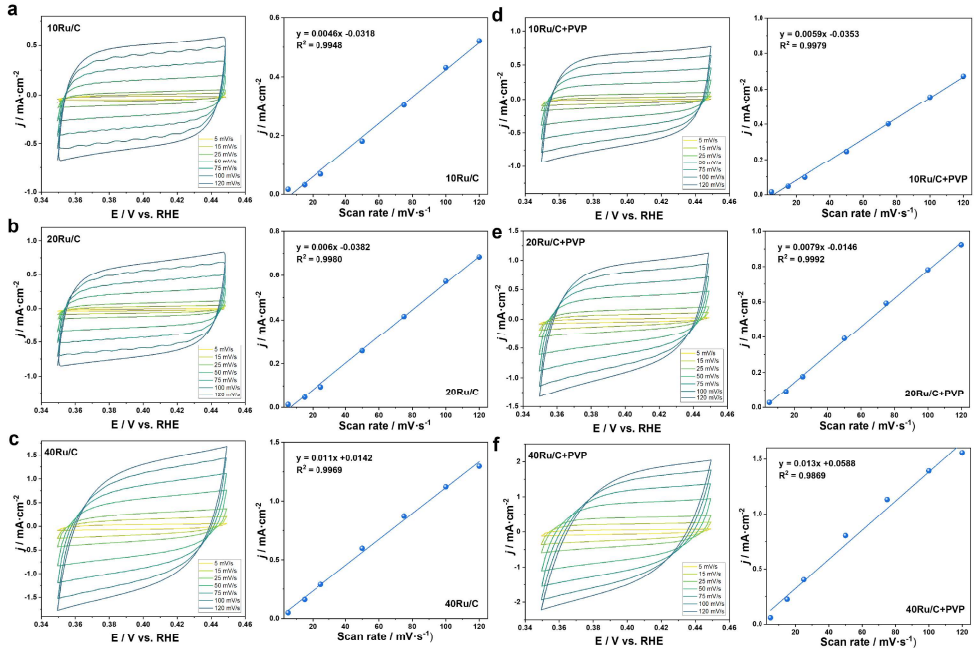

Figure 2.A.22: Double layer capacitors measurements of catalysts in 0.1 M H_2SO_4. Cyclic voltammograms took over a range of scan rates from 5 mV/s to 120 mV/s and fitting lines of the current density versus the different scan rates. (a) 10Ru/C; (b) 20Ru/C; (c) 40Ru/C; (d) PVP-10Ru/C; (e) PVP-20Ru/C and (f) PVP-40Ru/C.

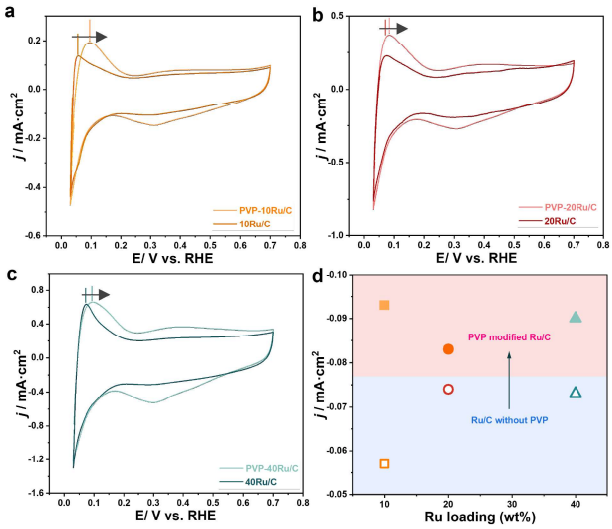

Figure 2.A.23: HBE measurements. (a-c) Cyclic voltammograms of catalysts in 0.1 M H_2SO_4 and (d) HBE as a function of designed Ru metal loading.

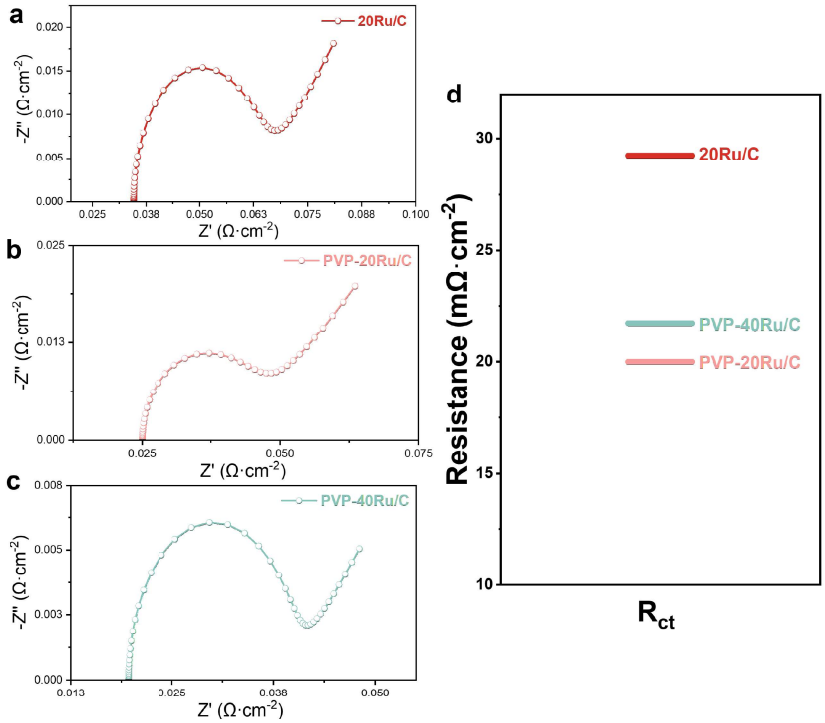

Figure 2.A.24: EIS measurements. (a-c) fitted Nyquist plots of the EIS data and (d) charge transfer resistance of 20Ru/C, PVP-20Ru/C and PVP-40Ru/C.

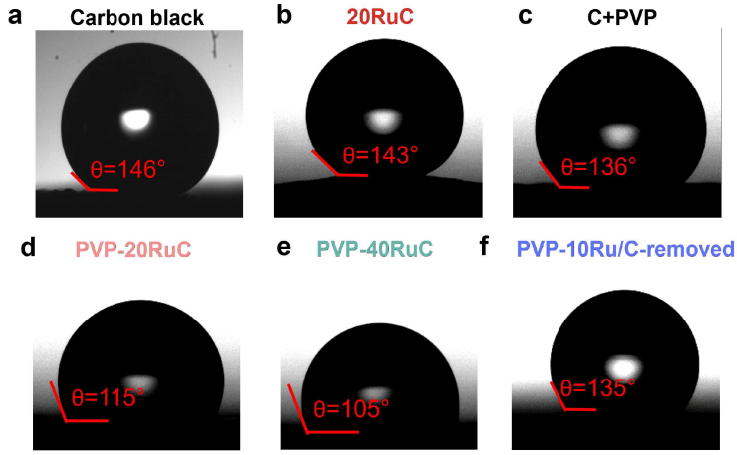

Figure 2.A.25: Contact angles of the water droplet on the MEA cathode catalyst surface. (a) carbon black; (b) 20Ru/C; (b) carbon black + PVP; (d)PVP-20Ru/C; (e) PVP-40Ru/C and (f) PVP-10Ru/C-removed.

Table 2.A.4: Charge transfer resistance and contact angle for as-prepared catalysts

As-prepared catalysts	Rct (m/cm2)	Contact angle (°)
10Ru/C	27	141
20Ru/C	29	143
40Ru/C	38	137
PVP-10Ru/C	14	127
PVP-20Ru/C	20	115
PVP-40Ru/C	22	105

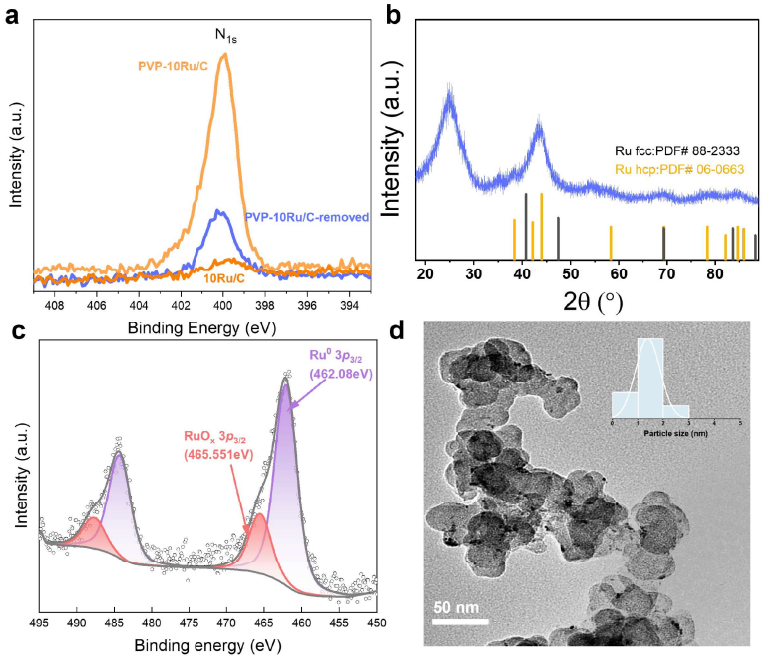

Figure 2.A.26: PVP-10Ru/C-removed. (a) N 1s spectra; (b) XRD; (c) Ru 3p XPS spectra and (d)TEM images and particle size distribution.

Table 2.A.5: ECSA, HBE, Rct and contact angle for PVP-10Ru/C-removed catalysts

As prepared catalysts	ECSA (m2/g)	HBE (eV)	Rct (m/cm2)	Contact angle (°)
PVP-10Ru/C-removed	74	-0.079	16	135

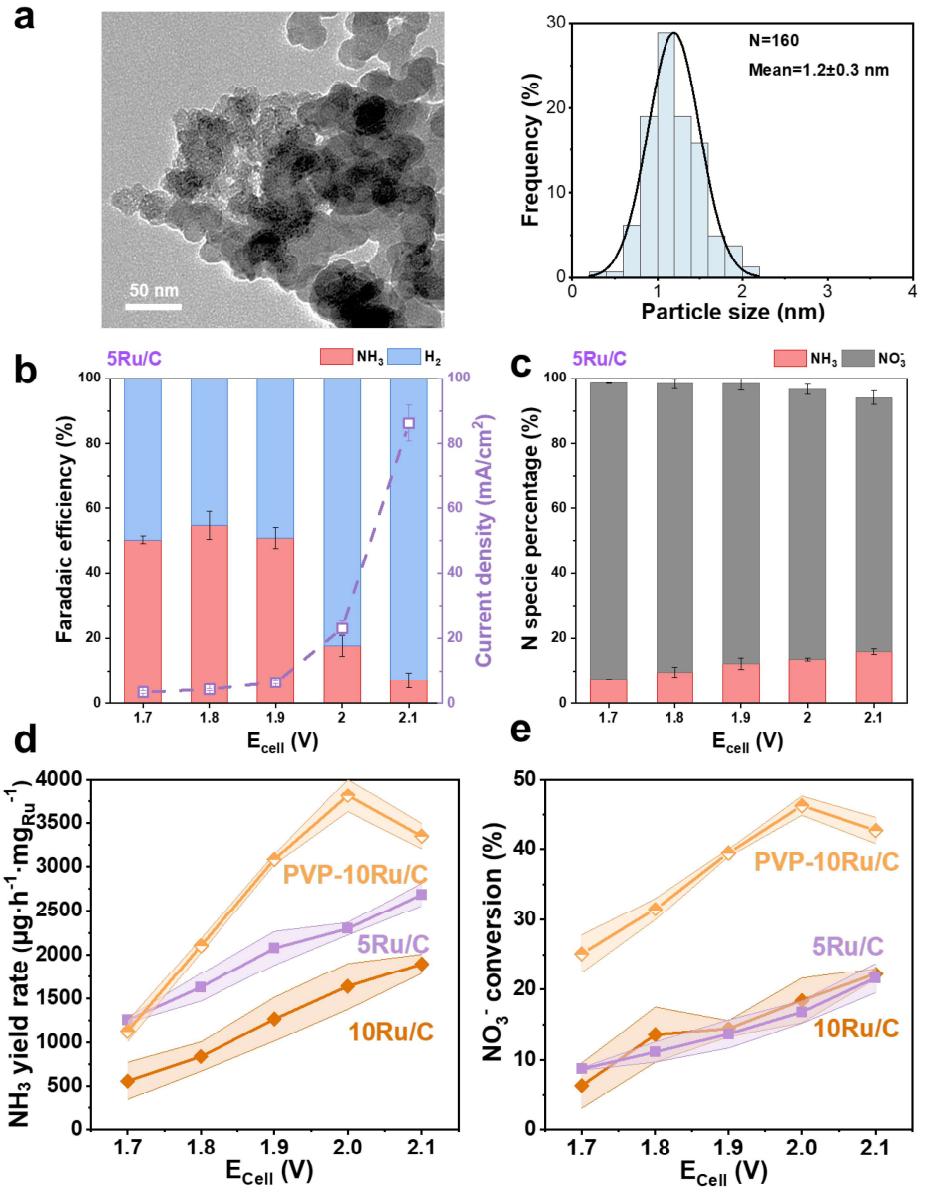

Figure 2.A.27: (a) TEM image and particle size distribution of as-prepared 5Ru/C; (b) electrochemical NO3RR performance for 5Ru/C; (c) N balances of 5Ru/C after NO3RR; (d) NH_3 yield rate regarding to Ru metal loading and (e) NO_3^- conversion.

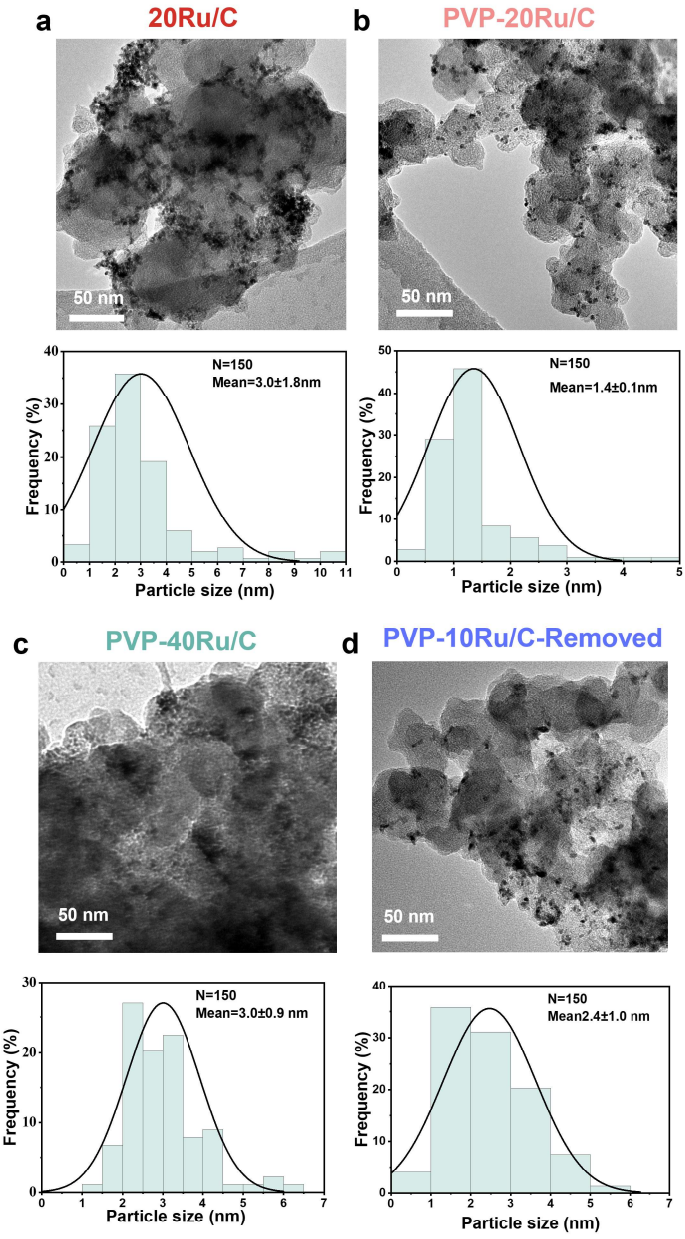

Figure 2.A.28: TEM images and histograms for the particle size distribution catalysts after NO3RR. (a) 20Ru/C; (b) PVP-20Ru/C; (c) PVP-40Ru/C and (d) PVP-10Ru/C-removed.

Table 2.A.6: Summary of average Ru NPs size before and after reaction

As-prepared catalysts	Before NO3RR (nm)	After NO3RR (nm)	Difference (nm)
10Ru/C	2.3± 1.3	2.9 ± 1.4	+ 0.6
20Ru/C	2.5 ± 1.7	3.0 ± 1.8	+ 0.5
40Ru/C	3.2 ± 1.5	6.0± 5.4	+ 2.8
PVP-10Ru/C	1.1 ± 0.4	1.2 ± 0.5	+ 0.1
PVP-20Ru/C	1.2 ± 0.5	1.4 ± 0.1	+ 0.2
PVP-40Ru/C	2.1 ± 1.8	3.0 ± 0.9	+ 0.9
PVP-10Ru/C-removed	1.4 ± 0.9	2.4 + 1.0	+ 1.0

3

Tuning Product Selectivity in Electroreduction of NO by MoS_2 Nanosheets

Electrochemical conversion of NO from gaseous pollutants into ammonia using abundant and cost-effective catalyst materials holds great promise for pollutant abatement and for advancing a more closed, sustainable nitrogen cycle. However, regulating product selectivity remains challenging because NO reduction involves complex multielectron/proton pathways. Here, we report two different crystal phases MoS_2 (2H and 1T′) exhibiting prominent activity in the electrochemical NO reduction reaction (NORR) but showing different selectivity. The faradaic efficiency of ammonia reaches 86% over 2H-MoS_2, outperforming 1T′-MoS_2 (31%) at 2.1 V. In contrast, 1T′-MoS_2 displays higher selectivity towards N_2, especially at lower cell voltage (50% at 1.7 V). Kinetic and spectroscopic analyses further suggest phase-dependent rate control characteristics, consistent with distinct pathway preferences on 1T′ versus 2H. Overall, these results demonstrate that NORR activity and selectivity can be efficiently tuned by choosing the appropriate MoS_2 phase, providing a simple strategy to tune product selectivity in complex multistep reactions.

This chapter has been prepared for submission.

3.1 Introduction

Nitrogen, the fifth most abundant element on earth, plays an essential role as a macronutrient for all living organisms [1]. Within the global nitrogen cycle, various inorganic nitrogenous compounds, including ammonia (NH_3), hydroxylamine (NH_2OH), hydrazine (N_2H_4), nitrous oxide (N_2O), nitric oxide (NO), nitrogen dioxide (NO_2), nitrite (NO_2^-), and nitrate (NO_3^-) are produced in significant quantities by industrial chemical processes [2]. Many of these species, notably NO_x (NO, NO_2 and N_2O) are prominent environmental pollutants. Consequently, mitigating NO_x emissions from fossil fuel combustion, such as power plants and automotive engines, represents a critical focus within nitrogen chemistry [3]. Among these pollutants, NO typically constitutes approximately 95% of NO_x in flue gas [4].

Conventional selective catalytic reduction (SCR) methods effectively convert NO into harmless dinitrogen gas (N_2) [5]. However, SCR requires the input of reducing agents such as NH_3 or H_2, imposing additional energy and material demands [6]. NH_3 itself holds significant importance in agriculture and has recently emerged as a potential H_2 energy carrier [7, 8]. Its industrial production is primarily achieved through Haber–Bosch process, a thermochemically intensive reaction that operates under high pressure (150–300 bar) and temperature (400–500 °C). This process accounts for approximately 1–2% of global energy consumption and 1–1.5% of global CO_2 emissions annually [9].

Thus, electrochemical approaches for the NO reduction reaction (NORR) offer a promising alternative for both NO abatement and NH_3 synthesis, thereby contributing to a more sustainable nitrogen cycle [10, 11]. In particular, the NORR presents thermodynamic advantages: the standard reduction potential of NO to NH_3 (0.71 V vs. RHE) is significantly more positive than that of the nitrogen reduction reaction (NRR, 0.093 V vs. RHE) [12] and hydrogen evolution reaction (HER), theoretically implying a more favorable reaction path [13, 14]. Nonetheless, the practical implementation of the NORR has been hindered by the low solubility of NO in aqueous media (1.92 $mmol \cdot L^{-1} \cdot atm^{-1}$ at 25 °C), which limits its availability at the electrode surface [15]. Therefore, utilizing membrane electrode assembly (MEA) configurations, more specifically in a polymer membrane (PEM) electrolyzer allows direct gaseous NORR, which improves control over reaction environment and reduces internal resistance. Beyond traditional H-cell configuration, a PEM electrolyzer facilitates more controlled reagent flow and reaction kinetics, making it attractive for future electrochemical NO conversion technologies (Figure 3.A.1) [16, 17].

To date, significant advances have been made in the development of catalytic materials for the NORR, including pure transition metals (TMs) [18] noble metals [19], alloys

[20], metal oxides [21] and single-atom catalysts (SACs) [22]. Nonetheless, challenges still remain due to the low abundance and thus high costs associated with noble metals, the limited activity of pure TMs, and the insufficient long-term stability of SACs, emphasizing the need to design cost-effective, efficient, and durable electrocatalysts for denitrification [23]. Among transition metal dichalcogenides (TMDs), monolayer molybdenum disulfide (MoS_2) stands out as an abundant, low-cost, and versatile electrocatalyst, having already demonstrated excellent HER [24]. Compared to the commonly studied semiconducting 2H phase, MoS_2 in its octahedral (1T) or distorted octahedral (1T′) configurations has shown superior catalytic activity for the HER [25]. A key advantage of TMDs is the tunability of their atomic-scale structure, which offers opportunities to adjust the selectivity of multielectron/proton reactions [26]. In this context, exploring phase-dependent electrocatalytic activity is vital to achieve a deeper understanding of the origins of catalytic performance. Nakamura et al. [27] identified a Mo(V) intermediate unique to 1T-MoS_2 that promotes N-N coupling selectivity by decoupling proton and electron transfer to sequential proton-electron transfer (SPET) pathway. In contrast, 2H-MoS_2 favors NH_3 production during NO_3^- reduction via concerted proton-electron transfer (CPET) pathway. Similarly, Yu et al. [28] investigated the reaction at near-neutral pH, reporting that the strong hydrogen affinity and favorable hydrogenation of nitrogenous intermediates on 1T-MoS_2 make this phase particularly promising for NO_3^- to NH_3 conversion. However, these studies have primarily focused on liquid-phase nitrate reduction under mild pH conditions (pH 4-7) in three-electrode cell configurations. Therefore, the role of MoS_2 crystal phases in the direct gas phase NO reduction under acidic conditions in industrially relevant PEM electrolyzers remains insufficiently understood and requires further investigation.

In this work, we explored phase-engineered MoS_2 nanosheets (2H and 1T′) as effective catalysts for direct gaseous NO electroreduction in a PEM electrolyzer, enabling a pronounced and controllable selectivity switch between NH_3 and NH_3. The 2H-MoS_2 achieved a high NH_3 yield of 558 $\mu mol \cdot cm^{-2} \cdot h^{-1}$ at 2.3 V and a highest FE of 86% at 2.1 V, exceeding the performance of the 1T′ phase. Notably, the 1T′ phase-dominant MoS_2 demonstrated greater selectivity for N-N coupling products (NH_3), particularly under low applied potentials, 50% FE towards NH_3 at 1.7 V. To uncover the origin of this phase-dependent selectivity, we establish a mechanistic picture by integrating LSV with local Tafel/derivative analysis, an apparent kinetic isotope effect, and ex situ NO-DRIFTS, revealing distinct apparent rate-control characteristics on 2H versus 1T′, thus we connect the stronger NO-derived adsorption signatures o 1T′ to coverage-enabled N-N coupling, whereas the pronounced apparent KIE on 2H supports a proton-coupled hydrogenation contribution consistent with enhanced NH_3 selectivity. Overall, these findings highlight

phase engineering of TMDs catalysts as a practical strategy to tune product selectivity in complex multistep proton-electron transfer reactions.

3.2 Experimental method

Chemicals and materials Thiourea ($SC(NH_2)_2$), ammonium heptamolybdatetetra hydrate ($(NH_4)_6Mo_7O_{24} \cdot 4H_2O$), hydrazine monohydrate ($N_2H_4 \cdot H_2O$), hydrogen peroxide (H_2O_2), sulfuric acid (H_2SO_4), potassium iodate (KIO_3), hydrolymine (NH_2OH) and neutral red were purchased from Sigma Aldrich. Iridium (IV) oxide Premion™ (IrO_2) 99.99% was purchased from Therma Scientific Chemicals. Vulcan XC72 carbon black was bought from Cabot Corporation. Nafion™ 115 membranes from Ion power, porous sintered titanium gas diffusion layers were purchased from Bekaert, and carbon gas diffusion layer (GDL) Sigracet 39 BB was from Fuel Cell Store.

Preparation of 2H-MoS_2 nanosheets 2H-MoS_2 was synthesized using hydrothermal method [29]. Briftly, 0.53 g (0.4 mmol) of $(NH_4)_6Mo_7O_{24} \cdot 4H_2O$ and 1.83 g (24 mmol) of $SC(NH_2)_2$ were dissolved in 30 mL of MilliQ water and stirred to form a homogeneous solution. After that, the solution was transferred to a 45 mL stainless-steel autoclave with Polyparaphenol (PPL) liner and heated to 220 °C for 12 hours. After cooling down naturally to room temperature, the products were extracted, filtered and washed with water and ethanol for 6 times. The obtained catalyst powder was dried the vacuum oven at 60 °C for 12 hours.

Preparation of 1T′-MoS_2 nanosheets 1T′ phase dominated MoS_2 was synthesized by one-step hydrazine assisted hydrothermal method which is modified by as described 2H-MoS_2 method previously [29]. Additionally, 0.29 mL (6 mmol) of $N_2H_4 \cdot H_2O$ with the molar ratio of N_2H_4/Mo of 2:1 was added into the solution. The synthesis was completed in 180 °C for 10 hours and rapidly cooled down to room temperature. The rest remained the same as the synthesis of 2H-MoS_2 samples.

Material Characterization The powder X-ray diffraction (XRD) was recorded using Bruker D8 ADVANCE X-ray diffractometer with Cu Kα radiation source in a range of 5° to 90° with a step of 0.05°. The surface morphology of the catalysts was characterized by scanning electron microscopy (SEM). Raman spectra were recorded from 500 to 3000 cm^{-1} on a Horiba Scientific LabRAM HR Evolution Raman Spectroscopy system with an excitation wavelength of 514 nm. The composition and chemical bonding were analyzed by Thermo Scientific Kα system with Al Kα radiation (1486.7 eV). All binding energies for XPS spectra were calibrated according to the C 1s peak at 284.8 eV. Contact angle measurements were performed via sessile drop using an OCA 25 goniometer (Dataphysics

instruments Gmbh, Filderstadt, Germany), and 2 μL of droplets were dispensed onto substrates using an automatic pipetting unit. Measurements were taken in ambient air with a temperature in the range of 20–24 °C. Specific surface areas were determined by the Brunauer-Emmett-Teller (BET) method. The Mo K-edge X-ray absorption near-edge (XANES) spectra and X-ray absorption fine structure (EXAFS) spectra were measured at the BL16-NOTOS beamline of the ALBA Synchrotron, Spain.

Electrode preparation Nafion™ 115 membranes ($3 \times 3 cm^2$) were pre-treated according to the procedure of 1 hour in 5 wt. % hydrogen peroxide (H_2O_2) solution and 1 hour in 0.5 M H_2SO_4 solution at 80 °C and 1 hour in boiling MilliQ water. 4 mg of commercial IrO_2 ($1\ mg \cdot cm^{-2}$) with 20 wt.% Nafion ionomers were ultrasonically dispersed in 1mL isopropanol and water (volume ratio: 50:50) for 1h to get a homogenous ink. The cathodic ink was prepared in the same way with as prepared 2H-MoS_2 or 1T′-MoS_2, Vulcan XC72 carbon black (from 10 wt.% to 70 wt.%) and 30 wt.% Nafion ionomers to get a constant catalyst loading of $1\ mg \cdot cm^{-2}$ 2H-MoS_2 or 1T′-MoS_2 with a $2 \times 2 cm^2$ active geometry area. The catalyst inks were finally sprayed at 60 °C onto both side of membranes using automatic spray coater (CNC Airbrush Singular). After spray coating, the membrane was hot-pressed at 120 °C and 1 tonne for 3 minutes.

Electrochemical NORR experiments The electrochemical experiments were conducted in the PEM electrolyser on an AUTOLAB PGSTAT302N potentiostat with a 20 A booster. The PEM electrolyser was set at an operating temperature of 80 °C. At the anode side, a peristaltic pump (Ismatec ISM597D) was used to pump MilliQ water through the chamber at a flow rate of $3\ mL \cdot min^{-1}$. At the cathode side, 5 vol% NO in He was sent to the chamber at a flow rate of $26\ mL \cdot min^{-1}$ and $1\ mL \cdot min^{-1}$ of CH_4 was sent as the external standard to correct the volume changes after reactions. The gas outlet was connected to an acid trap filled with 0.1 M H_2SO_4 solution to collect the produced NH_3 and NH_2OH. After the acid trap, the remaining gas was analysed by transmission Infrared (IR) Spectrometer (Bruker Alpha) and gas chromatography (GC). The reactions were carried out at constant potential in the range of 1.7 V to 2.3 V for 30 minutes each. Electrochemical impedance spectroscopy (EIS) was conducted at the catalytically relevant potential of 1.7 V over a frequency range of 100 kHz to 0.1 Hz, using 10 points per decade and an AC perturbation amplitude of 10 mV.

Product quantification The gaseous NO reduction products nitrous oxide (N_2O) and unreacted NO, external standard CH_4 were analysed by Bruker Alpha infrared spectrometer. N_2 and H_2 were analysed by a CompactGC (Global Analyser Solutions) equipped with a thermal conductivity detector (TCD). Ammonium (NH_4^+) collected at the acid trap were quantified using Ion Chromatography (IC, Metrohm 883 Basic ion chromatogra-

phy), equipped with a Metrosep C6 separation column. NH_2OH was quantified by UV-VIS spectroscopy (Unicam UV 500), measuring absorbance at 525 nm. The procedure consists in adding 1 mL of the sample with 5 mL of MilliQ water, 1 mL of 0.047 $mol \cdot L^{-1}$ KIO_3 and 1 mL of 3 M H_2SO_4 2 mL of neutral red is added after 5 minutes.

RDE measurements Cyclic voltammetry (CV) and linear scan voltammetry (LSV) were conducted using a three-electrode electrochemical glass cell (graphene rod as counter and Ag/AgCl as reference electrodes) at room temperature with Argon and NO purging. A glassy carbon disc of 0.196 cm^2 (5 mm diameter) was used as the working electrode in rotating disk electrode measurements (RDE, Pine Instruments). 15 μL of catalyst ink (details described in the previous section) was loaded onto the glassy carbon electrode for all the measurements in 100 mL of freshly prepared 0.1 M H_2SO_4 solution. Prior to the measurements, the electrode as electrochemically cleaned by repetitive potential scans between -0.4 V to 0.8 V vs. RHE until a stable cyclic voltammogram was obtained. All potentials were converted into the reversible hydrogen electrode (RHE) scale, and 85%iR corrections were applied to all results.

3.3 Results and Discussion

Material Synthesis and Characterizations 2H-MoS_2 (trigonal phase) material was successfully synthesized using an one-step hydrothermal method as illustrated in Figure 3.A.2(a). Meanwhile, distorted 1T′-MoS_2 (octahedral phase) was obtained by adding $N_2H_4 \cdot H_2O$ during the synthesis, as depicted schematically in Figure 3.A.2(b) [29]. XRD patterns of the as-prepared samples are shown in Figure 3.3.1(a). For the synthesized 2H-MoS_2, the (002) peak located at 13.9° shifted slightly towards lower angle compared to that of 14.4° in bulk 2H-MoS_2 (JCPDS Card no. 73-1508). This was ascribed to the interlayer stress as a result of disordered structures [30]. The calculated interlayer distance of the synthesized 2H-MoS_2 is 0.62 nm, originating from the interference among the 2H-MoS_2 layers along the c-axis. At higher angles, the appearance of (100) and (110) peaks in 2H-MoS_2 sample (hereafter referred to as 2H-MoS_2) indicated the same basal plane orientation with bulk 2H-MoS_2. For the synthesized 1T′-MoS_2 sample (hereafter referred to as 1T′-MoS_2), the (002) peak is drastically shifted to 9.2° compared to that peak of 2H-MoS_2, which indicates that the lattice expansion as the interlayers are intercalated with N_2H_4 [31]. According to the Bragg equation, the corresponding interlayer distances of the peaks were 0.93 nm and 0.49 nm at 9.2° and 18.2°, respectively [32]. The broad XRD diffraction peak can be an indication of the coexistence of both 2H and 1T′ phases in the hydrazine intercalated 1T′ sample [33]. Scanning electron microscopy (SEM) images of the prepared 2H and 1T′-MoS_2 samples were shown in Figure 3.3.1(b and c). Both pic-

tures show nano-flowers consisting of small, intersecting nanosheets. This morphology is characterized by short lateral dimensions and a lack of extended stacking, which geometrically necessitates a high density of exposed edge S atoms, which are the active sites, compared to flat for bulk 2H-MoS_2. The disordered arrangement of these nanosheets prevents the Van der Waals restacking typical bulk crystals, thereby maximizing the accessible surface area and defect density [34].

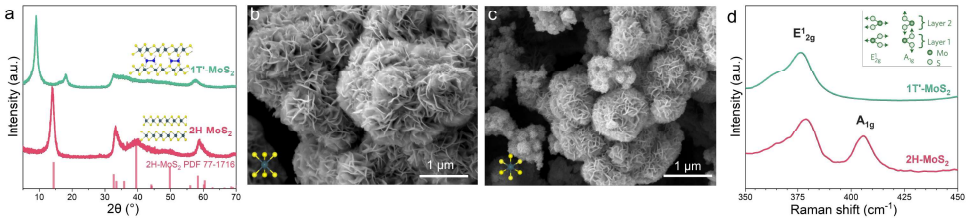

Figure 3.3.1: (a) XRD patterns of 2H- and 1T′-MoS_2; (b) and (c) SEM images of 2H- and 1T′-MoS_2; (d) Raman spectrum of 2H- and 1T′-MoS_2.

Figure 3.3.1 (d) presents Raman spectra of the synthesized 2H and 1T′ phase MoS_2 nanoflowers. The E^1_{2g} peak at 378 cm^{-1} and the A_{1g} one at 404 cm^{-1} show the opposite vibration of two S atoms with respect to the Mo atom and the out of plane opposite vibration of the S atoms in opposite directions , respectively. Compared to the 2H phase, 1T′-MoS_2 displays a slightly weaker E^1_{2g} band due to the existence of defects. Notably, there is no A_{1g} band presented in 1T′ phase MoS_2 which indicates the weakened interactions between the adjacent layers because of the intercalated molecules to the MoS_2 layers (Figure 3.3.1 (a)) [32].

To better understand the electronic structure of as-prepared 2H- and 1T′-MoS_2, X-ray absorption near edge structure (XANES) spectroscopy was performed. Commercial 2H-MoS_2 was taken as the standard. The results (Figure 3.3.2 (a)) suggest that the oxidation state of Mo in both samples is +4 as the energy positions of Mo K-edge are close to that of the commercial MoS_2 standard. However, the chemical state of Mo in 1T′-MoS_2 was a little lower than that of 2H-MoS_2 according to the spectra, which indicated the surface of 1T′-MoS_2 is electron rich. The valence state and near-surface composition of 2H and 1T′ phases were further identified by X-ray photoelectron spectroscopy (XPS). All the spectrums are calibrated using the C 1s peak at 284.8 eV. The energy shifts of the Mo (3d) and the S (2p) peaks further indicate the different electronic states of the 1T′ and 2H phases [35]. As shown in Figure 3.3.2 (c), two peaks of Mo^{4+} (3d) at around 229 and 232 eV correspond to binding energies of Mo^{4+} $3d_{5/2}$ and $3d_{3/2}$ electrons in 2H-MoS_2, respectively. In addition to these two peaks, a new doublet peak (228.4 and 231.6 eV) appeared for 1T′-MoS_2 [36]. The Mo ($3d_{5/2}$) peak of the 1T′ phase shifted to a lower binding energy

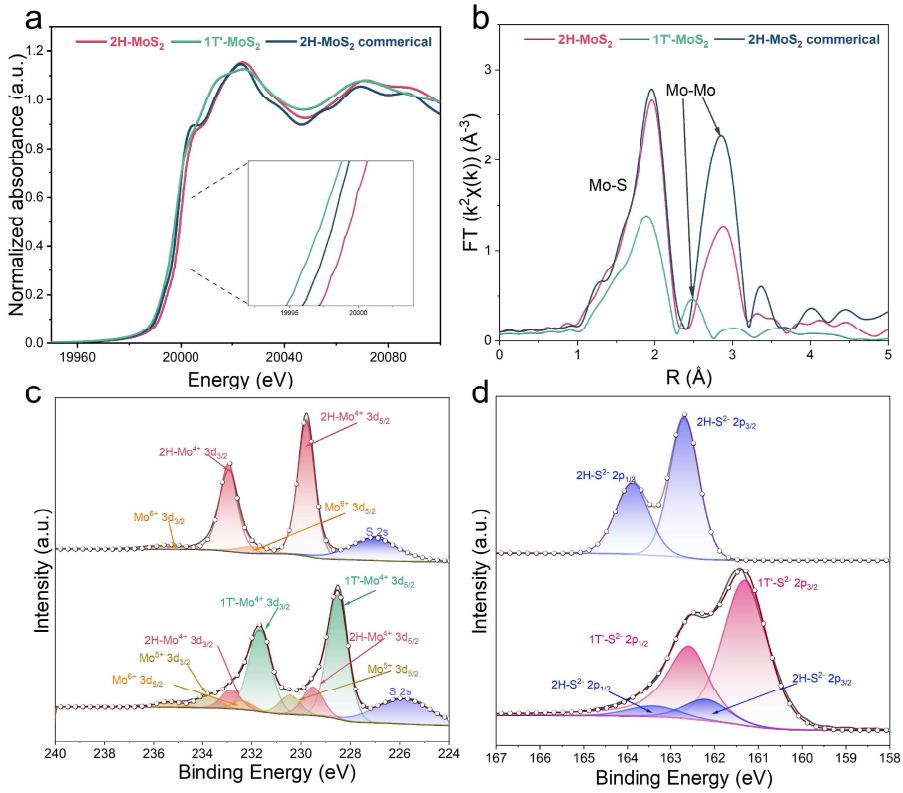

Figure 3.3.2: (a) XANES spectra and (b) k^2-weighted Fourier transformed EXAFS spectra of the Mo K-edge of the as-prepared and standard MoS_2 samples; (c) Mo 3d XPS spectra and (d) S 2p XPS spectra of as prepared 2H- and 1T′-MoS_2.

(0.88 eV) relative to the 2H-MoS_2, showing the increasing electron density on 1T′-MoS_2, which is consistent with the XANES studies. By deconvoluting the Mo (3d) peak, it can be estimated that 80% of Mo is in the 1T′ phase in the as-prepared 1T′-MoS_2 samples. The S ($2p_{3/2}$) peak also showed a similar shift as Mo ($3d_{5/2}$) (Figure 3.3.2 (d)). Compared to the 2H phase with one S (2p) doublet with the binding energy of 162.6 eV, the hydrazine-intercalated 1T phase has an extra split S (2p) doublet peak at 161.3 eV. In addition, the XPS spectra of N (1s) is presented in Figure 3.A.3. The peak at 399.4 eV can be ascribed to the characteristic signals of intercalated or adsorbed N_2H_4 species [37], suggesting the occurrence of charge transfer from N to MoS_2. Importantly, the presence of N as an n-type dopant in MoS_2 can shift the Fermi level closer to the valence band, thereby facilitating charge transfer. This effect arises from band bending induced by the formation of Mo–N covalent bonds and the preferential removal of sulfur atoms [38, 39]. Besides, the XPS analysis based on the survey scan indicates that the atomic ratio of Mo to S atoms

is approximately 1:1.86 for 2H-MoS_2 but decreased to 1:1.63 for 1T′-MoS_2, indicating an increased number of S vacancies in the 1T′ phase. (Figure 3.A.4 and Table 3.A.1).

Furthermore, the atomic coordination was investigated by extended X-ray absorption fine structure (EXAFS) spectroscopy. As shown in Figure 3.A.5, the Mo K-edge oscillation curve of 1T′-MoS_2 differs significantly from those of 2H-MoS_2 and commercial MoS_2, indicating substantial changes in local atomic arrangements. These differences are further clarified by the Fourier transform (FT) profiles in real space (Figure 3.3.2 (b)). For 2H-MoS_2, the FT curve features two main peaks at 1.96 Å and 2.85 Å, corresponding to the nearest Mo–S and Mo–Mo path b, respectively. In contrast, 1T′-MoS_2 exhibits a noticeable second peak at 2.48 Å instead of 2.85 Å in 2H-MoS_2, indicating a change in the Mo–Mo distance and the local structure changes. Additionally, the peak intensity of the Mo–S bond decreases for 1T′-MoS_2, likely due to defect formation induced by N_2H_4 intercalation, while the Mo–Mo peak intensity also decreased, suggesting a corresponding reduction in coordination number. These observations may indicate a structural transformation in which one sulfur basal plane of 1T-MoS_2 rotates by 60° along the c-axis relative to the 2H-phase trigonal prismatic structure, resulting in a distorted octahedral coordination (1T′) (Figure 3.A.6) [40]. To obtain quantitative structural parameters, EXAFS fitting was conducted in ARTEMIS [41] software, with results summarized in Table 3.A.2 and Figure 3.A.8.

Optimal carbon ratio for electrocatalytic NORR

Prior to the evaluation of the MoS_2 catalysts for NORR in PEM electrolyzer, the optimal ratio of mixing as-synthesized MoS_2 materials with electrically conducting carbon black was first investigated. Conductive carbon black is indispensable to drop-casted electrodes for ensuring smooth charge transfer at the catalyst interface and maximizing the utilization of the catalyst surface, especially for MoS_2 which is a semiconductor type material. The tests were first performed in a rotating disk electrode (RDE) setup, which allows for more precise control of mass transport, speeding up the investigation process compared to multi-steps preparation for testing in PEM electrolyzer [42]. 2H-MoS_2 was used for this investigation, and the iR-corrected polarization curves in 0.1 M H_2SO_4 were used to compare performance with different relative carbon amounts. In the MoS_2/C (carbon black) composition, the loading of 2H-MoS_2 (1 $mg \cdot cm^{-2}$) was kept constant and the amount of carbon black was changed with respect to the total weight of 2H-MoS_2 from 100 wt.% to 30 wt.%, decreasing with the step of 10 wt.%. The physically mixed 2H-MoS_2/C was drop-casted on a glassy carbon electrode in the RDE setup (see the method section for detailed description). The results are shown in Figure 3.A.7, 50 wt.% of Vulcan carbon black mixture exhibited the best electrochemical activity among

all the mixing ratios, while a further increase in the amount of carbon black resulted in decreasing activity. Pure MoS_2 exhibited activity, but the performance was poor and lower than all the samples with carbon black mixing. Also, the electrochemical surface area (ECSA) was investigated by measuring the double-layer capacitance (C_{dL}) in the non-faradaic region. The results are shown in Figure 3.A.9. Derived from cyclic voltammetry (CV) curves obtained at various scan rates, the C_{dL} value was the highest at 50 wt.% carbon black mixture with 7.7 $mF \cdot cm^{-2}$ and decreased with higher amount carbon black (Figure 3.A.10).

The results from the RDE study suggest that a physical mixture of 50 wt.% of carbon black would perform best, therefore, pure MoS_2, 40, 50 and 60 wt.% of MoS_2 on carbon black were selected to test for NORR in PEM electrolyzer. To better understand the relationship between the mass transfer limitation and reaction activity under relative low concentration NO (5 vol% in He), different types of gas diffusion layers, namely hydrophilic Ti GDL and hydrophobic carbon paper (Sargent 39BB), were investigated. Figure 3.3.3 (a) shows the FE towards different products during NORR for (i) pure MoS_2 with Ti GDL, (ii) pure MoS_2, (iii) 40, (iv) 50 and (v) 60 wt.% on carbon black with carbon paper (CP, for (ii)-(v)) at 2.1 V, respectively. The FE of the full tested cell potential range (from 1.7-2.3 V) is shown in Figure 3.A.11. Electrochemical NORR activity of only carbon black was also examined as a control experiment. Carbon black itself exhibits low total current density, intriguingly with a reasonable selectivity towards ammonia (Figure 3.A.12).

Mainly H_2 was produced when using a Ti GDL, due to its hydrophilic character. A thin water layer could possibility form on the membrane surface because of the electro-osmosis process. This layer slows NO gas diffusion to the MoS_2 active sites and as NO has low solubility in water, the reaction undergoes to HER instead of NORR. Changing the gas diffusion layer to hydrophobic carbon paper improves the removal of the water layer formed during the reaction, promoting the desired NORR reaction over HER. Therefore, using carbon paper as a gas diffusion layer is the best combination for NORR. From the study of carbon ratio, product selectivity results also align with the previous RDE test results. Without a mixture of carbon, HER is the dominant reaction (81.0% FE towards H_2) with zero $FENH_3$. HER reaction is suppressed by adding carbon black to the catalyst layer. FE_{NH_3} increases to 60.0% with 40 wt.% carbon, while FE_{H_2} drops to less than 12.7% at 2.1 V. The undesired HER is suppressed with an increasing carbon ratio, with $40MoS_2/60C$ showing the lowest FE (less than 10%) towards H_2.

Notably, pure MoS_2 with Ti GDL and carbon paper is more selective towards NH_2OH (Figure 3.A.11 (a)). NH_2OH is a reaction intermediate towards NH_3 production via a NO reduction process and has high solubility in water [43]. Water contact angle mea-

surements were performed to check the hydrophobicity of the as prepare catalyst layer on the membrane. Results are shown in Figure 3.3.3(c) and indicated that without additional carbon mixture, the contact angle of the catalyst layer is 125°, which is a bit more hydrophilic compared to that of adding extra carbon black (150° with 50 wt.% carbon black). Thus, we hypothesize that the water layer during the reaction or due to the electro-osmosis drag could not be removed efficiently, therefore the remaining water could potentially desorb NH_2OH from the active sites of MoS_2 and thus prevent further ammonia formation. Carbon black can also improve the mass transport limitation of insoluble reactants which allows a dramatic reduction in the gas diffusion pathway, especially with low concentration of NO. $50MoS_2/C$ displays the highest current density (78 $mA \cdot cm^{-2}$) and FE towards NH_3 (86% at 2.1 V), which indicates not only more active site but also more reactant are available for the reaction.

The NH_3 production rate and partial current density results align with the previous results (Figure 3.3.3(b)). $50MoS_2/C$ achieves an excellent performance of 466 $\mu mol \cdot cm^{-2} \cdot h^{-1}$, while pure MoS_2 produces only 134 $\mu mol \cdot cm^{-2} \cdot h^{-1}$ NH_3 at 2.1 V. The NH_3 yield of other studied configurations is shown in Figure 3.A.13 and a comparison table to the current literature is shown in Table S4. There is no NH_3 production using Ti GDL and the NH_3 production rate reached a plateau at higher voltage which indicates the HER takes over than NORR. NH_3 partial current density follows the same trend as NH_3 production rate for all measurements. The single pass NO conversion rate is summarized in Figure 3.A.14. A major advantage of conducting NORR in a PEM electrolyzer is that it is suitable for continuous NO conversion, which is beneficial for scaled-up operations often required in chemical industry. The enhanced performance by mixing with carbon black can be ascribed to the significant increase in the mass transport rate through hydrophobic carbon layer, which can further compensate for the low concentration NO gas inlet, thereby inhibiting excess *H for H_2 generation. However, with excess amount of carbon, the availability of active sides was hindered, and less catalytic activity was observed.

According to the previous findings, physical mixture with 50 wt.% carbon black was used to compare the catalytic performance of NORR between 2H- and 1T′-MoS_2. Electrochemical impedance spectroscopy (EIS) in Figure3.3.4(a) reveals that the 1T′ phase exhibits a significantly lower charge transfer resistance (R_{ct}) compared to the 2H phase. While R_{ct} primarily reflects the kinetic barrier for the reaction at the interface, this drastic reduction suggests that the semi-metallic character of the 1T′ phase facilitates rapid electron transfer to surface active sites. Furthermore, the lower ohmic cell resistance (R_s) observed in the 1T′ sample confirms the improved bulk electrical conductivity.

The reduction of NO to NH_4^+ is a 5-electron and 6-proton multistep reaction (NO + $6H^+$

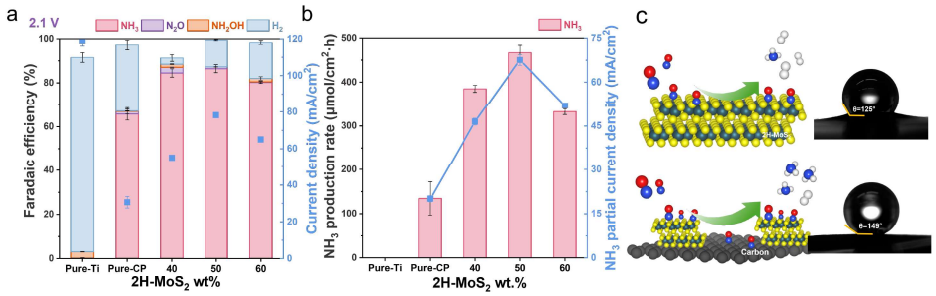

Figure 3.3.3: (a) Faradaic efficiency and total current density; (b) ammonia production rate and partial current density of 2H-MoS_2 at no or different degree of mixing with carbon black; (c) schematic illustrations and water-contact angle measurement of the enhanced NO mass transport.

$+ 5e^- \rightarrow NH_4^+ + H_2O$) and the N-N coupling is a critical step to detoxify NO to harmless dinitrogen. However, the NH_4^+ production in this reaction could compete with N-N coupling ($2NO + 4H^+ + 4e^- \rightarrow N_2 + 2H_2O$ and $2NO + 2H^+ + 2e^- \rightarrow N_2O + H_2O$). The faradaic efficiency and product selectivity of electrocatalytic NO reduction on 2H- and 1T′-MoS_2 at different cell potentials in PEM electrolyzer are shown in Figure 3.3.4(b & c). 2H-MoS_2 shows markedly higher selectivity toward ammonia than 1T′-MoS_2 over the entire cell-voltage range. As the cell voltage increases, FE_{NH_3} increases and reaches a maximum of 86% at 2.1 V with current density of 78 $mA \cdot cm^{-2}$. The ammonia production rate also increases with cell potential, although the rate of increase becomes smaller at higher voltages, indicating that the additional current is diverted to the competing HER rather than to NO reduction (Figure 3.A.15(a)). Consistently, at higher cell voltages FE_{NH_3} decreases while FE_{H_2} increases, confirming that HER becomes increasingly dominant.

In contrast, 1T′-MoS_2 shows a lower NH_3 selectivity, with FE_{NH_3} maximum of 48% at 1.9 V. Notably, 1T′-MoS_2 shows displays substantially higher NH_3 selectivity at low cell voltage, reaching around 50% FE_{NH_3} at 1.7 V, but this NH_3 selectivity rapidly diminishes to <1% at 2.3 V. With increasing cell voltage, the product distribution on 1T′ shifts away from N_2 toward NH_3 and ultimately toward H_2, suggesting that the higher driving force increasingly promotes proton-coupled processes and HER that suppress NORR. This is further supported by the decline in NH_3 production rate and the decrease in NH_3 partial current density at the highest voltages, despite the increase in total current, highlighting that the additional current is largely consumed by HER (Figure 3.A.15(b)).

The single pass NO conversion rate of 2H- and 1T′-MoS_2 is presented in Figure (d), 2H-MoS_2 exhibits higher NO conversion than 1T′-MoS_2, reaches around 67% at 2.3 V which is 3.4 times higher than that of 1T′-MoS_2 (Figure 3.A.15(c)). One way to assess the accessibility of active sites in both catalysts is by comparing the pore size distribution of

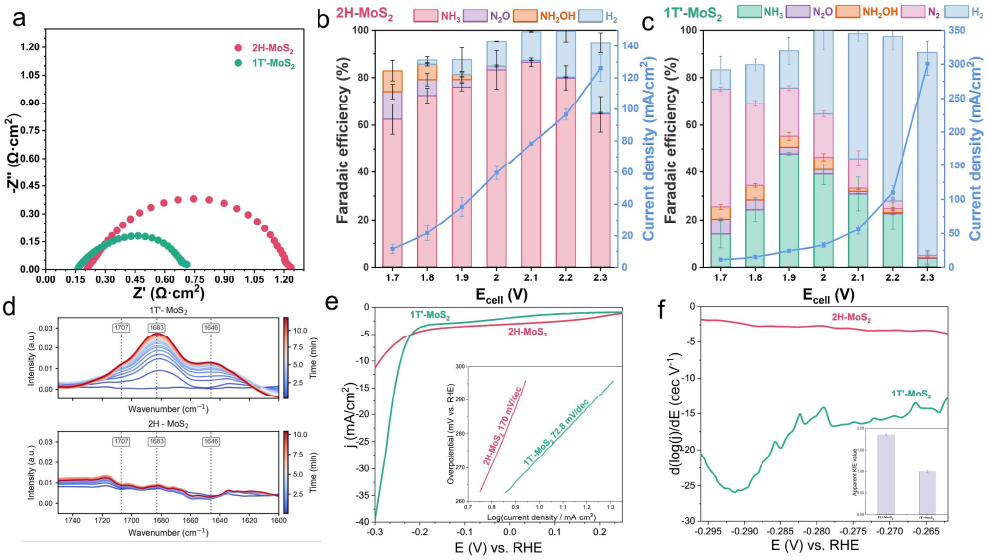

Figure 3.3.4: (a) EIS measurement for 2H and 1T′-MoS_2; (b and c) faradaic efficiency and total current density for 2H and 1T′ phase MoS_2; (d) NO adsorption for 2H and 1T′-MoS_2; (e) LSV and Tafel slop; (f) local Tafel derivative and apparent KIE values for 2H and 1T′ phase MoS_2.

these materials. Thus, the specific surface area and porosity of the as-prepared 2H- and 1T′-MoS_2 were characterized via N_2 adsorption-desorption isotherms (Figure 3.A.16). 2H-MoS_2 exhibited a specific surface area of 33 $m^2 \cdot g^{-1}$, which is approximately 3 times greater than that of the 1T′-MoS_2 (13 $m^2 \cdot g^{-1}$). The lower SSA of the 1T′ phase reflects this dense spherical aggregation, which limits the access of gas to the internal surfaces compared to the more open 2H morphology (Figure 3.3.1 (b and c)).Based on the above results, it implies that under electrocatalytic conditions, 2H-MoS_2 could offer more accessibility to the reactant NO, which is beneficial especially in low concentration NO feed.

Our experimental results show that two different phases of MoS_2 display markedly different NORR selectivity, with 1T′ favoring NH_3 formation and 2H favoring NH_3 formation. To rationalize this difference, we have performed kinetics study and ex situ Diffuse reflectance infrared Fourier transform spectroscopy (DRIFTS) measurements. As shown in Figure 3.3.4(d), 2H-MoS_2 does not show a clear growth of distinct NO-related adsorption bands and is dominated by water signal, whereas 1T′-MoS_2 displays pronounced NO adsorption peak. The intensity of the signal at 1683 cm^{-1}, which corresponds to the coupled mononitrosyl or dinitrosyl adsorption[44], increased substantially. This results also indicate that 1T′ phase has high surface coverage of NO compared to that of 2H phase, which can promote the N-N coupling.

To compare kinetics on a consistent basis, we evaluate the local Tafel/derivative behavior and the apparent NORR kinetic isotope effect (apparent KIE)[45] within the same potential window (-0.262 V to -0.296 V vs. RHE). The decision of the potential is shown in Figure 3.A.17. 2H exhibits a flatter and more stable d(log|j|)/dE response, whereas 1T′ shows a much steeper (more potential-sensitive) derivative, indicating different apparent rate-control characteristics Figure 3.3.4(e). Importantly, the isotope response in the same window reveals a pronounced apparent KIE for 2H (about 1.85) but an approximately unity KIE for 1T′ (Figure 3.A.18). The strong isotope sensitivity on 2H suggests that proton-involving sub-steps contribute substantially to the overall rate in this regime [46], consistent with enhanced NH_3 selectivity, while the near-unity KIE on 1T′ indicates that the dominant current-determining step is comparatively H/D-insensitive. Taken together, 1T′ stabilizes NO-derived adsorbates more strongly, enabling higher NO* coverage and facilitating N-N coupling routes toward NH_3, while 2H proceeds via more proton-coupled hydrogenation pathway that correlates with enhanced NH_3 selectivity[47].

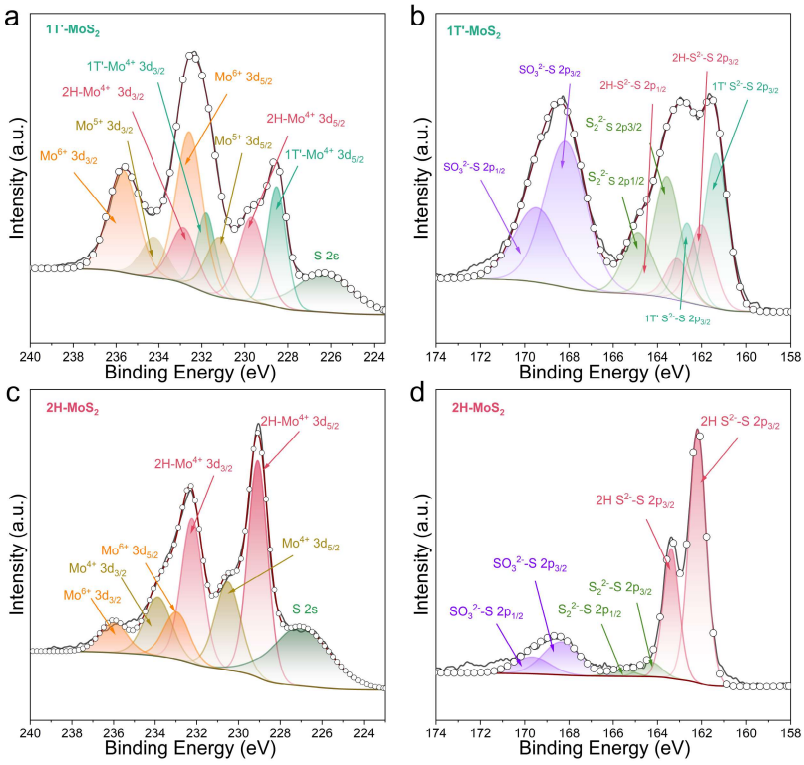

Figure 3.3.5: (a and c) Mo 3d XPS spectra; (b and d) S 2p XPS spectra of 2H and 1T′ phase MoS_2 after reaction.

The metallic phase 1T′-MoS_2 is known to be metastable with higher ground-state energy than the semiconducting 2H-MoS_2. Consequently, it can undergo phase transformation to the 2H structure during reactions [48, 49]. Ex situ XPS is performed to clarify the stability of both 2H- and 1T′-MoS_2 after the NORR (Figure 3.3.5 (a-d)). For 1T′-MoS_2, the XPS results indicate a reduction in the 1T′ phase after the reaction, accompanied by a pronounced increase in the 2H phase and Mo (V)/Mo (VI) species. This suggests the transformation of unstable Mo species into more thermodynamically stable forms. In comparison, 2H-MoS_2 exhibits similar changes in the Mo 3d spectra but with greater structural stability following the reaction. The relative atomic ratio of different Mo species is shown in Table 3.A.3. The results reveal a significant increase in Mo(V) and Mo(VI) compounds in 1T′-MoS_2-from 5% to 56% after reaction. This substantial increase implies that more Mo(V) species were formed during the reaction, which were subsequently oxidized to Mo(VI), likely due to exposure to NO, air, or H_2O [50, 51]. These findings corroborate the enhanced formation of N-N coupling products observed for 1T′-MoS_2, highlighting Mo(V) as a key intermediate in the reaction pathway. Notably, the S 2p spectra show an additional spin–orbit doublet (at 163.6 and 164.8 eV) in both MoS_2 phases after the reaction, relative to their fresh counterparts. This signal is attributed to S_2^{2-} species, commonly found in amorphous sulfur-rich MoS_3, indicating the possible formation of $MoOS_2$ during the reaction process [52–54]. The -MoS_2 sample shows a higher abundance of S_2^{2-} species compared to 2H-MoS_2, which is consistent with the corresponding Mo 3d spectra. These bridging disulfide species (S_2^{2-}) serve as active protonation sites, potentially enhancing the hydrogen evolution reaction (HER), particularly under higher applied voltages [55, 56].

3.4 Conclusion

In conclusion, our study explores 2H and 1T′ phases of MoS_2 and their effects on activity and selectivity towards multi-step proton-electron transfer electrocatalytic NO reduction. Through different carbon mixture experiments and testing different gas diffusion layer materials, we identified that the hydrophobicity of the catalyst layer enhances the adsorption of NO and improved the NO coverage on the catalyst surface, thus promoting NO reduction especially in low NO concentration steam. The optimal physically carbon mixture ratio of 50 wt.% led to high FE towards NH_3 and low HER reaction rate. By regulating different crystal phases of MoS_2 (2H and 1T′), the selectivity of products significantly changed from NH_3 to N_2. 2H exhibits a large apparent KIE (1.85) while 1T′ remains near unit, together with distinct local Tafel/derivative signatures, indicating fundamentally different apparent rate-control characteristics and a stronger proton-coupled contribution on 2H. Additionally, for 2H-MoS_2, 67% of single-pass NO conver-

sion rate and 558 μmol $\cdot$ cm^{-2} $\cdot$ h^{-1} ammonia production rate was achieved at 2.3 V. Our investigation showed that electrocatalytic selectivity of MoS_2 or other transition metal dichalcogenides can be markedly regulated by phase engineering, utilizing the sequential proton-electron transfer pathways could change the selectivity of complex multistep reactions. Our work could inspire future NORR electrocatalysts design, which could be further expanded to other complex multistep reactions like electrochemical CO/CO_2 reduction.

References

1. Sprent, J. I. *The ecology of the nitrogen cycle* (Cambridge University Press, 1987).
2. Rosca, V., Duca, M., de Groot, M. T. & Koper, M. T. M. Nitrogen cycle electrocatalysis. *Chemical Reviews* **109,** 2209–2244 (2009).
3. Leverett, J., Lie, W. H., Khan, M. H. A., Ma, Z., Daiyan, R. & Amal, R. Navigating the challenges of global NO_x emissions throughout the energy transition: state of play and outlook. *Sustainable Energy & Fuels* **9,** 3780–3790 (2025).
4. Alves, L., Holz, L. I. V., Fernandes, C., Ribeirinha, P., Mendes, D., Fagg, D. P. & Mendes, A. A comprehensive review of NO_x and N_2O mitigation from industrial streams. *Renewable and Sustainable Energy Reviews* **155,** 111916 (2022).
5. Okubo, M. & Kuwahara, T. in *New technologies for emission control in marine diesel engines* (eds Okubo, M. & Kuwahara, T.) 53–143 (Butterworth-Heinemann, 2020).
6. Praveena, V. & Martin, M. L. J. A review on various after treatment techniques to reduce NO_x emissions in a CI engine. *Journal of the Energy Institute* **91,** 704–720 (2018).
7. Pinzón, M., García-Carpintero, R., de la Osa, A. R., Romero, A., Abad-Correa, D. & Sánchez, P. Ammonia as a hydrogen carrier: An energy approach. *Energy Conversion and Management* **321,** 118998 (2024).
8. Van Damme, M., Clarisse, L., Whitburn, S., Hadji-Lazaro, J., Hurtmans, D., Clerbaux, C. & Coheur, P.-F. Industrial and agricultural ammonia point sources exposed. *Nature* **564,** 99–103 (2018).
9. Humphreys, J., Lan, R. & Tao, S. Development and recent progress on ammonia synthesis catalysts for Haber–Bosch process. *Advanced Energy and Sustainability Research* **2,** 2000043 (2021).
10. Long, J., Chen, S., Zhang, Y., Guo, C., Fu, X., Deng, D. & Xiao, J. Direct electrochemical ammonia synthesis from nitric oxide. *Angewandte Chemie International Edition* **59,** 9711–9718 (2020).
11. Wu, Y.-w., Wang, H.-w., Wu, Z.-l., Zhang, X., Dong, Y., Hu, Z., Lv, Y., Zhou, X.-y., Zhao, L., Zhang, B., *et al.* Mechanism of NO electrocatalytic reduction over the MoS_2-based single atom catalyst: A DFT investigation. *Separation and Purification Technology* **366,** 132813 (2025).

12. Montoya, J. H., Tsai, C., Vojvodic, A. & Nørskov, J. K. The challenge of electrochemical ammonia synthesis: A new perspective on the role of nitrogen scaling relations. *ChemSusChem* **8,** 2180–2186 (2015).
13. Ko, B. H., Hasa, B., Shin, H., Zhao, Y. & Jiao, F. Electrochemical reduction of gaseous nitrogen oxides on transition metals at ambient conditions. *Journal of the American Chemical Society* **144,** 1258–1266 (2022).
14. Wan, H., Bagger, A. & Rossmeisl, J. Electrochemical nitric oxide reduction on metal surfaces. *Angewandte Chemie International Edition* **60,** 21966–21972 (2021).
15. Sander, R. Compilation of Henry's law constants for water as solvent. *Atmos. Chem. Phys.* **23,** 10901–12440 (2023).
16. Bunea, S., Coppens, M. & Urakawa, A. Electrochemical conversion of NO to NH_3 in a PEM cell. *ACS Catalysis* **13,** 11345–11351 (2023).
17. Li, M., Verkuil, J., Bunea, S., Kortlever, R. & Urakawa, A. Towards higher NH_3 faradaic efficiency: Selective-poisoning of HER active sites by co-feeding CO in NO electroreduction. *ChemSusChem* **16,** e202300949 (2023).
18. Yang, W., Liu, H., Chang, X., Zhang, Y., Cai, Y., Li, Y., Cui, Y., Xu, B., Yu, L., Cui, X., *et al.* Electrosynthesis of NH_3 from NO with ampere-level current density in a pressurized electrolyzer. *Nature Communications* **16,** 1257 (2025).
19. De Vooys, A. C. A., Koper, M. T. M., van Santen, R. A. & van Veen, J. A. R. Mechanistic study of the nitric oxide reduction on a polycrystalline platinum electrode. *Electrochimica Acta* **46,** 923–930 (2001).
20. Wang, Z., Duan, H., Qu, W., Zhang, H., Han, L., Teng, Z., Chen, G., Cheng, D., Wang, X., Wu, Y. A., *et al.* Regulating local reaction environments for efficient nitric oxide reduction to ammonia via strengthening interactions between heteroatom-doped carbon and metallic alloys. *Advanced Functional Materials* **35,** 2507533 (2025).
21. Meng, J., Cheng, C., Wang, Y., Yu, Y. & Zhang, B. Carbon support enhanced mass transfer and metal–support interaction promoted activation for low-concentrated nitric oxide electroreduction to ammonia. *Journal of the American Chemical Society* **146.** doi: 10.1021/jacs.4c00898, 10044–10051 (2024).
22. Chen, H., Gao, Y., Du, J., Hao, R., Wu, X., Wang, L. & Wu, Z. Bridging cobalt single atom satellite and nanoparticle synergies for efficient low-concentration NO electroreduction to ammonia. *ACS Nano* **20.** doi: 10.1021/acsnano.5c18397, 2323–2336 (2026).
23. Theerthagiri, J., Karuppasamy, K., Mahadi, A. H., Moon, C. J., Rahamathulla, N., Kheawhom, S., Alameri, S., Alfantazi, A., Murthy, A. P. & Choi, M. Y. Electrochemical reduction of gaseous nitric oxide into ammonia: a review. *Environmental Chemistry Letters* **22,** 189–208 (2024).

24. Mukherjee, A., Ojha, N., Pant, K. K., Deb, A., Abdinejad, M., Mahapatra, S. S. & Ruidas, B. C. Recent advances in engineered MoS_2-based nanomaterials for CO_2 electro-reduction to CO and Beyond. *Environmental Science Technology Letters* **12.** doi: 10.1021/acs.estlett.5c00465, 1113–1138 (2025).
25. Zhai, W., Li, Z., Wang, Y., Zhai, L., Yao, Y., Li, S., Wang, L., Yang, H., Chi, B., Liang, J., *et al.* Phase engineering of nanomaterials: transition metal dichalcogenides. *Chemical Reviews* **124.** doi: 10.1021/acs.chemrev.3c00931, 4479–4539 (2024).
26. Liu, Y., Tursun, M., Hu, G., Abdukayum, A. & Wu, C. Non-metal single atoms anchored on defective MoS_2: a novel electrocatalyst for NO reduction to NH_3. *RSC Advances* **15,** 29323–29334 (2025).
27. He, D., Ooka, H., Kim, Y., Li, Y., Jin, F., Kim, S. H. & Nakamura, R. Atomic-scale evidence for highly selective electrocatalytic N-N coupling on metallic MoS_2. *Proceedings of the National Academy of Sciences* **117,** 31631–31638 (2020).
28. Wang, Y., Xu, Y., Cheng, C., Zhang, B., Zhang, B. & Yu, Y. Phase-regulated active hydrogen behavior on molybdenum disulfide for electrochemical nitrate-to-ammonia conversion. *Angewandte Chemie* **136** (2024).
29. Li, M., Zhou, Z., Hu, L., Wang, S., Zhou, Y., Zhu, R., Chu, X., Vinu, A., Wan, T., Cazorla, C., *et al.* Hydrazine hydrate intercalated 1T-dominant MoS_2 with superior ambient stability for highly efficient electrocatalytic applications. *ACS Applied Materials & Interfaces* **14,** 16338–16347 (2022).
30. Acerce, M., Voiry, D. & Chhowalla, M. Metallic 1T phase MoS_2 nanosheets as supercapacitor electrode materials. *Nature Nanotechnology* **10,** 313–318 (2015).
31. Zheng, J., Zhang, H., Dong, S., Liu, Y., Tai Nai, C., Suk Shin, H., Young Jeong, H., Liu, B. & Ping Loh, K. High yield exfoliation of two-dimensional chalcogenides using sodium naphthalenide. *Nature Communications* **5,** 2995 (2014).
32. Li, M., Wang, D., Li, J., Pan, Z., Ma, H., Jiang, Y. & Tian, Z. Facile hydrothermal synthesis of MoS_2 nano-sheets with controllable structures and enhanced catalytic performance for anthracene hydrogenation. *RSC Advances* **6,** 71534–71542 (2016).
33. Wu, K., Cao, X., Li, M., Lei, B., Zhan, J. & Wu, M. Bottom-up synthesis of MoS_2/CNTs hollow polyhedron with 1T/2H hybrid phase for superior potassium-ion storage. *Small* **16,** 2006532 (2020).
34. Xie, J., Zhang, H., Li, S., Wang, R., Sun, X., Zhou, M., Zhou, J., Lou, X. W. & Xie, Y. Defect-rich MoS_2 ultrathin nanosheets with additional active edge sites for enhanced electrocatalytic hydrogen evolution. *Advanced Materials* **25,** 5807–5813 (2013).
35. Fan, X., Xu, P., Zhou, D., Sun, Y., Li, Y. C., Nguyen, M. A. T., Terrones, M. & Mallouk, T. E. Fast and efficient preparation of exfoliated 2H-MoS_2 nanosheets by sonication-

assisted lithium intercalation and infrared laser-induced 1T to 2H phase reversion. *Nano Letters* **15,** 5956–5960 (2015).

36. Cai, L., He, J., Liu, Q., Yao, T., Chen, L., Yan, W., Hu, F., Jiang, Y., Zhao, Y., Hu, T., *et al.* Vacancy-induced ferromagnetism of MoS_2 nanosheets. *Journal of the American Chemical Society* **137,** 2622–2627 (2015).
37. Liu, Z., Ou, J., Wang, H., You, X. & Ye, M. Synthesis and characterization of hydrazide-linked and amide-linked organic polymers. *ACS Applied Materials & Interfaces* **8,** 32060–32067 (2016).
38. Feng, L., Zhang, L., Zhang, S., Chen, X., Li, P., Gao, Y., Xie, S., Zhang, A. & Wang, H. Plasma-assisted controllable doping of nitrogen into MoS_2 nanosheets as efficient nanozymes with enhanced peroxidase-like catalysis activity. *ACS Applied Materials & Interfaces* **12,** 17547–17556 (2020).
39. Azcatl, A., Qin, X., Prakash, A., Zhang, C., Cheng, L., Wang, Q., Lu, N., Kim, M. J., Kim, J., Cho, K., *et al.* Covalent nitrogen doping and compressive strain in MoS_2 by Remote N_2 Plasma Exposure. *Nano Letters* **16,** 5437–5443 (2016).
40. Liu, Q., Li, X., He, Q., Khalil, A., Liu, D., Xiang, T., Wu, X. & Song, L. Gram-scale aqueous synthesis of stable few-layered 1T-MoS_2: applications for visible-light-driven photocatalytic hydrogen evolution. *Small* **11,** 5556–5564 (2015).
41. Husain, H., Sulthonul, M., Hariyanto, B., Cholsuk, C. & Pratapa, S. Technical aspects of EXAFS data analysis using Artemis software. *Materials Today: Proceedings* **44,** 3296–3300 (2021).
42. Nösberger, S., Du, J., Quinson, J., Berner, E., Zana, A., Wiberg, G. K. & Arenz, M. The gas diffusion electrode setup as a testing platform for evaluating fuel cell catalysts: A comparative RDE-GDE study. *Electrochemical Science Advances* **3,** e2100190 (2023).
43. Garcia-Segura, S., Lanzarini-Lopes, M., Hristovski, K. & Westerhoff, P. Electrocatalytic reduction of nitrate: Fundamentals to full-scale water treatment applications. *Applied Catalysis B: Environmental* **236,** 546–568 (2018).
44. Van Haandel, L., Hensen, E. J. M. & Weber, T. FT-IR study of NO adsorption on MoS_2/Al_2O_3 hydrodesulfurization catalysts: Effect of catalyst preparation. *Catalysis Today* **292,** 67–73 (2017).
45. Gao, X., Yu, X.-Y. & Chang, C.-R. Perceptions on the treatment of apparent isotope effects during the analyses of reaction rate and mechanism. *Physical Chemistry Chemical Physics* **24,** 15182–15194 (2022).
46. Hammes-Schiffer, S. Explaining kinetic isotope effects in proton-coupled electron transfer reactions. *Accounts of Chemical Research* **58.** doi: 10.1021/acs.accounts.5c00119, 1335–1344 (2025).

47. He, D., Ooka, H., Li, Y., Kim, Y., Yamaguchi, A., Adachi, K., Hashizume, D., Yoshida, N., Toyoda, S., Kim, S. H., *et al.* Regulation of the electrocatalytic nitrogen cycle based on sequential proton–electron transfer. *Nature Catalysis* **5,** 798–806 (2022).
48. Duerloo, K.-A. N., Li, Y. & Reed, E. J. Structural phase transitions in two-dimensional Mo- and W-dichalcogenide monolayers. *Nature Communications* **5,** 4214 (2014).
49. Heising, J. & Kanatzidis, M. G. Structure of restacked MoS_2 and WS_2 elucidated by electron crystallography. *Journal of the American Chemical Society* **121,** 638–643 (1999).
50. Zhang, X., Jia, F., Yang, B. & Song, S. Oxidation of molybdenum disulfide sheet in water under in situ atomic force microscopy observation. *The Journal of Physical Chemistry C* **121,** 9938–9943 (2017).
51. Li, H., Chen, S., Zhang, Y., Zhang, Q., Jia, X., Zhang, Q., Gu, L., Sun, X., Song, L. & Wang, X. Systematic design of superaerophobic nanotube-array electrode comprised of transition-metal sulfides for overall water splitting. *Nature Communications* **9,** 2452 (2018).
52. Benoist, L., Gonbeau, D., Pfister-Guillouzo, G., Schmidt, E., Meunier, G. & Levasseur, A. X-ray photoelectron spectroscopy characterization of amorphous molybdenum oxysulfide thin films. *Thin Solid Films* **258,** 110–114 (1995).
53. Dupin, J. C., Gonbeau, D., Martin-Litas, I., Vinatier, P. & Levasseur, A. Amorphous oxysulfide thin films Mo_yS_z (M=W, Mo, Ti) XPS characterization: structural and electronic pecularities. *Applied Surface Science* **173,** 140–150 (2001).
54. Ryaboshapka, D. & Afanasiev, P. Molybdenum oxysulfide $MoOS_2$ as a hydrogen evolution catalyst: on the possible role of coordinated oxygen. *Journal of Catalysis* **426,** 30–38 (2023).
55. Tran, P. D., Tran, T. V., Orio, M., Torelli, S., Truong, Q. D., Nayuki, K., Sasaki, Y., Chiam, S. Y., Yi, R., Honma, I., *et al.* Coordination polymer structure and revisited hydrogen evolution catalytic mechanism for amorphous molybdenum sulfide. *Nature Materials* **15,** 640–646 (2016).
56. Santos, K. T., Sanchez, L. A. Z., Martin, V., Guillet, F., Kumar, K., Portier, X., Maillard, F., Oliviero, L. & Dubau, L. Unveiling the degradation mechanism of cathodic MoS_2/C electrocatalysts for PEMWE applications. *Electrochimica Acta* **507,** 145195 (2024).

APPENDIX

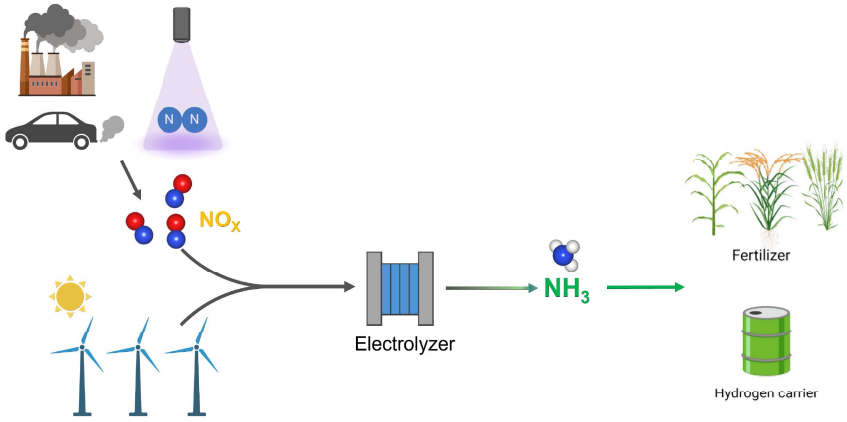

Figure 3.A.1: Schematic of electrochemical NO_x reduction for ammonia production.

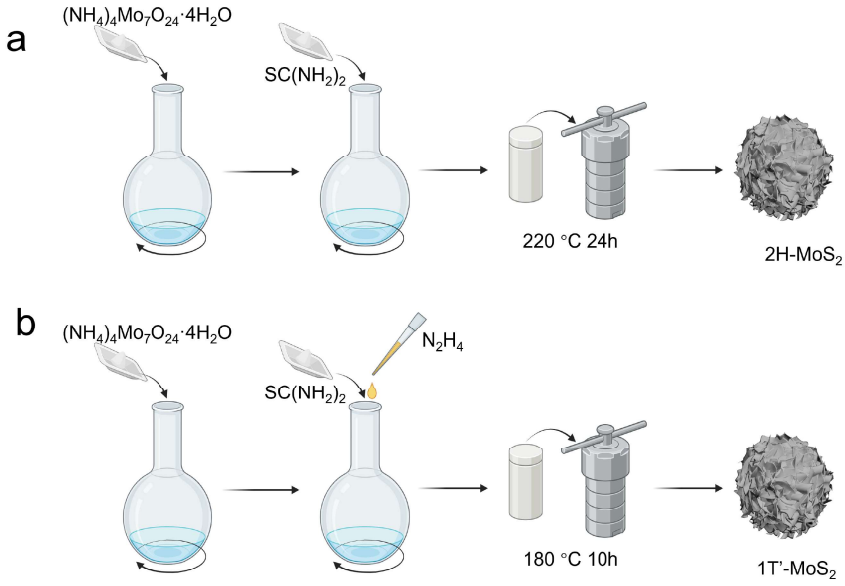

Figure 3.A.2: MoS_2 hydrothermal synthesis protocol (a) 2H-MoS_2 and (b) 1T′-MoS_2.

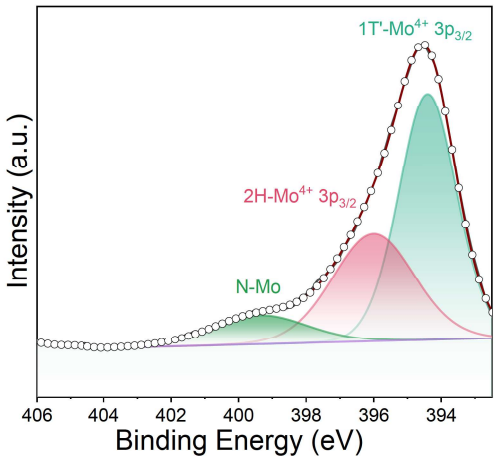

Figure 3.A.3: XPS spectra associated with N (1s) for 1T′- MoS_2

Table 3.A.1: Elemental analyses of 2H and 1T′ phases of MoS_2 using XPS

Catalyst	Atomic percentage of Mo	Atomic percentage of S	Atomic ratio
2H-MoS_2	35%	65%	1:1.86
1T′-MoS_2	38%	62%	1:1.63

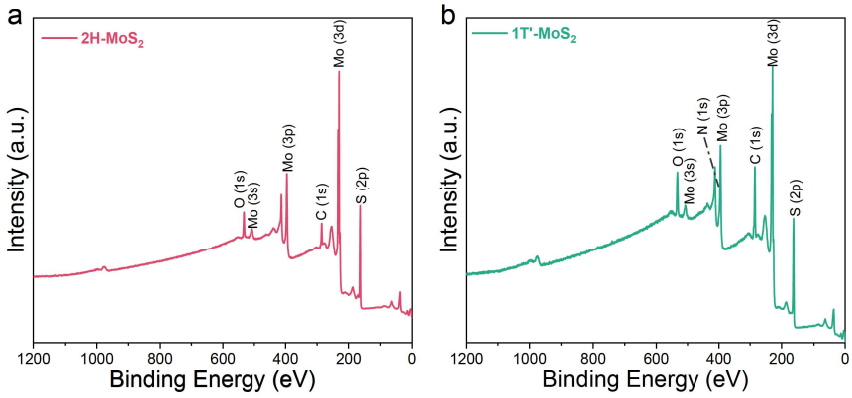

Figure 3.A.4: XPS survey scan of (a) 2H-MoS_2 and (b) 1T′-MoS_2

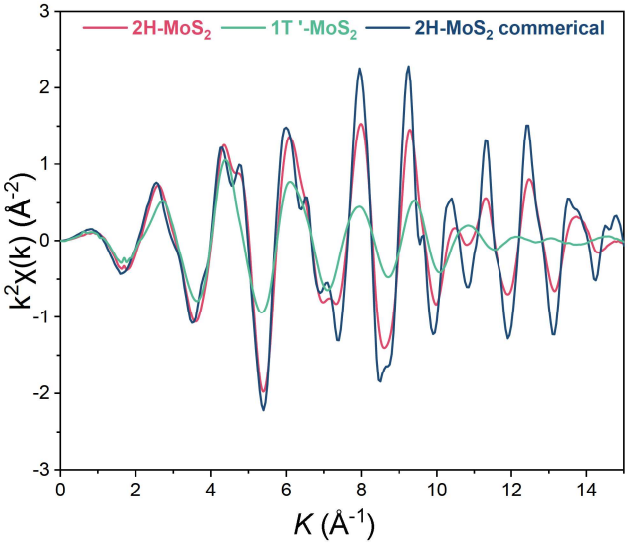

Figure 3.A.5: Mo K-edge oscillation functions $k^2\chi(k)$ for MoS_2 samples.

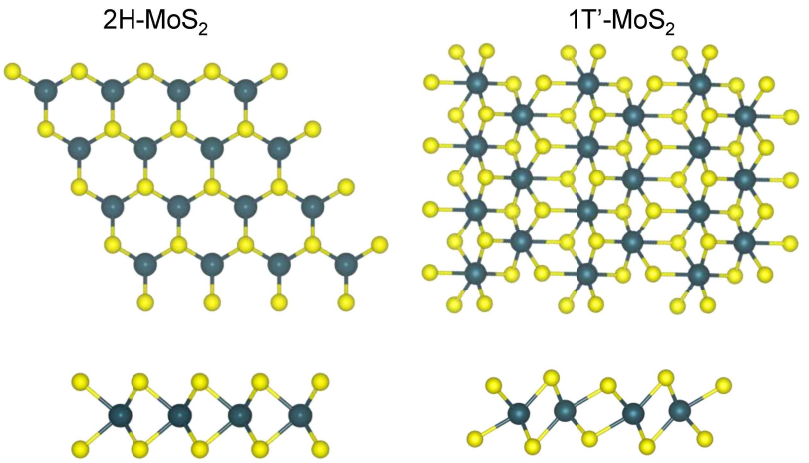

Figure 3.A.6: The atomic models of 2H and 1T′ phases of MoS_2. Upside: top view of the structure; downside: side view of the structures.

Table 3.A.2: Curve fit parameters for Mo K-edge EXAFS for MoS_2 samples

Sample	Path	E0 (eV)	N	R / Å	2 / Å^2	R factor
MoS_2 commercial	Mo-S	1±1	5.1(4)	2.41(1)	0.002(1)	0.0012
	Mo-Mo		6.0(1)	3.17(2)	0.003(1)	
2H-MoS_2	Mo-S	2±1	5.7(3)	2.41(1)	0.003(1)	0.0009
	Mo-Mo		4.5(8)	3.17(2)	0.004(1)	
1T′-MoS_2	Mo-S	0±1	4.6(4)	2.40(1)	0.007(1)	0.0016
	Mo-Mo		0.8(5)	2.77(3)	0.004(1)	

*S_0^2 was fixed as 0.9 and determined through fitting of a Mo foil using an available standard Mo.cif (mp-129). Data ranges: 3 k 15 Å, 1.0 R 3.3 Å. The total number of independent data points were 15.8, 17.3 and 17.3 for MoS_2 commercial, 2H-MoS_2 and 1T′-MoS_2, respectively.

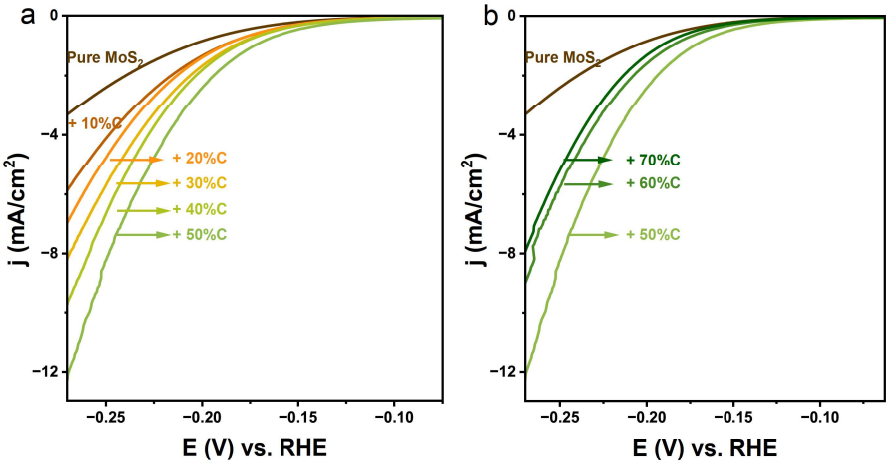

Figure 3.A.7: LSV curves of 2H-MoS_2 with different carbon ratio in 0.1 M H_2SO_4 electrolyte.

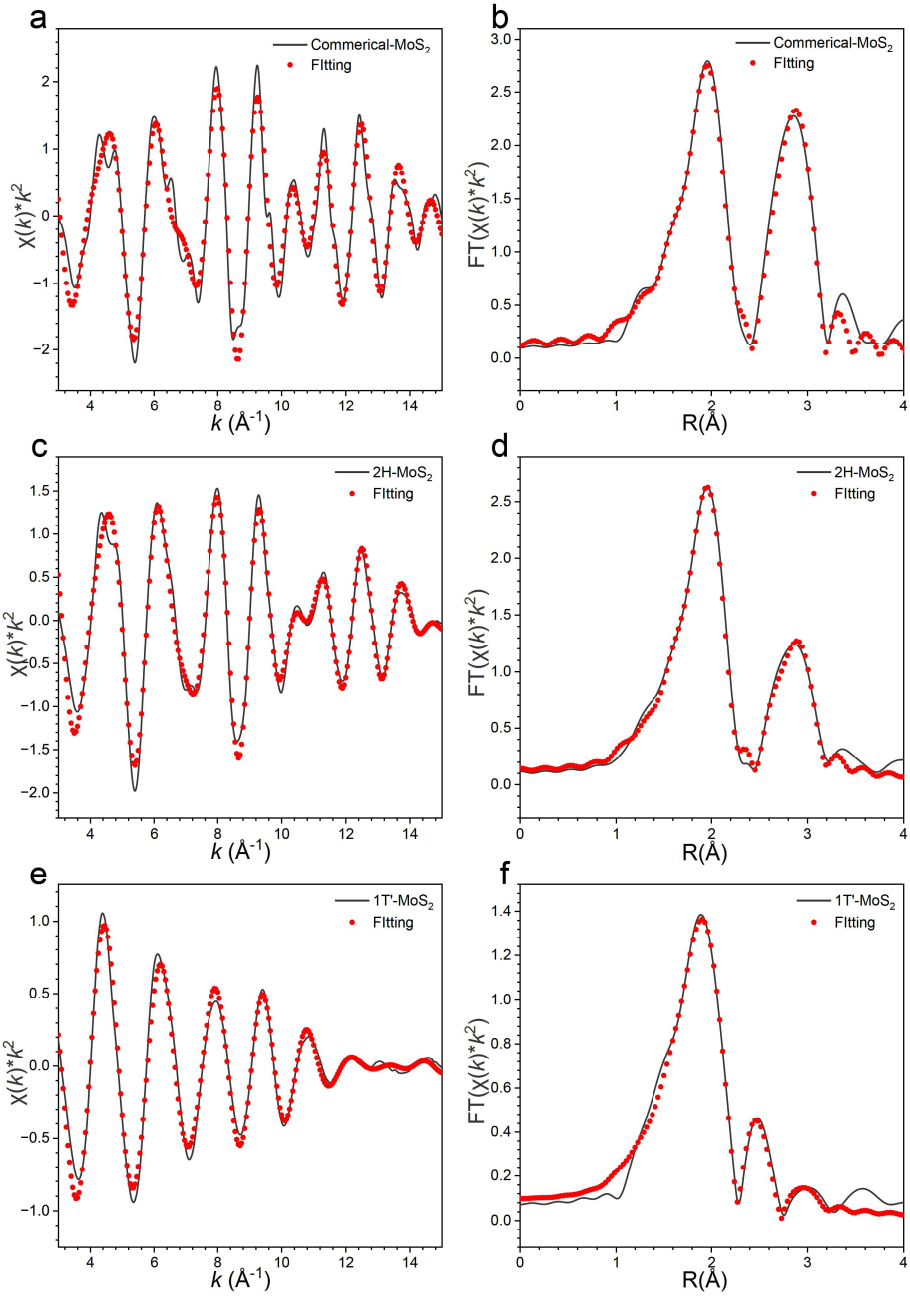

Figure 3.A.8: (a) Fitting curves for EXAFS data at the Mo K-edge for (a b) commercial MoS_2; (c and d) 2H-MoS_2 and (e and f) 1T′-MoS_2, respectively.

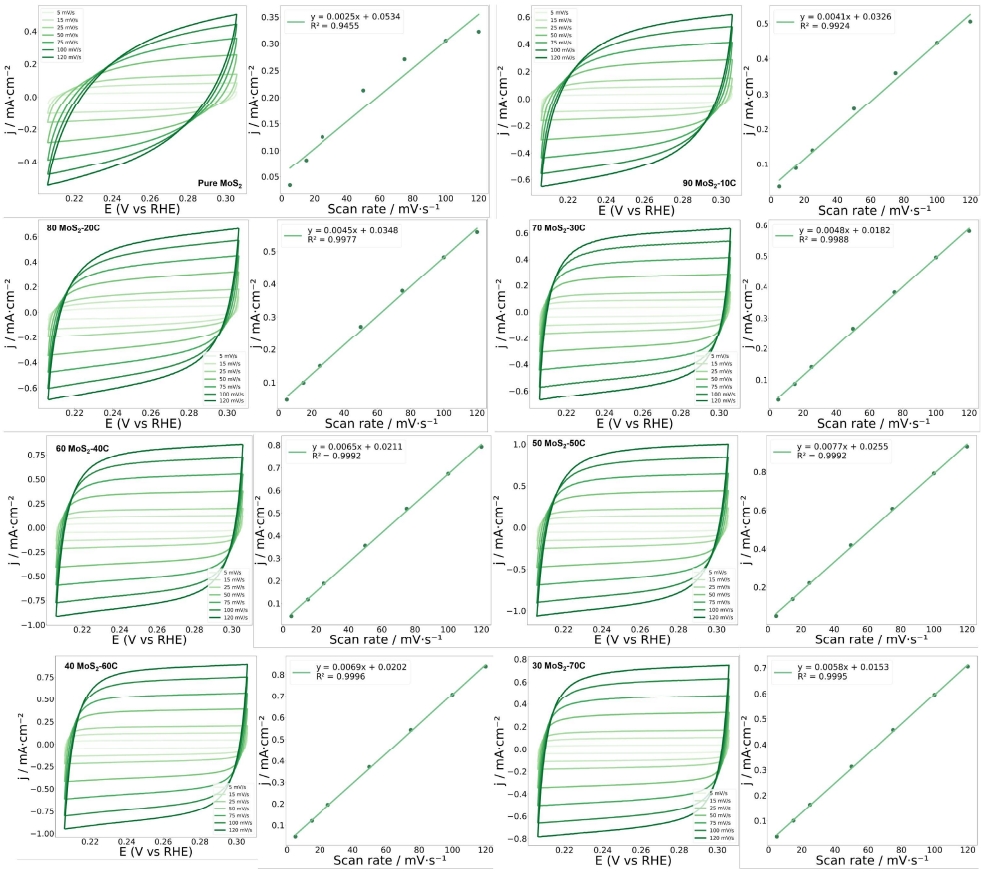

Figure 3.A.9: CV curves for Cdl at different scan rates (5–120 $mV \cdot s^{-1}$); (b) electrochemical double layer capacitance (Cdl) for 2H-MoS_2 with different carbon ratios.

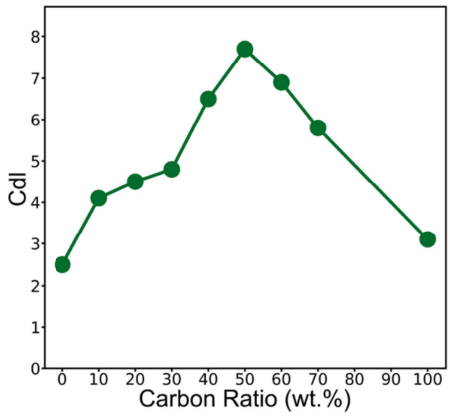

Figure 3.A.10: Comparasion of electrochemical double layer capacitance (Cdl) for 2H-MoS_2 with different carbon ratios.

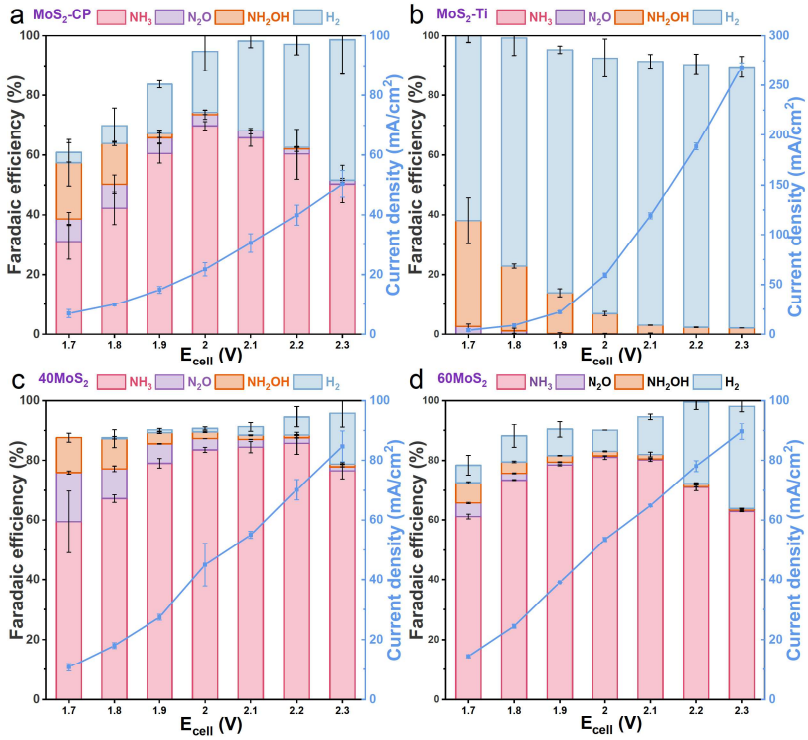

Figure 3.A.11: Faradaic efficiency for electrocatalytic NORR as a function of cell voltage (1.7 to 2.3 V) for (a) Pure MoS_2 with Ti GDL; (b) pure MoS2; (c) 40MoS_2/60C; (d) 60MoS2/40C with carbon paper.

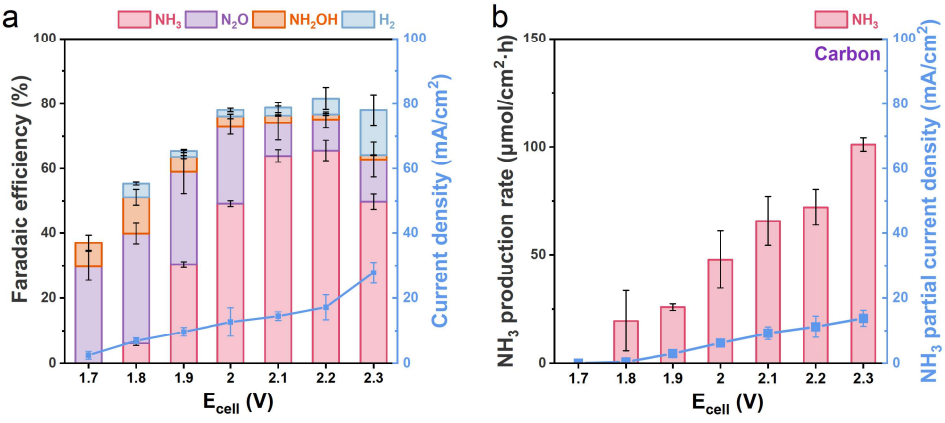

Figure 3.A.12: Faradaic efficiency; (b) ammonia production rate for electrocatalytic NORR as a function of cell voltage (1.7 to 2.3 V) for carbon black.

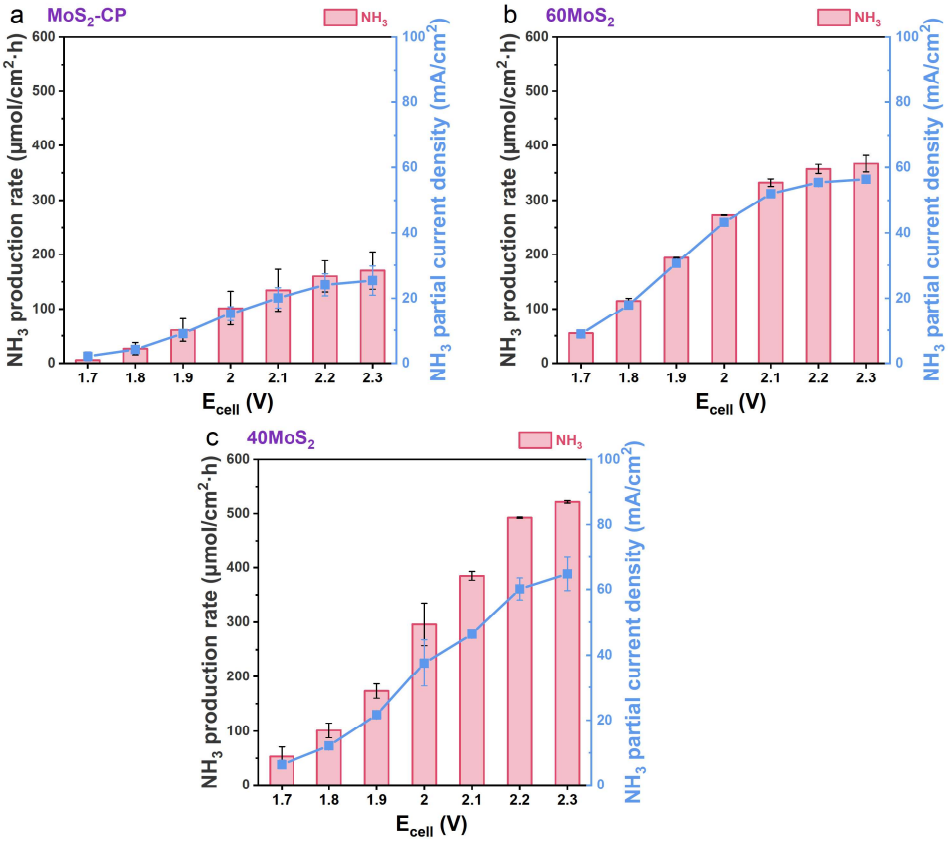

Figure 3.A.13: Ammonia production rate and partial current density for (a) MoS_2 with carbon paper (CP); (b) $60MoS_2/40C$ with carbon paper and (c) $40MoS_2/60C$ with carbon paper.

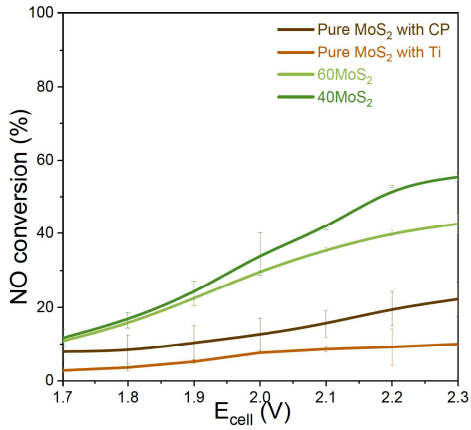

Figure 3.A.14: Single pass NO conversion rate.

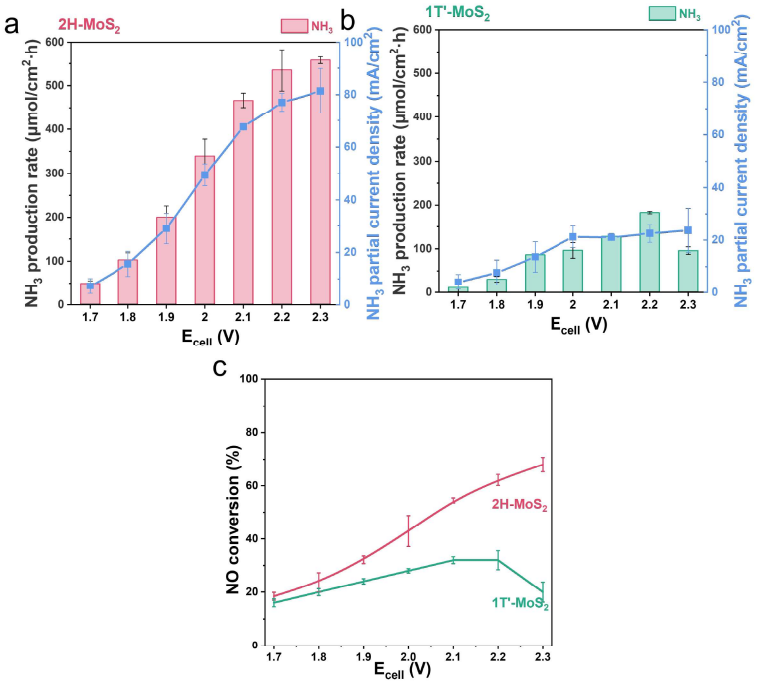

Figure 3.A.15: Ammonia production rate and partial current density on (a) 2H- and (b) 1T′-MoS_2.

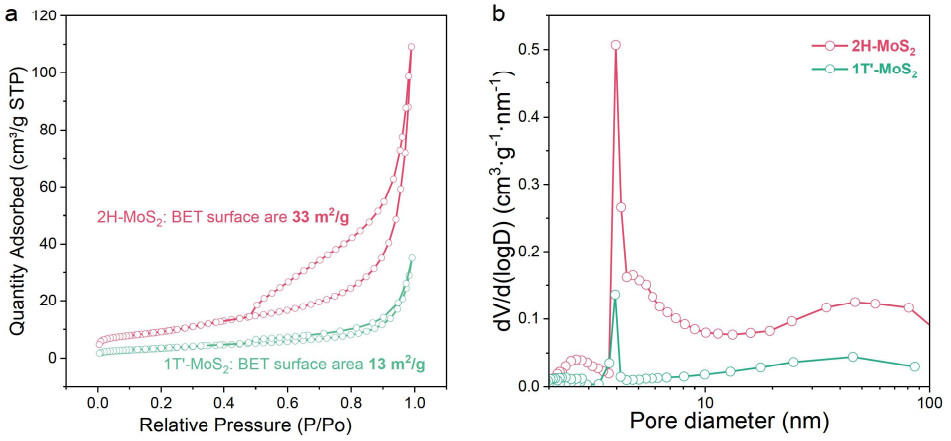

Figure 3.A.16: (a) BET surface area and (b) pore-size distribution curves of as-prepared 2H- and 1T′-MoS_2 samples.

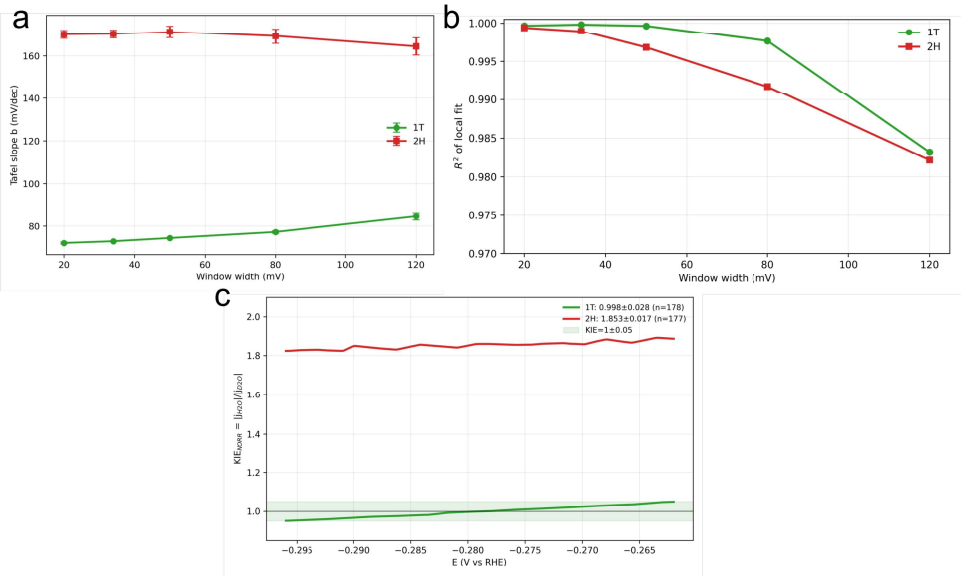

Figure 3.A.17: (a) Window-width sensitivity and (b) fitting linearity R^2 of extracted local Tafel slopes; (c) apparent KIE values across the window..

A potential window ($E_{\mathrm{RHE}} = -0.296$ to -0.262 V) was selected to ensure a locally consistent kinetic regime. Within this window, the local Tafel representation ($\eta^* = -E_{\mathrm{RHE}}$ vs. $\log|j|$) remains highly linear (high R^2), and the local derivative $\mathrm{d}(\log|j|)/\mathrm{d}E$ is comparatively stable, minimizing regime mixing in the extracted kinetic descriptors. The robustness of the extracted local Tafel slopes was further assessed by varying the window width around the same center potential: the fitted slopes remain essentially unchanged for moderate window widths (20–80 mV), whereas substantially wider windows (e.g., 120 mV) reduce linearity and indicate mixing of kinetic regimes. Extending the analysis to more negative potential is also avoided because it increases the likelihood of competing-current contributions (e.g., HER) and additional regime transitions that can confound interpretation.

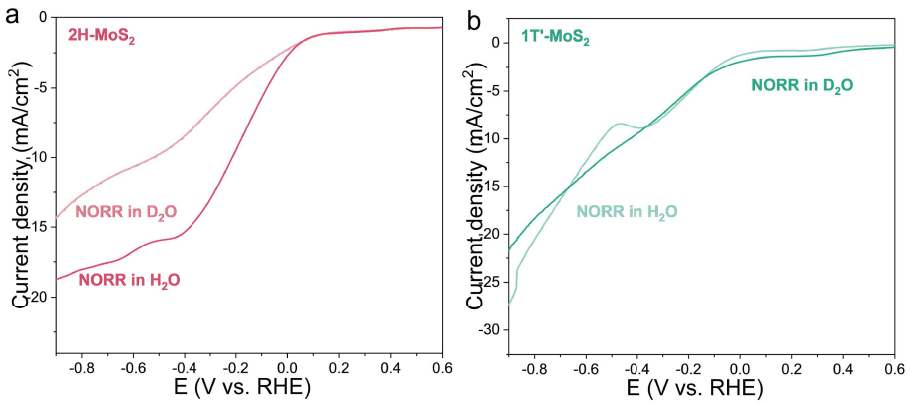

Figure 3.A.18: (a and b) LSV scan for 2H- and 1T′-MoS_2 in a batch cell

Table 3.A.3: Relative atomic percentage distribution of Mo for 2H and 1T′-MoS_2 using XPS

Sample	Relative atomic percentage of Mo			
	1T	2H	Mo^{5+}	Mo^{6+}
2H-MoS_2-Fresh		94%		6%
2H-MoS_2-Used		66%	11%	23%
1T′-MoS_2-Fresh	80%	15%	3%	2%
1T′-MoS_2-Used	22%	22%	16%	40%

4

Selective-poisoning of HER by CO in NO Electroreduction

Direct electroreduction of nitric oxide offers a promising avenue to produce valuable chemicals, such as ammonia, which is an essential chemical to produce fertilizers. Direct ammonia synthesis from NO in a polymer electrolyte membrane (PEM) electrolyzer is advantageous for its continuous operation and excellent mass transport characteristics. However, at a high current density, the faradaic efficiency of NO electroreduction reaction is limited by the competing hydrogen evolution reaction (HER). Herein, we report a CO-mediated selective poisoning strategy to enhance the faradaic efficiency (FE) towards ammonia by suppressing the HER. In the presence of only NO at the cathode, Pt/C and Pd/C catalysts showed a lower FE towards NH_3 than to H_2 due to the dominating HER. Cu/C catalyst showed a 78% FE towards NH_3 at 2.0 V due to the stronger binding affinity to NO* compared to H*. By co-feeding CO, the FE of Cu/C catalyst towards NH_3 was improved by 12%. More strikingly, for Pd/C, the FE towards NH_3 was enhanced by 95% with CO co-feeding, by effectively suppressing HER. This is attributed to the change of the favorable surface coverage resulting from the selective and competitive binding of CO* to H* binding sites, thereby improving NH_3 selectivity.

This chapter has been published in ChemSusChem. [1]

4.1 Introduction

Ammonia(NH_3) is essential to human society and is one of the most produced inorganic compounds in the world. The annual production of synthetic ammonia in 2021 is over 230 million tons, of which about 80% is applied to chemical fertilizers [2]. NH_3 has also gained great global interest in its use as hydrogen carrier and thus a chemical fuel [3]. Currently, ammonia is mainly synthesized by the Haber-Bosch process in which atmospheric nitrogen reacts with hydrogen at high temperatures (400-500 °C) and high pressure (200-300 atm) [4]. This widely employed process is energy intensive and causes massive CO_2 emissions mainly due to the hydrogen source commonly derived from natural gas. Therefore, it is important to explore other alternatives for obtaining green ammonia (carbon-neutral ammonia) at moderate conditions, ideally driven by green electricity.

Meanwhile, nitric oxide (NO) removal has been widely investigated in environmental catalysis [5, 6]. To date, the most established approach for NO removal is selective catalytic reduction (SCR) technology which can convert NO to harmless N_2 [7, 8]. However, those techniques require a constant supply of reductants such as ammonia or hydrogen [9]. While great efforts have been committed to the thermocatalytic NO_x removal process, converting NO_x to useful chemicals like NH_3 would be preferable due to the growing demand for nitrogen-based fertilizers for crops.

Electrochemical denitrification is an alternative strategy to remove NO_x species and produce value-added chemicals such as NH_3. Here, electrochemical NO reduction (NORR) is implemented in a polymer electrolyte membrane (PEM) flow cell, where water (H_2O) is employed as the proton source at the anode side. This process can driven by renewable energy, eliminating the drawbacks of grey hydrogen production from fossil fuels and reducing the overall CO_2 emissions. Recently, Feng Jiao and co-workers have investigated the NO electroreduction in flow cell systems and found that NH_3 synthesis is more favorable under acidic conditions [10]. This finding indicates that a PEM electrolyzer is ideal for electrochemical NH_3 synthesis from NO due to its acidic nature at the cathode side [11].

However, when operating at high cell potentials, the coverage of H* which is an intermediate of hydrogen evolution reaction (HER) increases [12, 13]. This enhances the HER that occurs in the same potential window as the NORR, resulting in a loss of selectivity towards NH_3 synthesis. It has been reported that increasing the CO* coverage on the surface can block H* active sites by weakening the H* binding energy, thereby suppressing the HER [14–16]. Herein, we propose a strategy to co-feed CO together with NO to moderate the local CO* coverage on different electrocatalysts to selectively inhibit the

HER active sites, which can decrease the H* coverage and suppress the HER. Five catalysts (Cu/C, Ru/C, Pt/C, Pd/C and Ag/C) were prepared and tested for their performance during NO electroreduction in the absence or presence of CO in a PEM electrolyzer. Notably, in the case of Pd/C, the FE towards NH_3 improved by 95%, while the FE towards H_2 decreased by 56% which suggest that CO^* preferentially and selectivity adsorbs on HER active sites, resulting in enhancement of the FE towards NH_3.

4.2 Experimental method

Chemicals and materials Vulcan XC72 carbon black was bought from Cabot Corporation. $Cu(NO_3)_2$ trihydrate (99.5%), $RuCl_3$ hydrate (99.9%), $PdCl_2$ (99.9%), $PtCl_2$ (98%), $AgNO_3$ (99.5%), $NaBH_4$, H_2O_2, H_2SO_4 were purchased from Sigma Aldrich.

Catalyst preparation All catalysts (Cu/C, Ru/C, Pd/C, Pt/C, Ag/C) with 40 wt.% metal loading on a Vulcan XC72 carbon black support were synthesized using the sodium borohydride reduction method [17]. Briefly, 120 mg Vulcan XC72 carbon black was first suspended in 200 mL MilliQ water. An amount of metal precursor that corresponded with the final metal loading of 40 wt.% was added to the solution. The solution was stirred with a stirring bar for 1h at room temperature and then transferred to an ultrasonic bath for another 30 min. Subsequently, $NaBH_4$ was added dropwise as a reducing agent in sixfold excess with respect to the stoichiometric amount of different catalyst precursors. After reduction, the sample centrifuged and washed with MilliQ water several times. The obtained catalyst powder was dried at 90 °C for 12 h.

Membrane electrode assembly (MEA) preparation Nafion™ 115 membranes from Ion power were pre-treated according to the procedure of 1h in 3 wt.% hydrogen peroxide (H_2O_2) solution at 80 °C, 1h in 1 M H_2SO_4 solution at 80 °C and 1h in boiling MilliQ water. 10 mg of the prepared cathode catalyst and 30 wt.% Nafion ionomer were ultrasonically dispersed in 2 mL of isopropanol for 30 min to generate a homogenous ink. Then, the catalyst ink was spray-coating onto a Nafion membrane with an active area of 2×2 cm^2 at 60 °C to obtain 2.5 $mg \cdot cm^{-2}$ catalyst loading. The anode ink was prepared via the same method consisting of 8 mg commercial IrO_2 (2 $mg \cdot cm^{-2}$ catalyst loading), 20 wt.% Nafion ionomer and 2 mL isopropanol. After spray coating, the catalyst-coated membranes (CCMs) were hot-pressed at 120 °C and 1 MPa for 3 min using an automatic press (Speca Press). The MEA was prepared by pressing two porous sintered titanium gas diffusion layers ($2 \times 2cm^2$) (GDL, Bekaert) on both sides of the membrane. The PEM cell was assembled by sandwiching the MEA, two titanium bipolar plates with flow channels, and two aluminium cartridge-heated end plates with 5 $N \cdot m$ screw torque.

Electrochemical experiments The electrochemical experiments were conducted in the PEM electrolyser (Figure 4.A.1) on an AUTOLAB PGSTAT302N potentiostat equipped with a 20 A booster. The PEM electrolyser was operating at 80 °C. For electrochemical NO reduction, at the cathode chamber, the mixture of 2.5% NO and 4% CH_4 in He flowed at 26 mL·min ^{1}. CH_4 was acting as the internal standard to correct the volume changes during reactions. For NORR+CO reactions, the mixture of 2.5% NO, 2.5% CO and 4% CH_4 in He flowed at 26 mL·min^{-1} at the cathode side. For both reactions, at the anode chamber, MilliQ water was supplied at the flow rate of 1 mL·min^{-1} by a peristaltic pump (Ismatec). After the reaction, the cathode chamber outlet was connected to an acid trap with 0.2 M H_2SO_4 solution to trap the produced NH_3 and NH_2OH. After the acid trap, the gas flowed to the connected Alpha infrared spectrometer and gas chromatography (GC).

Product quantification The outlet gas products (NO, N_2O, CO, and CH_4) were analysed via a Bruker Alpha infrared spectrometer. And the other gaseous products (N_2 and H_2) were quantified on a CompactGC from Global Analyser Solutions with a thermal conductivity detector (TCD).

Ammonium cations (NH_4^+) from the acid trap were executed by Metrohm 883 Basic ion chromatography with a Metrosep C6 separation column. NH_2OH was quantified by UV-Vis spectroscopy (Unicam UV 500), measuring absorbance at 525 nm. In detail, 200 μL of the sample was diluted to 6 mL with MilliQ water. Then, 1 mL of 0.047 mol·L^{-1} KIO_3 and 1 mL of 3 mol·L^{-1} H_2SO_4 were added in turn; the mixed solution stayed for 5 min at room temperature. Lastly, 2 mL of 3.46×10^{-4} mol·L^{-1} neutral red was added, and the absorbance at 525 nm was measured. The calibration curve of the natural red method for quantifying NH_2OH is shown in Figure 4.A.15.

Catalyst characterization The powder X-ray diffraction (XRD) was measured on Bruker D8 ADVANCE X-ray diffractometer with Cu $K\alpha$ radiation source in a range of 5° to 90° with a step of 0.05°. The surface morphology of the catalysts was characterized by a Transmission electron microscope (TEM, Jeol JEM-1400 plus).

4.3 Results and Discussion

Material synthesis and characterizations Electrochemical reduction of NO and NO+CO was performed in a PEM electrolyzer (Figure 4.A.1), where gaseous NO (2.5 vol% NO) or NO+CO (2.5 vol% NO and 2.5 vol% NO) was fed directly to the cathode catalyst surface and can be reduced to ammonia or other products. The cathode catalysts (Cu/C, Ru/C, Pt/C, Pd/C, and Ag/C) were prepared by a sodium borohydride reduction method with

40 wt.% metal loading on Vulcan XC72 carbon black. XRD results (Figure 4.A.2) show that all the catalysts are present in their metallic form, except for Cu/C which formed CuO and would be further reduced to Cu metallic during the reaction. Transmission electron microscope (TEM) images (Figure 4.A.3) indicated that all catalysts are highly dispersed on the carbon support.

NO and NO+CO electrolysis performance

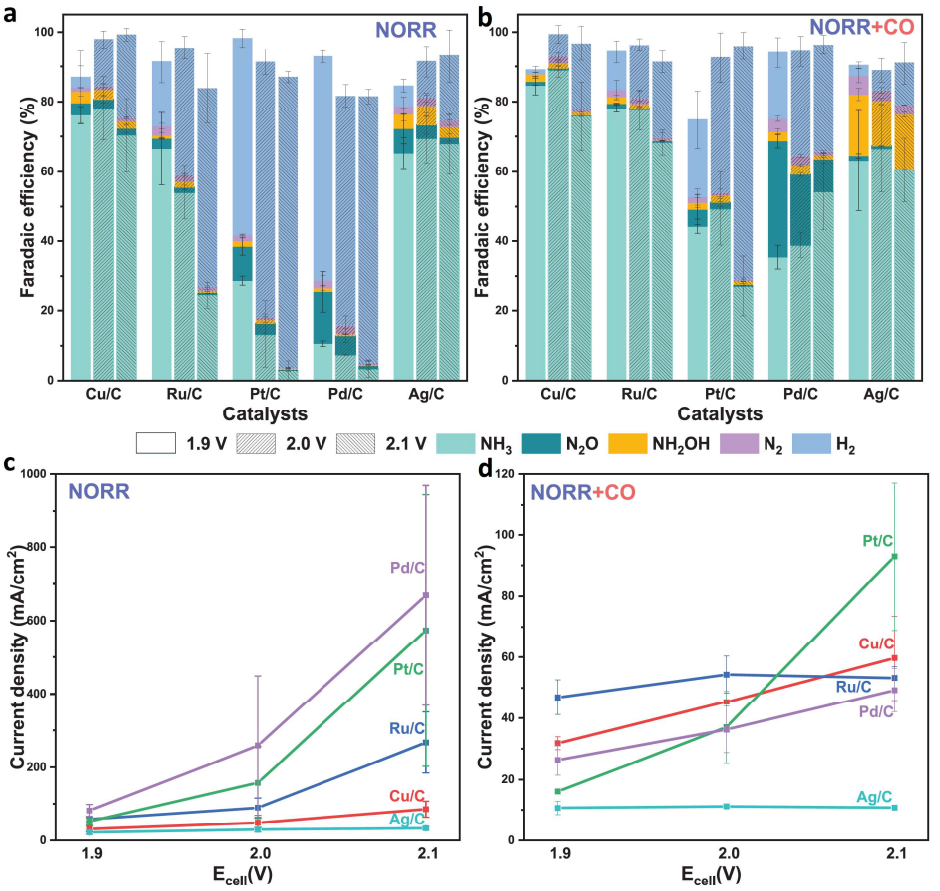

Figure 4.3.1: Faradaic efficiency at 1.9 V, 2.0 V, and 2.1 V of various catalysts in (a) NO electroreduction, and (b) NO electroreduction + CO. Total current density vs cell voltage of various catalysts in (c) NO electroreduction, and (d) NO electroreduction + CO.

First, the electrochemical reduction of NO was conducted in the PEM electrolyzer. The FE towards different NO reduction products of various catalysts under cell voltage from 1.9 to 2.1 V is presented in Figure 4.3.1(a) and the total current density is shown in Figure 4.3.1(c). Blank experiments with only carbon support were evaluated in our previous

work for the conversion of nitrate to ammonia in a PEM system, which behaves similar to NORR. It showed low current density and less than 1% FE towards NH_3 which indicates the carbon black has barely no activity in our reaction [18]. NH_3, N_2O, N_2, and NH_2OH were the detected nitrogen-containing products from NO electroreduction. As is shown in Figure 4.3.1(a), among the five catalysts evaluated, Cu/C exhibits the highest selectivity for electrochemical NO reduction to NH_3. The FE over a wide range of cell potentials of Cu/C is shown in Figure 4.A.4(a), where the FE towards NH_3 reached 62% at a low cell potential of 1.7 V. While increasing the cell voltage, the FE towards NH_3 increased and achieved the highest value of 78% at 2.0 V, at a current density of 48 $mA \cdot cm^{-2}$. Upon further increasing the cell voltage, the H_2 FE increased. Jianping Xiao et al. reported that copper is the most selective catalyst for NH_3 synthesis from the NORR [19]. Compared to other catalysts, Cu has a stronger binding affinity to NO* compared to H*, resulting in a well-balanced surface coverage of NO* and H*, which promotes the selectivity towards NH_3 than other nitrogen-containing products [20]. For Ru/C and Ag/C catalysts, the FE towards NH_3 dominates all studied cell potentials. In contrast, Pt/C and Pd/C were more efficient for HER than NH_3 synthesis. The FE of all the measured products during the NORR over the studied cell voltages of Ru/C, Pt/C, Pd/C and Ag/C are shown in Figures 4.A.5(a), 4.A.6(a), 4.A.7(a) and 4.A.8(a). We observe that at low cell potentials, the FE towards N_2O was higher than at higher cell voltages for all catalysts. Feng Jiao et al. proposed that NO* coverage on the surface of the catalyst significantly affects the distribution of N-containing products. At high NO* coverages, N-N coupling products like N_2O or N_2 are more likely to form, in contrast, low (or balanced) NO* coverages result in N products like NH_3 or NH_2OH [10]. However, most of the protons and electrons are heading toward the HER upon operating the reaction at high cell potentials. These results indicate that at a high voltage, the surface coverage of H* significantly exceeds that of NO* and therefore we have directed our research effort towards decreasing the H* coverage to enhance the selectivity and FE towards NH_3.

With CO co-feeding, the FE towards different products of various catalysts in NORR+CO under cell potentials from1.9 to 2.1 V is shown in Figure 4.3.1(b). With respect to the current density, it is obvious that the current density significantly decreased in the presence of CO, especially for Pt/C and Pd/C (Figure 4.3.1(d)). Interestingly at 2.1 V, the current density decreased by 91% and 86% for Pd/C and Pt/C, respectively. The adsorbed CO* on the surface seems affecting the binding of H* and decreases the H* coverage which is directly related to the decrease in the FE towards H_2, especially under high cell potential conditions. The tendency of HER suppresion is general. At 2.1 V, the FE towards H_2 decreased by 21%, 62%, 20%, 46% and 35% for Cu/C, Ru/C, Pt/C, Pd/C and Ag/C, respectively. Notably, NORR is not or less affected by the presence of CO. The FE towards

NH_3 for all the catalysts improved, except for Ag/C. For Cu/C, at 2.0 V, the FE towards NH_3 improved by 12% and achieved 89%, which is the highest among all the catalysts. More strikingly, the FE towards NH_3 was enhanced by 95%, 90% and 54% for Pd/C, Pt/C and Ru/C.

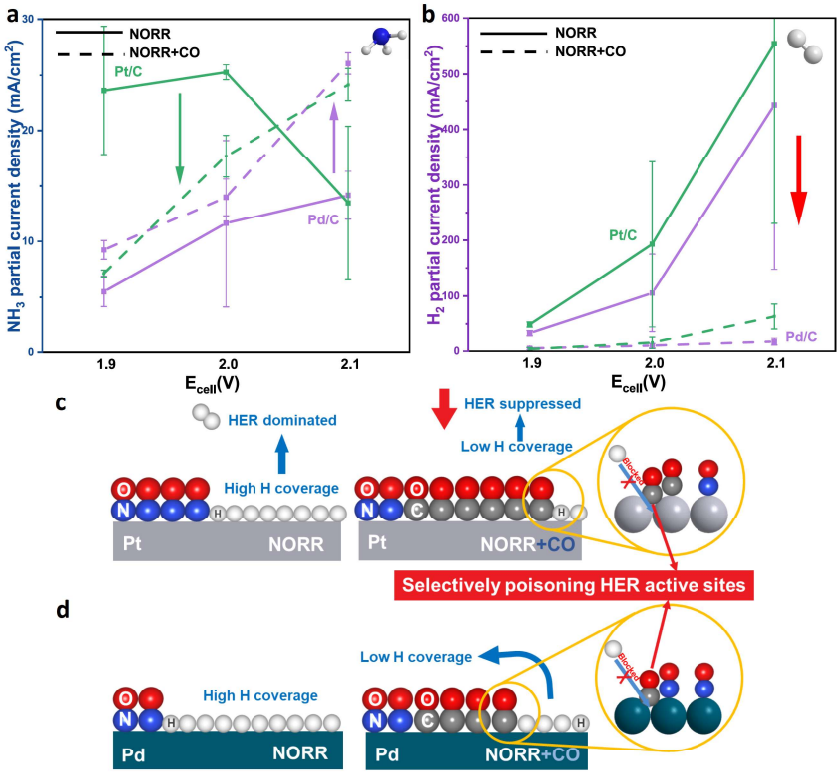

Figure 4.3.2: ((a) NH_3 partial current density and (b) H_2 partial current density at 1.9 V, 2.0 V, and 2.1 V of Pt/C and Pd/C. Schematics of surface coverage of NO*, CO* and H* on (c) Pt/C and (d) Pd/C.

To further understand the CO poisoning effect on the electrochemical NO reduction of different catalysts, partial current densities of NH_3 and H_2 in NORR and NORR+CO reactions were plotted for both Pt/C and Pd/C (Figure 4.3.2(a) and 4.3.2(b)). In the case of Pd/C, the partial current density towards NH_3 was enhanced while that of Pt/C decreased. Despite the difference in the effects of CO on the NH_3 selectivity using Pd/C and Pt/C, H_2 formation was greatly suppressed for both catalysts which can be seen from the drastically decreased H_2 partial current density (Figure 4.3.2(b)). Based on these results, we propose a selective CO poisoning effect on Pt/C and Pd/C (Figures 2c and 2d). For both catalysts, NO is known to favourably bind to the atop site on the surface of the catalysts [21]. In the case of Pt/C in the absence of CO, the HER is dominating during NO

electroreduction. When CO is introduced, we observe that the partial current density of NH_3 also decreased, which suggests that the adsorption of CO* is competitive with NO* on the surface lowering the NH_3 formation rate (Figure 4.3.2(c)). It is well documented that CO can bind on both the atop sites and bridge sites on Pt, while atop sites CO* dominates on Pt surface [22]. However, while increasing the surface charge, the preference of CO binding sites can change from atop to bridge sites [23, 24]. These results are consistent with our results. At lower cell potentials, NO conversion decreased significantly (Figure 4.A.11(a)) because the atop NO* adsorption is inhibited by atop CO*. With increasing cell potentials, the adsorption of CO* is weakened; hence the NO* coverage on the surface increases, leading to the enhancement of NH_3 partial current density at high cell potentials. For the HER active sites, since the binding affinity towards CO* is stronger than H*, which is well-known for Pt, the adsorption of CO* can block the active bridge sites and is also competing with the atop H* active sites, lowering the partial current density towards H_2 production.

For Pd/C, in the presence of only NO, the high coverage of H* on the surface leads to dominating HER and low FE towards NH_3. After introducing CO in the NO feed, which is more likely to bind to the bridge site of the Pd surface [25], CO* is selectivity binding to, thus blocking, the active bridge sites for the HER, resulting in the decreased of FE towards H_2 and current density. NO* which adsorbs on the atop sites would not be affected by bridge-bonded CO* (Figure 4.3.2(d)). Therefore, the FE towards NH_3 increased (Figure 4.A.12).

For the other catalysts, the NO conversion, NH_3 and H_2 partial current density of Cu/C, Ru/C and Ag/C are presented in Figures 4.A.9, 4.A.10, 4.A.13, respectively. For Cu/C, the partial current density towards NH_3 increased in the presence of CO (Figure 4.A.13(b)). It has been reported that Cu has a strong affinity to NO* compared to CO* [26]; therefore, the high FE towards NH_3 can be explained by the preferential NO coverage. However, for Ru/C and Ag/C, the partial current density towards NH_3 decreased in the presence of CO. Analogous to Pt/C, on the surface of Ru/C, NO* also competes with CO*, but the binding affinity to NO* is likely stronger than Pt/C, resulting in the observed higher partial current density toward NH_3. In the case of Ag/C, It has been suggested that NO*, H* and CO* bind on Ag weakly, which is in good accordance with our experiments. The current density and NO conversion on Ag/C (Figure 4.A.13(a)) was therefore much lower than with the other catalysts. Regarding NH_2OH formation, in the presence of CO*, the coverage of H* decreased so that there was not enough H* provided to reduce NH_2OH which is regards as an intermidiate product [27] in the pathway toward NH_3 production (Figure 4.A.13(b)). As a consequence, the FE towards NH_2OH increased.

Comparison of the NH_3 production rate on various catalysts of NORR and NORR +CO over a range of cell voltages is presented in Figure 4.A.14. Among all the catalysts, Ru/C exhibited the highest NH_3 production rate in NORR, reaching 376 μmol·cm^{-2}·h^{-1} at 2.0 V. Following closely, Cu/C demonstrated a production rate of 301 μmol·cm^{-2}·h^{-1} at 2.1 V. In contrast, Pd/C displayed the lowest NH_3 production rate, yielding only 63 μmol·cm ^{2}·h^{-1}, even at 2.1 V (Figure 4.A.14(a)). Upon co-feeding CO (Figure 4.A.14(b)), notably the NH_3 production rates for Pd/C and Cu/C increased significantly, while for the other catalysts, the values decreased. For Cu/C at 2.1V, the NH_3 production rate increased to 325 μmol·cm^{-2}·h^{-1}. However, the most striking result was observed with Pd/C, where the NH_3 production rate increased to 198 μmol·cm^{-2}·h^{-1} in NORR+CO, which is 3 times higher than the value in NORR. This indicates that the poisoning and suppression of HER can promote NH_3 production in case of Pd/C. A similar tendency was observed for Pt/C at 2.1 V to a lesser extent. In comparison to other electrochemical NH_3 production studies utilizing different cells (batch cell, H cell, etc.) with liquid electrolytes (Table 4.A.1), which naturally suffers from mass-transport limitations for NORR, our results is promising for continuous NH_3 production from NO.

4.4 Conclusion

We reported a CO-mediated selective poisoning HER active sites strategy to enhance the FE towards ammonia in NO electroreduction. Cu/C is the most active catalyst for NO electroreduction to NH_3, exbiting the highest FE of 78% at 2.0 V among all the catalysts. Pd/C and Pt/C show high FE towards H_2. In general, competing HER domiants when operating at high cell potentials. With co-feeding CO, the current density and FE towards H_2 of all the catalysts drastically decreased, which can be ascribed to the increased CO* coverage competitively and selectivity bind the HER active sites. Such effects are most pronouced for Pd/C and also clearly observed for Pt/C. This results in the enhanced NO* coverage on the surface, while poisoning HER sites, thus enbling higher FE towards NH_3.

References

1. Li, M., Verkuil, J., Bunea, S., Kortlever, R. & Urakawa, A. Towards higher NH_3 faradaic efficiency: selective-poisoning of HER active sites by co-Feeding CO in NO electroreduction. *ChemSusChem* **16,** e202300949 (2023).
2. Jain, M., Muthalathu, R. & Wu, X.-Y. Electrified ammonia production as a commodity and energy storage medium to connect the food, energy, and trade sectors. *iScience* **25,** 104724 (2022).
3. Kojima, Y. & Yamaguchi, M. Ammonia as a hydrogen energy carrier. *International Journal of Hydrogen Energy* **47,** 22832–22839 (2022).
4. Kandemir, T., Schuster, M. E., Senyshyn, A., Behrens, M. & Schlögl, R. The Haber–Bosch process revisited: on the real structure and stability of "ammonia iron" under working conditions. *Angewandte Chemie International Edition* **52,** 12723–12726 (2013).
5. Inaba, M., Kintaichi, Y., Haneda, M. & Hamada, H. Silica-supported cobalt catalysts for the selective reduction of nitrogen monoxide with propene. *Catalysis Letters* **39,** 269–274 (1996).
6. Miyamoto, A., Kobayashi, K., Inomata, M. & Murakami, Y. Nitrogen-15 tracer investigation of the mechanism of the reaction of nitric oxide with ammonia on vanadium oxide catalysts. *The Journal of Physical Chemistry* **86,** 2945–2950 (1982).
7. Sun, Y., Zwolińska, E. & Chmielewski, A. G. Abatement technologies for high concentrations of NO_x and SO_2 removal from exhaust gases: A review. *Critical Reviews in Environmental Science and Technology* **46,** 119–142 (2016).
8. Gholami, F., Tomas, M., Gholami, Z. & Vakili, M. Technologies for the nitrogen oxides reduction from flue gas: A review. *Science of The Total Environment* **714,** 136712 (2020).
9. Yadav, D. & Prasad, R. Low Temperature de-NO_x technology-a challenge for vehicular exhaust and its remedation: An overview. *Procedia Technology* **24,** 639–644 (2016).
10. Ko, B. H., Hasa, B., Shin, H., Zhao, Y. & Jiao, F. Electrochemical reduction of gaseous nitrogen oxides on transition metals at ambient conditions. *Journal of the American Chemical Society* **144,** 1258–1266 (2022).
11. Bunea, S., Coppens, M. & Urakawa, A. Electrochemical conversion of NO to NH_3 in a PEM cell. *ACS Catalysis,* 11345–11351 (2023).

12. Bagger, A., Ju, W., Varela, A. S., Strasser, P. & Rossmeisl, J. Electrochemical CO_2 reduction: A classification problem. *ChemPhysChem* **18,** 3266–3273 (2017).
13. Wan, H., Jiao, Y., Bagger, A. & Rossmeisl, J. Three-dimensional carbon electrocatalysts for CO_2 or CO reduction. *ACS Catalysis* **11,** 533–541 (2021).
14. Moradzaman, M. & Mul, G. Optimizing CO coverage on rough copper electrodes: effect of the partial pressure of CO and electrolyte anions (pH) on selectivity toward ethylene. *The Journal of Physical Chemistry C* **125,** 6546–6554 (2021).
15. Zhan, C., Dattila, F., Rettenmaier, C., Bergmann, A., Kühl, S., García-Muelas, R., López, N. & Cuenya, B. R. Revealing the CO coverage-driven C–C coupling mechanism for electrochemical CO_2 reduction on Cu_2O nanocubes via operando raman spectroscopy. *ACS Catalysis* **11,** 7694–7701 (2021).
16. Wang, X., de Araújo, J. F., Ju, W., Bagger, A., Schmies, H., Kühl, S., Rossmeisl, J. & Strasser, P. Mechanistic reaction pathways of enhanced ethylene yields during electroreduction of CO_2–CO co-feeds on Cu and Cu-tandem electrocatalysts. *Nature Nanotechnology* **14,** 1063–1070 (2019).
17. Ilinitch, O. M., Cuperus, F. P., Nosova, L. V. & Gribov, E. N. Catalytic membrane in reduction of aqueous nitrates: operational principles and catalytic performance. *Catalysis Today* **56,** 137–145 (2000).
18. Bunea, S., Clemens, K. & Urakawa, A. Electrified conversion of contaminated water to value: selective conversion of aqueous nitrate to ammonia in a polymer electrolyte membrane cell. *ChemSusChem* **15,** e202102180 (2022).
19. Long, J., Chen, S., Zhang, Y., Guo, C., Fu, X., Deng, D. & Xiao, J. Direct electrochemical ammonia synthesis from nitric oxide. *Angewandte Chemie International Edition* **59,** 9711–9718 (2020).
20. Wan, H., Bagger, A. & Rossmeisl, J. Electrochemical nitric oxide reduction on metal surfaces. *Angewandte Chemie International Edition* **60,** 21966–21972 (2021).
21. Ivanova, E., Mihaylov, M., Thibault-Starzyk, F., Daturi, M. & Hadjiivanov, K. FTIR spectroscopy study of CO and NO adsorption and co-adsorption on Pt/TiO_2. *Journal of Molecular Catalysis A: Chemical* **274,** 179–184 (2007).
22. Urakawa, A., Bürgi, T., Schläpfer, H.-P. & Baiker, A. Simultaneous in situ monitoring of surface and gas species and surface properties by modulation excitation polarization-modulation infrared reflection-absorption spectroscopy: CO oxidation over Pt film. *The Journal of Chemical Physics* **124,** 054717 (2006).
23. Kalhara Gunasooriya, G. T. K. & Saeys, M. CO adsorption site preference on platinum: charge is the essence. *ACS Catalysis* **8,** 3770–3774 (2018).

24. Sobkowski, J. & Czerwinski, A. Voltammetric study of carbon monoxide and carbon dioxide adsorption on smooth and platinized platinum electrodes. *The Journal of Physical Chemistry* **89,** 365–369 (1985).
25. Yudanov, I. V., Sahnoun, R., Neyman, K. M., Rösch, N., Hoffmann, J., Schauermann, S., Johánek, V., Unterhalt, H., Rupprechter, G., Libuda, J., *et al.* CO adsorption on Pd nanoparticles: density functional and vibrational spectroscopy studies. *The Journal of Physical Chemistry B* **107,** 255–264 (2003).
26. Schneider, W. F., Hass, K. C., Ramprasad, R. & Adams, J. B. Cluster models of Cu binding and CO and NO adsorption in Cu-exchanged zeolites. *The Journal of Physical Chemistry* **100,** 6032–6046 (1996).
27. Garcia-Segura, S., Lanzarini-Lopes, M., Hristovski, K. & Westerhoff, P. Electrocatalytic reduction of nitrate: Fundamentals to full-scale water treatment applications. *Applied Catalysis B: Environmental* **236,** 546–568 (2018).

Appendix

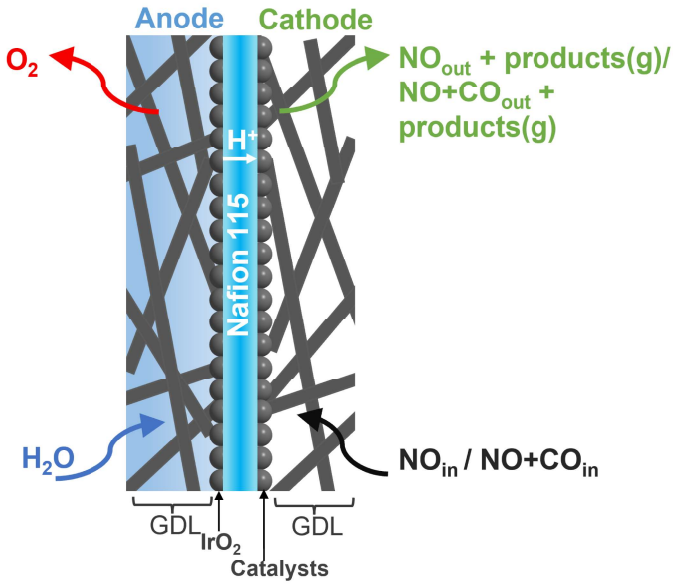

Figure 4.A.1: Schematic of a proton exchange membrane (PEM) cell.

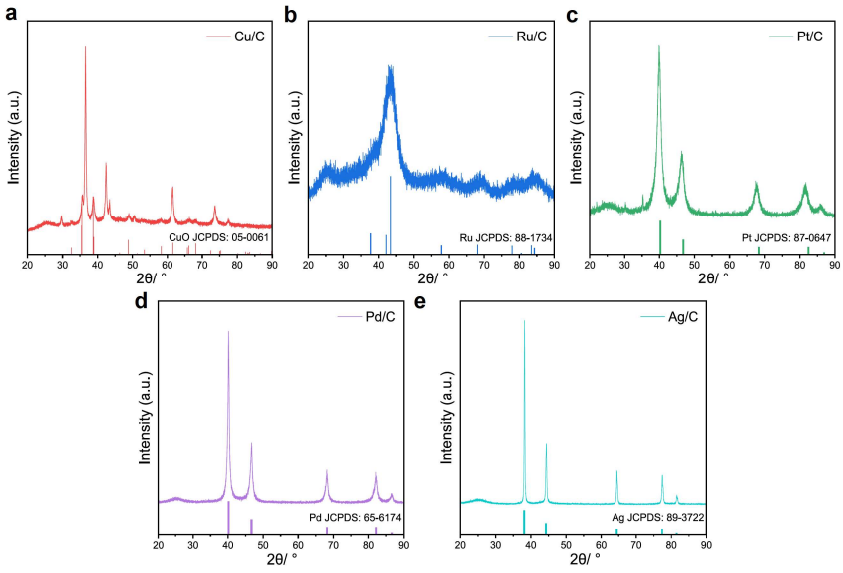

Figure 4.A.2: XRD patterns for prepared catalysts: (a) Cu/C; (b) Ru/C; (c) Pt/C; (d) Pd/C and (e) Ag/C.

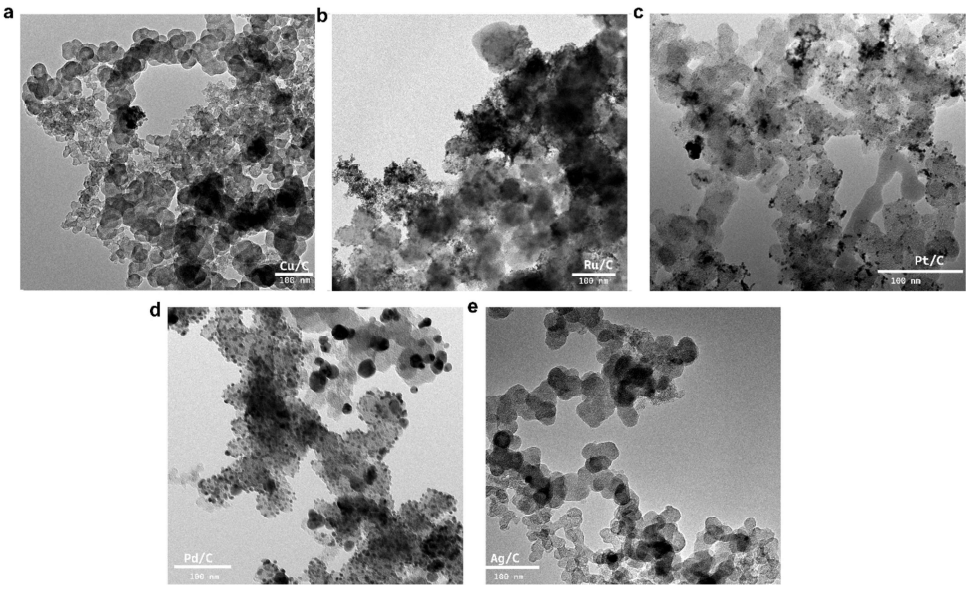

Figure 4.A.3: TEM figures for prepared catalysts: (a) Cu/C; (b) Ru/C; (c) Pt/C; (d) Pd/C and (e) Ag/C.

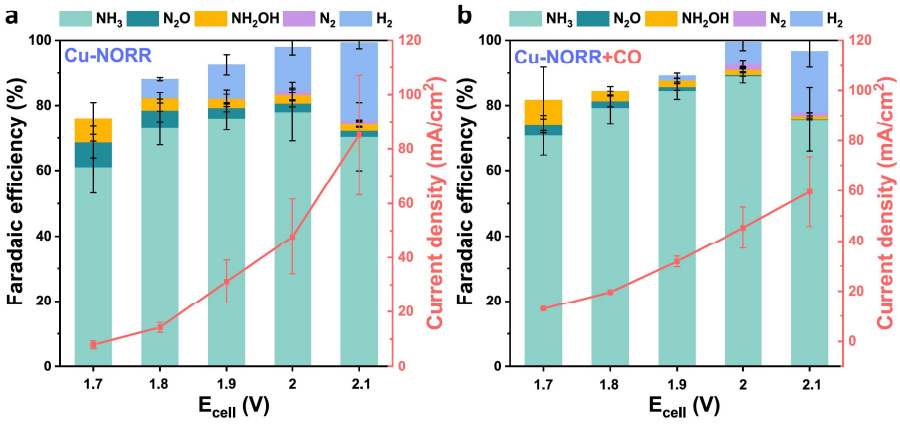

Figure 4.A.4: Faradaic efficiency and current density for Cu/C in (a) NORR and (b) NORR+CO.

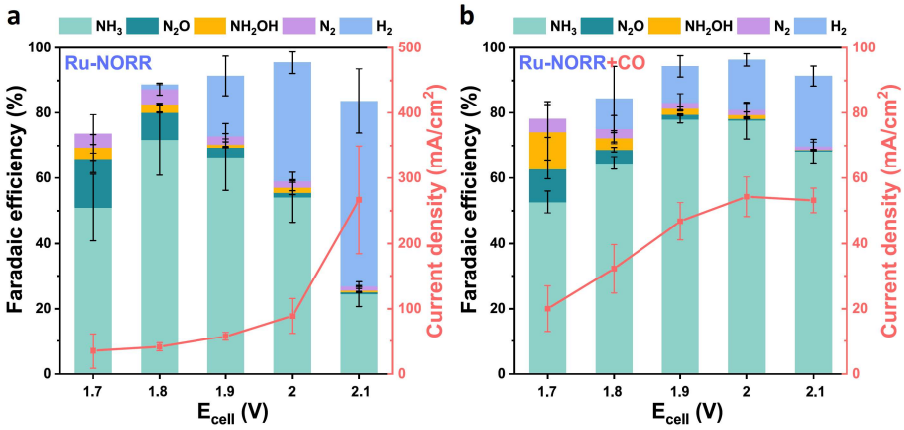

Figure 4.A.5: Faradaic efficiency and current density for Ru/C in (a) NORR and (b) NORR+CO.

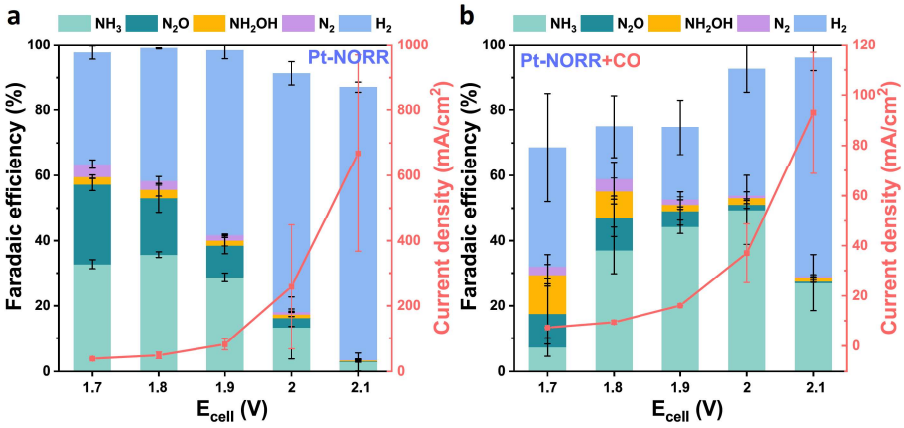

Figure 4.A.6: Faradaic efficiency and current density for Pt/C in (a) NORR and (b) NORR+CO.

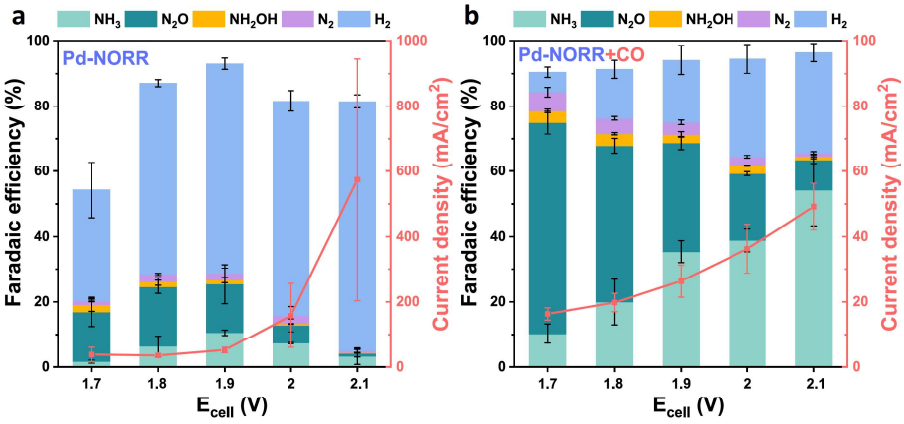

Figure 4.A.7: Faradaic efficiency and current density for Pd/C in (a) NORR and (b) NORR+CO.

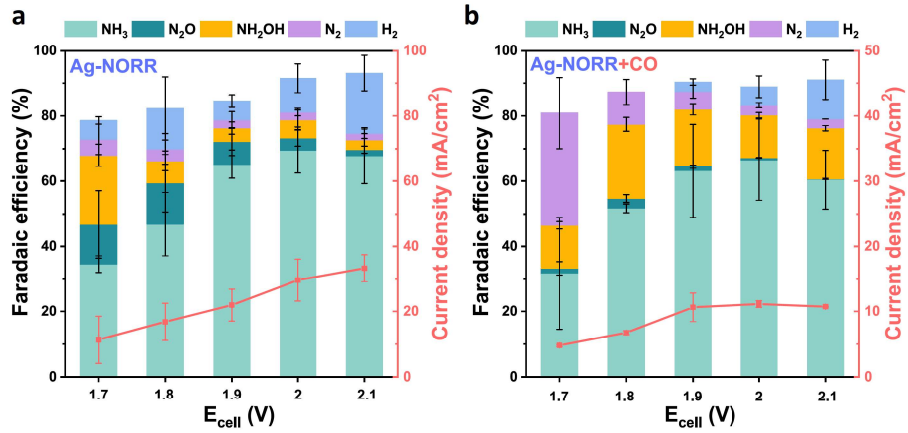

Figure 4.A.8: Faradaic efficiency and current density for Ag/C in (a) NORR and (b) NORR+CO.

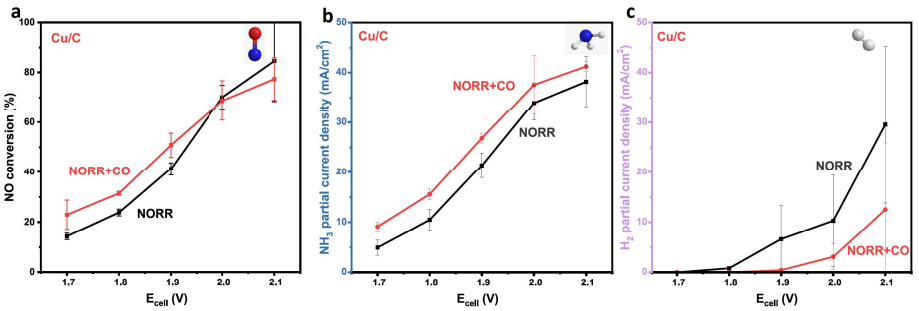

Figure 4.A.9: (a) NO conversion; (b) NH_3 partial current density and (c) H_2 partial current density of Cu/C in NORR and NORR+CO.

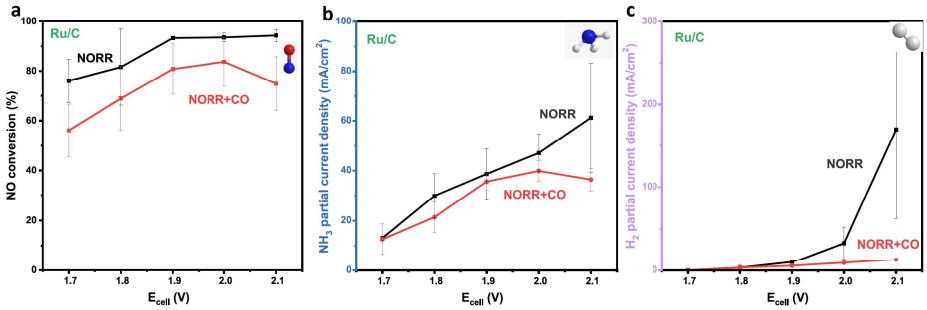

Figure 4.A.10: (a) NO conversion; (b) NH_3 partial current density and (c) H_2 partial current density of Ru/C in NORR and NORR+CO.

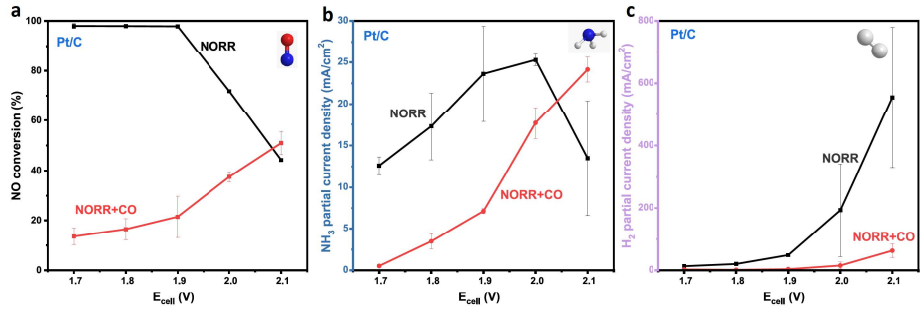

Figure 4.A.11: (a) NO conversion; (b) NH_3 partial current density and (c) H_2 partial current density of Pt/C in NORR and NORR+CO.

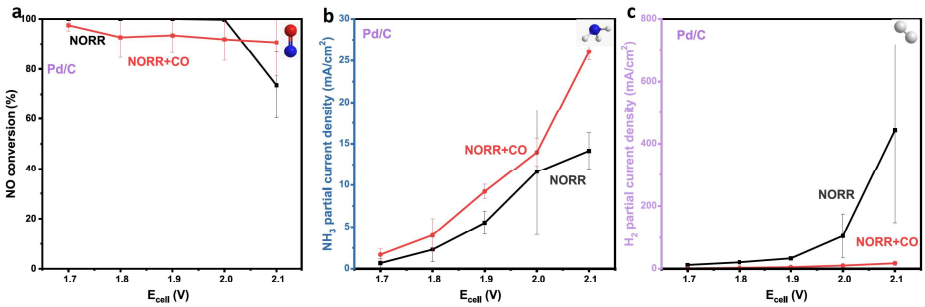

Figure 4.A.12: (a) NO conversion; (b) NH_3 partial current density and (c) H_2 partial current density of Pd/C in NORR and NORR+CO.

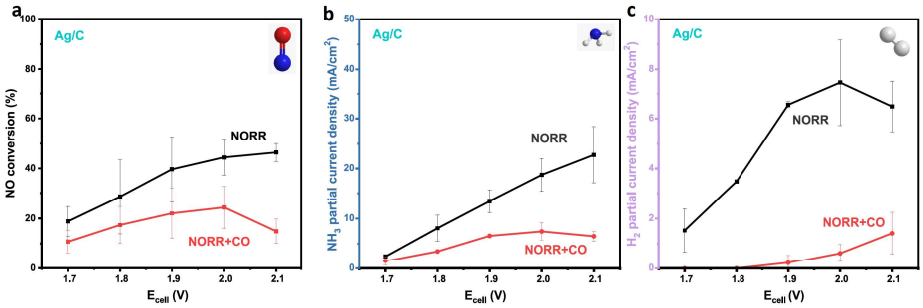

Figure 4.A.13: (a) NO conversion; (b) NH_3 partial current density and (c) H_2 partial current density of Ag/C in NORR and NORR+CO.

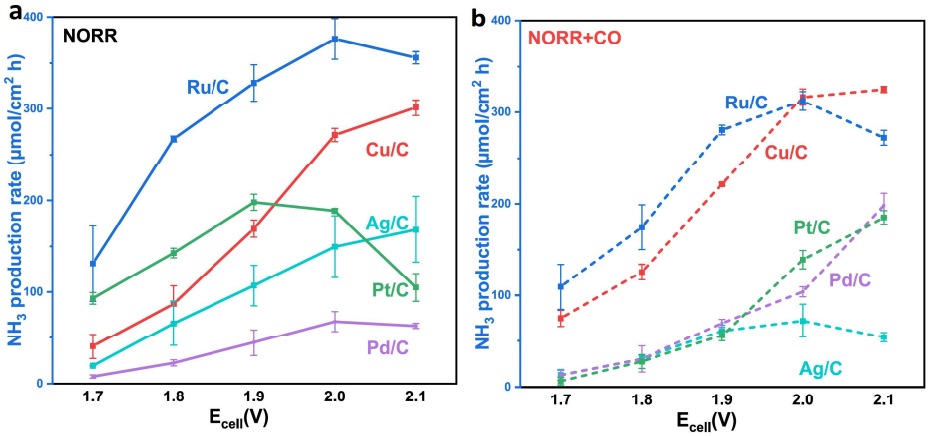

Figure 4.A.14: NH_3 production rate of various catalysts in (a) NORR, and (b) NORR+CO as a function of cell voltage.

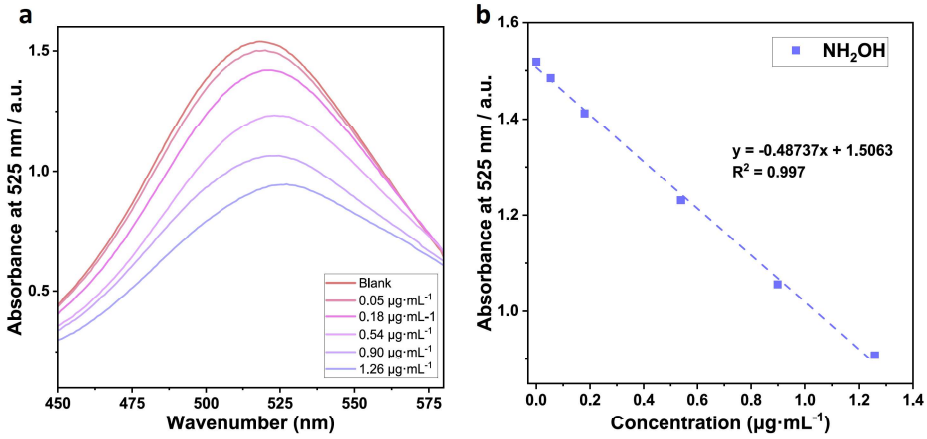

Figure 4.A.15: Neutral red method for hydroxylamine quantification. (a) UV-Vis absorption spectra of various hydroxylamine concentrations. (b) Calibration curve for hydroxylamine quantification.

Table 4.A.1: Comparison of NH_3 production rate vs. potential from reported studies.

Catalyst	Electrolyzer	N source	Liquid electrolyte	Potential	NH_3 FE (%)	NH_3 production rate (μmol·cm^{-2}·h^{-1})	Ref.
Cu foam	Batch cell	99.9% NO	0.25 M Li_2SO_4	-0.9 V vs. RHE	94	517	[1]
Cu-Ti fibers	H cell	10% NO	0.05 M H_2SO_4	-0.6 V vs. RHE	90	400	[2]
Cu nanoparticle	Vapor fed flow cell	99.5% NO	0.1M NaOH+ 0.9M $NaClO_4$	0.03 V vs. RHE	66	1806	[3]
Ag	H cell	99.9% NO	Designed electrolyte	0.165 V vs. RHE	99	28	[4]
Ru nanosheets	H cell	1% NO	0.5 M Na_2SO_4	-0.2 V vs. RHE	66	23	[5]
40 wt% Ru/C	PEM	2.5% NO	No	2.0 V	54	376	This work
					78	313 (NORR+CO)	
40 wt% Cu/C	PEM	2.5% NO	No	2.1 V	70	301	This work
					76	325 (NORR+CO)	
40 wt% Pd/C	PEM	2.5% NO	No	2.1 V	3	63	This work
					54	198 (NORR+CO)	

[1] Long, J. et al. Direct electrochemical ammonia synthesis from nitric oxide. *Angewandte Chemie International Edition* **59**, 9711–9718 (2020).
[2]Krzywda, P. M., Paradelo Rodríguez, A., Benes, N. E., Mei, B. T. & Mul, G. Effect of electrolyte and electrode configuration on Cu-catalyzed nitric oxide reduction to ammonia. *ChemElectroChem* **9** (2022).
[3] Ko, B. H., Hasa, B., Shin, H., Zhao, Y. & Jiao, F. Electrochemical Reduction of Gaseous Nitrogen Oxides on Transition Metals at Ambient Conditions. *Journal of the American Chemical Society*, 144, 1258–1266 (2022).
[4] Kim, D. et al. Unveiling electrode–electrolyte design-based NO reduction for NH_3 Synthesis. *ACS Energy Letters* **5**, 3647–3656 (2020).
[5] Li, Y. et al. Electrocatalytic reduction of low-concentration nitric oxide into ammonia over Ru nanosheets. *ACS Energy Letters* **7**, 1187–1194 (2022).

5

Bicarbonate and Nitrate co-electroreduction to Urea

Direct electrocatalytic synthesis of urea from captured CO_2 (as bicarbonate-HCO_3^-) and nitrate (NO_3^-) in a water-fed PEM electrolyzer offers a sustainable alternative to the energy-intensive Haber-Bosch and Bosch-Meiser process. Initial experiments with a standard catalyst-coated membrane (CCM) failed to reduce bicarbonate, producing mostly hydrogen. The key breakthrough was switching to a catalyst-coated substrate (CCS) configuration, which allowed protons (H^+) and HCO_3^- to react together on the same catalyst surface, enabling *in situ* CO_2 generation for further conversion. Further optimization focused on the gas diffusion layer (GDL). A carbon fiber-based GDL (Sigracet 39AA) with 5 wt.% Nafion on a copper (Cu) catalyst proved most effective, achieving a peak faradaic efficiency (FE) of 40% for carbon products by directly reducing liquid HCO_3^-. This optimized cell configuration also efficiently reduced NO_3^- to ammonia (NH_3) with a 20% FE. By co-feeding both HCO_3^- and NO_3^- into the system, urea was successfully synthesized with a reproducible FE of 16% at 5 $mA \cdot cm^{-2}$. This work establishes a viable and systematically optimized pathway for sustainable urea production directly from waste HCO_3^- and NO_3^- streams, providing a way for green fertilizer production.

Part of this chapter has been prepared for submission.

5.1 Introduction

The escalating global population and the corresponding demand for food security have necessitated a substantial increase in the production of nitrogen-based fertilizers, with urea being the most predominant products worldwide [1]. Conventionally, industrial urea synthesis proceeds via a sequential, energy-intensive thermochemical route. This process begins with the Haber-Bosch process for ammonia (NH_3) production from nitrogen (N_2) and hydrogen (H_2) at high temperatures and pressures (400-500 °C, 100-200 bar) [2]. Subsequently, the Bosch-Meiser process converts this NH_3 and carbon dioxide (CO_2) into urea, also under demanding conditions (150-200 °C, 150-250 bar) [3]. This established pathway is notoriously inefficient from an environmental and energy perspective. It is responsible for an estimated 2-3% of the world's annual energy consumption and contributes approximately 3% of global CO_2 emissions [4]. Furthermore, its reliance on H_2 derived from fossil fuels consumes 3-5% of the world's natural gas production [5]. The significant carbon footprint and fossil fuel dependency of conventional methods create a compelling case for developing alternative, sustainable technologies.

Electrochemical urea synthesis offers a promising alternative to fossil-fuel-based approaches [6]. Current research emphasizes the co-reduction of gaseous CO_2 with nitrogen-containing substances such as NO_3^- and NO_2^- with urea as the main target product [7, 8]. Conventional gas-fed CO_2 electrolysis CO_2 electrolysis relies on prior capture, release, and handling of gaseous CO_2, introducing additional energy and capital costs [9, 10]. By contrast, direct electroreduction of carbon-capture media, most notably aqueous bicarbonate (HCO_3^-) can bypass the CO_2 regeneration step [11, 12]. Conducting bicarbonate reduction (HCO_3RR) in PEM electrolyzer, where the H^+ flux from membrane can react with HCO_3^- and generate CO_2 *in situ* [13]. The in-situ generated CO_2 can then be adsorbed on the catalyst surface and undergo an electrochemical reduction process [14]. Coupling HCO_3RR with nitrate reduction sourced from wastewater thus provides a promising platform for electrocatalytic urea synthesis, simultaneously lowering energy input and valorizing two waste streams.

In this work, we aim to study the electrochemical synthesis of urea using bicarbonate and nitrate as the feedstock in a continuous water-fed PEM electrolyzer at room temperature (Figure 5.1.1). Since there were limited studies on liquid phase bicarbonate reduction but with good performance of nitrate reduction in a water-fed PEM system, we first optimized the reaction condition for bicarbonate reduction. Later, we performed electrochemical co-reduction of NO_3^- and HCO_3^- for urea synthesis using the optimized condition. Reliable assessment of electrocatalytic performance is relied on the accurate, reproducible quantification of urea [15, 16]. However, widely used methods

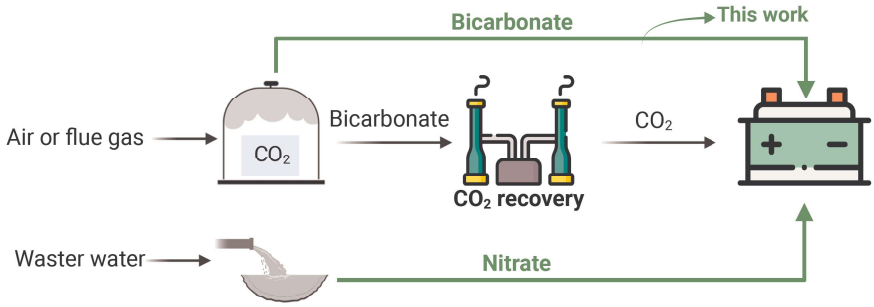

Figure 5.1.1: (Comparison of simplified process flow diagrams for current CO_2 and nitrate reduction to urea and direct bicarbonate and nitrate reduction to urea.

suffer from significant limitations: urease method suffers from poor accuracy and reproducibility [17]; the diacetylmonoxime–thiosemicarbazide (DAMO-TSC) colorimetric methods is susceptible to interferents [18]; and ^{1}H-NMR, while selective, is relatively slow and sensitivity-limited [19]. Properly configured high-performance liquid chromatography (HPLC) offers a faster, more reliable, and minimally interference-prone alternative [20, 21]. However, despite increasing uptake [22], variability in column and detector selection (e.g., UV-vis vs MS) and insufficient methodological detail impede the development of standardized protocols [20, 23]. To address these gaps, we establish a liquid-state NMR approach that achieves high sensitivity on broadly accessible spectrometers by adding paramagnetic ions (e.g., Gd^{3+}) to shorten spin-lattice relaxation times (T1) [24, 25], enabling direct, quantitative detection of urea. We hope this work draws attention to the foundational challenge of urea quantification in this emerging field and helps establish rigorous, standardized protocols for future studies in urea electrosynthesis.

5.2 Experimental method

Chemicals and materials Copper (Cu, nanopowder, 25 nm particle size), Nafion™ perfluorinated resin solution (5% in a mixture of lower aliphatic alcohols and water), hydrogen peroxide (H_2O_2, 30% (w/w) in H_2O), sulfuric acid (H_2SO_4, ≥97.5%), maleic acid (C_4H_4O, ≥99%), gadolinium(III) nitrate hexahydrate (99.9%), urease (Type IX from Jack beans), thiosemicarbazide (CH_5N_3S ,99%), 2,3-butanedione monoxime ($C_4H_7NO_2$, ≥98%), phosphoric acid (H_3PO_4, ≥85 wt.% in H_2O), iron(III) chloride ($FeCl_3$, 97%), potasium nitrate (KNO_3, ≥99.0%), potassium bicarbonate ($KHCO_3$, BioUltra, ≥99.5%), urea (NH_2CONH_2, 99%), sulfamic acid (NH_2SO_3H, 99.3%) were purchased from Sigma-Aldrich. D_2O (99% D_2O, 1% H_2O), dimethylsulfoxide D6 (DMSO-d6, 99.9% D) were obtained from Euriso-

top. Iridium (IV) oxide Premion™ (IrO_2) 99.99% was purchased from Therma Scientific Chemicals. Nafion™ 115 membranes from Ion power, and carbon gas diffusion layer (GDL) Sigracet 39 AA and Sigracet 39 BB were from Fuel Cell Store.

Electrode preparation Nafion™ 115 membranes (3×3 cm^2) were pre-treated according to the procedure of 1 hour in 5 wt.% H_2O_2 solution and 1 hour in 0.5 M H_2SO_4 solution at 80 °C and 1 hour in boiling MilliQ water. After the pre-treatment, the membranes were stored in MilliQ water to prevent swelling. The anode catalyst ink was prepared by dispersing 4 mg of IrO_2 with 20 wt.% Nafion in 1 mL mixture of isopropanol and water (volume ratio: 50:50). For the cathode catalyst ink, 4 mg of Cu nanoparticles were dispersed in 1 mL of the same isopropanol and water solvent mixture. To investigate the effect of Nafion content, various loadings-5 wt.%, 25 wt.%, 50 wt.%, and 100 wt.% relative to the amount of Cu. All catalyst inks were sonicated in an ultrasonic bath for 30 minutes, in the meantime using ice-cold water to minimize heating to ensure homogeneous dispersion of the catalyst nanoparticles. Fresh inks were prepared for each experiment and used immediately after sonication for spray coating. The anode catalyst ink consisting of IrO_2 was sprayed on one side on the Nafion membrane at 60 °C, on an area of 4 cm^2 to achieve a catalyst loading of 1 $mg \cdot cm^{-2}$. After spray coating, the membrane was hot-pressed at 120 °C and 1 tonne for 3 minutes. The cathode catalyst ink consisting of Cu and different concentrations of Nafion was sprayed on the 39BB and 39AA carbon papers in the same reaction area of 4 cm^2 and under the same temperature. For the control experiment, the cathode catalyst ink was sprayed on the other side of the membrane.

Material Characterization The powder X-ray diffraction (XRD) was recorded using Bruker D8 ADVANCE X-ray diffractometer with Cu Kα radiation source in a range of 5° to 90° with a step of 0.05°. The surface morphology of the catalysts coated GDLs was characterized by scanning electron microscopy (SEM). Contact angle measurements were performed via sessile drop using an OCA 25 goniometer (Dataphysics instruments Gmbh, Filderstadt, Germany), and 2 L of droplets were dispensed onto substrates using an automatic pipetting unit. Measurements were taken in ambient air with a temperature in the range of 20-24 °C.

Electrochemical experiments The electrochemical experiments were conducted in the PEM electrolyser on an AUTOLAB PGSTAT302N potentiostat (Figure 5.A.1). The PEM electrolyser was operated at room temperature. At the anode side, a peristaltic pump (Ismatec ISM597D) was used to pump MilliQ water through the chamber at a flow rate of 1 $mL \cdot min^{-1}$. At the cathode side, a solution of 1 M $KHCO_3$ or 1 M $KHCO_3$ and 1000 ppm KNO_3 was set at a flow rate of 0.5 $mL \cdot min^{-1}$. The gas and liquid products of the reaction were collected in a 25 mL trap with continuously purging with N_2. After the

liquid trap, the remaining gas was analysed by transmission Infrared (IR) Spectrometer (Bruker Alpha) and gas chromatography (GC). The reactions were carried out at constant current density of 2, 5, 10, 25 50 $mA \cdot cm^{-2}$ for 30 minutes each.

Product quantification The gaseous reduction products carbon monoxide (CO) and unreacted carbon dioxide (CO_2) were analysed by Bruker Alpha infrared spectrometer. Methane (CH_4), ethylene (C_2H_4), and hydrogen (H_2) were analysed by a CompactGC (Global Analyser Solutions) equipped with a thermal conductivity Detector (TCD) and flame ionization detector (FID).

The liquid products from bicarbonate reduction were analyzed by Nuclear Magnetic Resonance (NMR, 400 MHz pulsed Fourier transform NMR spectrometer by Agilent Technologies). The products to be detected in NMR were formate (8.35 ppm singlet), ethanol (1 ppm triplet), acetate (1.74 ppm singlet) and n-propanol (0.71 ppm triplet). The internal standard used was 40 mM solution of maleic acid in D_2O. In a typical measurement, 550 L of the sample was mixed with 50 L of the internal standard in a 2 mL sample bottle and then transferred into a clean and dry 5mm NMR tube (Wilmad). The chosen settings for analysis included water ES suppression, 128 scans with a relaxation delay of 2 seconds. The tube was cleaned with MilliQ water and ethanol 2-3 times and was dried at 60 °C in a vacuum oven for 24 h and stored in a dust-free environment.

For the nitrogen containing liquid products: ammonium (NH_4^+), nitrite (NO_2^-) and unreacted nitrate (NO_3^-) were quantified by cation Ion Chromatography (IC, Metrohm 883 Basic ion chromatography). A Metrosep C6 column was used for the quantification of NH_4^+ and a Metrosep Supp 4 column was used for the quantification of NO_2^- and NO_3^-.

Urea detection

The detection of urea will be discussed separately in this chapter. Although several detection methods were explored in this study, some exhibited limitations due to the low concentrations of urea, potentially leading to misleading results.

Colorimetric method Solution A is an acidic solution made of 1:3:6 volume ratios of H_3PO_4, H_2SO_4 and water, together with 10 mg $FeCl_3$ in 100mL. Solution B contains 500 mg of Diacetyl-Monoxime (DAMO) and 10 mg of Thio-semicarbazide (TSC) in 100 mL of water. Standard solutions of different concentrations of urea in water and electrolyte with 1M $KHCO_3$ were thus prepared (0, 0.5, 1, 2.5, 5, 10, 20, 25 ppm). Firstly, 1 mL of each of these reagents was added to 2 mL of urea sample, with heating at 100 °C for 15 minutes generates the pink color. The absorbance of this sample can be measured at 525 nm in a Unicam UV 500 spectrometer after cooling to room temperature.

NO_2^- **removal** 10 ppm urea standard solution with 100 ppm NO_2^- in MilliQ water and 1 M $KHCO_3$ and 1000 ppm KNO_3 was freshly prepared. Then 100 L of 0.15 M HSO_3NH_2 in 2 M HCl solution was added to 2 mL samples to remove the NO_2^- in the solution. The reaction is shown in Equation (5.1) [26]:

$$NO_2{}^- (aq) + HSO_3NH_2 (aq) \longrightarrow HSO_4{}^- (aq) + H_2O (l) + N_2 (g) \tag{5.1}$$

Urease method Urease method mainly refers to the hydrolysis of urea by urease to ammonium (NH_4^+), and then the urea concentration is indirectly calculated by analyzing the concentration of NH_4^+. Here, a series of standard urea solutions in H_2O and electrolyte (1 M $KIICO_3$ and 1000 ppm KNO_3) were hydrolyzed via urease at a room temperature for 30 minutes into CO_2 and NH_4^+. After hydrolysis, the moles of NH_4^+ were quantified by ion chromatography as described earlier, then the moles of produced urea ($n_u$rea) were concluded by Equation (5.2):

$$n_{\text{urea}} = \frac{n_{NH_4^+,\text{ after hydrolysis}} - n_{NH_4^+,\text{ before hydrolysis}}}{2} \tag{5.2}$$

Data processing

Faradaic Efficiency The faradaic efficiencies (FE's) were calculated according to Equation (5.3):

$$FE_{NH_3} = \frac{nzF}{Q} \tag{5.3}$$

Here, z represents the number of electron transfers required to the formed products, n is the number of moles of the product formed in the catholyte stream, F is the faraday constant 96485 $C \cdot mol^{-1}$, Q is the charge passing through the cell.

For the liquid products, the number of moles (n) was calculated by multiplying the molar concentration ($C_{liquid,product}$) obtained from different analysis techniques with the total volume (V_{liquid}) of the sample collected during the reaction. For the gas products, the volumetric concentration ($C_{gas,product}$) obtained from the GC and IR was multiplied with the gas flow rate (V_{gas}) and converted to moles by multiplying with the molar volume at STP (V_m = 22.4 $L \cdot mol^{-1}$) and the duration of the experiment (t, t = 30 minutes), as seen in equation (5.4) and (5.5).

$$n_{\text{liquid,product}} = C_{\text{liquid,product}} \times V_{\text{liquid}} \tag{5.4}$$

$$n_{\text{gas,product}} = C_{\text{gas,product}} \times V_m \times V_{\text{gas}} \times t \tag{5.5}$$

Single Pass Conversion of NO_3^-: The single pass conversion rate of NO_3^- was calculated based on equation (5.6):

$$X_{NO_3^-} = \frac{C_{NO_3^-}^{(t=0)} - C_{NO_3^-}^{(t=30)}}{C_{NO_3^-}^{(t=0)}} \times 100 \tag{5.6}$$

where $C_{NO_3^-}^{(t=0)}$ represents the initial nitrate concentration and $C_{NO_3^-}^{(t=30)}$ represents the nitrate concentration after 30 minutes reaction.

5.3 Results and discussion

5.3.1 Urea detection methods and challenges

Accurate detection of urea is crucial for studies on the electrochemical synthesis of urea, particularly because the concentrations are often at parts-per-million (ppm) level. Precise quantification of these low concentrations is essential for improving experimental design and advancing understanding in this field. Efforts to detect urea at low concentrations have been continuing for over decades, leading to the development of various methods, including colorimetric, enzymatic, spectroscopic, chromatographic, electrochemical, chemiluminescent, and NMR-based techniques [27, 28]. These approaches are generally classified as direct methods, which detect urea in a single step, and indirect methods, which require conversion of urea into another detectable form [29]. Among these, colorimetric, enzymatic, high-performance liquid chromatography (HPLC), and NMR methods are the most widely used and accepted [30], as illustrated in Figure 5.3.1.

Colorimetry The colorimetric detection of urea is by far the most popular method in the electrochemical urea synthesis literature [31]. Typical urea colorimetry (Figure 5.3.2 (a)) requires several steps of preparation, firstly mixing with solution A, B and samples (details procedure is described in the Method section). Then the solution is heated in an oil bath at 100 °C for 15 minutes and measure the UV absorbance at 525 nm [32]. Urea is known to react with ketones and aldehydes under acidic conditions to generate a yellow compound which is unstable. The stability of this compound can be increased in the presence of thio-semicarbazide (TSC), leading to pink-colored compound in the presence of Fe^{3+}. This property of urea is leveraged for detection at low concentrations. The most used method includes diacetyl monoxime (DAMO) as the carbonyl entity with TSC, to stabilize the colored compound [31].

The calibration curves of urea in water and electrolyte (1 M $KHCO_3$ + 1000 ppm KNO_3) are shown in Figure 5.3.2 (b and c) and (d and e). The lowest concentration of urea detected was 0.5 ppm. In another study by Li et.al, concentrations as low as 0.1 ppm were detected using the colorimetric method [16], while the maximum limit was identical to

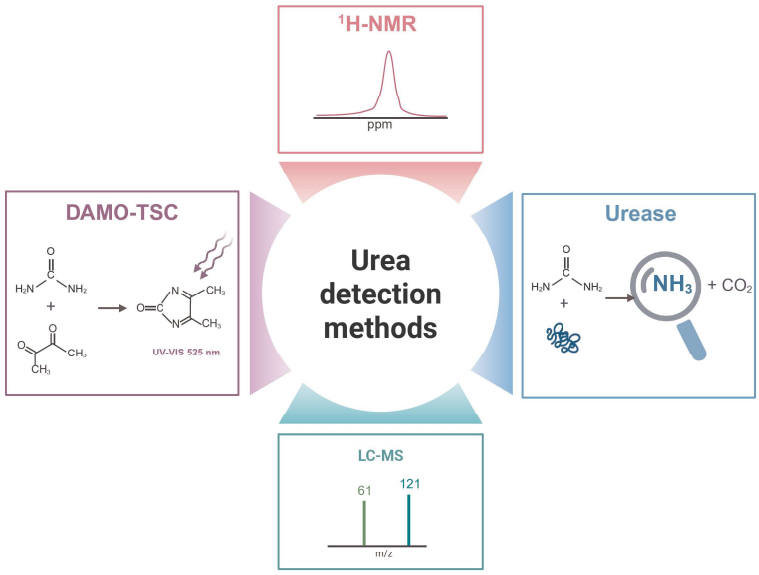

Figure 5.3.1: Most commonly use detection methods for electrochemical urea synthesis.

our results. For urea in water, linearity was observed until 10 ppm urea but in electrolyte conditions, the linearity can only reach until 5 ppm of urea, which indicates the importance of pH in this method. 1M $KHCO_3$ is a weak base that might neutralize the mixture solution A, it is important to ensure the acidity of the mixture solution.

Colorimetric urea determination is susceptible to interference from various ionic species [33, 34], with NO_2^- being particularly problematic as it suppresses the colorimetric signal, leading to potentially erroneous results [18]. This NO_2^--induced signal suppression limits the method's applicability, especially in systems where NO_2^- is a reactant or is generated from nitrate NO_3^- reduction [35]. This effect was confirmed experimentally, as the absorbance of a 10-ppm aqueous urea solution decreased with increasing NO_2^- concentration, with the signal being completely eliminated with 50 ppm NO_2^- (Figure 5.3.3 (a)). An attempt was made to mitigate this interference using sulfamic acid, which reduces NO_2^- to N_2 gas under acidic conditions [31, 36]. While this approach successfully restored the colorimetric signal in simple aqueous samples, it proved ineffective in the electrolyte matrix (Figure 5.3.3 (b)). This failure is attributed to the high alkalinity of electrolyte, which inhibits the acid-dependent reaction of sulfamic acid. Therefore, nitrite interference, especially in alkaline matrices, presents a significant challenge to the accurate colorimetric quantification of urea.

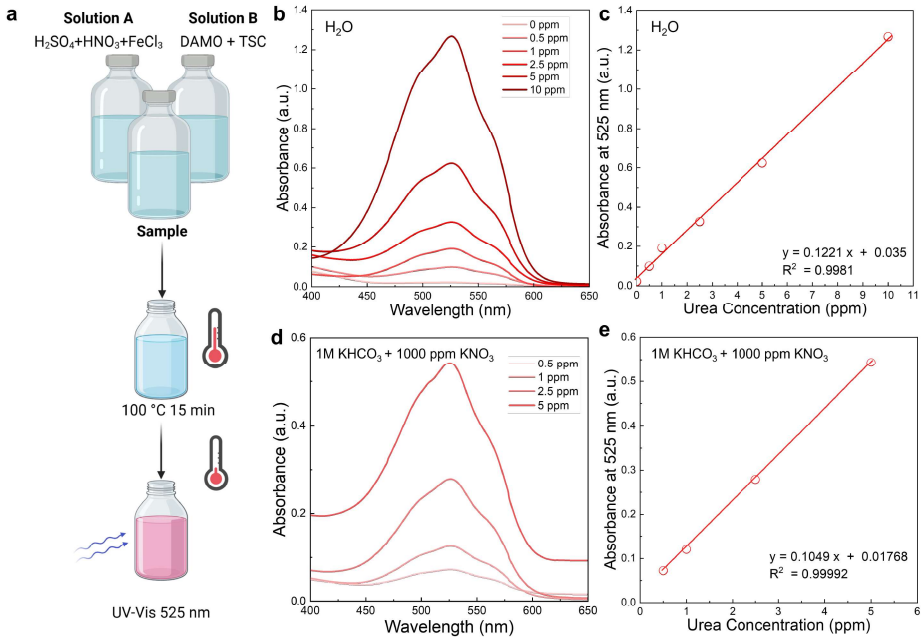

Figure 5.3.2: Urea Colorimetric Method (a) illustration of a typical urea colorimetric detection method; (b and c) urea calibration in water (d and e) urea calibration in 1 M $KHCO_3$ + 1000 ppm KNO_3.

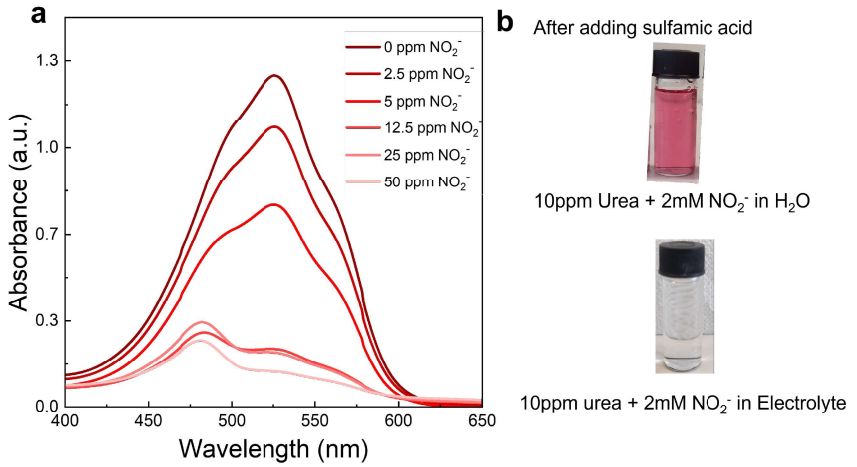

Figure 5.3.3: Effect of NO_2^- in 10 ppm urea solution(a) UV absorbance with different NO_2^- concentration; (b) color restoration with sulfamic acid.

Urease Enzymatic Method

The urease method is another common technique for urea detection, relying on the en-

zymatic hydrolysis of urea into CO_2 and $2NH_3$, as depicted in Figure 5.3.4 (a) [30, 37, 38]. To ensure accurate quantification, the enzymatic conditions were optimized for both aqueous and electrolyte samples (Figure 5.3.4 (b and c)). For urea in water, an enzyme concentration of 0.1 mg·mL^{-1} was proved insufficient for complete hydrolysis within 30 minutes. Increasing the concentration to 0.5 mg·mL ^{1} successfully resulted in complete urea decomposition in the same timeframe.

However, applying these optimized conditions directly to the electrolyte matrix was unsuccessful, as the higher pH inhibited all enzymatic activity [39, 40]. This required neutralizing the electrolyte samples to pH 7 using H_3PO_4, which was chosen because phosphate ions typically do not interfere with urease. Even after neutralization, the 0.5 mg·mL^{-1} enzyme showed minimal activity. Complete hydrolysis in the electrolyte matrix was only achieved after increasing the enzyme concentration tenfold to 5.0 mg·mL^{-1}, which allowed for full decomposition within 30 minutes.

a

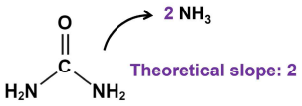

b

Condition	Solution 25 ppm urea	Time (min)	Urease concentration (mg·mL)	Urease vol (mL)	pH
1	in H_2O	30	0.1	0.5	7
2	in H_2O	30	0.5	0.5	7
3	in 1M $KHCO_3$ + 1000 ppm KNO_3	30	0.5	0.5	8.65
4	in 1M $KHCO_3$ + 1000 ppm KNO_3	30	0.5	0.5	Adjust to 7
5	in 1M $KHCO_3$ + 1000 ppm KNO_3	30	5	1	Adjust to 7

c

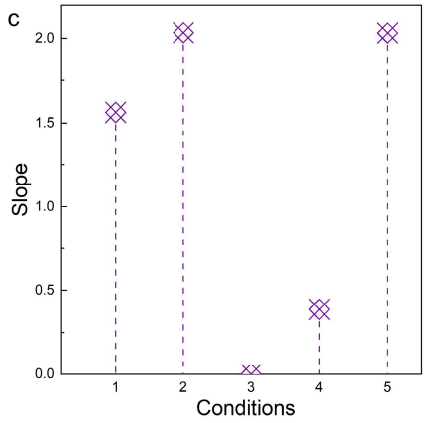

Figure 5.3.4: Illustration of urea hydrolysis; (b) tested conditions for the urease enzymatic method; (c) moles of NH_4^+ detected at different conditions.

NMR Method Nuclear Magnetic Resonance (NMR) spectroscopy, particularly ^{1}H-NMR, is a powerful method used to confirm the presence of and quantify urea. In aqueous solutions, urea exhibits a characteristic chemical shift at approximately 5.6 ppm [41]. A primary challenge is that urea is often present at low concentrations, which requires the use of high field spectrometers (e.g., 800 MHz) and extended acquisition times to achieve an adequate signal-to-noise ratio (SNR) [17]. To address the dominant water signal, various suppression methods were tested, with the ZGESP pulse sequence providing the most effective results (Figure 5.3.5). Using this optimized method, an excellent linear calibration was achieved for standard urea solutions in water, with a detection limit of 2 ppm (Figure 5.A.2).

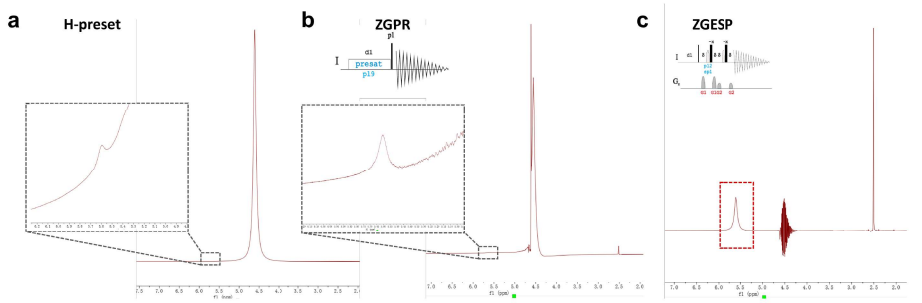

Figure 5.3.5: Different water suppression method applied in urea detection (a) H-preset; (b) ZGPR; (c) ZGESP

To improve SNR and reduce measurement times, especially in complex matrices, paramagnetic relaxation agents can be employed. The addition of gadolinium ions (Gd^{3+}), a well-known MRI contrast agent, was investigated. Due to its large magnetic moment, Gd^{3+} drastically shortens the longitudinal relaxation time (T1) of nearby nuclei [25]. Experimentally, adding Gd^{3+} resulted in the T1 value of urea decreasing from 9.5 s to just 0.1 s (Figure 5.3.6 (a)). This T1 reduction brings a significant practical benefit: for a 50-ppm urea sample in an electrolyte, the SNR more than doubled from 47 to 106 (Figure 5.3.6 (b)). This enhancement enabled the generation of a reliable calibration curve for urea within the electrolyte matrix, showing good linearity (Figure 5.3.6 (c and d)).

Beyond ^{1}H-NMR, isotopic analysis using ^{13}C-NMR and ^{15}N-NMR can confirm urea formation pathways from labeled precursors like $^{13}CO_2$, however, these methods present some challenges [42]. When using a bicarbonate electrolyte, the ^{13}C-NMR signal from urea can be obscured by the overwhelmingly large signal from HCO_3^-, which contains both natural abundance ^{13}C and labeled $H^{13}CO_3^-$ [43]. Meanwhile, ^{15}N-NMR suffers from intrinsically low sensitivity. Nitrogen isotopes also influence ^{1}H-NMR spectra. The most common isotope, ^{14}N (spin I > 1/2), possesses a nuclear quadrupole moment that interacts with the local electric field, causing significant broadening of the attached proton peaks in the ^{1}H-NMR spectrum [44]. In contrast, the ^{15}N isotope (spin I = 1/2) lacks a quadrupole moment [45]. Consequently, when ^{15}N -labeled precursors are used, the resulting ^{15}N -urea exhibits sharper, more defined peaks in the ^{1}H spectrum [46], facilitating more accurate detection and quantification.

5.3.2 Bicarbonate reduction

Commercial Cu nanoparticles were used as a catalyst for all the electrochemical tests. XRD pattern of the Cu nanoparticle was shown in Figure (5.A.3), both metallic Cu (PDF 040836) and Cu(I) oxide (PDF 050667) are present due to atmospheric oxidation of Cu [47].

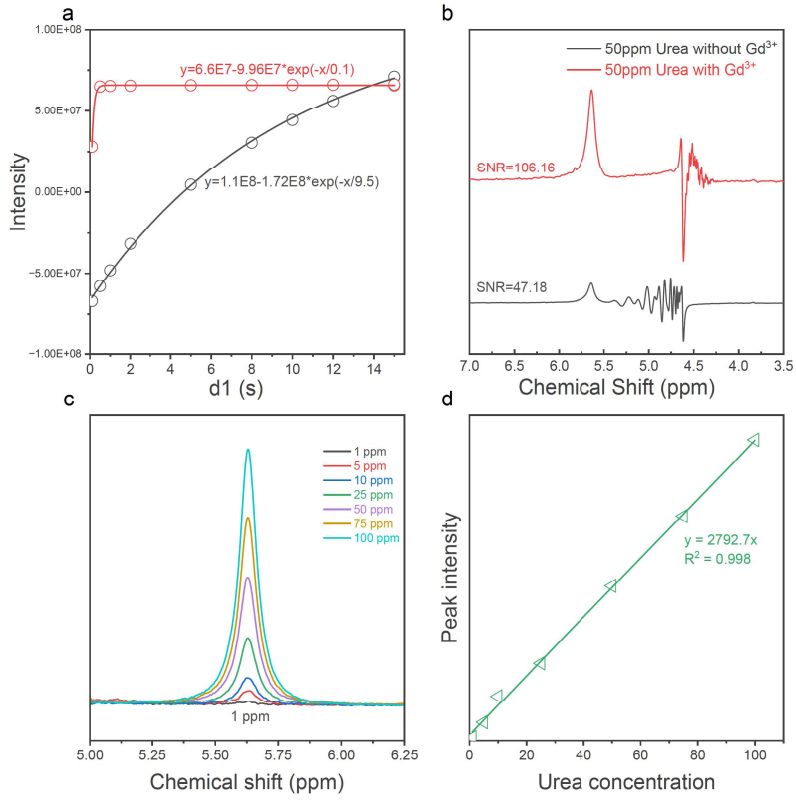

Figure 5.3.6: (a) T1 measurement of urea without Gd^{3+} (black) and with 1 mM Gd^{3+} (red) (b) effect of Gd^{3+} on SNR for 50 ppm urea in electrolyte; (c and d) spectrum and calibration curve of urea in electrolyte with 1 mM Gd^{3+}.

CCM configuration vs. CCS configuration Previous work in this dissertation utilized a catalyst-coated membrane (CCM) configuration [48], where catalysts are sprayed directly onto the membrane (Figure 5.3.7 (a)). This configuration predominantly yielded H_2 from bicarbonate electrolysis because rapid H^+ mass transfer through the proton exchange membrane favored the hydrogen evolution reaction (HER) [49, 50]. Concurrently, mass transfer limitations for HCO_3^- through the cathode catalyst layer resulted in negligible CO_2 reduction (Figure 5.3.7 (c)).

To facilitate HCO_3RR via in-situ CO_2 liberation, a catalyst-coated substrate (CCS) configuration was adopted, where the cathode catalyst (Cu) was sprayed onto the gas diffusion layer (GDL) instead of the membrane (Figure 5.3.7 (b)). This CCS design improves HCO_3^- mass transport, promoting its reaction with H^+ at the catalyst surface [51].

The shift to the CCS configuration increased the outlet CO_2 concentration to about 2.2%

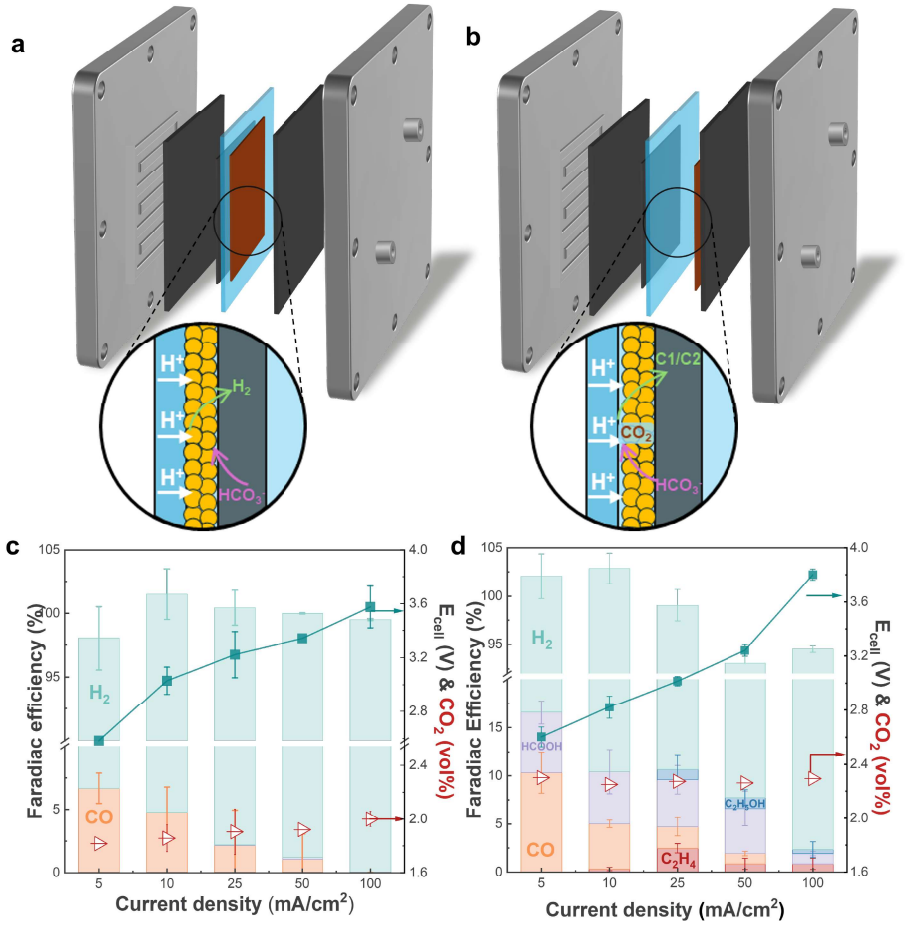

Figure 5.3.7: (a) illustration of catalyst-coated membrane (CCM) and (b) catalyst-coated substrate (CCS) cell configuration; HCO_3RR results on (c) CCM configuration and (d) CCS configuration.

and achieved a faradaic efficiency (FE) over 10% for CO_2 reduction products. At lower current densities (5-10 $mA \cdot cm^{-2}$), only CO and HCOOH were formed. As current density increased to 25-50 $mA \cdot cm^{-2}$, trace C2 products (C_2H_4, C_2H_5OH) were detected, but H_2 production became dominant at 100 $mA \cdot cm^{-2}$ (Figure 5.3.7 (d)). The higher CO_2 concentration in the CCS setup confirms increased CO_2 liberation near the electrode surface, which is a critical step for enhancing HCO_3RR.

To further optimize HCO_3RR in the PEM electrolyzer, different carbon-based gas diffusion layers were investigated. This study compared 39BB, which contains a microporous carbon layer and a PTFE-treated carbon fiber support, with 39AA, which only consists of untreated carbon fiber. Surface morphology and contact angle measurements revealed

significant differences (Figure 5.A.4). The porous structure of the carbon fiber substrate was clearly visible on the 39AA GDL, contrasting with the tightly packed surface of the 39BB. Notably, the 39AA GDL was substantially more hydrophilic than the 39BB GDL, with contact angles of 138° and 148°, respectively. This increased hydrophilicity in the 39AA is expected to improve the contact between the GDL and the aqueous feed.

Figure 5.3.8 presents the electrochemical HCO_3RR results at 50 $mA \cdot cm^{-2}$ in CO_2 saturated 1 M $KHCO_3$, comparing different GDLs with varying Nafion ionomer loadings on the Cu catalyst. For the 39BB GDL (Figure 5.3.8 (a), the FE of all tested current densities of different Nafion loading are shown in Figure 5.A.5), increasing the Nafion content to 50 wt.% enhanced the total FE for carbon products to approximately 25%. The FE for C2 products also increased with higher Nafion loading, which can be attributed to two factors: increased local H^+ availability and a longer residence time for the adsorbed carbon monoxide (*CO) intermediate [52]. As a cation-conducting ionomer, Nafion increases the local H^+ concentration, promoting both *in situ* CO_2 generation and subsequent reduction. Concurrently, a decrease in CO formation with increasing Nafion loading suggests enhanced utilization of adsorbed *CO for C-C coupling [53]. This aligns with *in situ* ATR-SEIRAS studies showing that Nafion increases signals for atop and bridged *CO species, with atop *CO being a known precursor for C2 products formation [53]. The stabilization of the *CO intermediate is attributed to hydrogen bonding between the sulfonate groups of the Nafion ionomer and the oxygen atom of the adsorbed CO [54].

The inherent hydrophobicity of the 39BB GDL likely required a higher Nafion loading (50 wt.%) to achieve improved performance (Figure 5.3.8 (b)), results of 25 wt.% Nafion loading are shown in Figure 5.A.6). Beyond stabilizing the *CO intermediate, the ionomer also imparted necessary hydrophilicity to the gas diffusion electrode (GDE), ensuring adequate contact with the aqueous electrolyte for reactant transport [55, 56]. The modest performance at lower Nafion loadings may come from the reduction of dissolved CO_2 rather than the *in situ* generated CO_2 from bicarbonate. However, further increasing the Nafion content to 100 wt.% diminished CO_2 reduction performance, likely due to mass transport limitations imposed by an excessively thick ionomer layer covering the catalyst surface. Therefore, a 50 wt.% Nafion loading was identified as the optimal ratio for the 39BB GDL.

Given that HCO_3^- is delivered in a liquid feed, the more hydrophilic 39AA GDL exhibited superior performance for total carbon products compared to the 39BB GDL (Figure 5.3.8 (c), the FE of all tested current densities of different Nafion loading are shown in Figure 5.A.7). Under identical reaction conditions and Nafion loadings (0, 5, 25, and 50 wt.%), a drastic increase in performance was observed when the Nafion content was increased

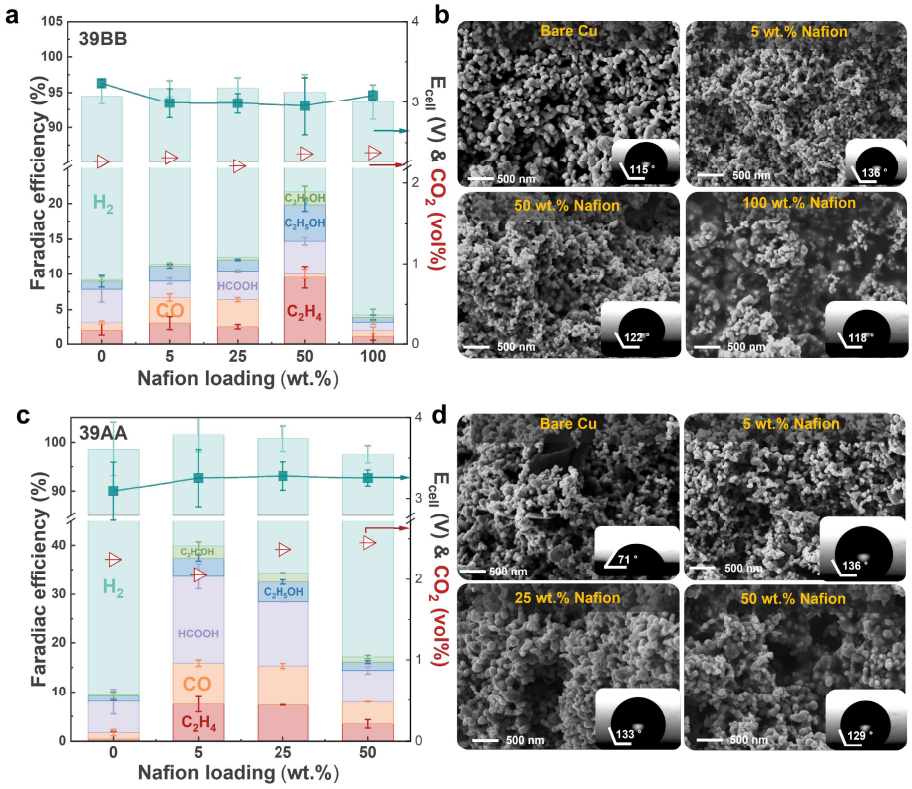

Figure 5.3.8: HO3RR on different Nafion loading on Cu catalyst on (a) 39BB and (c) 39AA; water contact measurement on (b) 39BB and (d) 39AA.

to only 5 wt.%, with the total FE for carbon products reaching a peak of 40%. With 25 wt.% Nafion, the total FE dropped slightly to about 36%, while the product distribution remained largely identical. At a higher loading of 50 wt.%, a significant drop in performance occurred, similar to the results observed with 100 wt.% Nafion on the 39BB GDL. For all experiments using the 39AA GDL, the full cell potential was slightly higher, likely due to a minor decrease in the conductivity of GDL from the absence of the conductive microporous carbon layer. This best performance at 5 wt.% Nafion on the 39AA GDL is attributed to a synergy between the inherent hydrophilicity of GDL and the ability of ionomer to stabilize the *CO intermediate (Figure 5.3.8 (d)), which together improve liquid contact without significantly blocking catalytic sites, an observation consistent with findings by Lees et al. [11].

To decouple the carbon source from either dissolved CO_2 or *in situ* generated CO_2 from liquid HCO_3^-, experiments were performed using an Ar-saturated electrolyte with the

optimal Nafion loading for each GDL (Figure 5.3.9). For the hydrophobic 39BB GDL with 50 wt.% Nafion, switching to an Ar-saturated electrolyte caused a drastic drop in the total FE for carbon products to less than 10% across all current densities (Figure 5.3.9 (a)). This suggests that the performance previously observed in CO_2-saturated conditions was primarily driven by dissolved CO_2, as the hydrophobicity of GDL prevented sufficient contact with the liquid bicarbonate. In contrast, for the hydrophilic 39AA GDL with 5 wt.% Nafion, the performance was not significantly affected, achieving a total carbon FE of about 36%, comparable to the 40% FE achieved in CO_2-saturated experiments (Figure 5.3.9 (b)). This result confirms that the carbon source for this system was indeed the *in situ* generated CO_2 from liquid HCO_3^-. Unsurprisingly, the outlet CO_2 concentration was far lower in both Ar-saturated experiments compared to the CO_2-saturated tests.

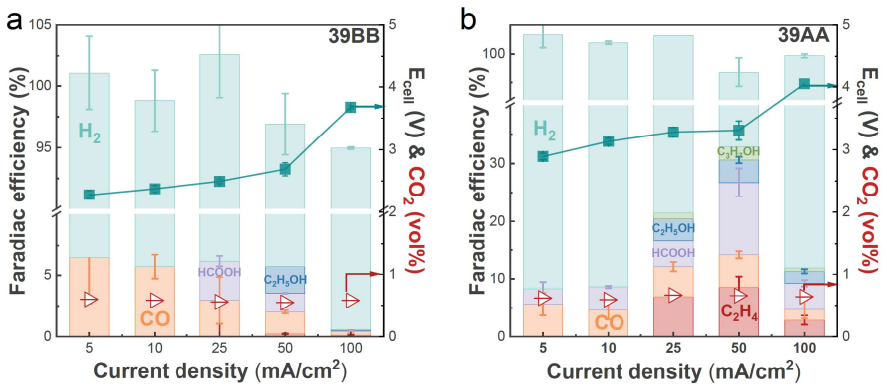

Figure 5.3.9: Argon saturated bicarbonate reduction. (a) Cu with 50wt.% Nafion on 39BB (b) Cu with 5wt.% Nafion on 39AA

The influence of bicarbonate concentration on performance was investigated using an Ar-saturated $KHCO_3$ solution with a 39AA gas diffusion layer (GDL), as shown in Figure 5.3.10 (a). For comparison, results from CO_2-saturated solutions are available in Figure 5.A.8. The optimal performance was achieved with a 1 M $KHCO_3$ solution. As the concentration decreased from this point, CO_2 saturation was required to enhance the HCO_3RR. Conversely, increasing the concentration to 2 M resulted in a drastic performance drop. This decline is likely caused by the accelerated conversion of HCO_3^- to CO_2 near the electrode at high concentrations, leading to bubble nucleation within the GDL pores. These bubbles can block active sites, increase local resistance, and cause both transient and steady-state performance losses. Furthermore, high concentration gradients, particularly with 3 M $KHCO_3$, can drive water flux across the membrane, potentially causing local dehydration or non-uniform hydration. The conductivity of the

Nafion membrane is highly dependent on water activity, and its decrease is reflected in the observed increase in the full cell voltage. Lastly, at high concentrations, the basic conditions created by carbonate (CO_3^{2-}) and hydroxide (OH^-) ions can lead to the precipitation of Cu as basic copper carbonate, often with a malachite-like structure, further degrading performance.

To evaluate the effect of temperature, experiments were performed at 25, 40, 60, and 80 °C using 1 M $KHCO_3$. As shown in Figure 5.3.10(b), the FE of all tested current densities of different temperatures are shown in Figure 5.A.9, the total FE for carbon products decreased as temperature increased across all tested current densities. Specifically, the FE for formate and C2 products declined, while the FE for CO increased. This trend is likely to be due to the decreased solubility of gaseous products at higher temperatures, leading to faster CO release from the catalyst surface. Concurrently, increased temperature enhances both HER and CO_2 liberation from the more soluble $KHCO_3$. Notably, elevating the temperature also improved energy efficiency by reducing the full cell voltage (e.g., from 3.8 V at 25 °C to 2.8 V at 80 °C, at 50 mA·cm^{-2} and decreasing electrolyte resistivity.

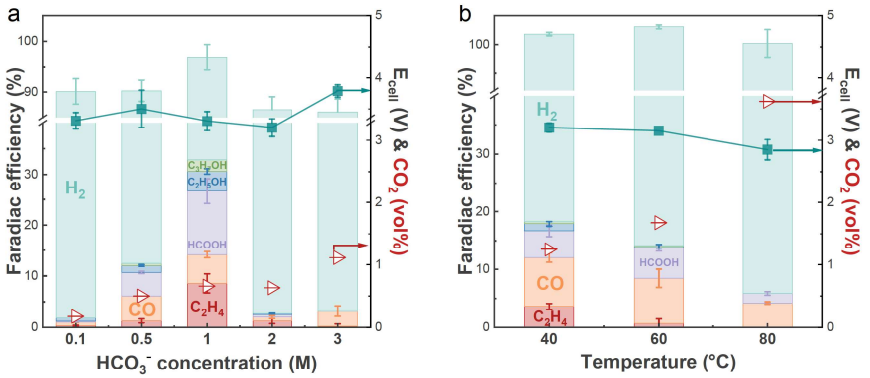

Figure 5.3.10: Argon saturated bicarbonate reduction. (a) different HCO_3^- concentration (b) Cu with 5wt.% Nafion on 39AA

5.3.3 Electrochemical nitrate reduction

The importance of GDL hydrophilicity was further demonstrated in nitrate (NO_3^-) reduction. Switching from the hydrophobic 39BB to the hydrophilic 39AA GDL increased the FE for NH_4^+ from 2% to 20% and boosted nitrate conversion from 0.2% to 23% (Figure 5.3.11). Nitrogen balances were shown in Figure 5.A.10, and nearly 100% N balances were achieved.

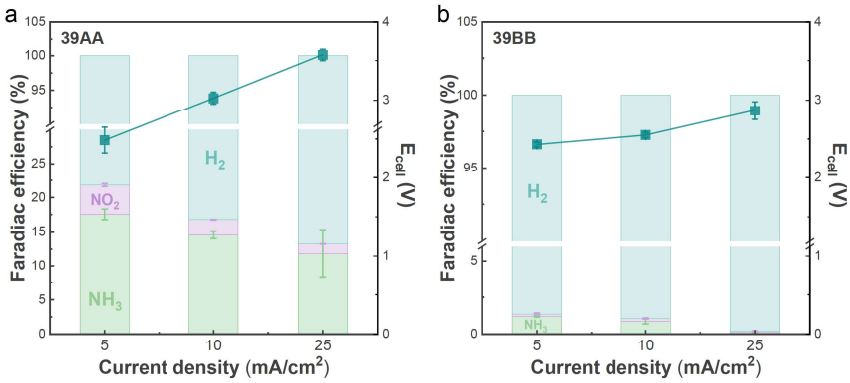

Figure 5.3.11: NO3RR on (a) Cu with 5wt.% Nafion on 39AA; (b) Cu with 50 wt.% Nafion on 39BB

5

5.3.4 Electrochemical urea synthesis

Urea synthesis was investigated using an electrolyte of 1 M $KHCO_3$ with 1000 ppm (0.016 M) NO_3^- at current densities of 5, 10, and 25 mA $\cdot$ cm^{-2}. The initial results, derived from the urease method, are presented in Figure 5.3.12 (a). At 5 mA $\cdot$ cm^{-2}, a promising FE of approximately 16% for urea was observed. While no NH_4^+ was detected, significant NO_2^- was formed, and CO was the only HCO_3^- reduction product detected, with an FE below 10%. As the current density increased, the performance declined sharply. The urea FE dropped to 6% at 10 mA$\cdot$cm^{-2}, and no urea was detected at 25 mA$\cdot$cm^{-2}. This decrease in urea production was accompanied by a rise in FE for competing products, mainly NH_4^+ and H_2. This suggests that at higher currents, the insufficient reaction of CO_2 and NO_3^- limits the availability of intermediates required for C-N coupling. Further complicating the analysis, the Faradaic efficiencies for all detected products did not sum to 100%, and a similar discrepancy was observed in the nitrogen mass balance Figure 5.3.12 (b). This imbalance suggests either the formation of undetected nitrogen-containing species or the loss of volatile products like ammonia during sample storage and handling.

However, a critical discrepancy emerged during analysis. While the conventional urease method indicated the presence of urea, follow-up analysis using the more specific ^{1}H-NMR spectroscopy method confirmed that no urea was present in any of the samples. This outcome serves as a cautionary tale, highlighting the unreliability of the urease method in this context and underscoring the critical need for robust, multi-faceted detection protocols in electrochemical research.

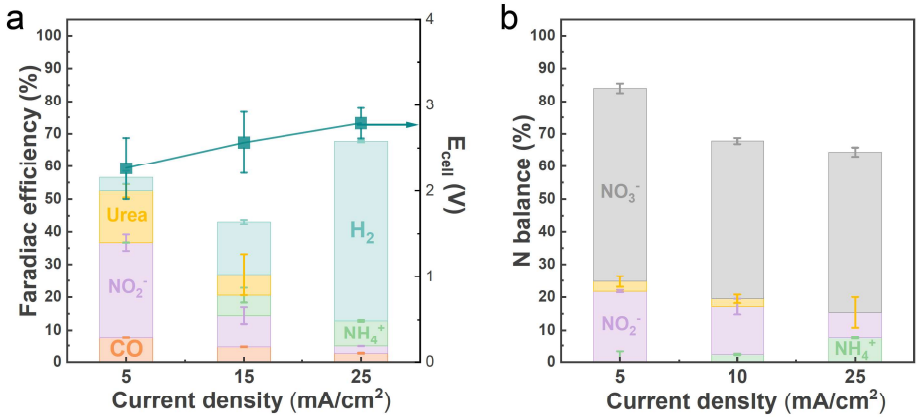

Figure 5.3.12: (a) Urea synthesis experiments with 5wt.% Nafion on 39AA GDL (a) FE and (b) N balance.

5.4 Conclusion

This study aimed to synthesize urea electrochemically from bicarbonate and nitrate in a continuous water-fed PEM cell, using copper as the catalyst. Initial experiments showed that a catalyst-coated membrane (CCM) configuration exclusively produced H_2. Shifting to a catalyst-coated substrate (CCS) configuration was critical for enabling in-situ CO_2 generation from bicarbonate, achieving >10% FE for carbon products. System optimization revealed that a hydrophilic GDL (39AA) was superior to a hydrophobic one (39BB). The addition of a Nafion ionomer stabilized the *CO intermediate, boosting the total carbon product FE to a peak of 40% (with 5 wt.% Nafion on 39AA). Crucially, Ar-saturated experiments confirmed that this optimized system facilitated true liquid-phase bicarbonate reduction, unlike the hydrophobic GDL which relied on dissolved CO_2. The hydrophilic GDL also enhanced nitrate reduction, increasing FE towards NH_3 by 10 times. Finally, co-feeding bicarbonate and nitrate successfully produced urea with a 16% FE at 5 $mA{\cdot}cm^{-2}$. Although an unclosed nitrogen balance suggests product loss, this work successfully demonstrates and optimizes bicarbonate reduction in a water-fed PEM system and achieves the primary goal of urea synthesis.

References

1. Galloway, J. N., Townsend, A. R., Erisman, J. W., Bekunda, M., Cai, Z., Freney, J. R., Martinelli, L. A., Seitzinger, S. P. & Sutton, M. A. Transformation of the nitrogen cycle: recent trends, questions, and potential solutions. *Science* **320,** 889–892 (2008).
2. Kyriakou, V., Garagounis, I., Vourros, A., Vasileiou, E. & Stoukides, M. An electrochemical Haber-Bosch process. *Joule* **4,** 142–158 (2020).
3. Meessen, J. Urea synthesis. *Chemie Ingenieur Technik* **86,** 2180–2189 (2014).
4. Mao, C., Byun, J., MacLeod, H. W., Maravelias, C. T. & Ozin, G. A. Green urea production for sustainable agriculture. *Joule* **8,** 1224–1238 (2024).
5. Song, Y., Johnson, D., Peng, R., Hensley, D. K., Bonnesen, P. V., Liang, L., Huang, J., Yang, F., Zhang, F., Qiao, R., *et al.* A physical catalyst for the electrolysis of nitrogen to ammonia. *Science Advances* **4,** e1700336.
6. Li, J., Zhang, Y., Kuruvinashetti, K. & Kornienko, N. Construction of C–N bonds from small-molecule precursors through heterogeneous electrocatalysis. *Nature Reviews Chemistry* **6,** 303–319 (2022).
7. Song, H., Chipoco Haro, D. A., Huang, P.-W., Barrera, L. & Hatzell, M. C. Progress in photochemical and electrochemical C–N bond formation for urea synthesis. *Accounts of Chemical Research* **56,** 2944–2953 (2023).
8. Haoxiang, C., Junyang, D., Tong, H., Tianran, W., Qian, L., Jun, L., Ligang, F., Wenxian, L. & Xijun, L. Recent progress in electrochemical synthesis of urea through C-N coupling reactions. *Chemical Synthesis* **4,** 54 (2024).
9. Luo, Y., Xie, K., Ou, P., Lavallais, C., Peng, T., Chen, Z., Zhang, Z., Wang, N., Li, X.-Y., Grigioni, I., *et al.* Selective electrochemical synthesis of urea from nitrate and CO_2 via relay catalysis on hybrid catalysts. *Nature Catalysis* **6,** 939–948 (2023).
10. Muhyuddin, M., Zuccante, G., Mustarelli, P., Filippi, J., Lavacchi, A., Elbaz, L., Chen, Y.-H., Atanassov, P. & Santoro, C. Electrochemical urea production using carbon dioxide and nitrate: state of the art and perspectives. *Energy & Environmental Science* **17,** 3739–3752 (2024).
11. Lees, E. W., Goldman, M., Fink, A. G., Dvorak, D. J., Salvatore, D. A., Zhang, Z., Loo, N. W. X. & Berlinguette, C. P. Electrodes designed for converting bicarbonate into CO. *ACS Energy Letters* **5,** 2165–2173 (2020).

12. Greenblatt, J. B., Miller, D. J., Ager, J. W., Houle, F. A. & Sharp, I. D. The technical and energetic challenges of separating (photo)electrochemical carbon dioxide reduction products. *Joule* **2,** 381–420 (2018).
13. Li, T., Lees, E. W., Goldman, M., Salvatore, D. A., Weekes, D. M. & Berlinguette, C. P. Electrolytic conversion of bicarbonate into CO in a flow cell. *Joule* **3,** 1487–1497 (2019).
14. Welch, A. J., Dunn, E., DuChene, J. S. & Atwater, H. A. Bicarbonate or carbonate processes for coupling carbon dioxide capture and electrochemical conversion. *ACS Energy Letters* **5,** 940–945 (2020).
15. Quadrini, L., Laschi, S., Ciccone, C., Catelani, F. & Palchetti, I. Electrochemical methods for the determination of urea: Current trends and future perspective. *TrAC Trends in Analytical Chemistry* **168,** 117345 (2023).
16. Li, D., Xu, N., Zhao, Y., Zhou, C., Zhang, L.-P., Wu, L.-Z. & Zhang, T. A reliable and precise protocol for urea quantification in photo / electrocatalysis. *Small Methods* **6,** 2200561 (2022).
17. Huang, Y., Wang, Y., Liu, Y., Ma, A., Gui, J., Zhang, C., Yu, Y. & Zhang, B. Unveiling the quantification minefield in electrocatalytic urea synthesis. *Chemical Engineering Journal* **453,** 139836 (2023).
18. Wei, X., Wen, X., Liu, Y., Chen, C., Xie, C., Wang, D., Qiu, M., He, N., Zhou, P., Chen, W., *et al.* Oxygen vacancy-mediated selective C–N coupling toward electrocatalytic urea synthesis. *Journal of the American Chemical Society* **144,** 11530–11535 (2022).
19. Kohlhaas, Y., Tschauder, Y. S., Plischka, W., Simon, U., Eichel, R. A., Wessling, M. & Keller, R. Electrochemical urea synthesis. *Joule* **8,** 1579–1600 (2024).
20. Yuan, T. & Voznyy, O. Guidelines for reliable urea detection in electrocatalysis. *Cell Reports Physical Science* **4,** 101521 (2023).
21. Rizzo, M., Ferrera, M., Pelli Cresi, J. S., Mandrup Bertozzi, S., Griesi, A., Goldoni, L., Kriegel, I., Ferri, M. & Manna, L. Yet another uREAlity check: compliant analytical tools, electrochemical insights, and cell configuration effects in urea electrosynthesis on polycrystalline Cu electrodes. *ACS Energy Letters* **10,** 3580–3585 (2025).
22. Jiang, J., Wu, G., Sun, M., Liu, Y., Yang, Y., Du, A., Dai, L., Mao, X. & Qin, Q. Cu–Mo dual sites in Cu-doped $MoSe_2$ for enhanced electrosynthesis of urea. *ACS Nano* **18,** 13745–13754 (2024).
23. Meng, N., Ma, X., Wang, C., Wang, Y., Yang, R., Shao, J., Huang, Y., Xu, Y., Zhang, B. & Yu, Y. Oxide-derived core–shell Cu@Zn nanowires for urea electrosynthesis from carbon dioxide and nitrate in water. *ACS Nano* **16,** 9095–9104 (2022).

24. Duan, X., Moreno, A., Xia, Y., Ji, Z., Cong, R., Ma, L., Xu, M., Zhang, X., Zhou, Y., Liu, C., *et al.* Fast proton NMR detection of aqueous ammonia with relaxation agent and nitrogen decoupling. *ACS Omega* **10,** 8729–8735 (2025).
25. Kolen, M., Smith, W. A. & Mulder, F. M. Accelerating ^{1}H NMR detection of aqueous ammonia. *ACS Omega* **6,** 5698–5704 (2021).
26. Chen, S., Lin, S., Ding, L.-X. & Wang, H. Modified diacetylmonoxime-thiosemicarbazide detection protocol for accurate quantification of urea. *Small Methods* **7,** 2300003 (2023).
27. Francis, P. S., Lewis, S. W. & Lim, K. F. Analytical methodology for the determination of urea: current practice and future trends. *TrAC Trends in Analytical Chemistry* **21,** 389–400 (2002).
28. Wilding, M. H. & Blanton, E. L. Spectrophotometric determination of urea in ammonium nitrate fertilizers. *Journal of Agricultural and Food Chemistry* **30,** 596–598 (1982).
29. KODAMA, S. & SUZUKI, T. Highly sensitive method for urea detection in wine. *Journal of food science* **60,** 1097–1099 (1995).
30. Reay, M. K., Yates, C. A., Johnes, P. J., Arthur, C. J., Jones, D. L. & Evershed, R. P. High resolution HPLC-MS confirms overestimation of urea in soil by the diacetyl monoxime (DAM) colorimetric method. *Soil Biology and Biochemistry* **135,** 127–133 (2019).
31. Rahmatullah, M. & Boyde, T. R. C. Improvements in the determination of urea using diacetyl monoxime; methods with and without deproteinisation. *Clinica Chimica Acta* **107,** 3–9 (1980).
32. Li, D., Xu, N., Zhao, Y., Zhou, C., Zhang, L.-P., Wu, L.-Z. & Zhang, T. A reliable and precise protocol for urea quantification in photo / electrocatalysis. *Small Methods* **6,** 2200561 (2022).
33. Rozet, E., Wascotte, V., Lecouturier, N., Préat, V., Dewé, W., Boulanger, B. & Hubert, P. Improvement of the decision efficiency of the accuracy profile by means of a desirability function for analytical methods validation: application to a diacetylmonoxime colorimetric assay used for the determination of urea in transdermal iontophoretic extracts. *Analytica chimica acta* **591,** 239–247 (2007).
34. Lilov, M. E. & Kirilov, P. P. Stability of urea solutions in presence of mineral acids and their ammonium salts. *J. Chem. Technol. Metall* **54,** 319–325 (2019).
35. Wu, Y., Jiang, Z., Lin, Z., Liang, Y. & Wang, H. Direct electrosynthesis of methylamine from carbon dioxide and nitrate. *Nature Sustainability* **4,** 725–730 (2021).
36. Liu ShuRong, L. S., Vereecken, H. & Brüggemann, N. A highly sensitive method for the determination of hydroxylamine in soils (2014).

37. Shibata, M., Yoshida, K. & Furuya, N. Electrochemical synthesis of urea on reduction of carbon dioxide with nitrate and nitrite ions using Cu-loaded gas-diffusion electrode. *Journal of Electroanalytical Chemistry* **387,** 143–145 (1995).
38. McCarthy, J. J. A urease method for urea in seawater. *Limnology and Oceanography* **15,** 309–313 (1970).
39. Tabatabai, M. Effects of trace elements on urease activity in soils. *Soil biology and Biochemistry* **9,** 9–13 (1977).
40. Cozzi, S. & Giani, M. in *Handbook of water analysis* 381–406 (CRC Press, 2007).
41. Huang, Y., Yang, R., Wang, C., Meng, N., Shi, Y., Yu, Y. & Zhang, B. Direct electrosynthesis of urea from carbon dioxide and nitric oxide. *ACS Energy Letters* **7,** 284–291 (2022).
42. Maimaiti, H., Xu, B., Sun, J.-y. & Feng, L.-r. Photocatalytic synthesis of urea ($CO_2/N_2/H_2O$) on coal-based carbon nanotubes with the Fe-core-supported $Ti^{3+} - TiO_2$ composite catalyst. *ACS Sustainable Chemistry & Engineering* **9,** 6991–7002 (2021).
43. Mani, F., Peruzzini, M. & Stoppioni, P. CO_2 absorption by aqueous NH_3 solutions: speciation of ammonium carbamate, bicarbonate and carbonate by a ^{13}C NMR study. *Green Chemistry* **8,** 995–1000 (2006).
44. Finer, E., Franks, F. & Tait, M. Nuclear magnetic resonance studies of aqueous urea solutions. *Journal of the American Chemical Society* **94,** 4424–4429 (1972).
45. Vold, R. L., Daniel, E. & Chan, S. Magnetic resonance measurements of proton exchange in aqueous urea. *Journal of the American Chemical Society* **92,** 6771–6776 (1970).
46. Schanda, P. & Brutscher, B. Very fast two-dimensional NMR spectroscopy for real-time investigation of dynamic events in proteins on the time scale of seconds. *Journal of the American Chemical Society* **127,** 8014–8015 (2005).
47. Thirugnanasambandan, T. & Alagar, M. X-Ray Diffraction studies of copper nanopowder. *Arch Phys Res* **1** (2010).
48. Bunea, S., Clemens, K. & Urakawa, A. Electrified conversion of contaminated water to value: selective conversion of aqueous nitrate to ammonia in a polymer electrolyte membrane cell. *ChemSusChem* **15,** e202102180 (2022).
49. Li, M., Verkuil, J., Bunea, S., Kortlever, R. & Urakawa, A. Towards higher NH_3 faradaic efficiency: selective-poisoning of HER active sites by co-feeding CO in NO electroreduction. *ChemSusChem* **16,** e202300949 (2023).
50. Lees, E. W., Mowbray, B. A. W., Parlane, F. G. L. & Berlinguette, C. P. Gas diffusion electrodes and membranes for CO_2 reduction electrolysers. *Nature Reviews Materials* **7,** 55–64 (2022).

51. Tan, Y. C., Lee, K. B., Song, H. & Oh, J. Modulating local CO_2 concentration as a general strategy for enhancing CC coupling in CO_2 electroreduction. *Joule* **4,** 1104–1120 (2020).
52. Kortlever, R., Shen, J., Schouten, K. J. P., Calle-Vallejo, F. & Koper, M. T. Catalysts and reaction pathways for the electrochemical reduction of carbon dioxide. *The journal of physical chemistry letters* **6,** 4073–4082 (2015).
53. Li, W., Yin, Z., Gao, Z., Wang, G., Li, Z., Wei, F., Wei, X., Peng, H., Hu, X. & Xiao, L. Bifunctional ionomers for efficient co-electrolysis of CO_2 and pure water towards ethylene production at industrial-scale current densities. *Nature Energy* **7,** 835–843 (2022).
54. Pan, H. & Barile, C. J. Electrochemical CO_2 reduction to methane with remarkably high Faradaic efficiency in the presence of a proton permeable membrane. *Energy & Environmental Science* **13,** 3567–3578 (2020).
55. Ito, K., Harada, M., Yamada, N. L., Kudo, K., Aoki, H. & Kanaya, T. Water distribution in Nafion thin films on hydrophilic and hydrophobic carbon substrates. *Langmuir* **36,** 12830–12837 (2020).
56. Li, X., Feng, F., Zhang, K., Ye, S., Kwok, D. Y. & Birss, V. Wettability of Nafion and Nafion/vulcan carbon composite films. *Langmuir* **28,** 6698–6705 (2012).

APPENDIX

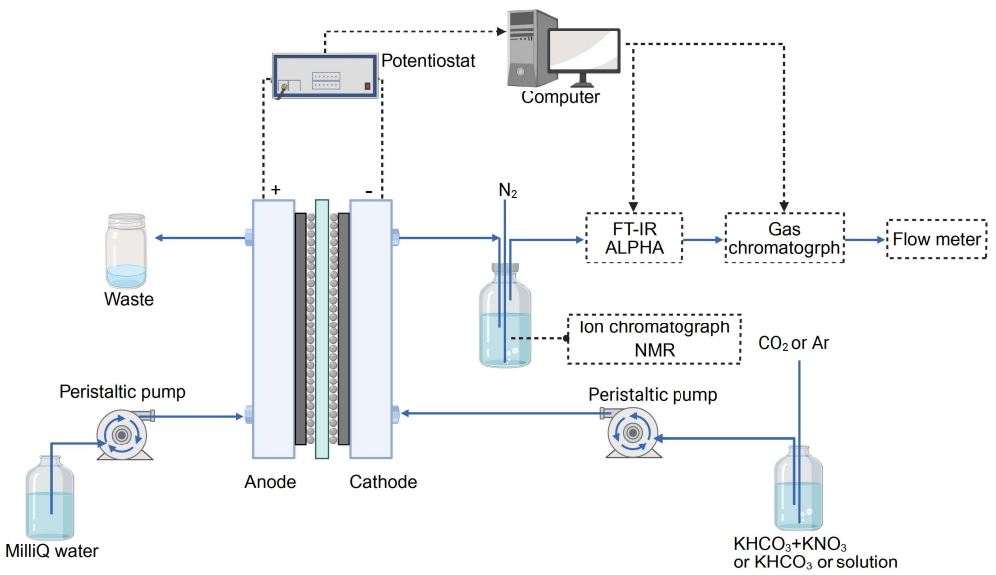

Figure 5.A.1: Flow diagram of electrochemical nitrate reduction to ammonia experimental setup.

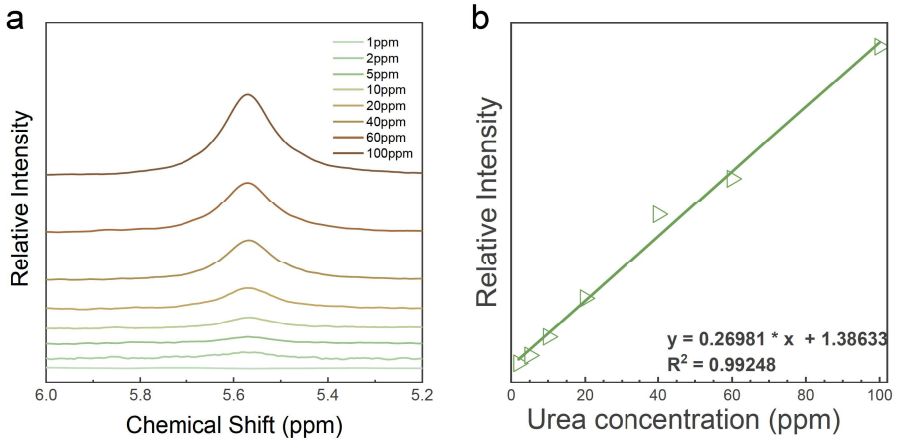

Figure 5.A.2: (a and b) spectrum and calibration curve of urea in water.

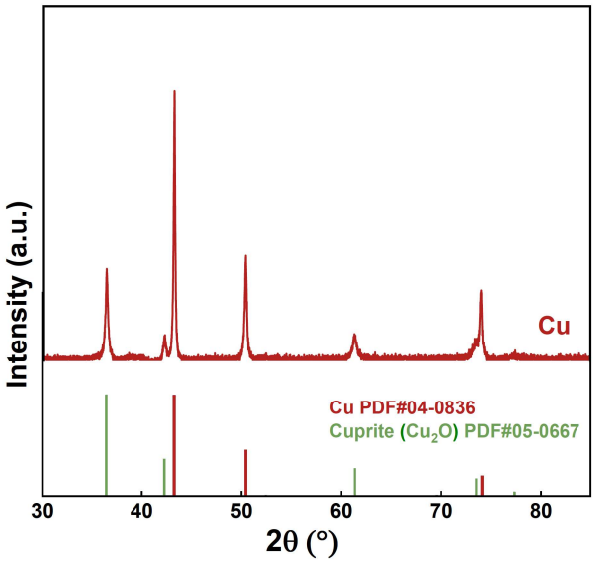

Figure 5.A.3: XRD patterns of Cu Nanoparticles.

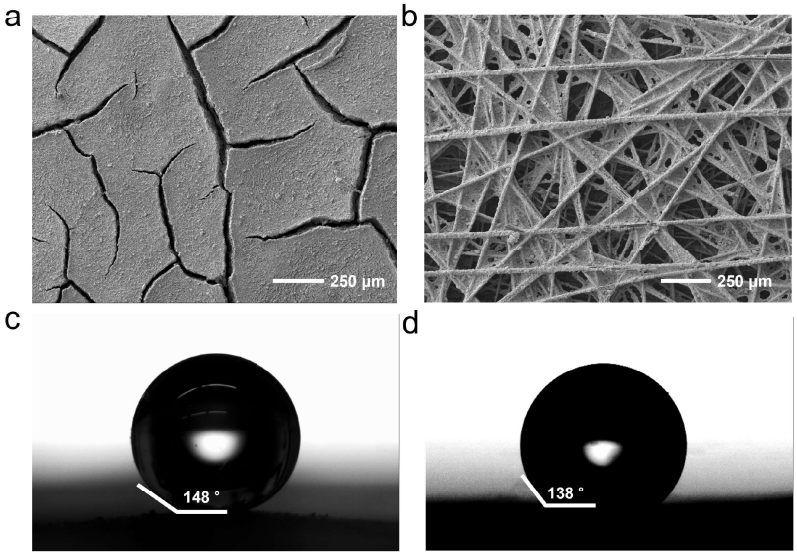

Figure 5.A.4: (a) SEM image of (a) 39BB GDL and b) 39AA ; Contact angle of top surface of (c) 39BB GDL and 39AA GDL.

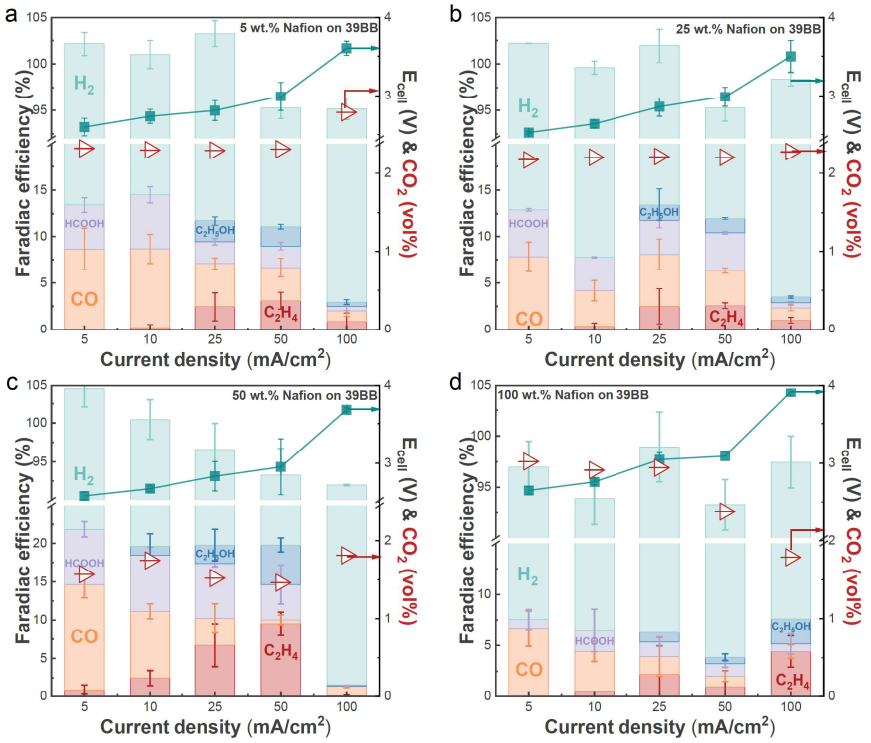

Figure 5.A.5: HCO_3RR with different Nafion on Cu on 39BB. (a) 5 wt.%; (b) 25 wt.%; (c) 50 wt.%; (d) 100 wt.%.

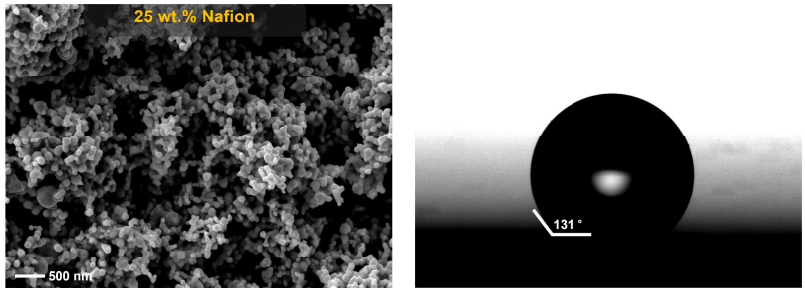

Figure 5.A.6: (a) SEM image and contact angle measurement of 25 wt.% Nafion on Cu on 39BB GDL.

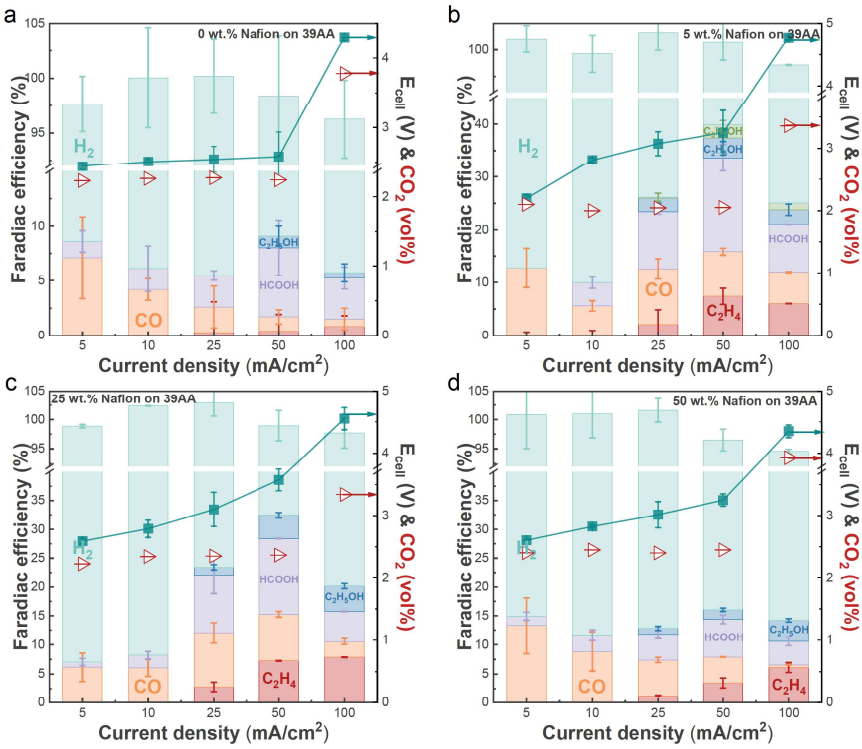

Figure 5.A.7: HCO_3RR with different Nafion on Cu on 39AA. (a) 0 wt.%; (b) 5 wt.%; (c) 25 wt.%; (d) 50 wt.%;

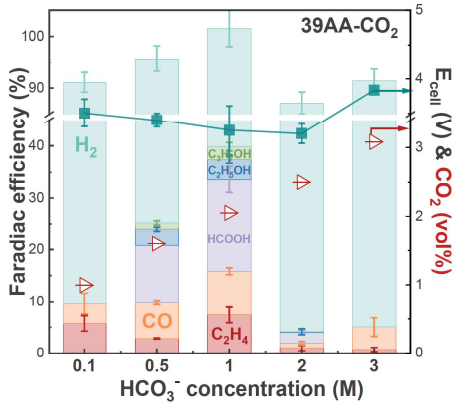

Figure 5.A.8: HCO_3RR with 5 wt.% Nafion on Cu on 39AA in 1M $KHCO_3$ with CO_2 saturation;

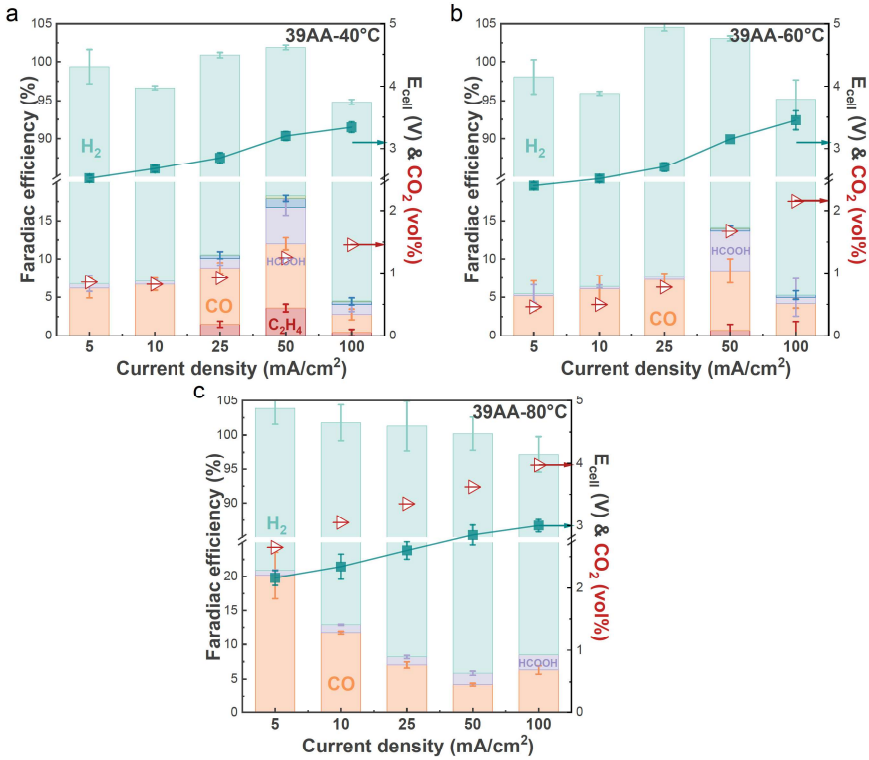

Figure 5.A.9: Temperature effect of HCO_3RR with 5 wt.% Nafion on Cu on 39AA in 1M Ar saturated $KHCO_3$ (a) 40 °C; (b) 60 °C; (c) 80 °C.

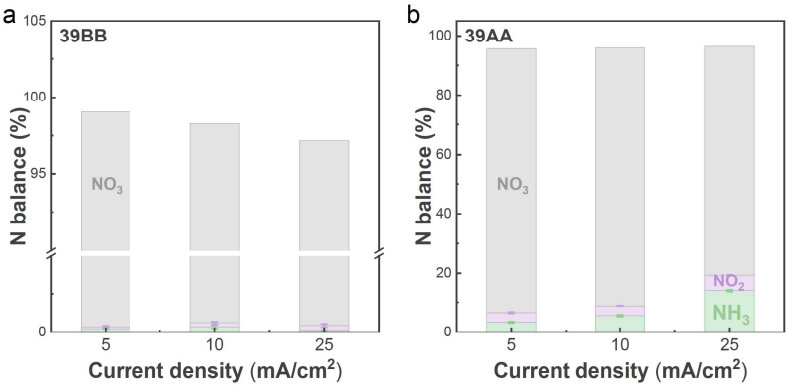

Figure 5.A.10: N balance of nitrate reduction on (a) 39BB and (b) 39AA.

6

Probing Mechanistic Insights via *operando* ATR-IR Spectroscopy-Cell Design

The societal demand for sustainable, large-scale ammonia synthesis has accelerated the development of electrochemical production approaches. Within this field, the electrochemical reduction of nitrogen oxides (NO_x) to ammonia is an area of rapidly expanding scientific interest. Despite recent advances in materials and technology, the reaction mechanisms on the electrocatalyst surface remain complex and poorly understood. This has led to significant scientific questions and experimental outcomes that often conflict with theoretical predictions. To properly investigate the active centers, reaction pathways, and intermediate species involved, *operando* spectroscopic techniques are essential. Therefore, based on the current literature and the known limitations of existing in situ cells, this chapter proposes a novel design concept for an *operando* attenuated total reflectance-infrared (ATR-IR) cell. The proposed design features a membrane and a thin-layer reactant flow to overcome previous challenges.

6.1 Introduction

Electrocatalytic nitrogen oxides (NO_x) reduction to ammonia (NH_3) is a promising technology for green ammonia production, wastewater treatment, and exhaust gases remediation [1]. The success of this process depends on the electrocatalyst, which dictates critical performance metrics like faradaic efficiency (FE), NH_3 production rate, and NO_x conversion efficiencies [2]. To improve catalyst efficiency, it is crucial to understand the specific reaction mechanisms and identify the actual active sites involved [3]. Initial studies often relied on ex-situ characterization, but this approach is limited as the active sites can be dynamic, changing under actual reaction conditions [4, 5]. This highlights the need for advanced techniques to probe electrocatalysts in their working environment.

To overcome the limitations of ex-situ characterization, in-situ spectroscopy has emerged as an indispensable tools which is a significant challenge in the field of electrocatalysis [6]. The term "in-situ spectroscopy" was traditionally used to describe investigations of catalysts under reaction conditions, though it was often applied more broadly, such as to monitor the regeneration of catalysts [7]. Among the various in-situ techniques, vibrational spectroscopies such as Raman and infrared (IR) are particularly powerful as they can offer molecular-level insights into surface phenomena [8]. Among them, IR spectroscopy is a powerful tool to distinguish the reaction intermediates and products [9], however, the spectrum regions of 1000-2000 cm^{-1} associated with oxygen-related compounds and 3000-4000 cm^{-1} with hydrogen-related compounds are strongly influenced by the electrolyte (mainly water) signal.

Therefore, two principal spectroelectrochemical cell configurations have been developed to address this issue: internal reflection and external reflection [10]. The internal reflection method, commonly known as attenuated total reflection-surface-enhanced IR reflection absorption spectroscopy (ATR-SEIRAS), and the external reflection technique, referred to as IR Reflection-Absorption Spectroscopy (IRAS), offer distinct solutions [11], as depicted schematically in Figure 6.1.1.

The ATR-SEIRAS technique operates by immobilizing the working electrode (WE) as a thin film directly onto an internal reflection element (IRE), such as a crystal prism. An IR beam is directed into the IRE at an angle sufficient to cause total internal reflection [12]. This generates an evanescent wave that penetrates a short distance beyond the surface, selectively probing the WE film at the electrode-electrolyte interface. This geometry yields high signal intensities from surface-adsorbed species. The signal-to-noise ratio can be further enhanced by leveraging the surface-enhanced infrared absorption (SEIRA) effect, which occurs with metals like Au, Ag, Pt, or Cu and can produce surface

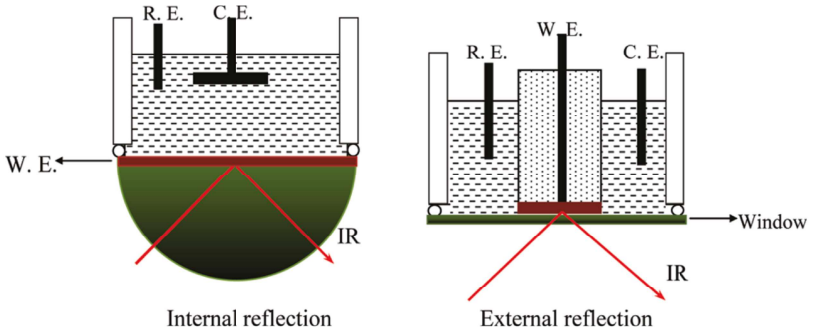

Figure 6.1.1: Schematic representation of the internal and external reflection cell configurations [12].

enhancement factors of approximately 1000 times [13]. Such significant signal amplification allows for the detection of reaction intermediates at very low concentrations. However, this internal reflection configuration has notable limitations. The technique is restricted to thin electrode films (< 100 nm) deposited on an IR-transparent prism, which limits the choice of materials and deposition methods (e.g., sputtering, electroless deposition) [14]. Moreover, its sensitivity is primarily confined to surface-adsorbed species [15].

In contrast, the external reflection (IRAS) configuration positions the WE separate from, and parallel to, an IR-transparent window (e.g., CaF_2) [16]. The electrochemical reaction takes place within a thin electrolyte layer confined between the window and the electrode. The IR beam passes through the window and the electrolyte reflects off the WE surface then travels back to the detector [12]. A major advantage of IRAS is its material versatility; since the electrocatalyst is not deposited on a prism, a wide array of materials, including powders, can be studied. Furthermore, this method can detect both surface adsorbates and species in the solution layer, offering a more complete picture of the electrochemical reaction [17]. The primary drawback, however, is that the requisite thin electrolyte layer can impose severe mass transport limitations. This can cause local depletion of reactants and accumulation of products, potentially distorting the observed reaction mechanism [18, 19].

While both methods are valuable, a critical disconnect exists between conventional spectroelectrochemical measurements and the operating conditions of applied electrolysis systems, particularly the membrane electrode assembly (MEA). Most studies employ batch-type cells which require a supporting electrolyte and, for gas-phase reactions, involve bubbling gas through the liquid electrolyte. This setup is fundamentally different from an MEA-based electrolyzer, such as the polymer electrolyte membrane (PEM) electrolyzer mainly used in this dissertation, where reactions often occur without a bulk sup-

porting electrolyte. Therefore, mechanistic insights gained from a batch cell may not be representative of that under true operating conditions in PEM electrolyzer.

This highlights an urgent need to bridge the experimental gap between classical spectro-electrochemistry and MEA-type electrolyzer performance. This is the purpose of *operando* spectroscopy [20]. The term "*operando*", from the Latin for "operating", signifies the characterization of a material while it is functioning under realistic reaction conditions. By performing spectroscopic measurements under true *operando* conditions, it is possible to assess active sites, identify reaction intermediates, and understand the factors governing the selectivity and efficiency of electrocatalysis. This approach provides the authentic insights required to guide the rational design of next-generation catalysts.

Herein, in this chapter, based on the PEM electrolyzer, we proposed a new cell design to simultaneously probe the adsorbates and the reactant species as formed during the electrocatalytic NO_3^-/NO reduction. Combined with surface enhanced effects, the signals of the dissolved products are also readily detected with properly restricted mass transport by tuning the parallel thickness of the electrolyte layer [21]. A key feature is the integrated micro-machined Si wafer IRE, which permits wide-frequency detection down to 650 cm^{-1} [22].

6.2 Design of a *operando* electrochemical ATR-IR cell

The design of the new *operando* ATR-IR cell was developed based on a comprehensive literature review and the limitations in the current in-situ spectroelectrochemical cell. The primary objectives for this new design are to achieve the followings: i) suitable for an MEA configuration for direct gas flow reaction; ii) enables real-time product analysis by coupling its outlet to external instruments like a mass spectrometer (MS), and iii) allows for operation at temperatures up to 80 °C.

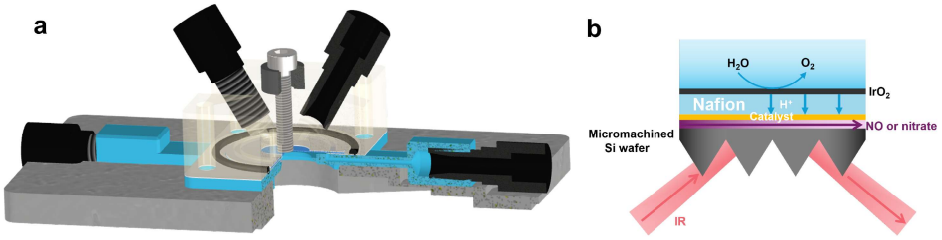

Figure 6.2.1: (a) The cross view of the new cell design; (b) schematic of new cell design .

As illustrated in Figure 6.2.1 (a and b), the two-electrode *operando* cell is constructed from two core components: the main cell body, which houses the cathode, and a lid that

incorporates the anode. A micro-machined silicon wafer is utilized as the IR window, permitting the sensitive detection of surface-adsorbed species in the wavenumber range above 650 cm^{-1}. Reactants flow through a channel created by a spacer situated between the IR window and the electrocatalyst. This spacer is also used to seal the cell assembly. A key feature of the design is a screw that allows for fine adjustment of the compression of the spacer, thereby controlling the thickness of the thin electrolyte layer. Meanwhile, the reactants can flow continuously which can overcome the mass transport limitations during the reaction.

For MEA configurations, a catalyst-coated membrane is placed directly on top of the spacer, with the cathode catalyst facing the silicon IR window and an IrO_2 layer used as the anode catalyst. The lid, or anode half-cell, features a chamber for the flow of the anolyte (e.g., Milli-Q water). To achieve operational temperatures, a heating pad can be placed on top of the lid. The entire cell is sealed to be leak-tight, and the outlet is designed for a direct interface with an MS or an IR spectrometer for continuous monitoring of reaction products.

References

1. Simonov, A. N., Koper, M. T. M. & MacFarlane, D. R. Practical prospects of electroreduction of dilute NO_x streams to ammonia. *Nature Chemical Engineering* **2,** 398–401 (2025).
2. Hermawan, A., Alviani, V. N., Wibisono & Seh, Z. W. Fundamentals, rational catalyst design, and remaining challenges in electrochemical NO_x reduction reaction. *iScience* **26** (2023).
3. Seh, Z. W., Kibsgaard, J., Dickens, C. F., Chorkendorff, I., Nørskov, J. K. & Jaramillo, T. F. Combining theory and experiment in electrocatalysis: insights into materials design. *Science* **355,** eaad4998 (2017).
4. Xiong, Y., Wang, Y., Zhou, J., Liu, F., Hao, F. & Fan, Z. Electrochemical nitrate reduction: ammonia synthesis and the beyond. *Advanced Materials* **36,** 2304021 (2024).
5. Theerthagiri, J., Karuppasamy, K., Mahadi, A. H., Moon, C. J., Rahamathulla, N., Kheawhom, S., Alameri, S., Alfantazi, A., Murthy, A. P. & Choi, M. Y. Electrochemical reduction of gaseous nitric oxide into ammonia: a review. *Environmental Chemistry Letters* **22,** 189–208 (2024).
6. Katayama, Y. *Operando* spectroscopy-inspired design of electrochemical interface. *Electrochemistry* **91,** 101004–101004 (2023).
7. Chen, P. & Somorjai, G. A. in *In-Situ Spectroscopy in Heterogeneous Catalysis* 15–52 (Wiley Online Books, 2002).
8. AlSalka, Y., Schwabe, S., Geweke, J., Ctistis, G. & Wackerbarth, H. Electrochemical and photoelectrochemical water splitting: *operando* raman and fourier transform infrared spectroscopy as useful probing techniques. *Energy Technology* **11,** 2200788 (2023).
9. Bieberle-Hütter, A., Bronneberg, A. C., George, K. & van de Sanden, M. C. M. Operando attenuated total reflection Fourier-transform infrared (ATR-FTIR) spectroscopy for water splitting. *Journal of Physics D: Applied Physics* **54,** 133001 (2021).
10. Harrick, N. J. & Beckmann, K. H. in *Characterization of Solid Surfaces* (eds Kane, P. F. & Larrabee, G. B.) 215–245 (Springer US, Boston, MA, 1974).
11. Zhou, Z.-Y., Lin, S.-C., Chen, S.-P. & Sun, S.-G. In situ step-scan time-resolved microscope FTIR spectroscopy working with a thin-layer cell. *Electrochemistry Communications* **7,** 490–495 (2005).

12. Ye, J.-Y., Jiang, Y.-X., Sheng, T. & Sun, S.-G. In-situ FTIR spectroscopic studies of electrocatalytic reactions and processes. *Nano Energy* **29,** 414–427 (2016).
13. Wang, H.-L., You, E.-M., Panneerselvam, R., Ding, S.-Y. & Tian, Z.-Q. Advances of surface-enhanced Raman and IR spectroscopies: from nano/microstructures to macro-optical design. *Light: Science & Applications* **10,** 161 (2021).
14. Wang, Y., Jiang, K. & Cai, W.-B. Enhanced electrocatalysis of ethanol on dealloyed Pd-Ni-P film in alkaline media: an infrared spectroelectrochemical investigation. *Electrochimica Acta* **162,** 100–107 (2015).
15. Yan, Y.-G., Yang, Y.-Y., Peng, B., Malkhandi, S., Bund, A., Stimming, U. & Cai, W.-B. Study of CO oxidation on polycrystalline Pt electrodes in acidic solution by ATR-SEIRAS. *The Journal of Physical Chemistry C* **115,** 16378–16388 (2011).
16. Faguy, P. W. & Fawcett, W. R. Infrared reflection-absorption spectroscopy of the electrode/electrolyte solution interface: optical considerations. *Applied spectroscopy* **44,** 1309–1316 (1990).
17. Chen, Y. X., Heinen, M., Jusys, Z. & Behm, R. J. Kinetics and Mechanism of the Electrooxidation of Formic Acid—Spectroelectrochemical Studies in a Flow Cell. *Angewandte Chemie International Edition* **45,** 981–985 (2006).
18. Moon, S. M., Bock, C. & MacDougall, B. Setup, sensitivity and application of thin electrolyte layer ATR-FTIR spectroscopy. *Journal of Electroanalytical Chemistry* **568,** 225–233 (2004).
19. Hiltrop, D., Masa, J., Botz, A. J. R., Lindner, A., Schuhmann, W. & Muhler, M. Micrometer-Precise Determination of the Thin Electrolyte Layer of a Spectroelectrochemical Cell by Microelectrode Approach Curves. *Analytical Chemistry* **89,** 4367–4372 (2017).
20. Bañares, M. A. Operando methodology: combination of in situ spectroscopy and simultaneous activity measurements under catalytic reaction conditions. *Catalysis Today* **100,** 71–77 (2005).
21. Ma, X.-Y., Zhang, W.-Y., Ye, K., Jiang, K. & Cai, W.-B. Electrolyte-Layer-Tunable ATR-SEIRAS for Simultaneous Detection of Adsorbed and Dissolved Species in Electrochemistry. *Analytical Chemistry* **94,** 11337–11344 (2022).
22. Morhart, T. A., Unni, B., Lardner, M. J. & Burgess, I. J. Electrochemical ATR-SEIRAS Using Low-Cost, Micromachined Si Wafers. *Analytical Chemistry* **89,** 11818–11824 (2017).

7

Conclusion and Outlook

7.1 Conclusion

This dissertation addresses critical challenges in the electrocatalytic synthesis of N-based fertilizers, focusing on catalyst engineering to overcome two primary shortcomings: i) the reliance on noble metals and the inefficient utilization of their active sites, and ii) a limited fundamental understanding of the reaction mechanisms and rate-determining steps. While this work does not present a perfect solution, it offers novel perspectives and methodologies for studying reaction mechanisms in electrochemical NO_x reduction under practical operating conditions. Advancing this mechanistic understanding is a crucial step toward the rational design of catalysts with improved performance and lower cost, which is essential for the eventual scale-up of this technology.

As a primary step, this dissertation first addressed the challenge of inefficient metal utilization. **Chapter 2** demonstrated the successful application of polyvinylpyrrolidone (PVP) as a surface modifier for Ru/C catalysts to enhance performance in the electrochemical nitrate reduction reaction. The use of PVP as a capping agent not only enabled a reduction in Ru loading from 40 to 10 wt.% but also synergistically suppressed the competing hydrogen evolution reaction while promoting the formation of adsorbed hydrogen (H*) required for nitrate hydrogenation. This initial work thus presents a viable strategy for developing low-loading, high-selectivity catalysts and provides fundamental insights into controlling reaction pathways via strategic surface modification.

To further move away from noble metals, **Chapter 3** investigated earth-abundant molyb-

denum disulfide (MoS_2) for the direct electroreduction of nitric oxide for ammonia synthesis. This work revealed that product selectivity is highly dependent on the crystal phase of catalyst. Specifically, 2H-MoS_2 achieved a high faradaic efficiency of 86% towards ammonia, while the 1T′-MoS_2 phase preferentially formed N_2 via a distinct reaction pathway. This demonstrates that the rational selection of a different catalyst structure is a powerful strategy for controlling reaction outcomes.

Chapter 4 provided foundational insights for C-N coupling by introducing a CO-mediated selective poisoning strategy. Co-feeding CO with NO suppressed the competing hydrogen evolution reaction by selectively blocking H* adsorption sites, which enhanced the ammonia faradaic efficiency on Pd/C by 95%. This work demonstrates how to control surface coverage through competitive adsorption, a critical prerequisite for designing catalysts for direct C-N coupling synthesis.

Building upon the insights from the previous chapters, **Chapter 5** focused on the direct synthesis of urea via the electrochemical co-reduction of bicarbonate and nitrate. This research began with the establishment of a robust urea detection method and a systematic optimization of the cell configuration. A key breakthrough was the switch to a catalyst-coated substrate design, enabling the *in situ* generation of CO_2 from liquid bicarbonate. Urea was successfully produced with a reproducible faradaic efficiency of 16% by co-feeding both reactants into the optimized system using a Cu catalyst, thereby demonstrating a viable pathway for the sustainable synthesis of urea from waste C and N sources in a PEM electrolyzer.

Lastly, **Chapter 6** addressed the need for deeper mechanistic understanding by developing an innovative *operando* ATR-IR cell. Bridging the gap between batch cells and practical MEA systems, this design incorporates a membrane and dynamic flow to enable mechanistic studies under realistic operating conditions. This methodological advance provides a crucial tool for investigating complex phenomena directly at the catalyst interface.

7.2 Outlook

Based on the findings discussed in this thesis, while significant progress has been made in the electrochemical synthesis of fertilizers, several hurdles must be overcome to achieve industrial-scale production. Future research should prioritize three key areas: advanced catalyst development, comprehensive system engineering, and a deeper mechanistic understanding under operating conditions.

Catalyst development - beyond noble metals: A critical future direction is the contin-

ued transition from nobel noble metals—such as ruthenium (Ru), platinum (Pt), and iridium (Ir) to earth-abundant materials. While catalysts based on elements like molybdenum disulfide (MoS_2) may initially exhibit higher operational expenses due to greater overpotentials, this can be offset by the falling cost of renewable electricity. This is a worthwhile trade-off to reduce the initial capital investment for future scalability.

Furthermore, developing the electrochemical NO_x reduction reaction in alkaline electrolytes could enable the use of non-noble metal catalysts, such as nickel oxide, for the anodic oxygen evolution reaction (OER). However, this approach introduces the operational challenge and cost associated with circulating highly corrosive alkaline solutions.

Product selectivity: ammonia, nitrogen, or other targets? Another fundamental question is which products should be targeted from the electrochemical NO_x reduction reaction. Much recent research has focused on producing ammonia (NH_3). However, using the low nitrate (NO_3^-) concentrations typical of polluted groundwater or industrial wastewater (often < 0.1 M) leads to a progressive deterioration of reaction rates. The resulting ammonia is often produced in a dilute stream, requiring energy-intensive downstream separation and concentration steps. A similar challenge exists for the reduction of diluted gaseous NO from exhaust streams.

To address this, one potential solution is to couple nitrogen (N_2) oxidation to NO_x with NO_x reduction processes or to develop efficient methods for recovering and concentrating NO_x contaminants from the environment. However, the energy efficiency of these preliminary steps requires much-needed improvement, as highly concentrated NO_x streams is essential for this technology to become a competitive alternative to the Haber-Bosch process.

Alternatively, targeting N_2 as a genuinely innocuous product could be a more pragmatic and environmentally friendly direction for the purpose of wastewater remediation or exhaust gas removal. In **Chapter 3**, we discovered that phase engineering of earth-abundant MoS_2 could shift selectivity toward N_2 production. This presents an intriguing avenue for further investigation, although more research (e.g. *in situ* near ambient pressure XPS (NAP-XPS)) is required to fully understand the mechanism driving this selectivity and optimize the process.

System and reactor engineering: To meet net-zero carbon emission pledges, some industries are beginning to use green hydrogen (H_2), generated from water electrolysis, for the hydrogenation of N_2 in a modified Haber-Bosch process. This serves as a transitional strategy while direct electrochemical routes like N_2-to-NH_3 or N_2-NO_x-NH_3 face scalability challenges.

Reflecting this push toward practical application, the research field is moving from testing catalyst performance in idealized H-cell or batch configurations to more industry-relevant electrolyzers, such as proton-exchange membrane (PEM) and anion-exchange membrane (AEM) systems. This transition necessitates a broader focus that extends beyond catalyst design to include reactor engineering. Key aspects requiring optimization include flow fields (e.g., serpentine vs. parallel), electrolyte flow rates to overcome mass transport limitations, and thermal management.

The need for deeper mechanistic understanding: Underpinning all these efforts is a critical need for a more profound mechanistic understanding of the reactions at the catalyst-electrolyte interface. The development and application of advanced *in situ* and *operando* characterization techniques are paramount. By directly probing reaction intermediates, active sites, and catalyst degradation pathways under operating conditions, the field can accelerate its move from empirical screening to the rational, predictive design of next-generation catalysts. While our own efforts to develop an *operando* attenuated total reflectance-infrared (ATR-IR) spectroscopy cell were promising, time constraints prevented its full implementation. Nonetheless, this and similar approaches deserve significant future investment to unlock a deeper understanding of these complex electrochemical systems, which could help addressing the above-mentioned challenges too.

In conclusion, addressing these interconnected gaps in catalyst cost, product strategy, system engineering, and fundamental understanding is essential for the development of electrochemical synthesis as a viable technology. Successfully doing so will not only revolutionize the production of N-based fertilizers but also offer a pathway to decarbonize the broader chemical industry, including the synthesis of C-based products, thereby significantly reducing its enormous carbon footprint.

ACKNOWLEDGEMENTS

Reflecting on the past 4 years, I realize that this dissertation represents not just my research but a significant chapter of personal growth and perseverance. Yet, research is rarely a lonely journey; this thesis is the result of countless hours of collaboration and discussion. While the words on these pages are my own, the ideas and motivation behind them were cultivated through the help of a supportive community, and it is a privilege to acknowledge those who have walked this path with me.

My sincerest thanks go first to **Atsushi**. Thank you not only for the opportunity to work in the Catalysis Engineering lab but also for fostering an environment of curiosity and creativity. You provided me with the freedom to pursue my research interests, and I am grateful for the trust you placed in me, allowing me to explore new directions, extend collaborations with others, and learn from my own mistakes. Your door was always open whenever I encountered difficulties, no matter how crazy your schedule was, you were always willing to help me out in the lab and find time for us. Your belief in my potential, even when things were not going according to plan, was a constant source of motivation. Beyond your scientific guidance, I am deeply grateful for your empathy. I have always been impressed by your friendly nature and your ability to greet everyone with a smile. Your dedication to your weekly gym sessions is inspiring and adds to what makes you such a unique and special professor. I have learned a tremendous amount from you about both research and life, thank you so much!

I would like to extend my special thanks to my co-supervisor, **Ruud**. I am grateful for your consistent support and valuable scientific advice over the last 4 years. You provided me with excellent mentorship, and our regular meetings were always a source of clarity and encouragement. Thank you for inviting me to the group meetings; I really enjoyed all the discussion there with our electrochemistry team.

I would like to express my sincere gratitude to my committee members: **Prof. dr. F.M. Mulder, Prof. dr. M.T.M. Koper, Prof. dr. F. Jiao, Dr. D.M. Morales Hernández, and Dr. T.E. Burdyny**. Thank you for taking the time out of your busy schedules to read and evaluate this thesis. I deeply appreciate your critical insights and your willingness to participate in my defense.

A special acknowledgment to my paranymphs: **Chunyu, Qing**, for being such incredibly supportive friends throughout this journey. Our amazing girls' sessions, filled with great food, shopping, and endless conversations, were the perfect way to recharge my batteries. Thank you for bringing so much joy and balance to my life outside of the university.

I would also like to express my gratitude to all the technicians who have supported my research. **Bart**, thank you for your technical support and for helping me optimize my experimental setup. Your effort to keep the instruments running and your practical solutions to all the technical problems were invaluable to all of us. You are the best engineer and also a passionate researcher in the CE lab. Hope you enjoy your retirement life. **Willy**, thank you for your help with the N_2 physisorption measurements and for always taking care of my chemical orders. I have always been deeply impressed by how organized you keep the chemicals in the lab and LabServant system. Knowing that the chemicals were always safe, perfectly organized, and easy to find made our daily life in the lab so much smoother. **Liliana**, thank you for helping me out with the GC, IC and HPLC, as well as for always taking care of my lab orders. It was always so incredibly nice and pleasant to chat with you. **Herman**, thank you so much for your invaluable help with the sputtering and ATR measurements; simply saying this work would not exist without you. It was always so nice chatting with you, and working alongside you was a genuine joy. **Joost**, thank you very much for your help with Inventor. Your engineering and design skills are incredibly impressive, and I learned a lot from you! I also really appreciated you inviting me to the coffee breaks. **Bart**, thank you for your help in XPS measurement and for your assistance with peak fitting. I know it is very hard to fit all the peaks in the spectrum correctly. **Harrie**, thank you for helping with finding the MFCs in building 67 and making the connection in my setup. Hope you enjoy your new roles in the other department! **Xiaohui**, thank you for helping me with the XRD measurement and for hosting such lovely parties and for all the nice discussions we shared. **Stephen**, thank you for your help with NMR measurement. It seems water is just as unavoidable in our NMR samples as the endless rain is in Delft! **Evgeny**, thank you for your invaluable assistance with the NMR measurements as well; I truly appreciate your time and expertise. **Els**, thank you for your help with all the administrative tasks. **Veby**, thank you for helping fix my lab access in the LabServant system. It was always such a headache when it did not work.

My time in CE would not have been the same without our wonderful group of colleagues that I was lucky enough to work alongside. To my colleagues, past and present: Thank you all for creating such a vibrant and enjoyable working environment! **Sorin**, your pioneering work laid the foundation for this thesis. I am deeply thankful for your time

training me on the experimental protocols, for answering my endless questions during my first year, and for sharing your understanding of the project. **Nat**, you are not only a fantastic colleague but also my best friend in the group. Thank you for always encouraging me to step outside the lab. Whether it was dragging me to Zumba/the gym or inviting me to your meetup events (book clubs and foodies), your friendship helped me relax and recharge when I needed it most. This journey would have been far more stressful without you. **Disha**, thank you so much for your constant encouragement and kindness during my first year, which helped me overcome my initial shyness and gave me the confidence to express my ideas freely. **Kei**, thank you for helping me with Python and improving my programming skills. Thank you for being a great friend outside the lab in my first year, sharing nice memories of social gatherings. **Donato**,thank you for always offering brilliant suggestions whenever I was stuck and for constantly encouraging me to take a vacation. Even though I rarely took your advice, your suggestions are appreciated, and I will certainly consider them in the future. **Atul**, thank you for mentorship and guidance. I truly appreciated your insightful suggestions. **Pratik sensei**, thank you for helping me with the synthesis. I admire your unique 'power' to bring people together. You have a natural ability to unite the group and create a warm, cohesive atmosphere that I truly miss. **Afreen**,our unforgettable trip in Vienna and Budapest with Nat as well is a memory I will always cherish. Thank you for being such an amazing travel companion and for the great conversations. **Jose**, your strong expertise and willingness to share your knowledge were incredibly helpful to my research. I will never forget the time that we both worked in the office during my first Christmas in the Netherlands. **Benjamin**, thank you for your quick, insightful discussion when I needed to bounce ideas around and for always keeping us strictly on schedule for lunch! Beyond our time in the lab, thank you so much for the invitation to your PhD defense and your wedding, and I am so grateful to have celebrated those milestones with you as a friend. **Ahmad**, having started our PhDs only a few months apart, we experienced the entire rollercoaster of this process together. Thank you for being such a wonderful, grounded colleague through all the highs and lows. We all miss all the insightful lectures from you. **Ezgi**, it was really nice having a colleague working on electrochemistry in our lab. Thank you for understanding the very specific challenges of our research area better than anyone else. **Jeroen**, thank you for sharing your experience and the nice discussion about ionomer! It was a nice experience in neutron scattering! **Manoj**, your engineering skills are incredibly impressive, especially watching you build your entire setup from scratch, and I have always appreciated how willing you were to help others in the lab. Thank you for always being such a kind and supportive lab mate. **Damian**, you have always acted as the ultimate 'catalyst' for our group. Your brilliant scientific mind and deep passion for catalysis are truly

contagious, and I always feel inspired by our discussions. **Harith**, you are the expert in Raman spectroscopy; thank you very much for helping me with Raman measurements and for your support during the last steps of my PhD with constant advice and fruitful discussions. **Dhanaji**, thank you for being a fun and supportive friend. Thank you for always patiently 'carrying' our team to victory despite my terrible gaming skills. **Kaustubh**, thank you for generously sharing your experience and knowledge regarding AEM water electrolysis and for taking the initiative to start our regular badminton sessions. **George**, thank you for helping me with the EXAFS data analysis. **Shota-San**, thank you for your hands-on help with the ATR measurements and for the helpful discussions regarding XPS data interpretation. **Tomone-San** and **Fumi-San**, thank you for the inspiring discussions we shared and for all the joyful memories we created. **Pietro**, a big fan of Prof. Ding Ma, thank you for teaching me Italiano; now I know more Italian than Dutch. **Ivan**, run more on the badminton court. **Julius, Letizia, Tsukasa, Charlotte, and Misaki**, thank you for the happy moment that we shared together.

Thanks also to all the members of Monique's group. To **Jelco**, thank you for sharing the common suffering in the lab and the mutual struggles of finishing our thesis. Our chats at the coffee corner-venting about our research with terrible coffee in hand, were kind of the perfect way to release the pressure. To **Jintao, Begum, Sven**, thank you for the great interactions both inside and outside the lab and for all the joyful moments we spent together.

I would also like to thank all the members from the ISE section. **Sumeia**, thank you for organizing all the amazing events, you are the best organizer! **Sasha**, thank you for the great discussions and your help with the DFT calculations. **Adarsh and Margareth**, thank you for the fun sports sessions we shared together; they were always a great time.

A huge thank you goes to all the bachelor and master students I had the pleasure of working with as a daily supervisor. **Jarco, Jinghan, Harsh, Frank, Joy, Sake, and Max**, thank you all for diving into the demanding lab work with me, helping with the data analysis, and sharing the many headaches that came with unexpected results. My whole PhD experience was profoundly shaped by your contributions. Thank you all for bringing a wonderful variety of perspectives and a constant stream of motivation that I will always be grateful for. A special thanks to **Frank**, a wonderful student with a great passion for electrochemistry. Thank you for your continued support, your tireless hard work, and your significant contributions to the MoS_2 work. I owe you a big acknowledgment! Thank you, Frank! You are the best, and you will definitely become a future electrocatalysis star. **Martino**, thanks for taking the challenge with COMSOL modeling, hope we could make it work!

I would like to extend my sincere thanks to colleagues from Process & Energy. **Shilong, Dr. Fu**, thank you for your unwavering support during my whole PhD, especially for your insightful advice and our fruitful discussions. Your level of scientific accuracy and exceptional work ethic stand out exceptionally. I am confident that these outstanding traits will lead you to great success in academia. **Ahmed**, thank you for helping with the experiment and sharing your knowledge about electrochemistry. **Boza**, thank you for helping me with the Raman measurement. I hope you are doing well in DTU. **Katie**, thank you for helping me with the spray coater. I wish you all the best with finishing your PhD. **Katherine, Shahid, Asvin, Kelvin, Nandalal**, thank you all for the warm welcome in the group during these years.

I would like to extend my gratitude to all my colleagues in the Chemical Engineering department. **Vineesh**, thank you so much for kindly helping with the UPD measurement, I am very much impressed by your electrochemistry knowledge. **Jesse**, thank you for your help with the product detection after bicarbonate reduction and for always being so kind and open to discussion. **Tiange**, thank you for sharing your suffering with urea synthesis and your experience with nitrate reduction, I really like the way that you think and approach the question. **Hugo**, thank you for patiently showing me how to perform the ATR experiments. **Ai-Yu**, thank you for your help with anion IC measurement. **Christal**, thank you for sharing your fascinating project on CO absorption and desorption with me. **Tu**, thank you for joining the badminton sessions; playing together was always so fun and the perfect way to relax.

A special acknowledgment goes to **Chuncheng, Guotai, Wenjun, Bowen, Ying, Juncheng, Mengran, and Nikki**. Thank you for being such a wonderful part of my life, for hosting so many great parties, and for preparing such delicious Chinese dishes. I truly cherish all the joyful moments we have spent together. A special thanks to **Ziqing**, thank you for sharing the mutual struggles of PhD life and for being such a comforting friend. From admiring your deep love for your pets to cycling together for dinner on warm summer evenings, I truly treasured our time together. Thanks to all my friends in Delft, **Xiaopeng, Ruipeng, Shuainan** for inviting me with parties during the traditional Chinese festivals. Thanks to **Yanwei, Daiqi, Chengtian, Mingliang, Ming, Gao** for sharing your experience and positive energy with me.

After years of living abroad, the concept of home sometimes feels far away. But no matter how much I travel, my heart remains firmly anchored in China, and that is all thanks to my lifelong friends. The goodness of our friendship has kept my ties to my hometown strong across the distance. I want to extend a special thank you to my friends from high school, **Zuanyi** and **Xiaoyuan**; from my undergraduate years, **Bochun** and **Zihan**; and

from my master study, **Prof. Bian**, **Dongxu (now Prof. Cui)**, **Li**, **Jiawei**, and **Yulin**. Thank you all for your continuous support from afar.

A very special thank you goes to **Yuan**. Words cannot fully express how grateful I am to have had you by my side throughout this journey. I will never forget the fateful day that we first met on the train, and I truly believe it was destiny that brought us together. Thank you for always believing in me, especially on the days I doubted myself. I cannot wait for all the destinations ahead of us!

Finally, to my family. This thesis, along with every other achievement in my life, is entirely dedicated to you. 爹地，妈咪，感谢你们这些年无条件的支持和关爱！谢谢你们一直以来对我的栽培与支持，是你们给了我追逐梦想的翅膀。无论我走得多远，你们永远是我最坚实的后盾和避风港! 霆锋，感谢你默默承担了更多陪伴和照顾父母的责任，希望未来的你能在自己的道路上闪闪发光！

Curriculum Vitæ

Min Li

She was born on July 15, 1995 in Guangzhou, China. She received her Bachelor's degree at Dalian University of Technology, China. Then, she pursued a Master's degree at Southeast University, Nanjing, China. She joined the Catalysis Engineering group as a PhD student under the supervision of prof. dr. ir. Atsushi Urakawa, at the Chemical Engineering department and co-supervision of dr. ir. Ruud Kortlever at the Process and Energy department of Delft Unversity of Technology in July 2021. Her research focus on electrocatalytic conversion of NO_x and CO_x in PEM electrolyzer. Most results of her doctoral research are presented in this dissertation.

List of Publications

6. **Min Li**, Frank Hernandez Baena, Shota Matsuo, Mingliang Chen, Boaz Izelaar, Ruud Kortlever, Atsushi Urakawa, *Tuning Product Selectivity in Direct Electroreduction of NO via Phase Engineering of MoS2 Nanosheets in Water-fed PEM Electrolyzer*, In preparation: Journal of Materials Chemistry A.

5. **Min Li**, Jinghan Zhao, Vineesh Thazhe Veettil, Shilong Fu, Ahmed Mohsen Ismail, Ruud Kortlever, Atsushi Urakawa, *Boosting the Electroreduction of Nitrate to Ammonia in a PEM Electrolyzer with Polymer-Modified Ru Nanoparticles*, ACS Catalysis (2026).

4. Shilong Fu, Boaz Izelaar, Ming Li, Qi An, **Min Li**, Wiebren de Jong, Ruud Kortlever, *The effect of carbon supports on the electrocatalytic performance of Ni-NC catalysts for CO_2 reduction to CO*, Nano Energy 133, 110461(2025).

3. Tiange Yuan, **Min Li**, Siddhartha Subramanian, Jesse Kok, Mengran Li, Atsushi Urakawa, Oleksandr Voznyy, Thomas Burdyny, *Sequential electrocatalytic reactions along a membrane electrode assembly drive efficient nitrate-to-ammonia conversion*, Cell Reports Physical Science 5, 6(2024).

2. Sorin Bunea, **Min Li**, Ezgi Demiroz, Peng Zeng, Marc Georg Willinger, Atsushi Urakawa, *Influences of Nanostructures of Sn and Ir for the Oxygen Evolution Reaction in Polymer Electrolyte Membrane Water Electrolysis*, Energy & Fuels 38, 1 (2023).

1. **Min Li**, Jarco Verkuil, Sorin Bunea, Ruud Kortlever, Atsushi Urakawa, *Towards Higher NH_3 Faradaic Efficiency: Selective-Poisoning of HER Active Sites by Co-Feeding CO in NO Electroreduction*, ChemSusChem 16, 22 (2023).



2026